Lead-Free Persistent Joints Between NbTi Wires



Timothy Davies

Wadham College

Supervisors: Professor S. C. Speller & Professor C. R. M. Grovenor

A thesis submitted for the degree of

Doctor of Philosophy

at the University of Oxford



Trinity Term 2019

Abstract

Lead-Free Persistent Joints Between NbTi Wires
Timothy Davies, *Wadham College*
A thesis submitted for the degree of Doctor of Philosophy at the University of Oxford

Commercial Magnetic Resonance Imaging (MRI) scanners are entirely dependent on persistent-mode superconducting magnets for the production of the high fields with excellent temporal stability required for high-resolution imaging. In turn these are reliant on the formation of persistent joints between the superconducting wires. For the superconductor of choice for MRI, Nb–45wt%Ti (NbTi), this has been performed routinely in industry using lead-based solders, but the environmental and health risks of using lead mean there is a strong desire to move to alternative solutions. Whilst the lead-solder solution has long been effective, there is still little understanding of much of the underpinning science behind effective joint formation. As such, the aims of this work were to try and understand more about the limiting factors of superconducting joint performance, and to use this to produce improved lead-free superconducting joints.

The work is split into three sections. The first section uses x-ray photoelectron spectroscopy to explore the oxidation of NbTi. The morphology, chemistry and thickness of oxides formed over industrially relevant timescales between 15 seconds and 1 hour were characterised using angular-resolved measurements. The earliest stages of oxide growth were explored by exposing the surface to very small controlled doses of pure oxygen. The implications of these results for joint manufacture are discussed.

The second section looks at some of the key problems associated with solder joint techniques currently used in industry. In particular, high current transport measurements were used to characterise the degradation of wire performance with applied temperature and time under conditions relevant to matrix replacement soldering. From these measurements a "safe" window for wire heat-treatment during jointing is presented. The effect of barrier layers was studied using a combination of magnetisation and decay measurements on lead-based joints on NbTi wires with and without a niobium diffusion barrier, with a clear difference in the decay performance observed due to the presence of the barrier. Interestingly no-such decrease was observed in the magnetisation measurement, demonstrating the the need for decay measurements to show true persistent performance. The section concludes by presenting a detailed characterisation of joints made from the best-performing lead-free solder known to me, $Bi_{15}In_{50}Sn_{35}$. A variety of superconducting measurements were performed on these joints, and the performance under each was compared and contrasted. The limiting factors of these lead-free joints are discussed.

Finally, in an attempt to improve the performance of lead-free solders, a composite incorporating NbTi filaments into a low-melting point matrix was developed. The production and microstructure of the composites are discussed, and then bulk composites were characterised with different filament geometries and matrix materials. The composites demonstrated an unexpected behaviour, with the NbTi filaments failing to carry current between neighbouring filaments at high field as desired. However, at fields above the matrix upper critical field there was a field at which the filaments appeared to join together and demonstrate a linked network behaviour, with a corresponding improvement in the superconducting performance of the bulk composite. A possible mechanism for this behaviour is presented.

Acknowledgements

Throughout my time in Oxford I have been so grateful for the fantastic support I have had from my colleagues, friends and family

Thanks must first go to my supervisors, Chris Grovenor and Susie Speller, who have always been there to provide advice, support and generally guide me throughout the course of my DPhil. Your openness to new ideas and encouragement to pursue those "Friday afternoon experiments" led to much of the more interesting areas of this thesis!

I am also grateful to my industrial supervisors at Siemens Magnet Technology, Adrian Thomas and M'hamad Lakrimi, both for the CASE studentship that funded the project and for the excellent technical advice you have provided. Many thanks also for the provision of samples and materials that were essential to the project. Thanks must also go to Mariusz Wozniak for the development of, and the help running, the large-scale decay measurement rig.

I must thank my collaborators at the Clarendon Laboratory, who made the superconducting property measurements possible. Thanks must go to Amalia Coldea and Dharmalingam Prabhakaran for allowing me to spend (a lot) of time on their apparatus. Special thanks must go to Kieran McCall and Matt Bristow for the help with measurements and apparatus, along with many useful discussions about superconductivity, and for generally making my time in the physics department a pleasure.

Thank you to David Morgan at Cardiff University/Harwell XPS and Tien-Lin Lee at the Diamond Light Source for help with XPS measurements

Thanks must go to all the staff in the materials department for help on equipment and training, especially Jennifer Holter, Graham Wyatt, Phil Holdway, Tony Wheeler, Alison Crossley and Colin Johnston. Thanks to Mimi Nguyen for various safety related advice. Thanks to Keyna O'Reilly and Paula Topping for allowing me to help with demonstrating in the lab. And to Jayne Shaw for getting me involved with as many outreach activities as possible

To the entirety of the CfAS materials group, past and present, I have thoroughly enjoyed your company and am grateful to have been able to spend time with you all. Special thanks must go to Clara Barker and Rob Gresham for your help with tasks to numerous to describe in the lab. And for helping replace all the hotplates I destroyed...

I am grateful to have made so many friends in Oxford, far too numerous to list here! Thank you so much for your company and for generally keeping me sane when things were hard

Last, and most definitely not least, I must thank my family. Nanny and Grandad, thank you for the many Blackwells lunches, it is always lovely to see you and I always love the company along with the inevitable grilling on obscure science! Thanks so much Mum, Dad and Emma for helping me when things were tough and really helping keep me going at all times!

Statement of Originality

The work described in this thesis was undertaken in the Department of Materials at the University of Oxford under the supervision of Professor Susie Speller and Professor Chris Grovenor between October 2015 and May 2019.

No part of this thesis has been previously submitted for a degree at this or any other university. The work of others has been freely drawn upon and is duly acknowledged in the text. A list of references is provided at the end of the thesis.

Some of the work described has been presented in journal articles and at international conferences listed below:

S. Santra, **T. Davies**, G. Matthews, J. Liu, C. Grovenor and S. Speller. *The effect of the size of NbTi filaments on interfacial reactions and the properties of lead-free superconducting solder joints.* Materials and Design, 2019. Accepted.

25th Conference on Magnet Technology, Amsterdam, Netherlands, August 2017, *Lead-free persistent-mode joints between NbTi wires*, Poster Presentation

13th European Conference on Applied Superconductivity, Geneva, Switzerland, September 2017, *Lead-free persistent-mode joints between NbTi wires*, Poster Presentation

27th International Cryogenic Engineering Conference – International Cryogenic Materials Conference 2018, Oxford, UK, September 2018, *Atmospheric oxidation of NbTi superconductors*, Oral Presentation

Applied Superconductivity Conference 2018, Seattle (WA), USA, October 2018, *Lead-free persistent-mode joints between NbTi wires*, Poster Presentation

This thesis is approximately 40,000 words in length.

Contents

1 Introduction **9**
- 1.1 Introduction . . . 9
- 1.2 Theory of Superconductivity . . . 10
  - 1.2.1 The Superconducting State . . . 10
  - 1.2.2 Flux Penetration: Type I and II Superconductors . . . 12
  - 1.2.3 Flux Pinning: J_c Control . . . 14

2 Literature Review **16**
- 2.1 Technological Superconductors . . . 16
- 2.2 NbTi Wires . . . 17
  - 2.2.1 Structure and Stabilisation . . . 17
  - 2.2.2 Microstructure and Manufacture . . . 17
- 2.3 Current NbTi Jointing Methods . . . 19
  - 2.3.1 Solder Joints . . . 19
  - 2.3.2 Direct Filament-Filament Bonding . . . 27
- 2.4 Persistent Joints Between Other Superconductors . . . 32
- 2.5 Oxidation of Niobium Titanium . . . 33
- 2.6 Outlook and Overview of This Work . . . 37

3 Experimental Methods: Characterisation of Superconductors **38**
- 3.1 Magnetic Measurements . . . 39
  - 3.1.1 Bulk Measurements . . . 39
  - 3.1.2 Hardware . . . 44
  - 3.1.3 Joint Measurements . . . 46
- 3.2 Decay Measurements . . . 50
  - 3.2.1 PPMS Decay Measurements . . . 52
  - 3.2.2 Large-Scale Decay Measurements . . . 53
- 3.3 Transport Measurements . . . 54
  - 3.3.1 Low Current . . . 55
  - 3.3.2 High Current . . . 56

4 Atmospheric Oxidation of NbTi Superconductors **64**
- 4.1 Background Theory . . . 65
- 4.2 Experimental Details . . . 69
  - 4.2.1 Spectrometer Details . . . 69
  - 4.2.2 Sample Details . . . 71
  - 4.2.3 Surface Preparation . . . 73
  - 4.2.4 Peak Fitting and Analysis . . . 74
- 4.3 Peak Models . . . 77

4.3.1 Titanium . . . 78
4.3.2 Niobium . . . 82
4.4 Air Oxidation Experiments . . . 85
4.4.1 Results . . . 85
4.4.2 Analysis . . . 87
4.5 Gas Dosing Experiments . . . 95
4.5.1 Gas Dosing Results . . . 95
4.5.2 Initial Oxidation of Heat Treated NbTi . . . 100
4.6 Chapter Conclusions . . . 101

5 Performance of Solder Joints 102
5.1 Transport Properties of NbTi Wires . . . 102
5.1.1 Supercon, Inc. 54S43 Wire . . . 103
5.1.2 Transport Properties of As-Received Wire . . . 103
5.1.3 Performance of Heat Treated NbTi . . . 106
5.1.4 Conclusions on Wire Performance . . . 112
5.2 Lead-Based Joints . . . 113
5.2.1 The Effect of Interfaces on Joint Performance . . . 114
5.2.2 Niobium Diffusion Barrier Wire . . . 114
5.2.3 Hysteresis Loop Analysis . . . 115
5.2.4 Decay Measurement Analysis . . . 118
5.2.5 Conclusions on PbBi Solder Joints . . . 121
5.3 Lead-Free Joints . . . 122
5.3.1 Joint Fabrication . . . 122
5.3.2 Bulk Solder . . . 123
5.3.3 Transport Measurements . . . 126
5.3.4 Magnetic Measurements . . . 127
5.3.5 Decay Measurements . . . 133
5.3.6 Scaled-Up Samples . . . 135
5.3.7 Conclusions on Lead-Free Joint Measurements . . . 140
5.4 Chapter Conclusions . . . 141

6 A Novel Composite Solder 143
6.1 Concept . . . 143
6.2 Production . . . 145
6.2.1 Preparation of Filaments . . . 145
6.2.2 Composite Consolidation . . . 147
6.2.3 Microstructure . . . 148
6.3 Bulk Superconducting Properties . . . 150
6.3.1 Resistivity Measurements . . . 151
6.3.2 Magnetisation Measurements . . . 153
6.3.3 A Model for the Magnetic Behaviour of Composites . . . 167
6.3.4 Performance of Composites with Different Matrices . . . 169
6.4 Discussion . . . 174
6.5 Composite Joints . . . 176
6.5.1 Joint Production . . . 176
6.5.2 Microstructure . . . 178
6.5.3 Superconducting Properties . . . 179
6.6 Chapter Conclusions . . . 181

7 Concluding Remarks **183**
7.1 Suggestions for Future Work 184

Chapter 1

Introduction

1.1 Introduction

By far the most common use of superconductors is in high-field electromagnets. Particle accelerators such as the Large Hadron Collider (LHC) and fusion reactors such as the International Thermonuclear Experimental Reactor (ITER) require hundreds of thousands of kilometres of superconducting wire, whilst nuclear magnetic resonance (NMR) scanners and scientific research magnets also make up substantial proportions of the market [1]. Field trapped in superconducting bulks is of interest as a replacement for the large permanent magnets needed for industrial generators and maritime motors [2]. However, it is in hospital magnetic resonance imaging (MRI) scanners that superconductors have found a mass market, with MRI representing a multi-billion dollar industry [3].

Compared to conventional conductors, the benefits of superconducting magnets are two-fold. Firstly, the extremely low resistance allows greater current densities to be carried with significantly lower cooling requirements; superconductors must simply be kept below a critical temperature, whilst copper coils must have enough cooling to counter resistive heating of the wire. This means superconducting magnets can be much more compact and generate considerably higher continuous magnetic fields than conventional electromagnets. Secondly, for MRI and NMR exceptional field stability is

required, necessitating maximum decay rates of less than 1 ppb/hr [4]. The extremely low resistance of superconductors allows for long decay times of current loops, characterised by the exponential time constant $\tau = L/R$ where L is the inductance of the coil and R is the resistance of the coil. With a superconducting magnet these decay times can extend to tens of thousands of years [4], a level of stability that cannot matched by any actively powered magnet as the instabilities in the power supply itself are much greater than this.

A typical MRI magnet will contain tens of kilometres of superconducting wire. For improved control of the field profile various different strands of superconducting wire will be used, necessitating the creation of joints between them. These typically make a significant contribution to the resistance of the circuit, so minimising joint resistance is critical [5]. A typical magnet joint requires a resistance $<10^{-12}$ Ω to allow currents to persist over time periods of several years, which necessitates the formation of a truly superconducting path between the two ends of the conductor. Current industrial jointing techniques rely on the use of lead-based solders [4, 6, 7]. Whilst the MRI industry currently has an exemption from laws prohibiting the use of these leaded solders [8], this is up for review in 2021 [9] so there is much interest in developing a commercially feasible lead-free jointing method.

1.2 Theory of Superconductivity

A full coverage of the theoretical physics behind superconductivity is beyond the scope of this work. Instead this section aims to provide the physics that underpins the key properties of technological superconductivity, namely the ability to carry large currents at high fields. A more thorough coverage is available in the textbook by Buckel and Kleiner [10]

1.2.1 The Superconducting State

For most technological applications, the key property of a superconductor is a sharp change to the zero resistivity superconducting state upon cooling below a critical tem-

perature. This was what Kamerlingh Onnes first discovered upon cooling mercury down to 4.2 K; the resistance suddenly dropped to zero [11] as shown in Figure 1.1. Whilst Onnes's precision in measuring resistance was limited, he later demonstrated that if a current was induced in a superconducting ring it would remain circulating without appreciable decay (known as persistence), showing conclusively the existence of a superconducting state [12]. Even now, the ability to form persistent currents in superconductors is critical in many superconducting applications, and is crucial for market-dominating MRI scanners.

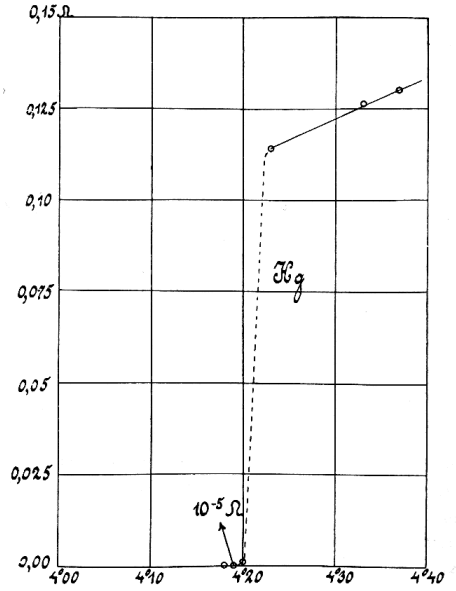


Figure 1.1: The sharp transition associated with the onset of the superconducting state. Reproduced from [13]

1.2.1.1 BCS Theory and Critical Limits

It was quickly discovered that it was not just temperature that could destroy the superconducting state; high currents and magnetic fields also prevent superconductivity. This is described by the Bardeen-Cooper-Schrieffer theory [14], in which electrons lower their energy and enter the superconducting state by forming Cooper pairs: pairs of electrons coupled by phonons. These pairs have a band gap energy of $2\Delta \approx 3.5 k_b T_c$ below the nearest unpaired energy state, so if a larger energy is supplied then the pairs can be broken (depaired) and the superconducting state destroyed. This energy can come

in the form of heat, magnetic field or current, providing the three critical parameters of superconductivity. As the energy supplied to the pair is the sum of these three contributions, increasing any of current, field or temperature will cause a decrease in the other two critical values, which can be represented as a critical surface for superconductivity as shown in Figure 1.2. In technological superconductors, the critical current is typically more than an order of magnitude lower than the current required for depairing, the reasons for which will be discussed later.

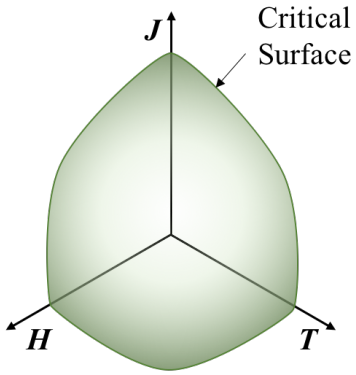


Figure 1.2: Critical current, field and temperature are all interlinked, giving a critical surface for superconductivity outside of which the superconducting state will be destroyed

1.2.2 Flux Penetration: Type I and II Superconductors

1.2.2.1 The Meissner Effect

In 1933 a second fundamental property of the superconducting state was discovered by Meissner and Ochsenfield [15]. They discovered that a material in the superconducting state would perfectly expel magnetic field, known as the Meissner effect, making the superconductor a perfect diamagnet. Perfect diamagnetism is not a direct consequence of zero resistivity, which would require only that the field does not change in the sample, but is instead a distinct property of the superconducting state. This allows for an alternative derivation of the critical field of a superconductor. Below T_c, it is energetically favourable for a superconductor to exist in the superconducting state. In the presence of a magnetic field, there is an energy cost to expel the magnetic field from the superconductor. The critical field of the superconductor is the field at which the

energetic benefit of the material being in the superconducting state equals the energy cost of expelling the magnetic field.

1.2.2.2 Ginzburg-Landau Theory and Type II Superconductivity

Ginzburg and Landau provided a thermodynamic description of the superconducting state [16]. This theory provides two characteristic lengths associated with superconductors, the coherence length, ξ, and the penetration depth λ, over which the magnetic field and Cooper-pair density decay respectively. According to Ginzburg-Landau theory, a boundary between a superconducting and non-superconducting (normal) region has an energy associated with it. If the Ginzburg-Landau parameter $\kappa = \lambda/\xi < 1/\sqrt{2}$, this energy is positive and so there is a penalty associated with the presence of magnetic field in the superconductor, leading to the total expulsion of magnetic field seen in the Meissner effect, as illustrated in Figure 1.3. Materials that demonstrate this behaviour are called type I superconductors.

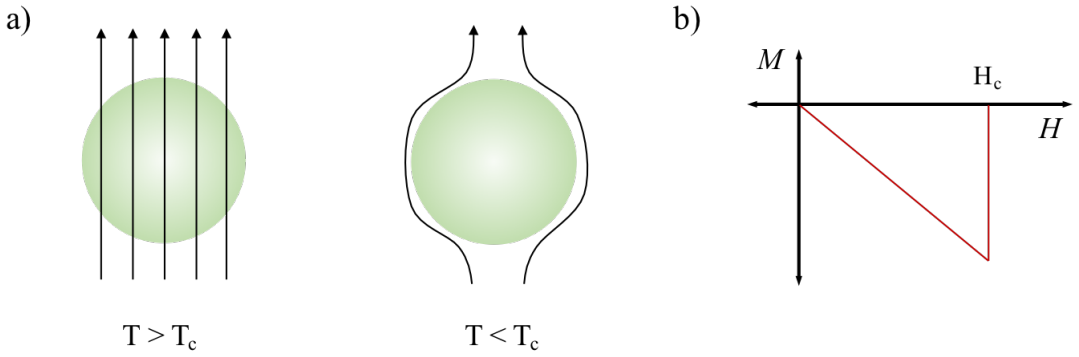


Figure 1.3: a) Complete expulsion of magnetic flux in type I superconductors below the critical temperature leads to b) a linear M(H) plot up to a critical field H_c

If $\kappa > 1/\sqrt{2}$, then the boundary energy is negative, making superconductor-normal boundaries energetically favourable, though there is still an energy penalty associated with the formation of normal regions in a superconducting material. At very low fields it is energetically favourable for a Meissner state to form, but above a particular field, known as H_{c1}, it becomes favourable for magnetic field to penetrate into the sample. The volumetric penalty of these normal regions is offset by the negative boundary energy, and so it is energetically favourable to maximise the surface area to volume ratio

of the normal regions. Abrikosov showed the lowest energy state was a periodic lattice of normal regions each containing a single quanta of magnetic flux, $\Phi_0 = h/2e$, in a superconducting matrix [17]. These regions are usually referred to as "flux lines" and are shown in Figure 1.4. Materials demonstrating this are known as type II superconductors, and maintain this so-called "mixed state" up to a second much higher critical field H_{c2}. As the applied field is increased towards this, the number of flux lines increases, leading to a decrease in spacing, but there is no change in the flux trapped in each normal region. H_{c2} can be considered as the field at which the flux lines start to overlap. For almost all technological applications it is type II superconductors that are required as they can maintain superconductivity up to much higher fields and can be engineered to have the greater critical current densities required for wire applications. Also, the ability to trap flux lines has led to interest in bulk type II superconductors as replacements for permanent magnets [2].

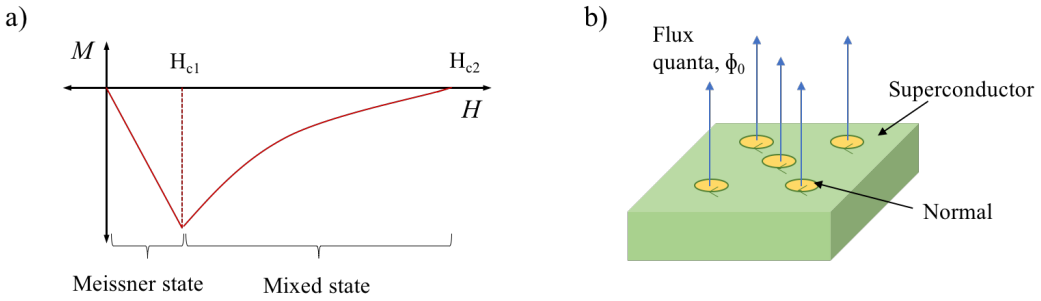


Figure 1.4: a) A type II superconductor acts like a type I with total expulsion of magnetic flux up until H_{c1}, above which quantised flux lines of field $\Phi_0 = h/2e$ start to penetrate the sample (b)

1.2.3 Flux Pinning: J_c Control

The movement of flux lines in a type II superconductor dissipates energy, quickly destroying the superconducting state. Even a small current will produce a Lorentz force $F_L = J \times B$ that can move the entire lattice, leading to critical currents (the maximum resistance-free current) much lower than the theoretical depairing current if flux lines are free to move. However, as the presence of normal regions has a volumetric energy cost, it is favourable for the flux lines to locate at defects in the material that

are already normal or poorly superconducting. Moving a flux line away from one of these sites has an energy penalty due to the creation of extra normal volume, and so only when a large enough force (and so a large enough current or field) is applied will the flux lines de-pin. This greatly increases the critical current of the material. The most effective pining is generally achieved by sites on the length scale of the coherence length of the superconductor, which can be from defect sites such as grain boundaries, precipitates or dislocations.

In real materials the nature of the flux pinning is commonly investigated by plotting the pinning force $F_p = J_c \times B$ as a function of reduced field $b = B/B_{c2}$. One common model for understanding these was proposed by Dew-Hughes in an in-depth review of flux pinning and critical current [18]. The Dew-Hughes model considers two main pinning mechanisms. The first is when the pinning is caused by the interaction of flux lines with non-superconducting material. The second mechanism is when the pinning sites are regions with suppressed order parameter, known as $\Delta\kappa$ pinning. There is also a dependence on the geometry of the pinning site, with points, surfaces and large volumes giving peaks at different reduced fields. This gives a total of six possible pinning contributions, with the total pinning force related to a summation of all six. Other authors have also considered magnetic interactions between vortices and matrix features, and variations in critical field as sources of pinning [19, 20].

Chapter 2

Literature Review

2.1 Technological Superconductors

Whilst there are many materials that display superconductivity, there are only six materials that have been widely used as conductors. These are the so called "technological superconductors": the metallic niobium-titanium (NbTi), the intermetallics niobium-tin (Nb_3Sn) and magnesium diboride (MgB_2), and the ceramic cuprates yttrium (or other rare-earth (RE)) barium copper oxide (YBCO or RE-BCO) and two bismuth strontium calcium copper oxide (BSCCO) compounds. The two stoichiometries of BSCCO used in technological applications are $Bi_2Sr_2CaCu_2O_{8-\delta}$ (2212) and $Bi_2Sr_2Ca_2Cu_7O_{10-\delta}$ (2223). The key properties of all these materials are summarised in Table 2.1.

Material	T_c(0 T)/ K	ξ(4 K)/nm	B_c(4 K)/T	B_{irr}(77 K)/T	γ
NbTi	9	4	12	N/A	1
Nb_3Sn	18	3	27	N/A	1
$Bi_2Sr_2CaCu_2O_{8-\delta}$	108	1.5	>100	0.3 [2]	50 [2]
$Bi_2Sr_2Ca_2Cu_3O_{10-\delta}$	90 [2]	2 [10]	>100 [10]	<0.1 [2]	165 [21]
$YBa_2Cu_3O_{7-\delta}$	92	1.5	>100	5-7	7
MgB_2	39	6.5	15	N/A	2–2.7

Table 2.1: A summary of the properties of technological superconductors. The anisotropy, γ is the ratio of in and out of plane coherence lengths. For anisotropic samples, the in-plane values for ξ and B_c are quoted. Unless otherwise stated, all information is from [22]

Whilst kilometre long lengths can now be produced from all these materials [23–25], NbTi is still the dominant material in the MRI industry due to its high ductility, ease of processing and low cost [26, 27]. BSCCO, MgB_2 and Nb_3Sn are all brittle and so must be reacted only after winding into the desired shape. REBCO suffers from weak-linked behaviour, where grain boundaries with misorientation greater than 5° provide an obstacle to current flow [28]. To counter this, REBCO conductors are made as tapes using a variety of complicated and expensive epitaxial deposition processes to produce a biaxial texture [29]. Only when performance at elevated temperatures or fields beyond 10 T is essential will any of these materials be considered over NbTi.

2.2 NbTi Wires

2.2.1 Structure and Stabilisation

Commercial NbTi wires are a composite of at least one, typically many, NbTi filaments in a copper or copper/nickel matrix as shown in Figure 2.1. The copper acts as both a thermal and electrical shunt in case of a localised loss in superconductivity (known as a quench), allowing both heat and current to be transferred quickly away from the superconductor, preventing further heating and uncontrolled quenching of the superconductor. Keeping the filaments below about 50 microns in diameter is also beneficial for preventing the spread of a quench, meaning most NbTi conductors contain a large number of fine filaments, known as multifilamentary wire [26].

For applications where the field is switching very quickly the filaments are often made as small as 5 microns as this acts to limit the hysteretic loss on each cycle, known as AC loss. Another contribution to AC losses comes from eddy currents coupling between filaments, which is minimised by twisting the filaments.

2.2.2 Microstructure and Manufacture

From the phase diagram in Figure 2.2a, the expected microstructure of the typical wire composition of Nb–47wt%Ti is a Nb(Ti) solid solution, with α-Ti precipitates.

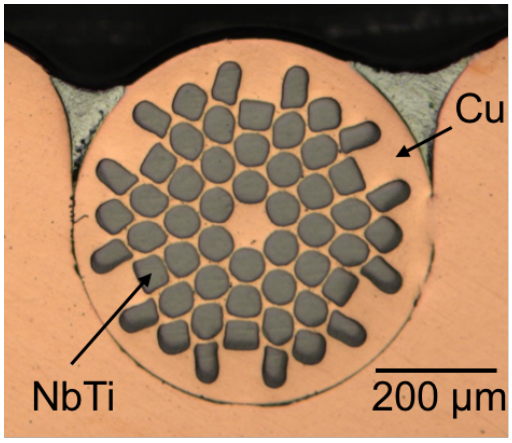


Figure 2.1: Optical micrograph of a typical NbTi superconducting wire for MRI applications

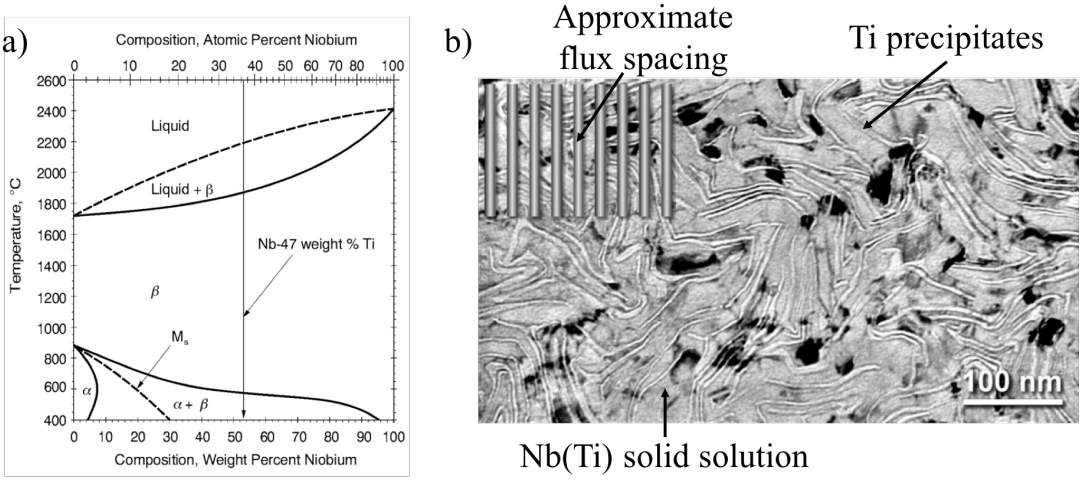


Figure 2.2: a) Binary phase diagram of the NbTi system and b) TEM image of NbTi wire, showing ribbon-like α-Ti precipitates and an approximate flux line spacing at 5 T. Both reproduced from Lee [26]

The wire is manufactured by stacking NbTi rods into a copper billet then repeatedly mechanical drawing and annealing to produce the composite wire with an extremely fine microstructure, as shown in Figure 2.2b. A full review of this process is presented by Lee [26]. The fine microstructure of Ti precipitates is crucial for achieving high current densities, as the best pinning comes from sites of similar scale to the coherence length of the superconductor, which is about 5 nm in NbTi. It is important to note that heat treating the wires above about 400°C leads to a severe reduction in critical current in the wires through coarsening (at moderate temperatures) or dissolution (at higher temperatures) of the α-Ti precipitates [30]. As such, care must be taken not

to heat the superconductor above 400°C for any significant length of time, which is a vital consideration in many joining processes, where higher temperatures would often be beneficial. However, there is little information about the effect of more moderate temperatures for the longer times required by many jointing techniques.

2.3 Current NbTi Jointing Methods

For MRI scanners, the formation of persistent superconducting joints is essential for field stability. This means that the copper stabiliser must be removed from the wire and a superconducting path formed between the filaments of the two wires. In reality, there will be some decay of currents in all real type II superconductors. Decays associated with normal regions (such as an interface in a joint), lead to currents decaying exponentially with a time constant inversely proportional to resistance. In bulk superconductors, currents will decay due to flux creep (thermal depinning of flux lines), which leads to a logarithmic decay. Typical MRI magnets require decay rates of <1 ppb/hr, which corresponds to a resistance below about 10^{-12} Ω [7, 31].

2.3.1 Solder Joints

2.3.1.1 The Matrix-Replacement Method

By far the most common industrial jointing technique is soldering. This involves removing the copper stabiliser then immersing the filaments in a superconducting solder with a low melting point. Whilst the copper is often removed by nitric acid etching, hydrofluoric acid (HF) is added to the mixture to prevent oxidation of the NbTi. As HF is highly toxic it adds extra expense to industrial processes and training, so is undesirable. Perhaps the most common alternative is the so-called "matrix-replacement method" illustrated in Figure 2.3, originally patented by Thornton [6] and since used in most publications on soldered joints [4, 7, 31, 32]. This involves placing the wires in liquid tin at about 350°C to dissolve the copper and substitute it for tin without exposing the filaments to air, known as "tinning". This technique also works for Cu-Ni matrix

wires [6, 31]. The tin-coated filaments are then placed in the solder, which dissolves the tin and coats the filaments in solder. They are commonly then twisted together and dipped in solder one final time to form the joint, and are often left in the pot of solder to provide both magnetic and mechanical shielding [6]. Early authors performed this in an inert atmosphere or vacuum [4,6,7] to avoid the formation of oxide layers on the tin or solder bath. This has been shown to be unnecessary as the oxide layer can be skimmed off the top of the liquid bath [31]. There are many potential variables in this process, including time and temperature of both steps, but there is no controlled study that compares the effect of these. However in the first step alone, the times for tinning vary between ten minutes [33] and over two hours [31]. The possible formation of reaction layers between the niobium titanium and the tin or solder [33] means that there is the potential for different influences on joint performance depending on reaction time [34]. The use of tin for this process was driven mainly by its low price, but there is no reason another material would not be more effective.

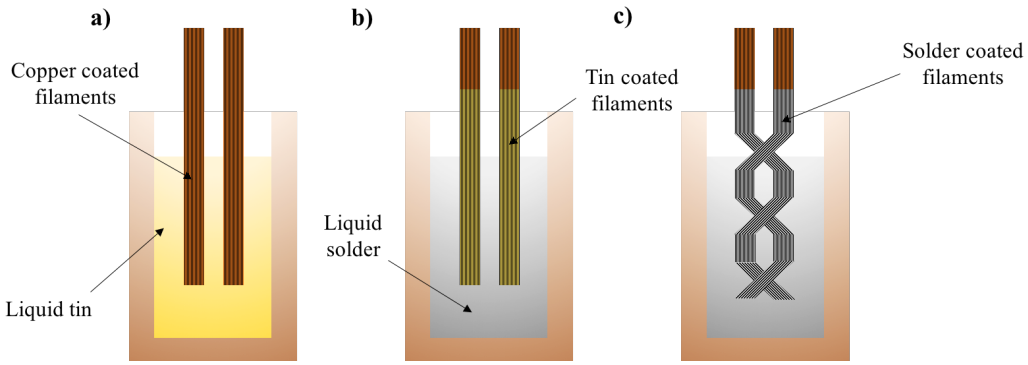


Figure 2.3: A schematic of the Thornton matrix replacement method [6] a) Copper matrix is dissolved in liquid tin, b) tin is dissolved in solder c) solder coated filaments are twisted together and dipped in the solder to join. Very often they are left in the pot of solder

2.3.1.2 Lead-Based Solder Materials

All reported solder joints use lead-bismuth (PbBi) [4, 6, 31, 34, 35] or lead-bismuth-tin (PbBiSn) alloys [4,6,7,32,35] except a few early cases where Wood's metal (PbBiSnCd) is used [35].

The binary phase diagram of the PbBi system, shown in Figure 2.4a shows two lead-rich

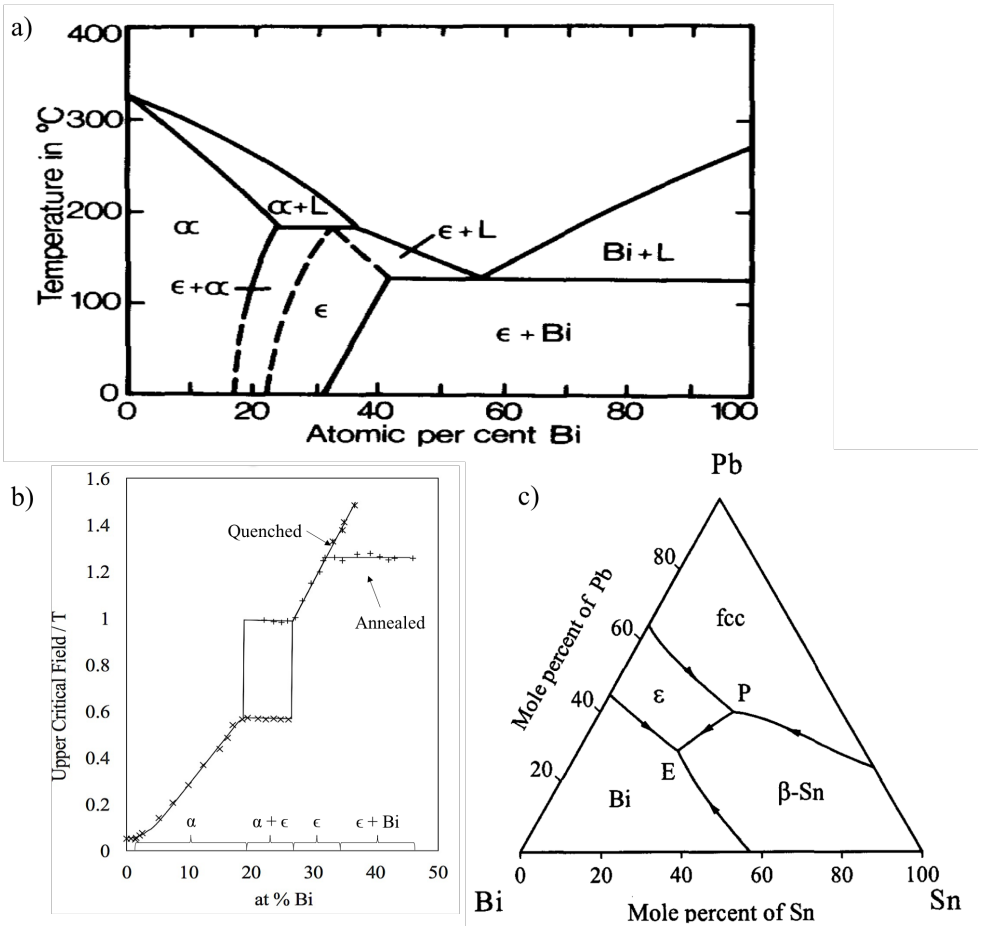


Figure 2.4: a) Binary phase diagram of the PbBi system. Reproduced from [36] b) The superconducting critical field as a function of bismuth content. Adapted from [37]. The ϵ phase has the highest critical field, and thermal history is important c) Liquidus plot of the PbBiSn system, showing the ternary eutectic (E) and peritectic (P) compositions. Reproduced from [38]

solid solutions: the α and ϵ phases [36]. The ϵ phase is the better superconductor, with critical temperature [39, 40] and critical field [37, 41] increasing with bismuth content within the phase field as seen in Figure 2.4b. Most PbBi used for joints involves either $Pb_{60}Bi_{40}$ or eutectic $Pb_{45}Bi_{55}$ by atomic percent. Many reports fail to give the exact composition used, making it difficult to draw comparisons, though both Campbell et al. and Kodama et al. report that the critical current is higher in the eutectic alloy due to a greater specific surface area of normal-phase bismuth particles providing more flux pinning [34, 41].

The slope of the solvus of the ϵ phase leads to the possibility of solid-state precipitation of non-superconducting bismuth over time, demonstrated by the difference between

the properties of the quenched and slow-cooled samples in Figure 2.4b. Other authors report similar dependence on cooling rates, and eutectic samples are also seen to age dramatically, leading to changes in both microstructure and critical field with time [34, 40, 42]. Despite this, the effects of ageing and thermal history have barely been studied or even considered with reference to lead-bismuth joints. However, a recent study into lead-free alternatives has shown significant variations in critical current with time and thermal history [43], which could explain differences seen between various PbBi and PbBiSn joints. This dependence on sample history makes it impossible to draw full comparisons between joints produced by different authors. As yet there has been no published study on how this ageing affects the performance of superconducting joints over time.

Very effective joints can be made by soldering with PbBi, with Liu et al. [31] reporting a critical current of 1160 A at 0.6 T and presumably 4.2 K for a PbBi joint. Swenson and Markiewicz report that PbBi has a lower resistance than PbBiSn alloys [4], but this is disputed by Seo et al [35]. It is worth noting that whilst both use the same tin content Seo et al. use a more lead-rich alloy, which is likely to improve the performance. Other authors have also demonstrated truly persistent performance with PbBiSn alloys [7,32], though neither quote their exact composition. Brittles demonstrates that in bulk form eutectic PbBiSn has a higher critical current density than PbBi, perhaps due to an increase in pinning sites [33] and suggests the lower performance seen by Swenson and Markiewicz could be due to the formation of non-superconducting reaction layers.

There has been very little microstructural analysis performed on soldered joints, but with the pronounced ageing effects seen in bulk samples [40, 42] and the formation of interface layers [33, 34], this must be considered essential for future improvements in solder technology. Kodama et al. used transmission electron microscopy (TEM) and energy-dispersive x-ray spectroscopy (EDX) to study the interface region and proposed a layered interface shown in Figure 2.5. This has a layer of Nb_3Sn forming closest to the niobium titanium, with a layer of titanium sulphide (TiS) forming closer to the solder due to impurities found in the copper. This seems somewhat unlikely, as TiS is known not to superconduct above 1 K, and the impurity content in copper used in

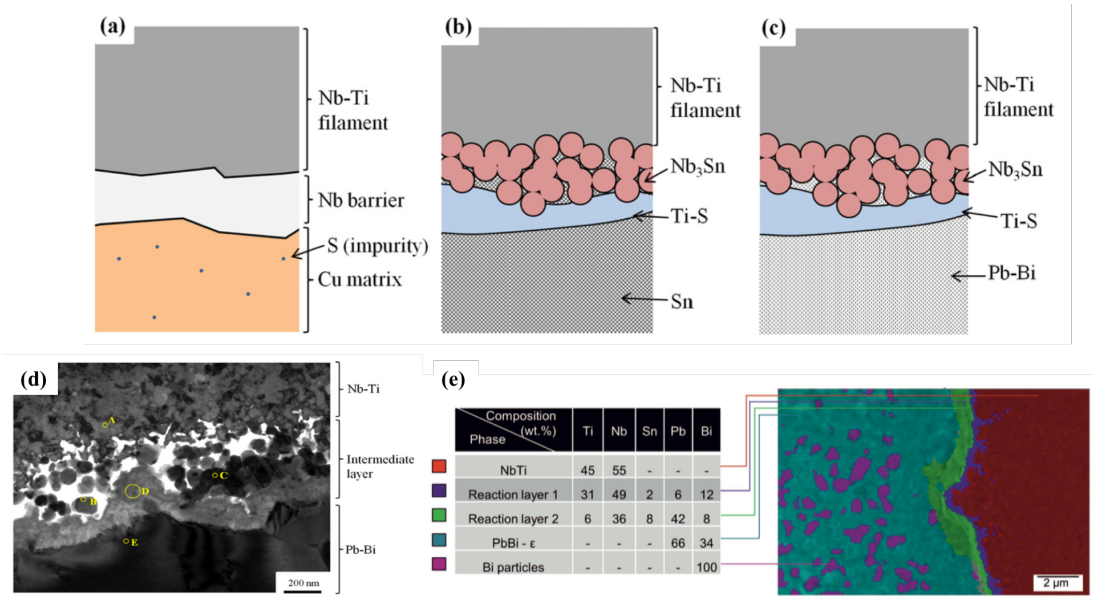


Figure 2.5: a-c) Kodama's proposed mechanism of interface formation based on d) TEM micrograph of the interface. Reproduced from [34] e) Interface layers in PbBi joints. Reproduced from [33]

superconducting wires is typically very low. No TEM micrographs are shown of the intermediary tinned stage, which would show when this layer actually formed. Brittles used scanning electron microscopy (SEM) and EDX to investigate similar interfaces and found no evidence of sulphur. However, it is worth noting that the energies of the main quantifiable EDX peaks of sulphur and lead are 2.342 and 2.307 keV respectively, too close for many EDX systems to differentiate. Kodama makes no mention about whether higher peaks were present, which would indicate the presence of lead, and Brittles only quotes the use of 10 keV electrons which would not allow the distinction to be observed. As such there must be some doubt over the presence of sulphur in the interface layer, a much more likely suggestion is that the layer is lead-based and formed during the soldering step. This could be determined by analysing the layers formed on a sample that had been tinned but not soldered. As yet there has been no study into how the presence of these interface layers affect joint performance, though it must be assumed they are present in all matrix-replacement joints. Another key factor mentioned by Kodama et al. is the presence of a niobium diffusion barrier sometimes added during wire production. The critical field of niobium is 0.7 T at 4.2 K with critical current decreasing dramatically above 0.4 T [33], so it can act to provide a

normal barrier at room temperature and can limit joint performance [32]. Yet Kodama et al. demonstrate critical currents of over 1000 A at 0.7–1.0 T, raising questions about the influence of the barrier. They propose it reacts to form Nb_3Sn during the tinning stage, but more study is needed to confirm this theory.

One advantage of the solder method is that it can be used to make joints between NbTi and A15 superconductors such as Nb_3Sn [4] and Nb_3Al [32]. These are prepared as for NbTi joints, but require different heat treatments for the A15 end. The presence of niobium and tantalum diffusion barriers in A15 conductors means that the joint can be limited by the performance of the barrier [32]. This can be partially avoided by scarfing the joint – polishing the ends at an acute angle to increase surface area of the end of the joint [4]. However, this leads to the risk of oxidation and still leaves limited surface area, limiting current transfer.

2.3.1.3 Lead-Free Solder Materials

The MRI industry currently have an exemption from EU laws against the use of leaded solders, but this is up for review in 2021 and there is much desire for a lead-free alternative to be discovered [8, 9]. By far the best solution for industry would be an alternative solder that could directly replace lead-bismuth. However from Table 2.2, it is clear that most lead-free systems have much lower critical fields and temperatures. The next best binary system is the indium-tin (InSn) system, which has been thoroughly investigated both in the 1960's [44, 45] and more recently specifically for superconducting joints [43, 46]. The only other promising candidates include materials such as cadmium, mercury or thallium that are highly toxic and so are not appropriate replacements for lead.

The phase diagram of the InSn system, shown in Figure 2.6a, is much like that of the PbBi system, with a eutectic between the indium-rich β and tin-rich γ phases [47]. Both phases superconduct, with the highest critical temperatures and fields seen in the β phase [43, 44]. Exact values of these for InSn solders vary dramatically even for similar compositions, with critical temperatures recorded between 5.6 [43, 48] and 7.4

Composition/wt%	T_c/K	B_{c2}/T	Reference
$Pb_{60}Bi_{40}$	8.4	1.77 (at 4.2 K)	[40]
$Pb_{32}Bi_{53}Sn_{15}$	8.68	1.985 (at 1.3 K)	[45]
$Pb_{50}Sn_{50}$	7.75	0.2 (at 1.3 K)	[45]
$Pb_{50}In_{50}$	6.35	0.48 (at 1.3 K)	[45]
$Pb_{50}Sn_{50}$	7.75	0.2 (at 1.3 K)	[45]
$In_{50}Sn_{50}$	7.45	0.64 (at 1.3 K)	[45]
		0.348 (at 0 K)	[44]
$In_{50}Sn_{50}$ quenched	6.7	0.145 (at 4.2 K)	[43]
$In_{50}Sn_{50}$ air cooled	5.6	0.04 (at 4.2 K)	[43]
$In_{50}Sn_{50}$ quenched and aged	6.1	0.08 (at 4.2 K)	[43]
$Sn_{35}In_{50}Bi_{15}$ air cooled	6.9	0.18 (at 4.2 K)	[43]
$In_{78}Bi_{22}$	—	0.225 (at 0 K)	[44]
$Sn_{85}Zn_{15}$	—	0.103 (at 0 K)	[44]
$Sn_{43}Bi_{57}$	2.25	0.038 (at 0 K)	[45]

Table 2.2: The superconducting properties of commonly used solder materials

K [45, 49] for the eutectic composition. As noted by multiple authors, this is due to the thermal history of samples, with quenched samples demonstrating higher critical fields and currents [43, 50]. Merriam and Von Herzen put this down to extra internal strains caused by differential thermal contraction of the two phases [50], but Mousavi et al. recently demonstrated that the key parameter is the concentration of tin in the β phase [43]. They demonstrated that during quenching, the steep solvus means an above-equilibrium quantity of tin is trapped in the beta phase, leading to improved superconducting properties. However, this is only of minimal use for the manufacture of superconducting joints, as samples have been shown to decrease dramatically in performance over time due to high room-temperature diffusion rates leading to a return to equilibrium composition and properties [43]. The critical current is high enough for joint manufacture at very low fields [51], but the low critical field of 0.15 T at 4.2 K for even a quenched sample [43] would require excessive shielding for industrial use.

One consideration when investigating the InSn system is the very low melting temperature. This means that diffusion is fast even below room temperature. This is particularly important for the InSn system as the β phase has been shown not to be stable below 140 K, where the equilibrium phases are indium solid solution and γ [52, 54]. The extended phase diagram is shown in Figure 2.6. β phase samples cooled very quickly from room temperature to 4.2 K were shown to have a higher critical tem-

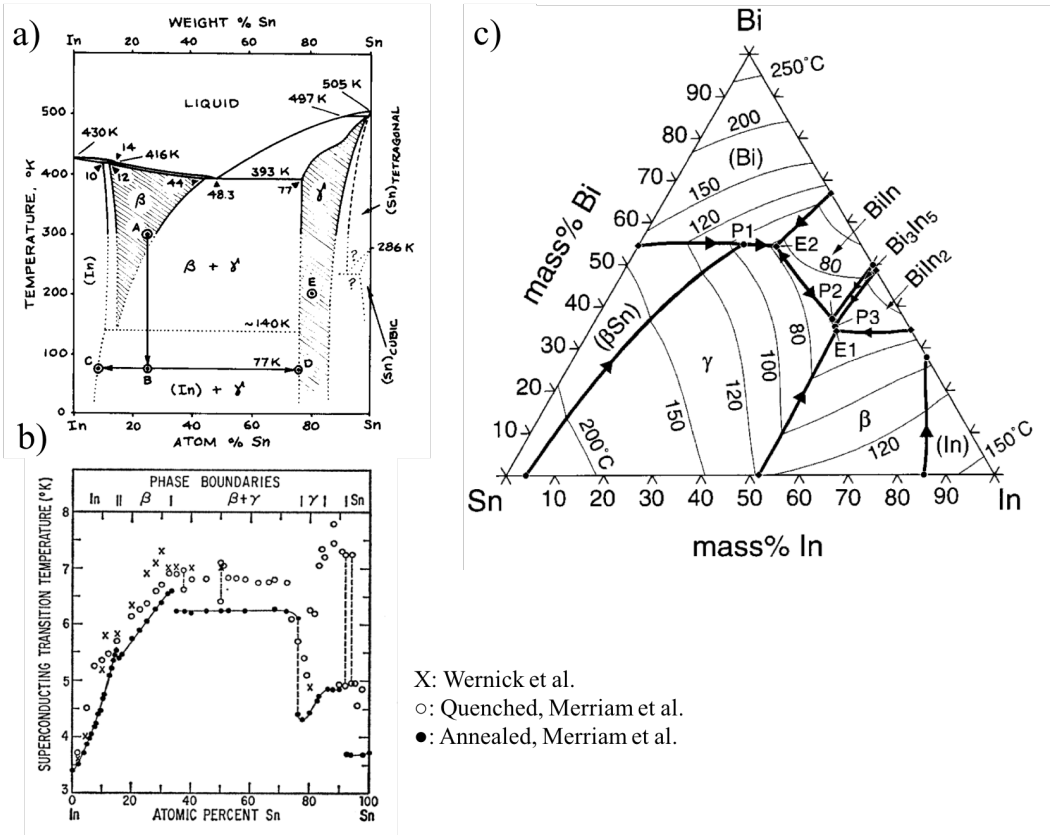


Figure 2.6: a) Extended binary phase diagram of the InSn system. Reproduced from [52], based on high temperature data by Heumann et al. [47] b) The superconducting critical temperature as a function of tin content. Reproduced from [50], including earlier results of Wernick et al. [49]. There is a strong dependence of the critical temperature on thermal history, as well as on tin content in the β phase c) Ternary InSnBi phase diagram. Reproduced from [53]

perature than those cooled slowly as the quenched samples maintained the supercooled β phase, whilst the slow cooled samples reverted to equilibrium [52]. Whilst many authors discussing superconductivity in the InSn system consider the effects of quenching samples to room temperature, the effect of cooling below room temperature is not considered, so the possibility of a phase transition occurring whilst cooling a sample for measurement cannot be ignored. This may lead to some of the discrepancies in properties.

Similar to the addition of tin to the PbBi, ternary additions to the InSn system can lead to a change in superconducting properties. In particular, the addition of bismuth at the ternary eutectic composition of $Sn_{35}In_{50}Bi_{15}$ by weight leads to an increase in both critical field and critical temperature, recorded as 0.18 T and 6.9 K respectively for an

air-cooled sample [43] which, whilst much lower than PbBi, is the best lead-free system reported to date. Ternary solders with antimony have also been investigated, and found to give a much smaller improvement over the base InSn system [55]. This is likely to be because only a small amount of antimony dissolves in the β phase, instead forming the poorly superconducting InSb phase. Bismuth has a higher solubility in the β phase, and also forms the relatively good superconducting phase $BiIn_2$ [51]. Interestingly, Santra recently demonstrated that the addition of Bi to InSn solders greatly reduces the activity of Sn, with InSn solders forming non-superconducting $NbSn_2$ reaction layers when heated with NbTi wires whilst BiInSn solders form no such reaction layer [56], which is likely to be beneficial to persistent performance.

Even the best known lead-free solder is currently worse than the requirements of the MRI industry, who require critical fields of 1.0 T at 4.2 K and the ability to carry over 1000 A [57], so much further development is needed to gain a lead-free alternative. The most promising lead-free elements with low melting points have already been investigated, but there are other elements such as niobium and tantalum with much better superconducting properties. However, these are refractory, with melting points far too high to use as solders, and it has been demonstrated that they do not dissolve in or react with InSn solders at low temperatures [55].

2.3.2 Direct Filament-Filament Bonding

Even the best PbBi solder has considerably lower critical field than the wires themselves so there is a considerable advantage at high-fields joints in directly joining niobium titanium filaments without an intermediary.

2.3.2.1 Cold Pressing

One of the simplest persistent joining methods is cold pressing (also known as crimping). In this technique, originally patented by Nuding [58], the copper stabiliser is removed with acid, the exposed filaments are twisted together and placed in a tube, known as a crimp, which is then pressed at room temperature and in air. In this manner,

resistances below 10^{-13} Ω can be regularly attained [5, 59] and currents of over 100 A carried [59–62], suggesting a true persistent joint has been formed. However, there is little consistency in how joint performance has been measured, with variability in joint length, wire performance and field applied. This makes drawing conclusions between different results difficult.

There are several factors expected to affect crimping performance. The first is crimping pressure. Liu et al. demonstrated that at low pressures for hydrofluoric acid (HF) etched filaments, critical current and resistivity stays constant [5], but Cheng et al. demonstrated that at higher pressures the resistance decreases linearly in three regimes [63]. A key difference between the two experiments is that Liu et al. cleaned their filaments in HF to provide an oxide free surface, as do most other crimping procedures [58,60], whilst Cheng used only nitric acid, which further oxidises the niobium-titanium. Cheng et al. put their linear decrease in resistance down to decreasing contribution of the interface layer, which is broken up at more higher pressures. This is not a problem with the clean surfaces used by Liu et al, which is likely to be the reason they could obtain good joints at low pressures, however the use of HF is industrially undesirable. The surface properties of the materials to be cold-welded are critical to producing good metallic bonds [64], but little research on this has been applied to crimped joints. The oxidation of filaments is clearly a problem, and will be discussed in Section 2.5. Another issue is the presence of copper inter-metallic nodules formed during wire manufacture, that have been shown to remain after nitric etches [1] as can be seen in Figure 2.7. It is unknown whether these remain after HF etching.

The shape of the crimp and direction of the pressing also has a dramatic effect, with different shaped crimps shown by finite element modelling (FEM) to provide very different contact areas between filaments and also different uniformities of deformation [65]. Zhou et al. demonstrate that initially, increasing pressure increases contact area, leading to a fall in resistance, but very high pressures cause filament breakage, leading to poor joint performance [66]. Similar effects were observed by Brittles [33]. It is worth noting both these studies were performed on nitric etched filaments, with HF etching and no oxide the results would be expected to differ, with much lower pressures needed

to gain low resistances. Further finite element modelling of the process would enable the effect of different wire geometries and crimp materials to be explored quickly and efficiently.

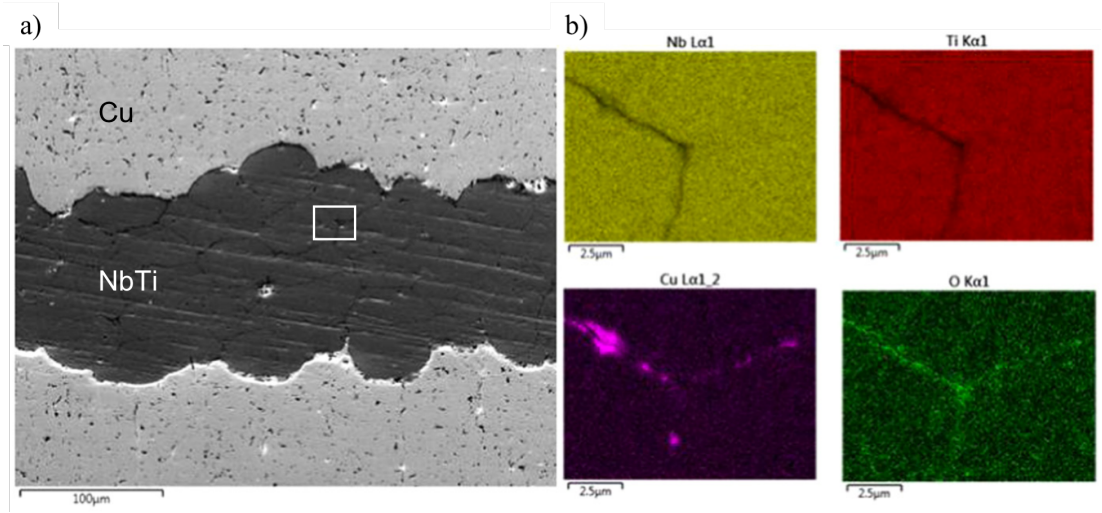


Figure 2.7: a) Cold pressed joint with a copper crimp and nitric only etch b) Chemical mapping of the interfaces reveals the presence of oxygen and copper, suggesting little metallic bonding. Reproduced from [1]

Another key property is the choice of crimp material, with copper [59], niobium [1,5,60] and niobium-titanium alloys [63] all having been reported. Often the crimp is a composite tube with a copper outer layer and niobium or niobium-titanium inner layer [5,63]. Brittles suggests a key factor is that the crimp-filament contact area is often much greater than the filament-filament contact area, meaning the current flow through the crimp can dominate [33]. Niobium has a much lower critical field than NbTi of around 0.7 T at 4.2 K [33], though it is worth noting that this is highly dependent on the purity of the niobium, with impure samples with higher resistivities demonstrating considerably higher critical fields [67]. As many measurements on crimped joints are taken in self-field only, it is often impossible to tell whether filament-crimp or filament-filament current flow dominates. It is expected that the NbTi crimp would be beneficial for high field applications, though there is no evidence either way for this in the literature. A recently patented modification of the crimping process aims to instead bond the filaments to an intermediate superconducting plate [68]. Whilst this gives a resistance below 10^{-13} Ω and claims better quench protection, there is little evidence presented as to whether the presence of the plate actually improves the joint.

The simplicity of crimping and the potential to form joints with good high-field performance make it a promising technique. However, more work is needed, particular in terms of characterising the effect of different surface conditions and crimp materials to develop the reproducibility and control needed for wide-spread use in MRI scanners.

2.3.2.2 Spot Welding

Another technique that can produce direct joints between NbTi filaments is spot welding. This clamps exposed filaments between two electrodes, which then provide a high current. Resistive heating at the wire surface leads to localised melting, allowing metal-metal bonds to form [69]. This has been shown to produce very good persistent joints, with resistances below 10^{-13} Ω and the ability to carry currents over 200 A [60, 70, 71]. Most authors bond the filaments to a niobium sheet, which offers a heat sink both during the welding process and also during a magnet quench. The current carried by a joint bonded to a sheet rather than just to itself is much higher [70], though it is unclear whether this is due to improved welding or due to extra supercurrent flowing through the sheet. A key advantage of this technique is that it melts through the oxide layer on the NbTi surface, and so there is no difference between filaments etched in nitric or the more dangerous hydrofluoric acid [57, 62]. This is advantageous for a production-line technique.

Many authors have noted the unreliability of the spot welding process [57, 60] and the results compared to cold pressing are variable, with Phillip et al. finding slightly improved properties in the spot weld [62] whilst Tominaka et al. find the cold pressed joint to be better [61]. This unpredictability is due to the process causing localised melting [1], which is much more apparent in multifilamentary wires, where the increased surface area to volume ratio causes increased melting. Figure 2.8a shows a distinct cast microstructure in multifilamentary wires, caused by complete melting during the welding process. This destroys the highly tailored microstructure of the wire and dramatically decreases the critical current values. Figure 2.8b shows that this is not present in monofilamentary wire, though large copper inclusions from the electrodes

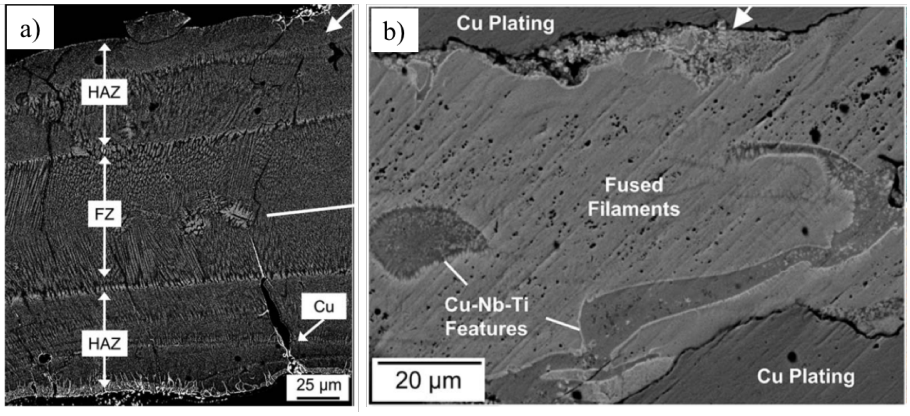


Figure 2.8: a) A welded multifilamentary joint demonstrating distinct signs of re-melting b) This re-melted microstructure is not present in a spot welded monofilament joint, but there are large copper features probably from the electrodes both reproduced from [57]

are found [57]. The success of the spot welding technique requires the perfect match of welding conditions and wire, and also depends on the skill of the operator to avoid copper inclusions and not overly melt the filaments, which is why the process is so unpredictable. This unpredictability makes it undesirable for large production lines such as for MRI scanners, but it is still useful for specialist one-off joints.

2.3.2.3 Other Direct Techniques

Various other techniques to join superconductors have been attempted. The most common is diffusion bonding, where filaments are stripped of copper and heated to 450°C whilst they are pressed, encouraging interdiffusion and bonding of the niobium-titanium filaments [4, 72, 73]. Whilst this allows persistent joints to be made [4] it requires long times under an inert atmosphere or vacuum, making it unfeasible on a production line. Whilst the process could be sped up by using higher temperatures, this would lead to damage to the highly engineered microstructure of the wires [30]. Ultrasonic welding has been proposed for welding two composite conductors together [74], but there are no published examples of it being performed on exposed filaments.

2.4 Persistent Joints Between Other Superconductors

Whilst persistent solder joints for both NbTi wires and Nb_3Sn wires are standard practice in the MRI and NMR industries, until very recently there had been little interest in persistent joints between other wires. However, recent successes in the development of high-field HTS magnets such as the 36 T hybrid [75] and 32 T [76] all superconducting magnets recently completed at the High Magnetic Field Laboratory in Florida, has led to much interest in the development of persistent joints between non-niobium based superconductors, particularly for ultra high field NMR projects, such as the MIRAI project in Japan that aims to deliver the superconducting joints required for a 30.5 T NMR scanner [77].

Of these, the simplest are joints between MgB_2 wires. Multiple groups have reported success using powder-processing based techniques, densifying MgB_2 powder around exposed filaments [78–80], usually by ensuring the joint is heat treated at the same time as the main coil. These joints have been shown to demonstrate low resistance at high currents, with Nardelli reporting a resistance of 10^{-14} Ω at 300 A and 20 K in self-field [81]. The powder processing technique has also been successfully transferred to BSCCO-2212, with Chen reporting a joint that could carry a current that matched that of the wire at fields from 0-14 T and also demonstrated a resistance of 5×10^{-12} Ω at 271 A in self-field at 4.2 K [82].

Joints between REBCO tapes have proved more challenging, with early examples requiring impracticably long heat treatments and delivering low critical currents [83, 84]. Recently reported joints have shown more promise, often using an intermediate REBCO layer with lower melting temperature than the tape [85] or fabricated from solution with lower temperature heat treatments [86]. Nishijima has reported joints of this latter type that can carry currents matching that of the REBCO tapes at 77 K, and demonstrate resistances of the order 10^{-14} Ω whilst carrying 100 A.

Designs for high-field NMR magnets use a combination of different superconductors for the coils, with NbTi and Nb_3Sn outserts providing some of the field due to their low price and improved strain resistance, with only the inner most windings (that experience

the highest field) being made from HTS material [77]. As such, the realisation of persistent joints between dissimilar superconductors is essential. One possible solution for this is reported by Matsumoto [87], who demonstrated a joint made using PbBi solder and the matrix replacement technique between BSCCO-2223 and NbTi wires. Mousavi (with contributions from myself) has reported similar joints made between BSCCO-2212 wires [88]. Together this presents the possibility of jointing between NbTi, Nb_3Sn and BSCCO wires. However, it is worth noting that only transport measurements have been performed on these joints, with not enough sensitivity to determine if true persistent performance has been attained. Indeed, the work by Mousavi reveals the presence of a SnO layer between the solder and BSCCO filaments, which brings into question the ability of such joints to carry persistent currents.

2.5 Oxidation of Niobium Titanium

For many jointing techniques the oxidation of the niobium titanium superconducting filaments is problematic, with oxide layers acting as a barrier to supercurrent, decreasing wettability and preventing metallic bonding [1]. It is commonly known that both niobium [89] and titanium [90] readily form thin, well-adhered surface oxides. No studies have yet investigated the formation of room-temperature oxides on the Nb–47wt%Ti alloy used in superconducting wire, but the wealth of information available on niobium and titanium provides the perfect background for such a study

For a general oxide coating on a metal it would be expected that oxides would form in layers, with increasing oxidation state from metal surface to oxide outer surface [91]. This is what is observed in high temperature oxidation studies of niobium by Hurlen [92] and Sheasby [93], with a thick outer layer of Nb_2O_5 and inner sub-oxides. Ultraviolet photoemission spectroscopy (UPS) experiments by Lindau and Spicer [94] suggest this is also the case in ambient oxides, with a layer of Nb_2O_5 over a mixed NbO and NbO_2 layer. Using the changes in work function during oxidation, they suggest that the NbO layer forms first, then is broken up by the formation of NbO_2 amongst that layer. The Nb_2O_5 is then believed to form a complete flat over-layer as shown in Figure 2.9a.

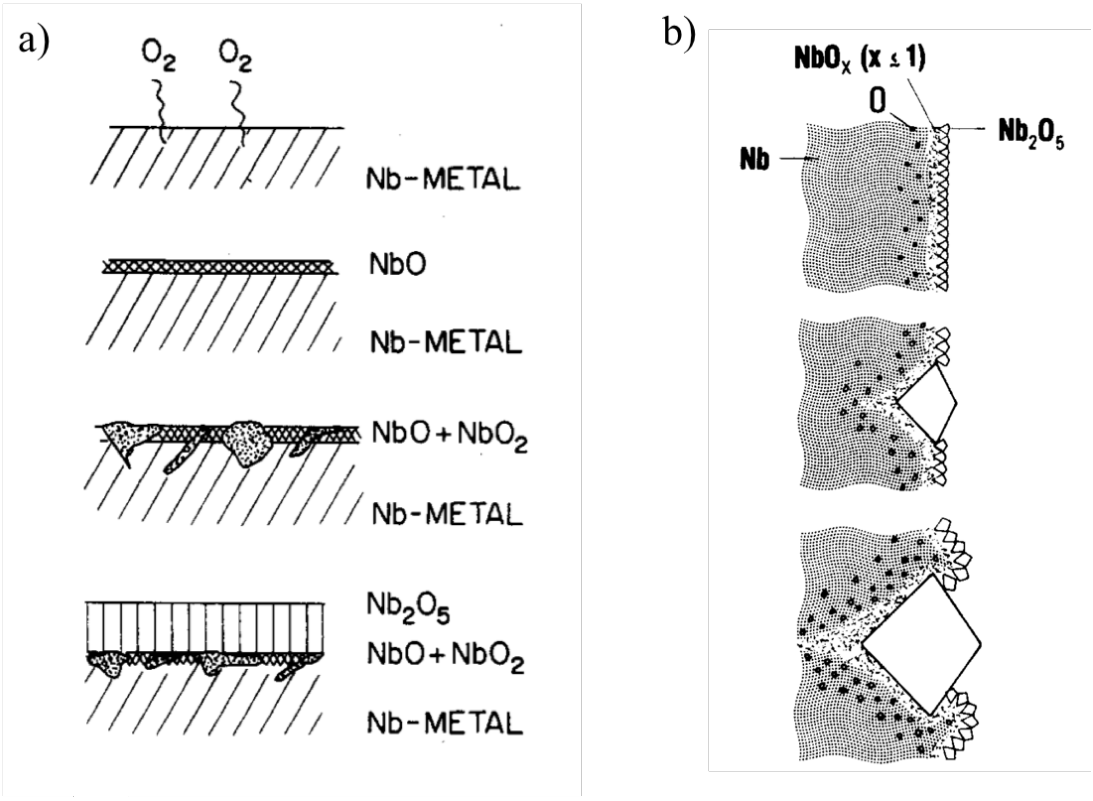


Figure 2.9: Growth mechanisms of oxides on niobium metal proposed by a) Lindau and Spicer [94] and b) Darlinski and Halbritter [95]

All the studies on room temperature oxides on niobium show the oxide layer to be very thin, typically less than 10 nm [96–98]. The final thickness values reported vary considerably between studies, with Delheusy et al. [97] and Hurlen et al. [99] reporting oxides 2 nm thick, King et al. [100], Ma and Rosenberg [101] and Sokhey et al. [102] 4 nm thick, and Dacca et al. [96] and David Henry et al. [103] 6 nm thick. There are two possible reasons for these discrepancies. Ma and Rosenberg [101] show that oxidation is fast over the first hour then slows to a negligible growth rate after a day or two, but Olsson and Landolt [104] show that the oxide is not entirely passivated at this point, with the oxide layer continuing to grow over the course of a year, as shown in Figure 2.10. This means that the exact time the oxide has been left affects the thickness, even once it appears to be passivated. Furthermore, Olsson and Landolt demonstrate that the oxidation rate in laboratory atmosphere is faster than oxidation in dry atmosphere [104], which corroborates an earlier study by Grundner and Halbritter [89]. As such there will be a difference between experiments performed in-situ in UHV analysis

chambers by allowing a controlled volume of oxygen to enter the chamber, which often fail to fully oxidise the sample, and those done by exposing the sample in ambient conditions. Even then, local humidity levels during experiments are likely to have some influence on oxide growth, though this is not something usually reported.

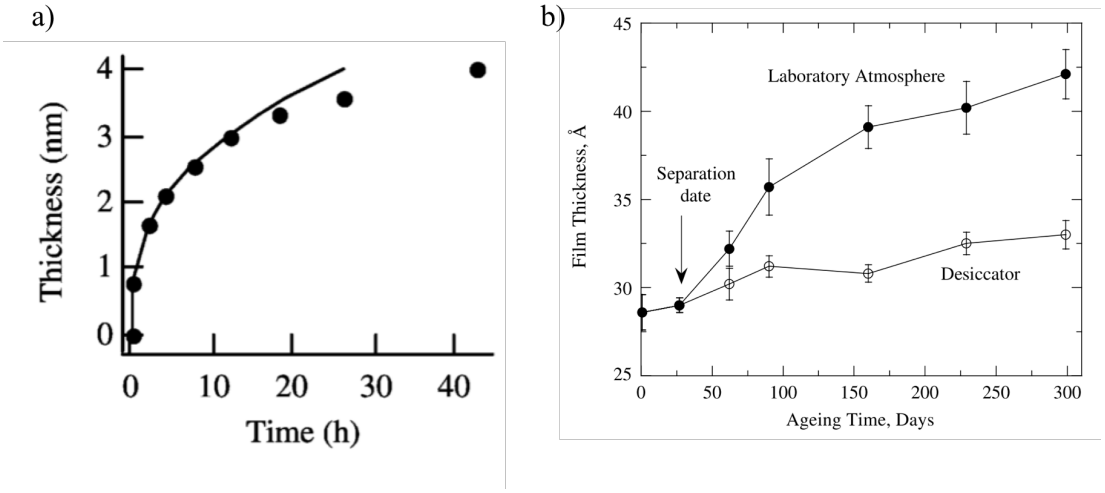


Figure 2.10: a) Early variation of thickness with time during oxidation by Ma and Rosenberg [101] b) Longer term oxidation in dry and laboratory air by Olsson and Landolt [104]

Much less work into the morphology of the titanium/oxide boundary has been performed for atmospheric oxides than for the niobium/oxide system, with the general assumption being a flat overlayer structure [105–108]. There are great discrepancies in the thicknesses of titanium oxides observed. Some authors report this to be on the order of a monolayer or two (1 nm) [109–111], whilst others report layers of 5-8 nm [106, 107, 112]. A large part of this discrepancy is in the method of oxidising the sample. Monolayer level oxides tend to be found on samples oxidised in-situ in the vacuum chamber, where only small volumes of oxygen are admitted. These samples may not have enough oxygen exposure to fully saturate their oxide growth.

Another key difference is the nature of the oxidising gas. Much like for niobium, titanium oxides formed in wet atmospheres grow faster at high temperatures [113], but to my knowledge no single study exists to show this effect at room temperature. However, all of the thickest oxides reported at room temperature have been grown in wet air, whilst the thinnest are all grown in controlled volumes of dry oxygen.

It is worth noting though that oxidation of titanium is slow in pure water vapour atmospheres [114, 115]

A small number of studies have been performed on the surfaces of niobium-rich titanium alloys. However, in most examples the surface of the alloy is treated either by thermal or anodic oxidation to produce an artificially thickened oxide layer, with very little literature available on ambient oxidation. Anodic oxidation uses an oxidising solution and a voltage to drive the oxidation reaction. The oxide formed is dependent on a variety of parameters, including the solution strength and potential used, as well as the anodisation time [116, 117]. For oxides below a particular breakdown potential, the oxide formed has been shown to be of similar composition to the bulk [116], though in some alloys the outer surface has been seen to be rich in niobium and poor in titanium [117]. Thermal oxidation tends to give a different pattern, with several authors reporting titanium rich surfaces [116, 118, 119].

The room temperature study by Tanaka et al. into a Ti–29Nb–13Ta–4.6Zr (TNTZ) alloy by mass is of particular relevance [120]. The alloy is mechanically polished and then stored in a desiccator at 25% humidity for several hours to produce a relatively stable oxidised surface. The surface oxide thickness on TNTZ is 3.7 nm, compared to 4.1 nm and 2.8 nm for titanium and niobium respectively prepared in the same way. The composition of the surface is shown to be enriched in titanium relative to the bulk. However, it is also shown that the fraction of Nb^{5+} cations is higher in TNTZ than in bulk niobium after the same time period, whilst the fraction of Ti^{4+} cations is lower than in bulk titanium. This suggests that the oxidation rate of niobium has been increased in the alloy and the oxidation rate of titanium has been slowed. There is no comparison of the effects of time though, with all samples left for the same time period. Zorn et al. briefly examine an electropolished sample of Ti-45wt%Nb, later used for thermal and anodic oxidation, to determine the initial surface composition. They give no information about the oxide thickness or the growth time, but again show a slightly titanium-rich surface layer [116].

2.6 Outlook and Overview of This Work

The MRI industry demands reliable, high quality persistent joints between NbTi wires. Soldering with PbBi has long proved to be a highly successful technique for this, but moving to the future there is a strong desire to move away from lead-based solders. Development of soldered joints has been primarily industrially led and there are still many scientific questions to be raised, such as what are the effects of the interface layers and what effects the geometry and amount of current sharing has on the joint performance. Other techniques such as spot welding and cold pressing offer the potential for improved performance, but limited reliability makes them undesirable to the MRI industry and so this thesis will focus on solder-based techniques.

This thesis starts by describing the key techniques used for analysing the performance of superconducting joints in Chapter 3. The question of the NbTi surface is addressed in Chapter 4, which presents a detailed x-ray photoelectron spectroscopy characterisation of NbTi surfaces after both short exposures to air and exposure to controlled doses of pure oxygen. Chapter 5 then looks at the solder joints available today, using a wide array of characterisation techniques to understand key limiting factors such as heat-damage in wires and the effect of diffusion barriers on wires, before presenting a detailed characterisation of a lead-free solder joint. Finally, in an attempt to improve the properties of lead-free solders, in Chapter 6 a novel approach of mixing NbTi filaments into a lead-free solder matrix is described, and samples made using this technique are characterised in detail.

Chapter 3

Experimental Methods: Characterisation of Superconductors

Characterisation of a superconductor typically involves mapping out its critical surface; understanding how the critical current of the material varies as a function of applied magnetic field and temperature. Whilst there are many ways of probing these properties, there are two main techniques that have been used throughout this thesis. These are magnetisation measurements where the magnetic moment of a superconducting sample is recorded as a function of applied field, temperature or time, and transport measurements where the resistance of a sample is measured, with particular focus on the departure of a sample from the zero-resistance superconducting state due to critical temperature, field or current being exceeded. Both techniques offer differing benefits and drawbacks, and together provide a detailed characterisation of sample behaviour.

3.1 Magnetic Measurements

The first key characterisation method used throughout this thesis is the measurement of magnetic properties. Superconductors demonstrate a strong diamagnetic response to an applied field through the generation of persistent screening currents that is highly dependent on the critical current, applied magnetic field and temperature of the sample. Magnetometers detect the total magnetic moment (m) of the sample, but it is much more useful to consider the volume (V) normalised moment, known as the magnetisation (M), where

$$m = \int_V M dV \tag{3.1}$$

3.1.1 Bulk Measurements

Understanding the intrinsic materials properties of materials used for jointing is critical to understanding the performance of superconducting joints. The critical surface of bulk materials is easily probed by magnetometry, by sweeping temperature at a constant applied magnetic field (moment-temperature or m–T sweeping) or by sweeping the applied field at a constant temperature (moment-field or m–B loops).

3.1.1.1 Moment-Temperature Measurements

Information about the critical temperature of a sample as a function of magnetic field is easily obtained from moment-temperature (m–T) curves, where the moment of the sample is recorded as a function of a temperature at a fixed applied magnetic field. All measurements in this thesis are performed in the zero-field cooled (ZFC) regime, where the sample is cooled from above its critical temperature to the start temperature in the absence of an applied field, the measurement field is then applied and the moment of the sample measured during warming.

From these measurements, the observed susceptibility, χ_{obs}, of the sample can be calculated as $\chi_{app} = M/H_{app}$, where $\mu_0 H_{app}$ is the applied field. In real magnetic materials

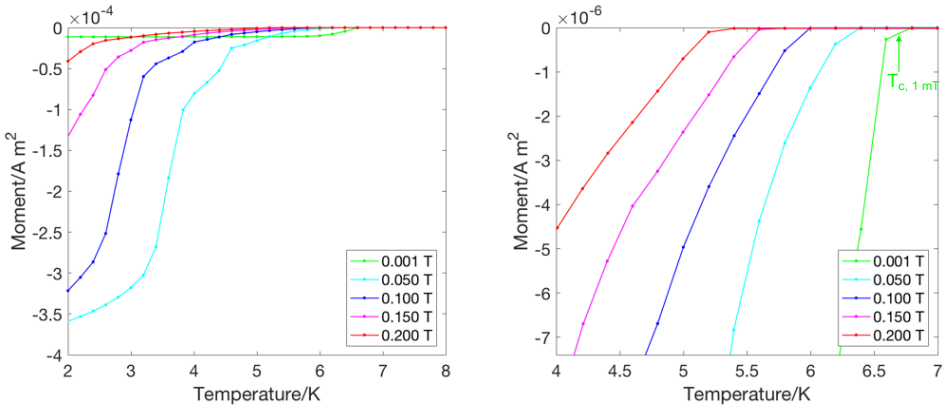


Figure 3.1: Example m–T curves at different applied field measured in the Quantum Design MPMS for a cast cylinder of $Bi_{15}In_{50}Sn_{35}$ solder. The critical temperature was determined by eye when the susceptibility deviated from the straight line (at susceptibility of approximately 0) at high temperatures, as can be seen more clearly in the right hand plot showing only the low-moment region

of non-ideal geometries this is inaccurate due to demagnetising fields. These can be corrected for to obtain the true susceptibility, χ_{act} of the sample as:

$$\frac{1}{\chi_{act}} = \frac{1}{\chi_{obs}} - N \tag{3.2}$$

where N is a geometry dependent demagnetisation factor. Throughout this thesis, demagnetisation factors are taken after Prozorov and Kogan [121], who approximate the demagnetising factor for a finite cylinder in an axially applied field as:

$$\frac{1}{N} \approx 1.6 \times \frac{c}{a} \tag{3.3}$$

where $2a$ and $2c$ are the diameter and height respectively.

At fields lower than B_{c1} this leads to a Meissner state in the sample, with a perfect diamagnetic response, giving a true susceptibility of -1 if the entire sample is in the superconducting state. Susceptibilities greater than -1 at fields less than B_{c1} give an estimate of the superconducting volume fraction of the sample, though this is complicated by connectivity of the inclusions and the differing demagnetising factors of differently shaped inclusions [122].

3.1.1.2 Moment-Field Sweeps and Critical Current

The second main magnetic measurement protocol is moment-field (m–B) sweeping. The sample is zero-field cooled, and the moment of the sample is measured as the applied magnetic field is varied. Above B_{c1}, magnetic flux penetrates the sample and is pinned, leading to hysteretic behaviour. In the technological materials investigated in this project, B_{c1} is considerably than B_{c2}, and the region below B_{c1} can be neglected from further analysis. The penetrated flux leads to two contributions to a superconductor's magnetic moment: a reversible component m_{rev} due to the intrinsic currents of the flux lattice, and an irreversible component m_{irr} due to macroscale currents able to flow in the sample to oppose an applied magnetic field. In technological materials, m_{irr} is much greater than m_{rev}, giving hysteretic behaviour.

The characterisation of superconductors involves understanding the correlations between critical temperature, critical field and critical current. Whilst the first two are easily deduced from magnetisation measurements by mapping $T_c(B)$, deducing the critical current is more complicated. Bean's critical state model [123] provides a good approximation for doing this. As mentioned previously, pinned flux in a type II superconductor leads to macroscale eddy currents that oppose an applied magnetic field. Bean's critical state model assumes that there are three possible conditions for the induced currents in the superconductor: free of current, or carrying $\pm J_c$. Whilst the most basic formulation assumes J_c to be constant, the formulation may be generalised for J_c as a function of applied field. This allows the shape of a magnetic hysteresis loop to be interpreted.

As can be seen in Figure 3.2, upon initial application of a magnetic field onto a sample cooled in zero field, and hence in the Meissner state, flux penetrates the superconducting sample from the outside (a). This leads to a ring of shielding currents of J_c in an outer region of the sample, causing a net diamagnetic (negative) moment, with the central region of the sample still in the Meissner state. When a large enough magnetic field is applied (b), the sample becomes fully penetrated by magnetic flux, and the whole sample has a current of $\pm J_c$. As the field is increased further, J_c decreases leading to

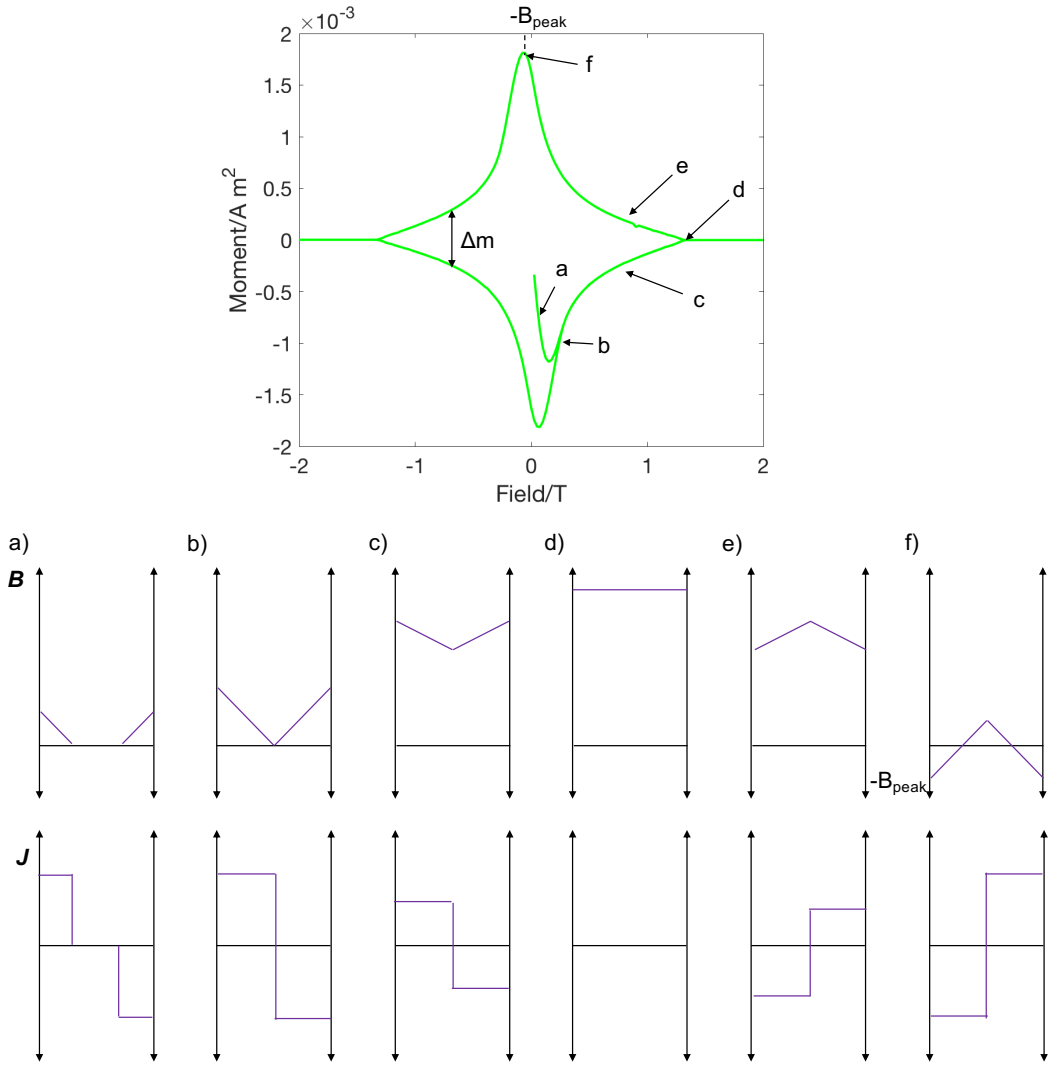


Figure 3.2: Example magnetic hysteresis loop at 4.2 K for a PbBi cylinder. Below are the magnetic field and current profiles predicted by the Bean model at different parts of the hysteresis loop. Note that the slope of the field diagrams is proportional to J_c. More detail about this plot is given in the main text

a smaller flowing current and smaller measured moment (c). At B_{c2}, J_c becomes zero, leading to no net magnetic moment (d). On reversal of the field, the fully penetrated state is re-formed, with currents flowing in the opposite direction, leading to a net moment in the opposite direction (e). It is worth noting that if the field is reversed below B_{c2}, there will be a separate region where the superconductor is penetrated by the reversing magnetic field from the outside. The maximum moment is attained (f) at an applied field B_{peak}, which is not quite at zero applied field due to a finite trapped field generated from the sample itself.

The irreversible moment of the sample can then be correlated to the critical current at any field as the summed contribution of all the current loops in the superconductor. For example, for a cylindrical sample radius R and height $2c$ with field applied parallel to the height:

$$m_{irr} = \frac{1}{2}\int_{-c}^{c} dz \int_{0}^{R} J_c(B) 2\pi r^2 dr = \frac{RV}{3} J_c(B) \tag{3.4}$$

Whilst in theory it is possible to directly calculate J_c in this manner, it is simple to exclude any reversible component of the magnetisation by taking the difference between the ascending and descending branches of the hysteresis loop: $\Delta m = m^+ - m^- = 2m_{irr}$. From this, the well-known link between critical current and magnetisation for a cylindrical bulk is:

$$J_c(B) = \frac{3\Delta M}{2R} \tag{3.5}$$

Similar formulations exist for other geometries of sample. This provides a simple and effective conversion between magnetic hysteresis loops and critical current densities. One consideration for this formula is that it assumes a homogenous sample with uniform critical current density throughout. Whilst this is a reasonable approximation for many samples, it requires careful thought and good understanding of the microstructure of samples before it can be applied. For some samples later in this project this assumption does not hold, which will be discussed further later.

3.1.1.3 Critical Field Measurement

The upper critical field, B_{c2}, of a superconductor can be determined from magnetic measurements as the field at which the hysteresis loop closes. Strictly speaking this is the irreversibility field, B_{irr}, at which flux pinning fails rather than the true B_{c2} [124], however in LTS materials there is very little difference between the two fields and so it is common to use the measured irreversibility field to define the critical field. In technological materials, performance is limited by the irreversibility field of the

material, so the distinction is of little importance in real applications. In practice, accurate determination of hysteresis loop closure is difficult, so critical fields in this project were determined using a critical current criterion, taking the critical field to be the field at which the J_c value had dropped below 10^5 A m^{-2} as shown in Figure 3.3. It is worth noting that values of $B_{c2}(T)$ and $T_c(B)$ are interchangeable, and so more critical field data can be gathered using a combination of m–T and m–H sweeps.

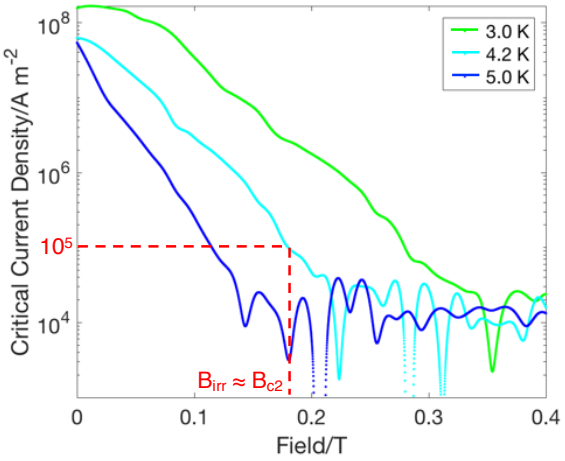


Figure 3.3: Critical current density as a function of applied field calculated from mH measurements on an $Bi_{15}In_{50}Sn_{35}$ cylinder. A 10^5 A m^{-2} critical current criterion is used to extract the irreversibility field. The plateau below this is indicative of the noise level of the experiment rather than any feature of the sample behaviour

3.1.2 Hardware

The majority of the magnetisation measurements reported in this thesis were performed using a Quantum Design Inc. Physical Properties Measurement System (PPMS). The sample is placed in a helium gas controlled variable temperature insert (VTI), capable of continuous temperature sweeping between 1.9 and 400 K with a stability of ±0.2% below 10 K and ±0.02% above it. The system contained a 16 T Oxford Instruments magnet with a field homogeneity of ±0.1% over a 1 cm diameter spherical volume. This platform allows for a range of different measurements to be made using an interchangeable set of options. For magnetometry, a vibrating sample magnetometer (VSM) could be attached, with a linear motor added to the top of the cryostat, and a set of detection coils inserted into the centre of the magnet. The system is shown schematically and

pictorially in Figure 3.4

3.1.2.1 Vibrating Sample Magnetometry

In vibrating sample magnetometry, the sample is oscillated at a constant frequency and amplitude. The moving magnetic field from the sample induces a voltage in the pickup coil, which is proportional to the sample moment, the vibration frequency and the vibration amplitude. Typically magnetometers are calibrated against known reference samples to ensure ensure accurate moments can be calculated. The pick-up coils are wound in a gradiometer configuration to minimise any contribution from varying external magnetic fields.

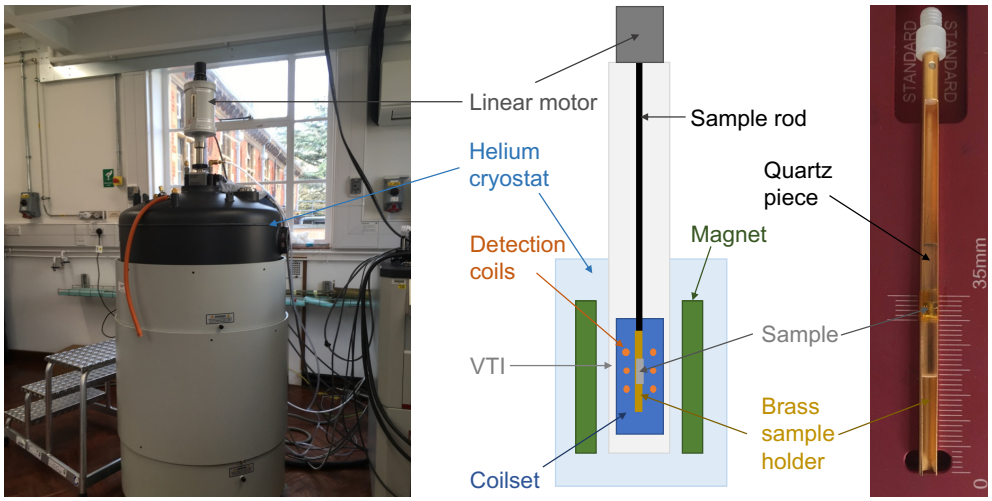


Figure 3.4: Left: photograph of the Quantum Design PPMS with VSM option installed. Centre: Schematic of the VSM operation. Right: Photograph of mounted sample. The sample is held in place by two pieces of quartz that press fit into the brass sample holder. It is then secured with Kapton tape

The PPMS-VSM has a typical oscillation amplitude of 2 mm and frequency of 40 Hz. Signals were detected in the coil set, amplified using a lock-in amplifier to reduce noise. Measurements were averaged over a period of 1 second. The moment sensitivity was 10^{-9} A m^2, which is an order of magnitude larger than achieved in a SQUID magnetometer, but this is offset for most measurements by higher data collection rates (most SQUID systems can only collect about 1 measurement per minute). The system was calibrated against a 3 mm cylindrical palladium reference sample. Samples were mounted in a brass sample holder and pressed between two pieces of quartz to prevent

them moving as shown in Figure 3.4. The sample holder was mounted on the end of a long carbon fibre rod which was suspended from the motor unit at the top of the cryostat. After cooling, but prior to measurements, samples were oscillated whilst lowering through the detection coils in the presence of a small field, giving a voltage trace for each sample location. As a diamagnet, the samples gave a peak negative moment when centred in the coils, allowing the position of the sample to be accurately determined and aligned with the coilset.

3.1.2.2 SQUID Magnetometry

The PPMS only became available part way through the project. Some measurements were instead performed on a Quantum Design magnetic properties measurement system (MPMS). Magnetic measurements are based around a superconducting quantum interference device (SQUID) sensor that allows for extremely sensitive measurements of magnetic moments as low as 10^{-11} A m^2. However, it uses a DC extraction method, lowering the sample then pulling it through a detection coil over a 4 cm typical travel distance. This limits the rate at which data could be collected to around 1 point per minute. Samples were mounted in a VTI with a continuous temperature range between 1.9 and 400 K and magnetic fields up to 7 T could be applied.

3.1.3 Joint Measurements

Whilst the methods above are ideal for measuring bulk samples, the ultimate goal of this thesis is to determine the properties of superconducting joints. Commercial magnetometers allow for measurements over a huge range of temperatures and magnetic fields with much higher rates of data collection than other techniques like transport measurements. So using magnetic methods to probe joints is highly beneficial. Brittles et al. [33, 125] demonstrated the principles of this method, using a single-turn loop with a joint far enough from the loop to not significantly affect the magnetic signal of the sample, whilst at the same time being close enough to be within the homogenous central region of the magnet.

3.1.3.1 Sample Mounting

A special holder for mounting joints for magnetisation was designed by Brittles, with further details described in his thesis [33]. This holder with a mounted joint is shown in Figure 3.5. The former is made from G10 epoxy due to its resilience to cryogenic conditions, ease of machining and low magnetic moment. A central groove is just wider than the wire for the joint, allowing joint loops to be tightly and reproducibly wound to the same shape. This former was designed to be the exact dimension required to fit into a straw for mounting in older magnetometers.

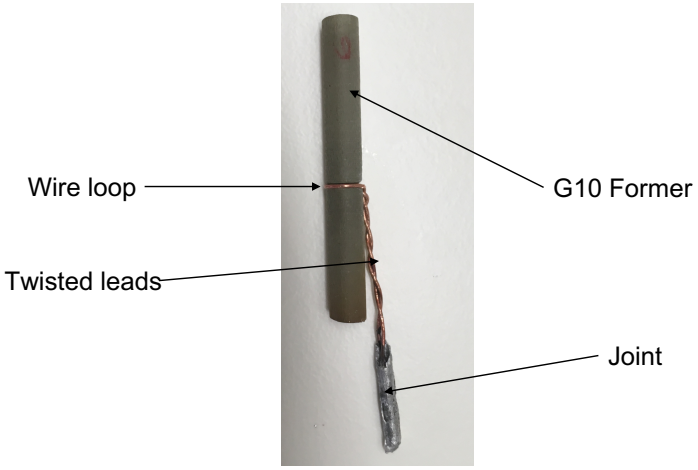


Figure 3.5: Cast solder joint mounted for magnetic measurements

3.1.3.2 Hysteresis Loops and Current

Brittles devised a simple Bean critical state model approximation to describe the magnetic response of these samples as shown in Figure 3.6 [33]. For a completely open loop, the behaviour would be much as described previously for a bulk sample, with currents of J_c penetrating the wire from the outside in rings. For a completely closed loop, currents of J_c will instead circulate the loop. If there is a joint with critical current (not critical current density) lower than that of the wire as in Figure 3.6a, current loops of J_c penetrate the wire from the outside until the critical current of the joint is achieved (b). As field is increased beyond this (c), the critical current of the joint (and so that can be transferred round the loop) decreases. The area of wire carrying J_c decreases to accommodate the lower current, and loops of current (known as magnetising currents)

are induced in the remainder of the wire, much as in a disconnected loop. Once the critical field of the joint is surpassed (d), only the magnetising currents flow in the wire, leading to a moment similar to that of an open loop. In this project, joints were small with lower critical current than the wire. In the extreme case of a perfect joint, it is expected that the wire would behave like a perfect loop.

A single current loop generates a magnetic moment $m = IA$, where A is the area enclosed by the loop. Approximating the loop as an infinitely thin perfect circle, the current giving a particular moment can be deduced from:

$$I = \frac{m}{\pi r^2} \tag{3.6}$$

where r is the radius of the loop. By the critical state analogy above, when fully penetrated the wire must be carrying I_c, or if a joint is present $I_{c,joint}$, hence the moment produced is directly relatable to $I_{c,joint}$. It is worth noting that the magnetising currents previously mentioned will produce a small net moment of their own that will cause a slight error in this value, as will errors associated with the fact the sample is not a perfect circle, so it is only an approximation of the true critical current of the joint.

The wires described by Brittles were large single core wires. In this thesis it was desirable to understand joints between the multifilamentary wires used in magnet production. The same basic theory as to penetration of currents into the wire apply for these samples, but on a filament by filament basis. Converting moment into a circuital current can be considered in the same way as for a single core loop, with the exception that there are multiple loops. A good approximation is to consider these as independent, ignoring the potential for current sharing between filaments. The multiple filaments of the multifilamentary wire are beneficial for these measurements, as their narrower diameter helps prevent against flux-jumping, allowing for good measurements at low temperatures, something not attainable with monocore wires. The narrow diameter also reduces the size of the magnetising currents [33]. The multiple twisted filaments in the wire makes the true current paths more complicated to understand so a true

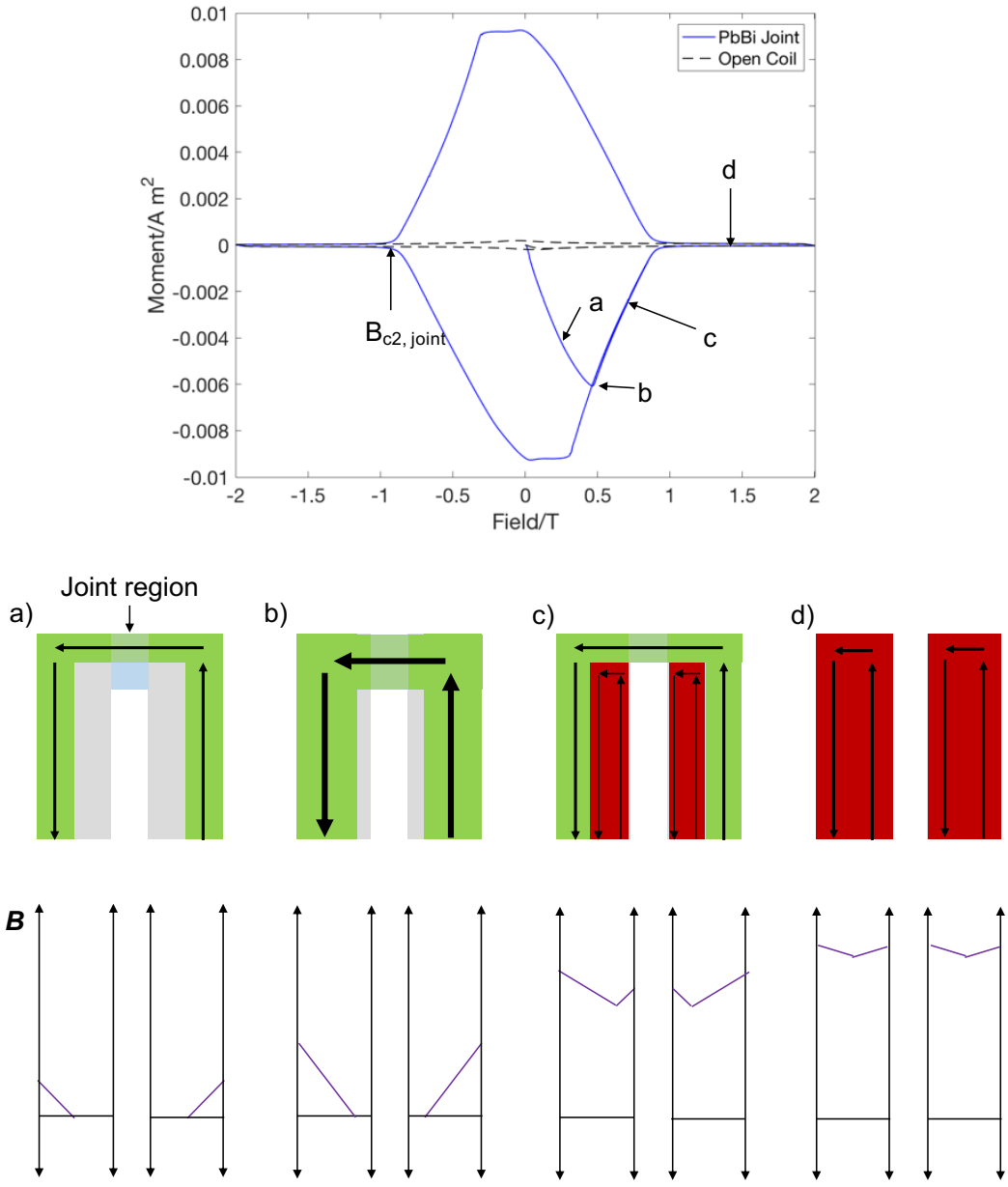


Figure 3.6: Top: Hysteresis loop of a PbBi joint at 6 K. The performance of an unjointed coil is also shown, and only when the PbBi joint is superconducting does the moment differ from this. Plots (a) to (d) show the position of the current in the joint and wire system and the magnetic fields in this region using a simple Bean model explanation as described by Brittles [33]

conversion of moment to current is difficult, but the technique provides a good first order estimate of the current.

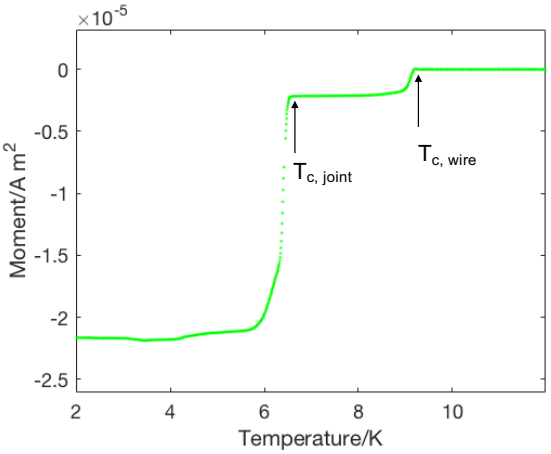


Figure 3.7: m–T curve for a cast $Bi_{15}In_{50}Sn_{35}$ joint at 1 mT. There are two distinct critical transitions corresponding to the critical temperatures of the wire and the joint.

With this circulating current strongly linked to the properties of the joints, the technique can very easily measure critical temperature and critical field much in the same ways as described for bulk material, with the only difference being that there will be two transitions: a large one when the critical parameter of the joint is exceeded, and so circulating currents can no longer flow, and a smaller one where the critical parameter of the NbTi wire is exceeded so no supercurrent can flow in the joint loop.

3.2 Decay Measurements

Whilst understanding the critical surface of joints is useful to understanding their use in applications, it is also essential to understand the properties of jointed circuits over time. Persistent-mode circuits are used for their extremely high temporal stability, so investigating this is of key importance. Typically this is performed using a custom-built system, but it is possible to get a good estimate of performance using commercial magnetometers using the small-scale method described previously. Late in this project, access became available to a system at Siemens Magnet Technology built by Mariusz Wozniak. This allowed a small number of samples closer to industrial size to be analysed.

The principle of decay measurements, also known as inductive resistive testing (IRT), is that a current is introduced into a coil or loop of wire containing a joint. This current can either be induced magnetically using a transformer-like set-up [72, 125] or by quenching the joint and driving a current in directly with a power supply. This current is then measured as a function of time, usually by measuring the magnetic field generated by the coil or loop, though measurements directly measuring the field around a straight wire are also possible [72,126]. Simple theory relates resistance to the change in current with time:

$$L\frac{dI}{dt} + IR = 0 \tag{3.7}$$

where L is the inductance of the coil. Solving this equation for current gives an exponential decay with time constant $\tau = L/R$, so fitting exponential curves to decay curves allows the resistance of the circuit to be deduced. Typically in these measurements the wires are comfortably within their operating parameters and it is the joint that is the limiting factor, so it is reasonable to assume that all the measured decay is attributable to the joint.

Measurements can be performed in a background field, typically applied in the plane of the detection loop to decouple the loop from any decay in the background magnet. The minimum measurable resistance using a decay can be estimated as:

$$R_{min} = \frac{L}{t - t_s}\frac{|\delta I|}{I} \tag{3.8}$$

where t_s is the start time of the measurement, t is the current time of the measurement and $\frac{\delta I}{I}$ is the minimum measurable change in current over this time, typically due to the magnetic field sensitivity $\frac{\delta B}{B}$ of the detector. Field detection in the loop is typically done using a Hall probe, though a SQuID sensor or other magnetometer technique can be used using the method developed by Brittles, which increases sensitivity, allowing measurement times to be reduced accordingly.

3.2.1 PPMS Decay Measurements

Most decay measurements in this project were performed using the magnetic decay technique described by Brittles [33]. This mounts a joint as described for the magnetisation measurements, and then measures the decay of currents induced in the loop. This differs from conventional IRT set-ups in that the current induction and background field are performed by the same magnet. This can lead to problems with coupling between the background magnet and the loop, but is necessary for implementation in a commercial magnetometer. These offer greater magnetic field sensitivity and a much greater variety of field and temperature conditions than available with conventional IRT rigs, whilst also not requiring the building of highly specialised kit.

As current could not be induced with a separate transformer coil, it had to instead be induced through a field-cooling regime. Samples were cooled in a background field, B_{FC}, and then the magnet was set to the desired measurement field, B_{BG}, in the *no-overshoot* mode, where the desired field is approached in a heavily over-damped manner. This induces a moment in the coil given by:

$$m = \frac{dm}{dB_{app}}(B_{BG} - B_{FC}) \tag{3.9}$$

Hysteresis loops were first taken to directly measure $\frac{dm}{dB_{app}}$ as the gradient of initial current induction, allowing the necessary B_{FC} to be calculated. Measurements could be performed in two regimes: varying the induced moment in a constant background, or varying the background. In this project, this second option was generally desirable to explore the performance of persistent joints as a function of applied field. To ensure consistency between fields, the largest possible magnetic moment, and so current, was induced in the sample.

Brittles performed this in a SQUID magnetometer offering the ultimate magnetic moment, and so current, sensitivity. However, drifts in the background field induced drift voltages of $10^{-12} - 10^{-14}$ V, meaning the ultimate sensitivity of the system could not be reached [33]. As a result, I used the PPMS-VSM to perform the same measurements

with the higher data collection rate allowing easier interpretation of results. Measurements were performed over a period of three hours, which was long enough for settling effects to be minimal in the small test loops used.

3.2.2 Large-Scale Decay Measurements

Larger samples were measured on a new decay rig at Siemens Magnet Technology designed and built by Mariusz Wozniak. Current was driven into the sample with a superconducting step-down transformer with a roughly 100 times current amplification factor that easily allowed currents in excess of 1000 A to be induced without the need for a large power supply. The sample consisted of a four turn loop 8 cm in diameter, with the joint made approximately 30 cm below the loop. A heater coil was wound around the straight sections of wire to allow the loop to be quenched out of the superconducting state during the current induction process. The magnetic field, and so indirectly the current, from the sample loop was measured by a Hall probe. This was calibrated during the set-up of each sample to calculate the inductance of each loop, and to ensure a reliable conversion from Hall voltage to loop current. The set-up is shown in Figures 3.8 and 3.9.

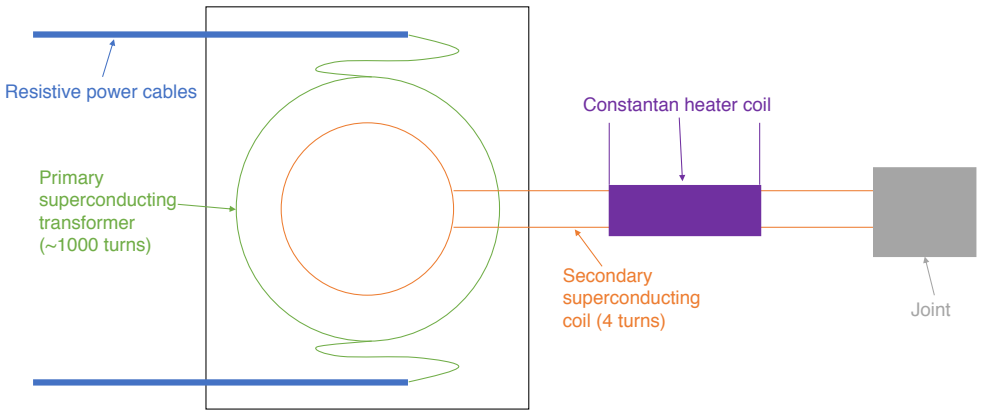


Figure 3.8: A schematic of the IRT rig at Siemens Magnet Technology

The protocol for running the IRT measurements is illustrated in Figure 3.10. Initially, the heater was used to quench the circuit, ensuring no current flowed in the joint. As the current was ramped up in the primary coil to a known value, a corresponding current was induced in the secondary coil. The joint was quenched again, allowing

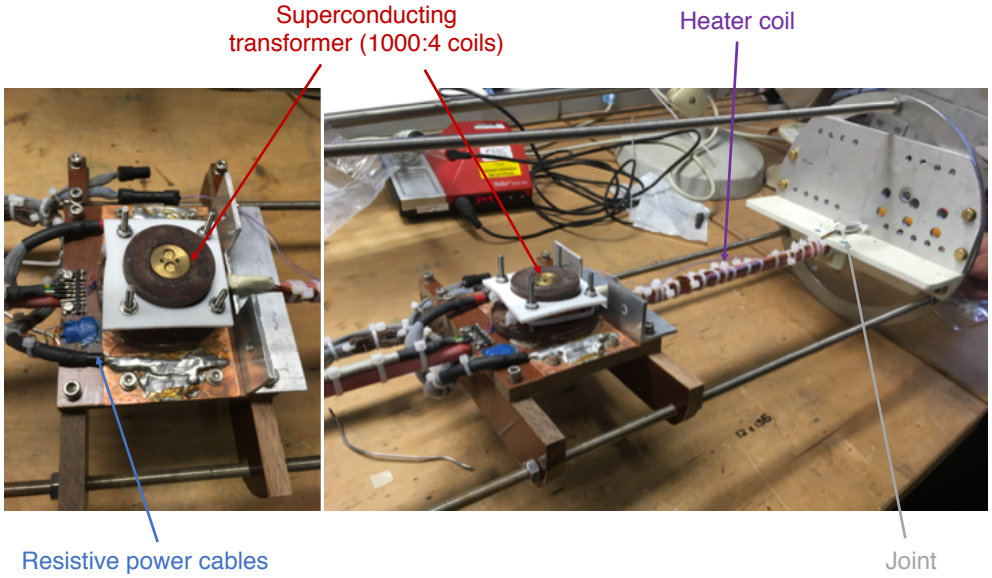


Figure 3.9: A photograph of the IRT rig at Siemens Magnet Technology with a sample mounted

the Hall voltage to only relate to the signal from the primary coil. This allowed the field-to-signal conversion for the Hall probe to be calculated using a known current. The current in the primary coil was then reduced to zero, inducing a current in the secondary coil. This procedure allowed the mutual inductance of the system to be calculated. The primary coil was then ramped to a value that will induce the correct current in the secondary coil, the joint was quenched to remove any current from the secondary loop, and then the primary coil was discharged, inducing the measurement current in the secondary coil. The Hall probe was then used to measure the magnetic field created by the secondary coil, and so the current flowing in it. Measurements were carried out continuously over periods of over 24 hours due to the large helium capacity of the cryostat.

3.3 Transport Measurements

Whilst magnetic measurements give a clear indication of the behaviour of a superconductor within its critical surface, it is also possible to probe the outside of the surface by measuring the resistivity of the superconductor. In the superconducting state, the resistivity of a superconducting sample is zero or at least significantly lower than can

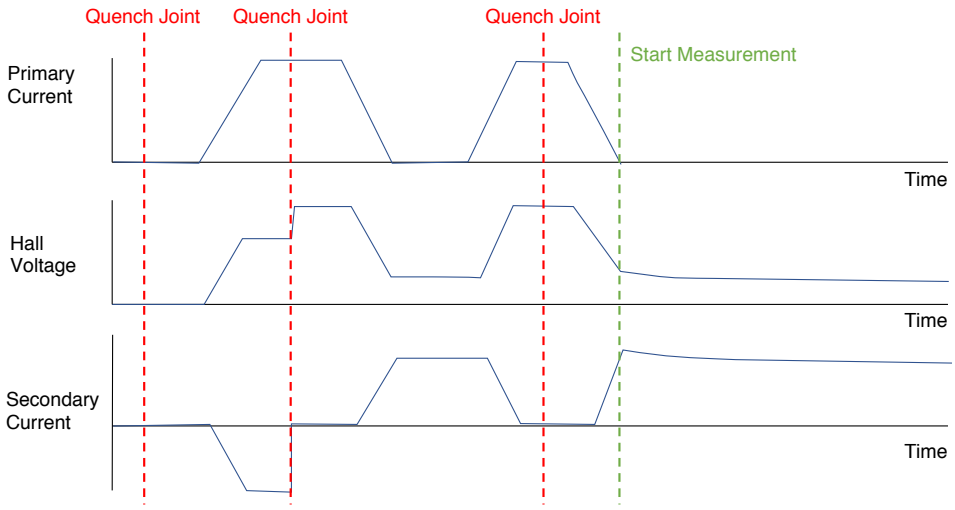


Figure 3.10: Schematic of the measurement procedure for decay measurements on the rig at Siemens Magnet Technology, showing the applied current in the primary transformer coil, the induced current in the secondary coil, and the signal to the Hall probe, which is a combination of the two signals

be measured by conventional means, but it is highly instructive to understand how the sample transitions out of the superconducting state. The best transport measurements are made using a 4-point method, where current is passed into a sample via two current leads, and the voltage across a section of interest is measured using a separate set of voltage taps. This allows only the resistance of the region of interest to be measured, negating the effect of the resistance of the current leads. For superconductors, there are two main areas of interest for transport measurements. The first is to use a very low current, sweeping either the magnetic field or the temperature to determine the critical parameters. The second is to sweep the current at a particular field and temperature. Repeated measurements at different temperatures and fields allow $J_c(B, T)$ to be investigated.

3.3.1 Low Current

Low current measurements are important in understanding the fundamental physics of many superconductors, but only played a small part in this thesis so will not be discussed in detail. Samples were fixed to a piece of quartz with GE varnish. A pair of 15 micron gold wires were attached to the ends of the sample to act as current

leads, and a second pair attached to the middle to form voltage tap as shown in Figure 3.11. All contacts were made with silver paint due to the low melting point of the samples. Measurements were performed in the 16 T Quantum Design PPMS described previously using the electro-transport option (ETO). This allowed two samples to be measured simultaneously.

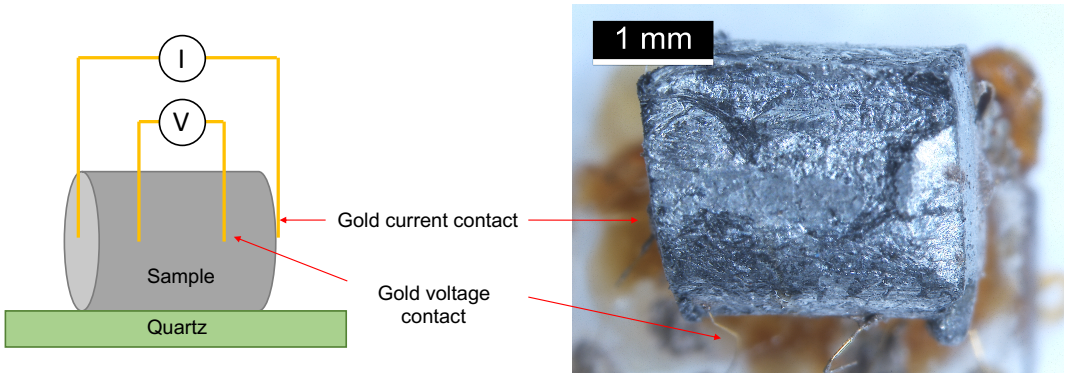


Figure 3.11: Left: Schematic of low-current transport measurements. Right: Photograph of a sample with current and voltage contacts attached with silver paint

3.3.2 High Current

The second type of transport measurement commonly performed on superconductors is high current sweeping. This is very commonly performed on larger scale technological superconductors, especially when processed into wires or tapes, where the transport measurements give a strong indication of the performance of the wires under real-world conditions. Facilities for these measurements have recently been re-developed in the Clarendon Laboratory, providing a useful tool for routine investigation of superconducting joints.

3.3.2.1 Theory and Analysis

In principle, high current transport measurements are amongst the most simple techniques available for the analysis of superconducting wires. Current is driven through the sample, and the voltage across a section of the wire is measured. In the superconducting state, the sample has no resistance and so zero voltage is measured. As the sample transitions to the normal state, it has non-zero resistance and so a small volt-

age can be detected. More commonly, the voltage is normalised against the distance of sample between voltage taps, the so-called "tap distance", L, to give an electric field $E = V/L$. The critical current is defined as the current at which a particular electric field criterion is exceeded. Typically criteria of 10 or 100 μV m^{-1} are used, though it is worth noting this will always give a critical current, even with a wholly resistive sample. It is also possible to use a resistivity criterion, $\rho_c = VA/IL$, where A is the cross-sectional area of the conductor, which increases linearly with current.

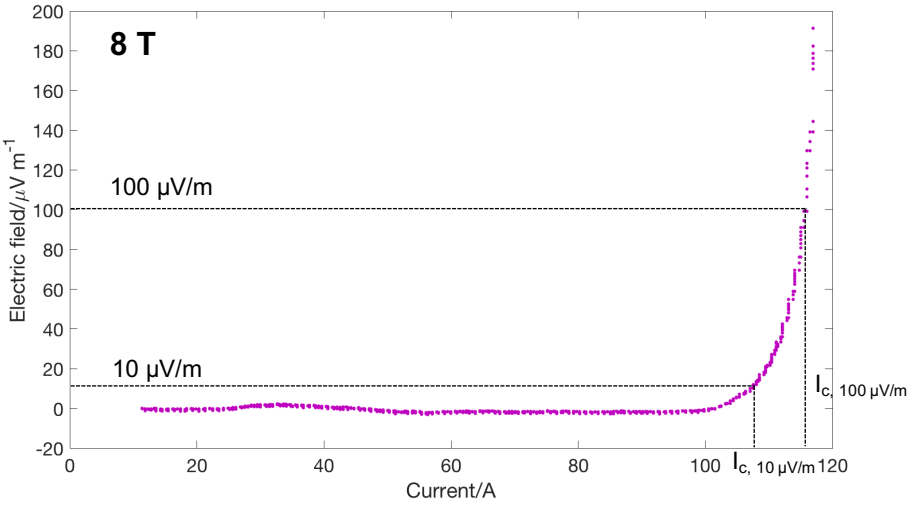


Figure 3.12: An example plot of electric field against current for Supercon 54S43 NbTi conductor at 8 T and 4.2 K. The 10 and 100 μV m^{-1} criteria are marked, giving critical currents of 107 and 116 A respectively.

Figure 3.12 shows an example transport measurement taken at 8 T and 4.2 K on Supercon 54S43 NbTi conductor. The critical current is determined using both 10 and 100 μV m^{-1} criteria, giving critical currents of 107 and 116 A respectively. This marks a common feature of all transport critical current measurements – there is a strong dependence of critical current on the criterion used. As such, it is important when comparing transport data to ensure the same criterion is used, though the exact criterion does not make a huge difference as long as it is consistently applied. In this thesis, a 10 μV m^{-1} criterion is used for all wire measurements, as it allowed consistent measurements without sensitivity to sample noise. It was also found that at higher currents, samples would occasionally exhibit thermal runaway behaviour leading to sudden transitions before a 100 μV m^{-1} criterion was reached. All transport measurements give an over-

estimate of critical current as the sensitivity of 4-point measurements is considerably lower than that of magnetic measurements [127], so it is desirable to use as low a field criterion as possible when investigating fundamental wire properties.

When measuring joints, the sample is no-longer homogenous along its length. As the joint is typically the weakest point in the circuit, it is likely that all of the voltage is produced in the joint, and so the distance along the wires of the voltage taps is arguably irrelevant. However, there is little literature on how the voltage produced depends on the joint geometry, and so it was decided that a simple voltage criterion would be applied for determining the performance of joints. This is likely to lead to some variation in results depending on joint geometry, so it was important to keep this consistent when comparing different joints.

For an idealised perfectly homogenous superconductor, the transition from superconducting to normal state might be expected to be infinitely sharp, with the electric field reverting instantly to the value expected of an ohmic sample. However, real conductors are not perfectly uniform, containing variations on both a micro- and macroscopic scale, meaning any transition will not be perfectly uniform. Furthermore, many superconductors demonstrate dissipative effects such as flux creep or flow prior to reaching their critical current, again leading to voltages being recorded. A good approximation for the shape of the superconducting transition is to assume a power-law dependence:

$$E = kI^n \tag{3.10}$$

where k is an arbitrary constant and n is the n-value of the transition – a common figure of merit in engineering applications. The n-value for typical conductors is between 10 and 100, and is indicative of the homogeneity of the conductor, with highly homogeneous conductors having the highest n-values.

Figure 3.13 shows the same data as in Figure 3.12 but on a logarithmic scale. From this, a straight line fit at high currents gives the n-value of the transition to be 31. This linear regime extends down to currents of approximately 90 A, before sharply flattening off with a wide scatter of electric fields. In this low-current regime, measurements

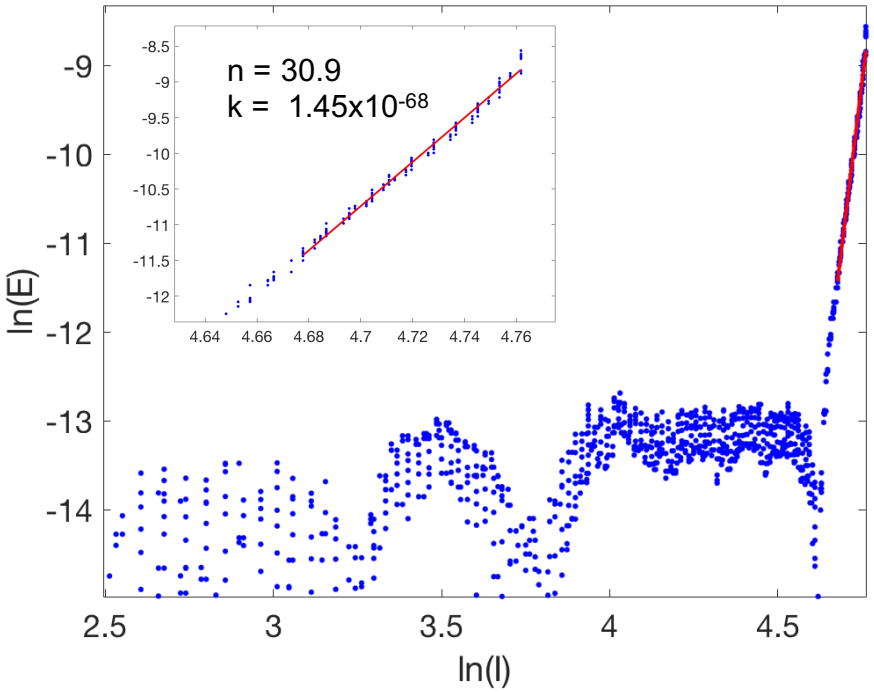


Figure 3.13: The same data as in Figure 3.12 plotted on logarithmic axis. Around I_c there is a linear increase, the gradient of which gives the n-value of the transition. The inset shows this in detail, with the red line representing the fitted n-value. At low currents there is just noise

are limited by the sensitivity of the system rather than the fundamental properties of the sample, and so little can be deduced. However, it gives a good indication of the noise level of our apparatus, representing an electric field sensitivity of approximately 2 μV m^{-1}. It is worth noting that Ryan et al. [128] demonstrated using inductive measurements that the power law approximation holds considerably beyond the sensitivity limit of a 4-point measurement.

3.3.2.2 Hardware

Due to ongoing development of the Clarendon facilities, the apparatus available changed during the project. Early experiments were performed in an Oxford Instruments cryostat with a 14 T superconducting magnet, whilst later experiments were performed using a Cryogenic Limited cryostat with 14 T superconducting magnet due to the latter system's larger helium chamber allowing for improved cryogenic efficiency. Measurements were performed using a probe built in-house, rated to 500 A. This is shown

schematically in Figure 3.14. Current was transferred to the sample via thick copper then brass leads, whilst the voltage taps were run as twisted pairs of much finer wire to minimise noise. Along with these, a Cernox thermometer was connected with fine wire in twisted pairs down to the sample to monitor the sample temperature. The probe wass hollow with a top outlet for the helium. During experiments the main helium outlet was closed, forcing any boil-off through the probe, acting to cool the current leads. A thermometer connected to the top of the probe monitored for excessive heating of the probe leads during measurements to prevent damage from thermal load at high current.

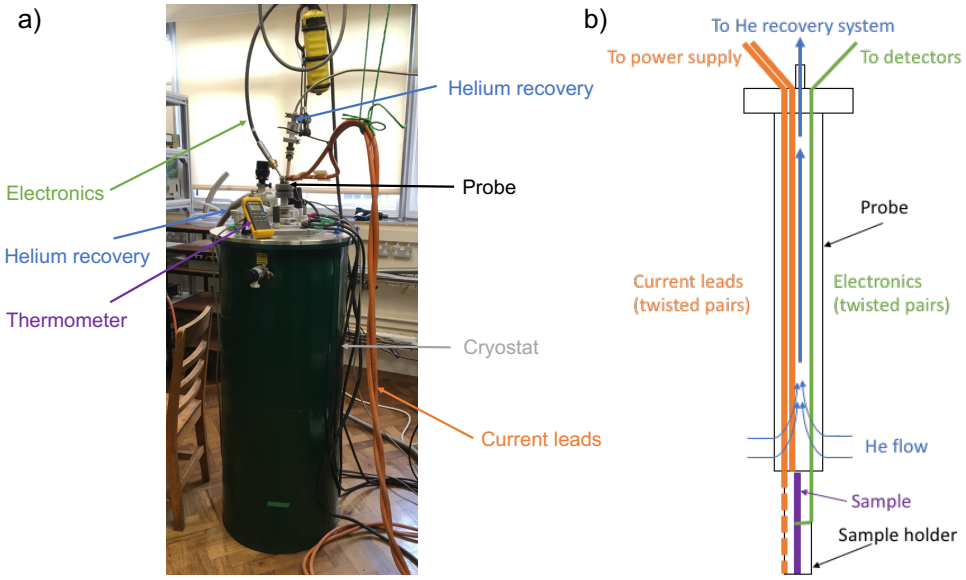


Figure 3.14: a) Photograph of transport measurement set-up and b) schematic of measurement probe

Current was supplied using either a Glassman Europe BPI1200 power supply capable of a maximum current of 1200 A or an Agilent 6680A with a maximum current of 875 A, though the probe limited the maximum current during experiments to 500 A. When only a low current was required a 100 A Keysight N9650A power supply was used. The Oxford Instruments magnet was controlled using an Oxford Instruments Mercury IPS120 magnet controller, whilst the Cryogenic Limited system was controlled by a Cryogenic Limited SMS power supply. The signal from the voltage taps was amplified by 10,000 times using an in-house amplifier, which also incorporates a low-pass filter to reduce noise, before being measured by a Keithley 2182A nanovoltmeter. The resistance

from the Cernox thermometer was read using a Lakeshore 336 thermal controller with a pre-determined calibration installed. The instruments were all controlled using the Department of Physics's home-built *Fridge Control* software.

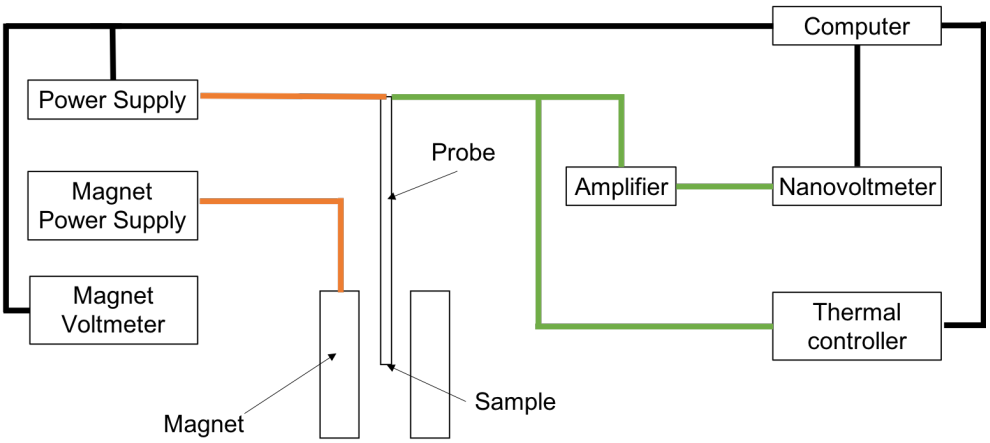


Figure 3.15: Schematic of the electronics used for the high current measurements

3.3.2.3 Sample Mounting

The probe allowed for two main sample mounting techniques. The first was known as the "short-straight" sample holder. This was a long Tufnol block with two copper pads for contacting the sample. The sample was fixed to the holder with pure indium solder, and the voltage taps connected to the sample with lead-tin solder. This holder leaves the sample parallel to the applied field, but enables thick wires that cannot be bent, or those of brittle superconductors to be measured easily and effectively. The distance between the voltage taps is limited by the size of the sample and the need to be far enough away from the current contacts to allow full transport of current through the copper stabiliser of the wire and into the superconducting filaments. If this is not the case, spurious voltages will be measured due to this incomplete current transfer. Due to the limited voltage tap distance, the sensitivity is lower for this sample holder. However, it allowed for fast changing of samples without needing any other preparation, so was useful for proof-of-concept joint testing.

The second sample holder is the well-known "barrel-type" sample holder. For this type of sample holder, the sample is wound around a stainless steel barrel with copper ends.

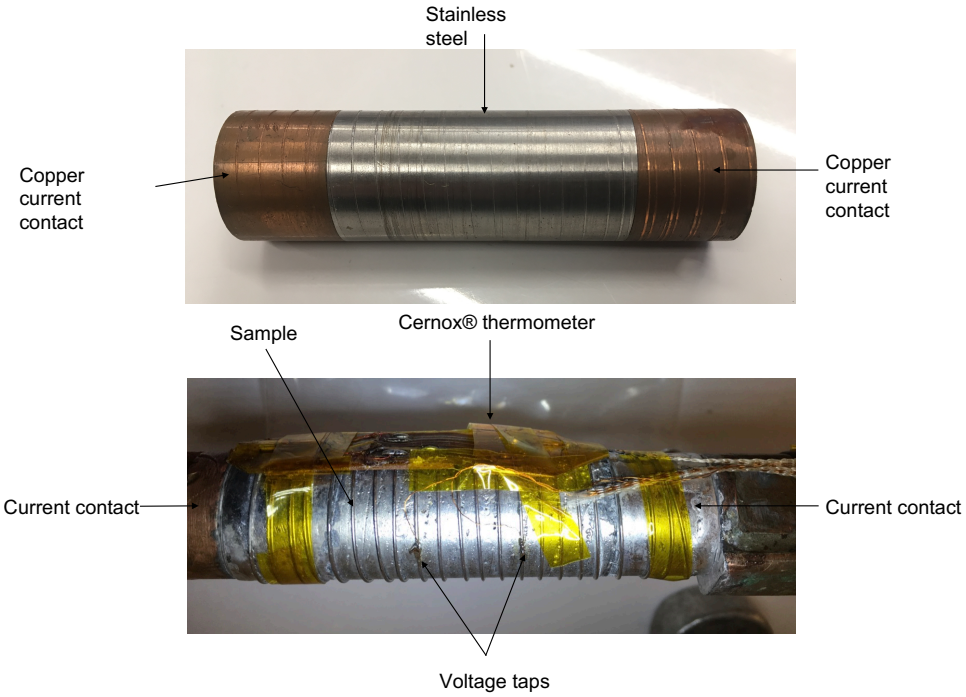


Figure 3.16: a) A clean, empty barrel type holder. b) A wire mounted on a barrel-type sample holder. Current is driven into the copper ends of the barrel, and then transfers into the sample

The ends of the barrel are coated in indium and it is then mechanically fixed to the probe by screwing it between copper contacts, with the indium forming a cold-weld to allow good current transfer into the holder. Current transfers from the probe into the copper ends of the barrel, and then into the sample. Samples were wound onto the barrels using a lathe to ensure an even winding tension throughout. They were then soldered onto the barrel with PbSn solder to fix the wire in place during measurement and provide electrical and thermal contact between the sample and barrel. In this geometry, the current is nearly perpendicular to the applied field with a maximum twist pitch of approximately 6°. Goodrich and Fickett note that twist pitches less than 7° have negligible effect on measurement of critical current [129]. The barrel geometry is ideal due to the long length of wire between the voltage taps, typically about 30 cm, allowing a longer tap distance to be used and so greater measurement sensitivity can be achieved. There is also a larger area available to transfer current into the sample, minimising current-transfer voltages and heating under the current contacts. The steel barrel acts as a heat-sink, transferring any excess heat during a sample quench out of

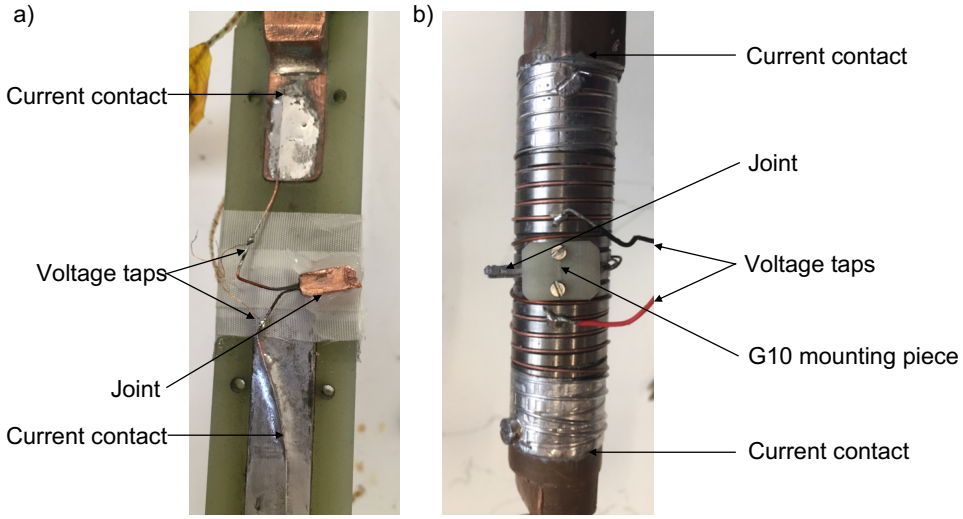


Figure 3.17: The short-straight sample holder a) and barrel-holders set up for joint measurement. On the barrel holder, a Tufnol bridge has been added to pin samples down, allowing termination joints to be easily wound onto the holder.

the wire, giving extra sample protection.

Almost all the joints made in this project were termination style joints, where wires came in and out on the same side of the jointing material. This greatly simplifies manufacture, and is the geometry generally used in MRI magnets, but is harder to mount on these sample holders. Joints could be reasonably easily mounted on the short-straight holder by bending the wires so the joint ran perpendicular to the applied field, allowing the weakest part of the circuit to be parallel to the field and so easily detectable. It was found joints on this holder failed more regularly due to poor thermal protection during quenching. As such, a barrel-type holder was modified by adding a Tufnol strip that could be screwed over the joint, allowing the wires to be wound in opposite directions around the barrel without movement during soldering. Solder contacts from the wire to the copper barrel could be made by dipping only the ends of the wire. For solder joints with low melting temperatures, considerable care had to be taken during soldering to prevent heating of the joint during soldering the barrel, so a protective plastic and foil wrap was used and temperature of the barrel was monitored during soldering to ensure the barrel stayed below the melting temperature of the jointing material.

Chapter 4

Atmospheric Oxidation of NbTi Superconductors

It is well-known that oxidation of NbTi conductors is a fundamental problem for many jointing processes. Yet, whilst some knowledge exists about the oxidation of the individual components [89, 101, 104, 105, 107] I know of no study that considered the oxidation of superconducting NbTi alloys under ambient conditions. Information about the kinetics and morphology of the oxide growth are essential for understanding how oxides could influence joint formation, whilst chemical information about the composition of the oxide is required to allow the electronic properties of the oxide to be understood for modelling the effect of such an oxide layer on joint performance. This chapter uses angular-resolved x-ray photoelectron spectroscopy to investigate oxides forming on the surface of NbTi alloy samples, allowing compositional information about the surface of the sample to be determined as a function of depth.

Samples of Nb–45wt%Ti sheet with carefully prepared surfaces were analysed after oxidation in laboratory air for short time periods between 15 seconds and 1 hour to represent conditions seen in real jointing processes. The initial stages of oxidation were then studied by gas dosing the sample at very low partial pressures of oxygen to allow earliest stages of oxidation to be understood. From this data, the structure and composition of the oxide is presented as a function of oxidation time, with a particular

focus on the thickness of the oxide.

4.1 Background Theory

For analysing surface layers over depths on the nanometre scale, X-ray photoelectron spectroscopy (XPS) is by far the most heavily used spectroscopic technique. It is based on the photoelectric effect, where photons incident on a material are absorbed and electrons are emitted with a particular kinetic energy dependent on the frequency of the incident light [130]. As incident photons are both chargeless and massless, they completely transfer their energy to the emitted electrons. This means any difference between the kinetic energy of the electron emitted and the photon energy is due to the energy required to remove the electron from the material, known as the binding energy (E_b). This depends on the particular electronic transitions that correspond to the removal of the electron from a particular electronic orbital, which vary by element and the chemical state of the atom. The kinetic energy (E_k) of detected electrons is given by the standard photoelectric equation:

$$E_k = h\nu - \phi_{\mathrm{XPS}} - E_b \tag{4.1}$$

where $h\nu$ is the energy of the incident photons and ϕ_{XPS} is the work function of the XPS: the energy required to remove an electron from the instrument (as opposed to the sample surface) for a conductive sample in electrical contact with the XPS. As the binding energy is sensitive to both the element present and its environment, XPS allows for the differentiation of different oxidation states of the same element – invaluable for close analysis of surface interactions. Whilst XPS can give information about valence band electrons, laboratory-based systems are optimised to study core-level electrons for all elements from lithium to uranium, often with sensitivities down to 0.1 at%.

Whilst x-rays penetrate a long way into the surface of a material, emitted electrons are much more quickly attenuated. This is described for homogeneous materials by the inelastic mean free path (λ), with the intensity of signal recorded from a depth

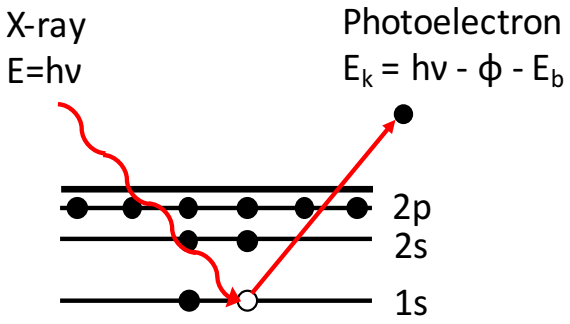


Figure 4.1: Schematic of photoemission from a surface. Incident photons cause emission of electrons, the energy of which is determined by the well known photoelectric equation [130]

z decreasing exponentially such that the intensity of a buried layer of thickness δz is given by [131]:

$$\delta I = \sigma T(E) A N(z) \exp\left[\frac{-z}{\lambda \cos\theta}\right] \delta z \tag{4.2}$$

where $N(z)$ is the atomic concentration of the species belonging to a specific peak at depth z, σ is the Scofield photoemission cross-section, $T(E)$ the analyser transmission function, A the photoelectron emissivity area and θ the angle between the detector and the surface normal. The analyser transmission function and photoemission emissivity area are two constants that are instrument and set-up specific. The photoemission cross-section describes the probability that a photoelectron from a particular atomic orbital will be emitted after irradiation by a photon of particular energy. For laboratory-based instruments with Al-Kα x-ray sources these were collated by Scofield [132]. In laboratory based XPS analysis, these three factors are commonly combined to give a sensitivity factor, S, for a particular elemental peak. If multiple elements are present in a sample, the concentration of a particular element, x_a, in the sampled depth can be given by:

$$x_a = \frac{I_a/S_a}{\sum_n I_n/S_n} \tag{4.3}$$

Whilst this is useful for analysing homogeneous samples, many key uses of XPS involve analysing samples with a non-uniform composition with depth. Perhaps the most common example of this, and the one most significant to this work, is the analysis of overlayer structures, in particular the analysis of native oxides [133–135]. These can be simply modelled as a single homogeneous layer of oxide of thickness t_{ox} over the bulk metal. In metal oxides the metal exists as positive ions, leading to reduced shielding of electrons from the nucleus, and so a small increase in the binding energy for the oxidised species. As such, signal from a metal oxide can be differentiated from the bulk metal. Integrating Equation 4.2 over the two layers gives the total intensity from photoelectrons released from the bulk metal as:

$$I_{met} = \lambda_{met} N_{met} \sigma T(E) A \cos\theta \exp\left(\frac{-t_{ox}}{\lambda_{ox} \cos\theta}\right) \tag{4.4}$$

And the intensity of photoelectrons from the oxidised metal in the oxide overlayer:

$$I_{ox} = \lambda_{ox} N_{ox} \sigma T(E) A \cos\theta \left[1 - \exp\left(\frac{-t_{ox}}{\lambda_{ox} \cos\theta}\right)\right] \tag{4.5}$$

Crucially, when combining two peaks from the same atom and electronic transition with just a small chemical shift, any variations in the cross section and instrumental factors are negligible. This means that taking ratios of the intensities allows for more accurate calculations of layer thickness without any dependence on the instrumental factors. Combining the two intensities gives the well-known Strohmeier equation for the oxide thickness [134]:

$$t_{ox} = \lambda_{ox} \cos\theta \ln\left[1 + \frac{\lambda_{met} N_{met}}{\lambda_{ox} N_{ox}} \frac{I_{ox}}{I_{met}}\right] \tag{4.6}$$

Comparing the intensities ratios of two similar peaks allows the layer thickness to be calculated. Exploring more complicated depth information is possible in two main ways. In Equation 4.2 it is clear that the intensity contribution from a particular thin layer δz at depth z is dependent on $\lambda_{ox} \cos\theta$. Commonly, the sampling depth is

approximated as $3\lambda \cos\theta$, corresponding to when a signal has decayed by 95% of its original intensity [136]. There are two main variables that can be explored to gain depth related information. The first is the collection angle θ. As can be seen in Figure 4.2, the effective sampling depth is reduced if the sample surface normal is tilted away from the detector, meaning signals from surface-related features are enhanced at the expense of bulk-related features. This is known as Angular-Resolved XPS (AR-XPS), and is described in detail in the review by Paynter [137].

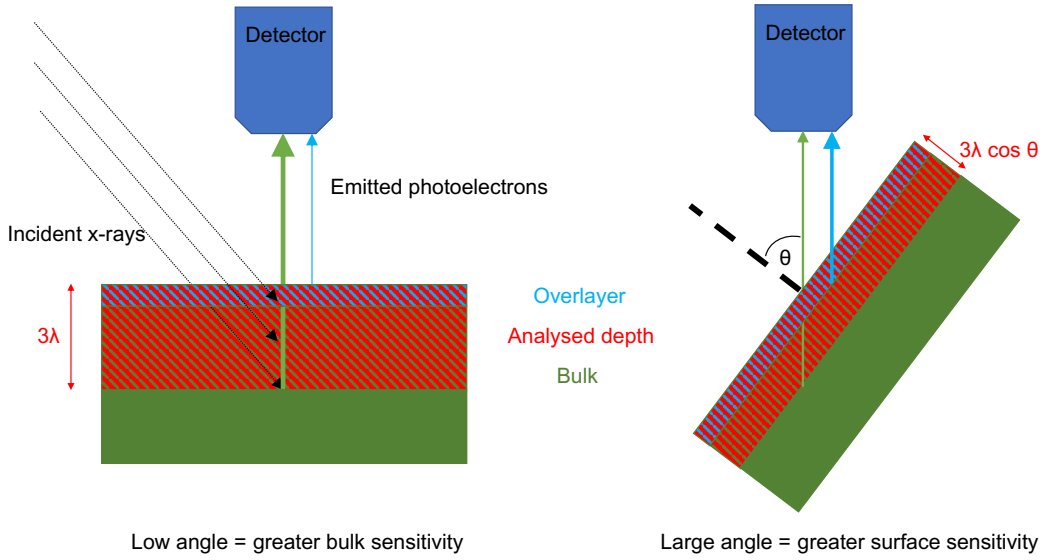


Figure 4.2: Schematic of AR-XPS of an overlayer on a bulk material. With the detector parallel to the surface normal photoelectrons from deep into the bulk can reach the detector, so a larger proportion of the intensity detected is from the bulk material. As the angle between surface normal and detector is increased the sampling depth is decreased and so a greater proportion of the detected photoelectrons are from the overlayer

A second method for exploring depth related information is to change λ. This varies strongly with the kinetic energy of the photoelectrons and so, for a particular transition, with the incident photon energy. For kinetic energies >150 eV, a reasonable estimate is that $\lambda \propto E^{0.5}$ [138], though better approximations are available using the TPP-2M formula [139]. In simple terms, higher kinetic energy photoelectrons are able to escape from deeper in the sample, allowing more information about the bulk material to be determined. This is known as Energy Resolved or Hard X-Ray XPS (ER-XPS or HAXPES). The advantage of varying the photon energy is that the relative angle of the detector and sample remains constant, meaning that any geometric factors have

little effect. There is also the ability to probe much deeper than standard laboratory XPS set-ups. With a standard Al-Kα source at 1.5 keV the escape depth is typically around 6-10 nm, at 6 keV the escape depth can be 20-30 nm [140]. However, the ability to generate these high energy x-rays has been limited to synchrotron facilities, though a few higher energy laboratory sources are becoming available.

It is also possible to obtain depth-related information by sputter etching of the surface [141–143]. Whilst this is useful for analysing deeper lying structures much larger than 3λ, it is less useful or appropriate for samples where the full structure is present in 3λ as it goes through the layers relatively quickly and calibration of the analysed depth is poor for unknown systems. For many systems, known to include both niobium and titanium oxides [144, 145], the ion beam also causes chemical changes, reducing the oxides as well as removing them. This makes sputter etching inappropriate for analysis of niobium and titanium oxides, though it is still useful for complete removal of the oxide.

4.2 Experimental Details

4.2.1 Spectrometer Details

The measurements performed were performed using three main spectrometers to allow different experiments to be performed.

The first spectrometer used was a TermoScientific K-Alpha$^+$ at the University of Cardiff as part of the EPSRC National Facility for X-Ray Photoelectron Spectroscopy. This had a monochromated Al-Kα x-ray source with photon energy 1486.6 eV. The base pressure in the analysis chamber was approximately 10^{-7} mbar, and there was a fast-entry load-lock in which samples could be pumped to approximately 10^{-6} mbar. Spectra throughout the project were collected in two forms: "survey" spectra that covered the full energy range of the spectrometer and allowed the presence of different elements to be determined, and "detailed" spectra where only particular intervals were measured with smaller energy steps and higher resolution. On the K-Alpha$^+$ instrument, survey

spectra were collected with a pass energy of 100 eV averaged over four scans, whilst detailed spectra were collected with a pass energy of 20 eV averaged over 10 scans. Samples could be sputter etched using a monatomic argon ion beam with energy between 500 eV and 4 keV, with 4 keV typically used on my samples. The imaging spot size was approximately 100 microns, with the ion beam covering approximately 2 by 5 mm. This spectrometer allowed angle-resolved measurements to be acquired by mounting the sample on a rotating bar, such that the angle between the detector and sample surface could be varied from 0 to 90 degrees, without having to alter the angle between source and detector. There was no ability to admit gas into the chamber on this spectrometer, but samples could be pumped from atmospheric to measurement pressure in less than one hour, allowing them to be exposed to real laboratory air and then quickly pumped back down.

The second spectrometer used was a Kratos Axis Ultra spectrometer at the University of Cardiff. This had a delay line detector (DLD), a monochromated Al-Kα x-ray source at 1486.6 eV and a base pressure of approximately 10^{-9} mbar. Samples could be cleaned by sputter etching with monatomic argon ions at 4 keV over a 5 mm square raster. Survey spectra were collected with a pass energy of 160 eV, whilst detailed spectra were collected with a pass energy of 40 eV. The detector was operated in the hybrid mode, and the analysis area covered approximately 700 by 300 microns. Much like the other system, angle-resolved measurements were taken by rotating the sample platen relative to the detector, with an angular range between 0 and 85 degrees available. The system had a separate sample preparation chamber, into which controlled amounts of pure oxygen could be flowed using a needle valve.

Finally, some spectra were taken on the I-09 beamline at the Diamond Light Source. The synchrotron allowed a wide range of incident x-rays to be used, from 100 eV to 2.1 keV on one branch and from 2.1 keV to 18 keV, with much higher brightness than a lab based spectrometer [146]. This variable energy allowed energy-resolved XPS experiments to be performed at two different energies. The energies chosen were 999.64 eV "soft" x-rays and 5934.15 keV "hard" x-rays. Both were monochromated and defocussed to give a spot size of approximately 300 by 300 microns, and the two

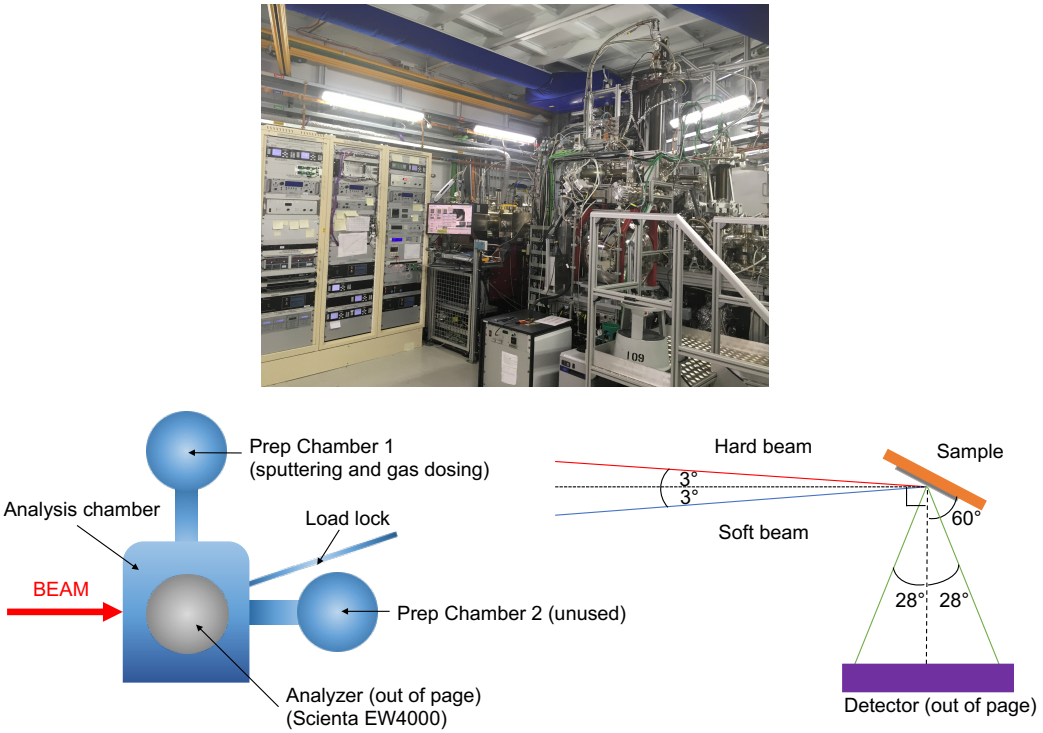


Figure 4.3: Top: A photograph of the experimental hut for the I-09 beamline at the Diamond Light Source. Left: Schematic of the different vacuum chambers. The sample was pumped down in the load-lock, then transferred to the first prep-chamber for sputtering and gas-dosing. Analysis was performed in the analysis chamber. Right: Detailed layout of the analysis chamber. The sample was on a rotating platen, but the sample normal to detector angle was typically fixed at 30°. The detector had a typical acceptance angle of 56°, which could be split into segments to allow for angular-resolved measurements to be obtained in parallel)

beams were separated by approximately 6 degrees. The detector was a VG Scienta EW4000, angled at right angles to the line between the soft and hard x-ray beams. This had a wide collection angle of up to 60°, allowing angular data to be collected in parallel, rather than by tilting the sample. The base pressure of the main chamber was 10^{-9} mbar. In a separate preparation chamber, samples could be sputtered with argon at 2.5 keV and then gas dosed to particular partial pressures of oxygen using a needle valve.

4.2.2 Sample Details

XPS typically requires a reasonably large area of flat surface for measurements to be performed, so it was not possible to use commercial wire for the oxidation experiments.

Instead, all measurements were performed on a sheet of Nb–45wt%Ti sourced from Siemens Magnet Technology. This consisted of a large NbTi monocore strand that was extracted during the early stages of wire manufacture, before most of the heat treatment and drawing stages. This monolith was instead rolled to form a flat sheet, approximately 15 by 0.5 mm in cross section. Much like a wire, this was still clad in copper and had a niobium diffusion barrier as seen in Figure 4.4, both of which had to be removed prior to surface preparation.

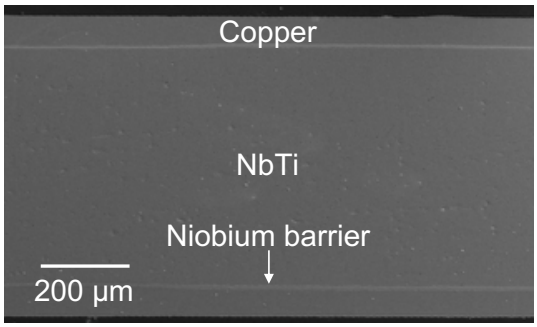


Figure 4.4: Backscattered SEM cross-section of NbTi sheet used in surface science experiments. The outer copper layer and the niobium diffusion barrier are clearly visible

Energy dispersive x-ray (EDX) measurements confirmed the bulk composition of the sheet to be Nb–45.3 ± 0.3 wt%Ti (61 at%Ti) across multiple regions of the sample. X-ray diffraction (XRD) experiments shown in Figure 4.5 demonstrated the sample to be single phase: a body-centred cubic β-Nb(Ti) solid solution. This differed from the final wire microstructure shown in Figure 2.2, where hexagonal α-titanium precipitates are present. Whilst these precipitates are thermodynamically favourable below 600°C, kinetics prevents their formation without heavy deformation and long heat treatments [26]. Most measurements were performed on this precipitate-free material as this simplifies the XPS measurements. Some sheets were heat treated for 60 hours at 420°C to introduce precipitates, so that any effect of the α-titanium on the oxide growth mechanism could be confirmed. Whilst these precipitates were too fine to be observed in the SEM, so must be much smaller than 1 micron, their presence is confirmed by XRD, with additional peaks present in Figure 4.5 corresponding to the α-Ti phase. The fact that these precipitates remain much smaller than the XPS spot size (>30 microns) is crucial for the XPS experiments, as it means each area will contain

large numbers of precipitates and so the analysed region will be representative of the entire sample surface.

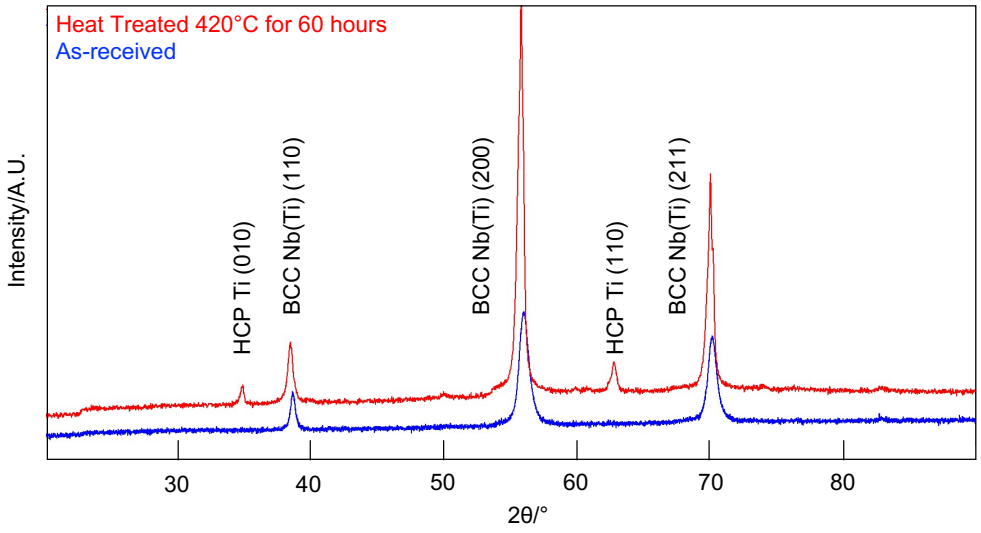


Figure 4.5: XRD scans of the NbTi sheet as-received and after heat treatment at 420°C for 60 hours. The heat treated sample has a pair of strong extra peaks corresponding to the presence of α-Ti

4.2.3 Surface Preparation

Oxidation of the NbTi sheet first required the removal of the copper outer layer and the niobium diffusion barrier. This was achieved by etching the copper in 30% HNO_3:H_2O, removing the copper but leaving the niobium layer. The surfaces were then ground with SiC grit papers from grade 600 to 4000. Enough time was taken to ensure complete removal of the thin niobium diffusion barrier (as confirmed by EDX measurements of the surface and a change in the surface colour). The samples were then polished with aqueous diamond suspension with particle sizes 6, 3 and 1 microns to give a flat surface. Finally, the samples were cleaned in an ultrasonic bath for 10 minutes each in acetone and water to remove any contaminants. Figure 4.6 demonstrates the effectiveness of this process on the as-received surfaces, with stronger Nb and Ti signals observed after the water treatment, suggesting reduced surface contamination.

In many cases, contamination can be entirely removed by ion beam sputtering of the sample. However, this is known to reduce the oxides of both niobium and tita-

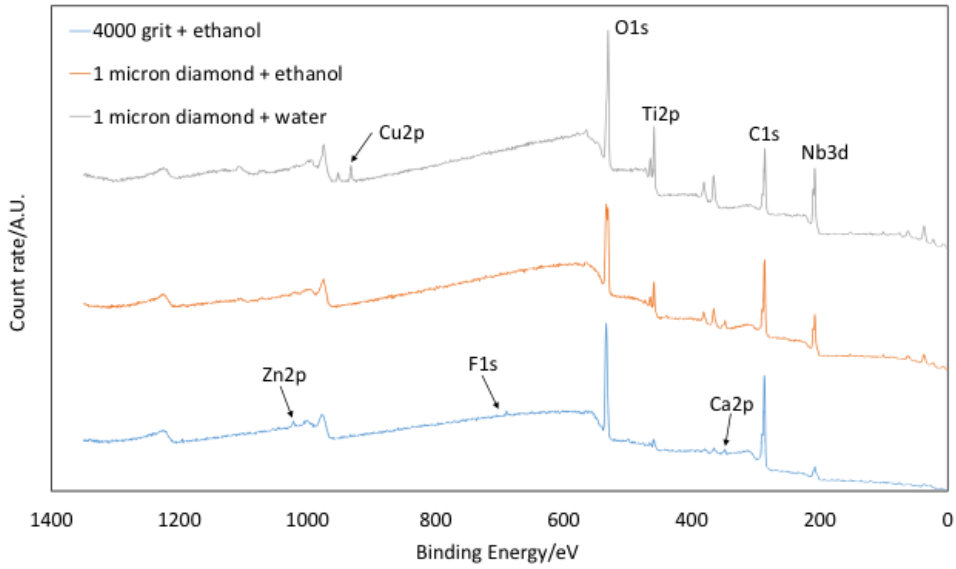


Figure 4.6: Survey XPS scans of NbTi surface prepared in three ways: by grinding to 4000 grit and sonicating in acetone and ethanol, or by finishing to a 1 micron diamond polish and then sonicating in acetone and either ethanol or water. A small amount of copper contamination appeared in the water treated sample, this was not seen for later samples

nium [144, 145], as well as removing them, making it undesirable for simply cleaning oxidised surfaces. As such, it is accepted that any air-exposed samples will have a layer of organic contamination on their surface, consisting mostly of carbon and oxygen. Typical contamination layers are around 1 nm thick, and should lead to equal attenuation of similar species with similar energies, so will not affect calculations when comparing closely related signals, such as chemically shifted signals from the same transition [134]. However, care must be taken when comparing species with drastically different kinetic energies which will have different attenuation by the carbon layer. Higher doses of ion sputtering allow for complete removal of the oxide layer, and so proved useful for obtaining oxide-free surfaces for measurement and as reproducible initial conditions for oxidation.

4.2.4 Peak Fitting and Analysis

The interpretation of XPS spectra typically requires the fitting of multiple peaks to the acquired data. This fitting was performed using CasaXPS version 2.3.18 software by

Casa Software Ltd. Further analysis of the fitted data, particularly calculations using the AR-XPS data, were performed using my own code in MATLAB. When fitting peaks, a peak model was developed for each detailed spectral region for each spectrometer. This was then fitted to the spectra collected under different experimental conditions such as oxidation time or sample angle to allow consistent analysis of the results. Once the peak model was developed, the only free parameters in the fitting procedure were the position and the full-width half maxima (FWHM) of the peak fit (but not their relative values) to allow for any difference in charging-related shift to be compensated for. Details of how the peak models for each species were derived are presented in Section 4.3, but the same basic principles were applied to all the peak fits:

1. Peaks were only fitted that could be assigned to features of real, physical significance and could be related to features reported in the literature
2. The freedom of the fit was limited to ensure similar features had similar full-width half maxima (FWHM)
3. The minimum number of peaks were used to fit the data

A key aspect of attaining reliable peak fits is determining the background of the spectra. Commonly there are three main background types used for XPS analysis: linear, Shirley and Tougaard backgrounds. The linear background is the simplest, considering a straight line approximation between the two edges of the spectral features of interest. This technique has little theoretical or data driven basis, but is simple and easily applied. The most commonly used XPS background is the Shirley background [147]. Again, this has no particular theoretical basis, but is based on using the collected data to produce an appropriate background. It is calculated using the formula:

$$S(E) = I_2 + (I_1 - I_2)\frac{A_2(E)}{A_1(E) + A_2(E)} \tag{4.7}$$

where $S(E)$ is the Shirley background at binding energy, E, I_1 and I_2 are the intensities at the start and end of the background region, and $A_1(E)$ and $A_2(E)$ respectively are the areas of the spectrum above and below the binding energy at which the back-

ground is calculated. Multiple iterations of this are required to converge on a particular background. In this project, Shirley backgrounds provided a poor fit for the titanium data, not allowing the expected physical features to be maintained. As such, the background used for spectra in this work was the Tougaard background [148]. This makes an attempt to model the physical processes occurring in a sample and is based on the probabilities of electrons undergoing loss events. This is calculated as:

$$T(E) = \int_{E}^{\infty} F(E' - E)I(E')dE' \tag{4.8}$$

where $I(E')$ is the measured spectral intensity at binding energy E' and

$$F(x) = \frac{Bx}{(C + x^2)^2} \tag{4.9}$$

where B and C are adjustable parameters, with B influenced by the intensities at the start and end of the spectral region to ensure the background and spectra meet.

All of these background models have advantages and disadvantages, and their use will lead to slight differences in the results of curve fitting. The crucial thing is that the same type of background has been applied to ensure consistency between the different experiments.

Another key consideration for peak fitting is the shape of peaks. In this work, most peaks were fitted using a standard Gaussian/Lorentzian blend, implemented in CasaXPS as [149]:

$$GL(x : F, E, m) = \exp\left[-4\ln 2(1 - \frac{m}{100})\left(\frac{x - E}{F}\right)^2\right] \cdot \frac{1}{1 + 4\frac{m}{100}\left(\frac{x-E}{F}\right)^2} \tag{4.10}$$

where GL is the intensity of a peak of area 1 at binding energy x for a peak with maximum at binding energy E and FWHM F. The parameter m describes the percentage blending of the Lorentzian form into the Gaussian form, with 0 being true Gaussian and 100 being completely Lorentzian. The only user entered parameter is m, the rest are determined from curve fitting, so this peak shape is typically labelled in the form

GL(m). For some metal peaks it is necessary to add asymmetry, performed in this thesis using the LA (asymmetric Lorentzian) peak option in CasaXPS. This is modelled by:

$$LA(x:\alpha,\beta,F,E) = \begin{cases} L(x:F,E)^{\alpha} & :x \leq E \\ L(x:F,E)^{\beta} & :x > E \end{cases} \tag{4.11}$$

where α and β are parameters selected to add asymmetry. $L(x:F,E)$ is a Lorentzian with FWHM F and maximum at binding energy E. The lineshape is entered in the form LA(α,β, m) where m defines the width of a Gaussian to convolve with the LA form.

4.3 Peak Models

The development of peak models that could be consistently fitted to spectra from samples prepared in different ways was key to maintaining consistency between results. This section briefly describes the development of these for each set of peaks. The focus will be on samples measured in the Thermo Scientific K-Alpha^{+} spectrometer and oxidised in laboratory air, as this will form the main section of work for this chapter. Data from the other spectrometers will also be drawn upon to clarify certain points, and the peak models developed for fitting data from the gas dosing experiments will be briefly mentioned. Each spectrometer leads to a different FWHM due to differences in instrumental broadening, so separate models had to be drawn up for each spectrometer, though care was taken to ensure consistency between these.

Orbital	l	m_s	j (l + m_s)	Area Ratio (2j+1)
p	1	+1/2, -1/2	3/2, 1/2	2:1
d	2	+1/2, -1/2	5/2, 3/2	3:2
f	3	+1/2, -1/2	7/2, 5/2	4:3

Table 4.1: Spin orbital splitting for electrons from particular orbitals after [136], showing spin numbers l, m_s and j. The theoretical area ratio of the spin orbital splitting is also shown

In fitting XPS data, maintaining the physics of the transitions is important. This puts

extra constraints on the peak fit, which is key to maintaining trustworthy fits. The main such constraint is the effect of spin-orbit splitting. Electrons in orbitals beyond the s orbital have non-zero angular momentum. The coupling between this and the electron spin leads to a splitting in energy levels. This energy splitting is commonly discernible in laboratory XPS systems, and so two peaks rather than one can be attributed to a particular orbital. When fitting such doublets, it is important to note that the relative area of each peak in the doublet is specified by the degeneracy of the orbital (2j+1), so should be fixed to a particular ratio depending on the orbital involved. These are summarised in Table 4.1. Similarly, it is expected that the FWHM of the two split states is the same, though this will be discussed more later.

4.3.1 Titanium

Titanium has three main stable oxides: TiO, Ti_2O_3 and TiO_2 [110, 150]. These correspond to the Ti(II), Ti(III) and Ti(IV) oxidation states. For XPS studies of titanium, the main peaks used are the 2p peaks. Each of these form a doublet corresponding to the j=3/2 and j=1/2 states. Most authors follow the statistical 2p doublet peak area ratio of 2:1 [108], but this ratio is debated due to errors in determination of the background field, with others fitting peak area ratios of between 1.8 and 2.5 to 1 [107, 151]. The positions of the $2p_{3/2}$ and $2p_{1/2}$ peaks are generally well agreed in the literature, with only slight variations due to different charge compensation techniques between samples.

The starting point for any fit can be considered by looking at the extremes of the NbTi sample surfaces: the as-received surface that is heavily oxidised and the sputter cleaned surface, both shown in Figure 4.7. After the sputter etch, minimal oxide is present and so the metallic doublet is the dominant feature. This peak is strongly asymmetric, with a spin-orbit splitting of approximately 6.1 eV. The asymmetry was fitted using an LA(1.1, 5, 7) peak shape as suggested by Biesinger [152]. The as-received surface demonstrates only a very small contribution from the metal, with the dominant feature being the Ti(IV) doublet, corresponding to TiO_2. Interestingly the Ti(IV) $2p_{1/2}$ appears notably shorter and wider than the Ti(IV) $2p_{3/2}$ peak. This is

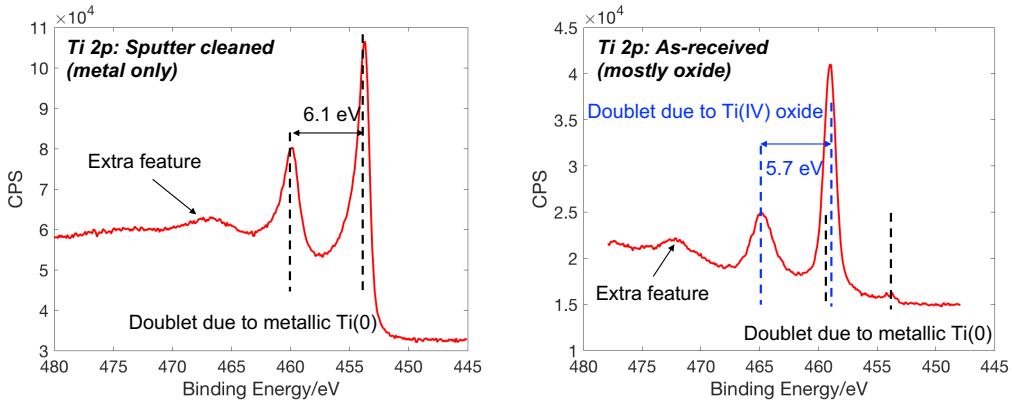


Figure 4.7: Left: Detailed scan of the Titanium 2p region of a sputter cleaned NbTi sample, taken on the ThermoScientific K-Alpha$^+$ spectrometer parallel to the surface normal. The metallic doublet demonstrates strong asymmetry. Right: Detailed scan of the Titanium 2p region of an as-received NbTi sample, taken on the Kratos Axis Ultra spectrometer parallel to the surface normal. Both scans show one very strong doublet, though detailed fitting would show small contribution from other oxidation states (this is discussed in detail for the as-received sample in Figure 4.19b and for the general case in 4.9). In each case, there is an extra feature, the details of which will be discussed in the main text

commonly attributed to the Coster-Kronig effect where the 1/2 spin state is less stable than the 3/2 state [153], leading to peak broadening. For detailed fits this was accounted for by allowing the FWHM of the two doublet peaks to differ from one another, though the theoretical area ratio of 2:1 was maintained. This was only possible when utilising a Tougaard-type background and therefore a Tougaard background was applied for all samples. The Ti(0) $2p_{1/2}$ and Ti(IV) $2p_{3/2}$ peaks occur at approximately the same binding energy, so overlap when both species are present, demanding a careful fitting of the peaks to deconvolve the two contributions.

Both of the samples prepared under the extremes of conditions also demonstrate an extra feature at high binding energies, at approximately 467 eV in the sputter cleaned sample and 472 eV in the oxidised sample. Neither of these features are obviously assignable to transitions in titanium, occurring above the binding energy of even the highest oxide peak. However, there is a niobium 3s peak that might be expected at approximately 467 eV [154]. Little information exists in the literature about this peak, but the peak at 472 eV is likely to correspond to the Nb 3s transition in the oxidised state. This was confirmed during the measurements at the Diamond Light Source, where spectra in that region were recorded from a pure niobium sample first in the

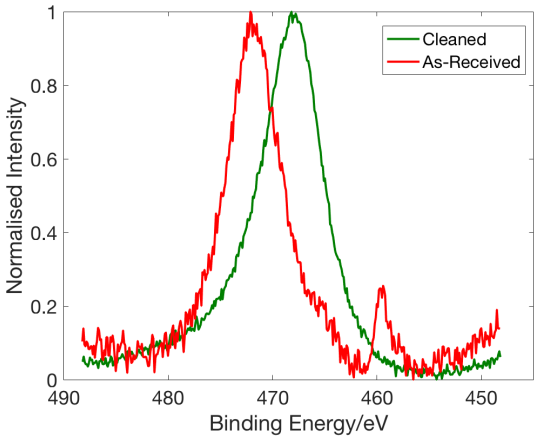


Figure 4.8: The Ti 2p/Nb 3s region measured at the Diamond Light Source with 1 keV soft x-rays and summed across the full angular range for a pure niobium sample in the as-received and sputter cleaned states

as-received state and then after sputter cleaning. These are plotted in Figure 4.8 for measurements with more the more surface sensitive soft x-rays. There is a distinct peak at 467.9 eV in the cleaned sample corresponding to the Nb(0) oxidation state and at 472.0 eV in the as-received sample corresponding to the Nb(V) oxidation state, matching well with the extra peaks observed in the titanium 2p spectra.

Samples oxidised for an intermediate amount of time demonstrate a signal that is a convolution of the two extreme cases. This is well illustrated by the titanium 2p region shown in Figure 4.9 for an NbTi sheet oxidised for one minute in laboratory air. Two extra doublets are required for a good fit, corresponding to the presence of Ti(II) and Ti(III) oxidation states. The main fit is based on the work of Biesinger et al. [152], fitting each oxidation state with a doublet matching the theoretical 2:1 area ratio. The positions and FWHM of these peaks are described in Table 4.2. The peaks in the Ti(0) and Ti(IV) doublets were allowed to have different FWHM values to account for the Coster-Kronig effect, whilst each spin state in the Ti(II) and Ti(III) doublets were fixed to have the same FWHM. Unlike Biesinger, the FWHM of these oxidation states were allowed to differ from one another, though the final fitted values are similar to one another. All peaks were fitted with a GL(30) peak shape apart from the Ti(0) peaks, which had an asymmetric LA(1.1, 5, 7) peak shape. The extra Nb 3s contributions were accounted for by adding two extra singlet peaks using symmetric GL(30) line shapes.

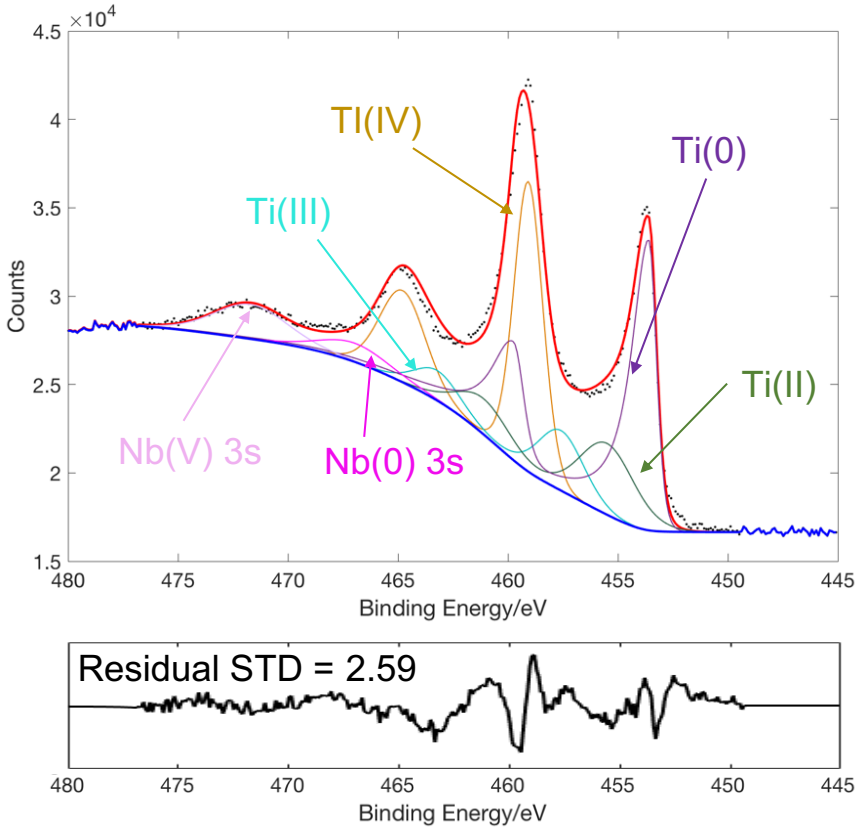


Figure 4.9: Top: Detailed scan of the titanium 2p region of a NbTi sample oxidised in laboratory air for one minute, taken on the ThermoScientific K-Alpha$^+$ spectrometer parallel to the surface normal. The contributions to the fit from each of the Ti(0), Ti(II), Ti(III) and Ti(IV) oxidation states are shown, along with the extra contributions due to Nb 3s peaks. Bottom: Plot of the residuals of the fit calculated as the difference between the observed and fitted intensities

Species	Binding Energy/eV	Peak Splitting/eV	FWHM/eV	Peak Shape
Ti(0) 2p	453.59	6.15	0.85 (1.10)	LA(1.1, 5, 7)
Ti(II) 2p	+1.91	5.60	2.95	GL(30)
Ti(III) 2p	+4.00	5.62	2.47	GL(30)
Ti(IV) 2p	+5.48	5.72	1.55 (2.45)	GL(30)
Nb(0) 3s	+13.39	n/a	3.72	GL(30)
Nb(V) 3s	+18.12	n/a	3.91	GL(30)

Table 4.2: Summary of the fit parameters used for the titanium 2p region of a NbTi sample oxidised in laboratory air for one minute and measured in the ThermoScientific K-Alpha$^+$ spectrometer parallel to the surface normal. For some fits the FWHM of the doublet peaks was allowed to differ. For these the FWHM of the 1/2 spin peak is shown in brackets. The same fit was transferred to all other samples in this series, with only the total FWHM and position (but not the relative spacing) allowed to vary

Technically the Nb 3s contribution would be better fitted with four peaks to account for all the possible niobium oxidation states, but as the intensity of all the extra peaks was low and the position of the intermediate peaks unclear, fitting these was difficult and unreliable. To transfer this model to other spectra, all peak positions and FWHM were fixed relative to the Ti $2p_{3/2}$ peak.

4.3.2 Niobium

Quantification of XPS results on niobium described in the literature focuses almost universally on the Nb 3d peak, which gives a clear pronounced doublet corresponding to the 5/2 and 3/2 spin states [155, 156]. There are three potentially stable oxides commonly expected at low temperatures in the niobium system: NbO, NbO_2 and Nb_2O_5. This is further complicated by many authors [96,104] fitting asymmetric peaks for the Nb(0) state. This is common in many metals, and can generally be attributed to electronic or vibrational transitions with energies smaller than the resolution of the instrument [136]. Other authors consider an extra peak attributed to a NbO_x sub-oxide where $x << 1$ [89, 157], but these fail to include an asymmetric metal peak, necessitating including extra peaks to achieve a good fit.

The main niobium peaks for my samples are illustrated in Figure 4.10, showing the Nb 3d region from a NbTi sheet in the as-received condition (exposed to air for more than a day, plus exposed to water during the cleaning process) and after sputter etching. The sputter etched sample illustrates the metallic doublet, with a clear tail on the high binding energy side of each peak attributable to asymmetry. Few authors in the literature describe the exact peak-shape used, but fitting used here was based around an online article by Biesinger [158] who described the asymmetry of the metal with an LA(1.2, 5, 12) peak shape. The spin orbital splitting is 2.7 eV, in good agreement with the literature values [155, 156].

The as-received sample in Figure 4.10, demonstrates a very strong doublet at around 207.6 eV with a splitting of 2.7 eV. The oxide is clearly symmetric, and was fitted using a GL(30) peak shape. Small amounts of the metallic peak are still observable in

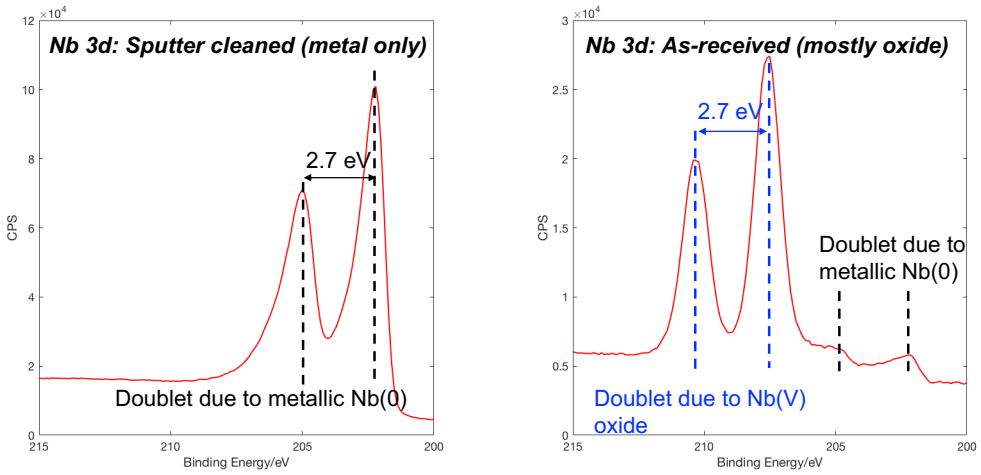


Figure 4.10: Left: Detailed scan of the niobium 3d region of a sputter cleaned sample, taken on the ThermoScientific K-Alpha$^+$ spectrometer parallel to the surface normal. The metallic doublet demonstrates strong asymmetry. Right: Detailed scan of the Niobium 3d region of an as-received sample, taken on the Kratos Axis Ultra spectrometer parallel to the surface normal. Both scans show one very strong doublet, though detailed fitting would show small contribution from other oxidation states, as is shown later in Figure 4.19

this sample, suggesting any oxide is close to, but not more than, 3λ in depth, though further quantification is hard due to the low intensity of the metal signal.

Air-oxidised samples tended to include strong contributions from both metal and oxide, and so show a much more complicated picture. This is shown in Figure 4.11, which shows the detailed fit over the Nb 3d region for the NbTi sheet after exposure to air for one minute. The spectra were collected parallel to the surface normal in the the ThermoScientific K-Alpha$^+$ spectrometer. A Tougaard-type background was used. There are four clear peaks corresponding to the Nb(0) and Nb(V) doublets. However, two extra doublets must be added with energies in between these relating to the Nb(II) and Nb(IV) oxidation state to achieve a good fit. The positions of the j=5/2 peak is listed in Table 4.3. Each of the doublets were fitted with a spin-orbital splitting of 2.72 eV, in good agreement with the values described by both Bahl [155] and Fontaine [156]. The metal doublet was fitted with the LA(1.2, 5, 12) peak shape and the oxide peaks with a GL(30) peak shape. The FWHM of all the oxide peaks was restricted to a single value, whilst the two peaks of the metallic doublet were allowed to differ both from the oxide and from each other after Olsson [104]. However, on fitting it was found

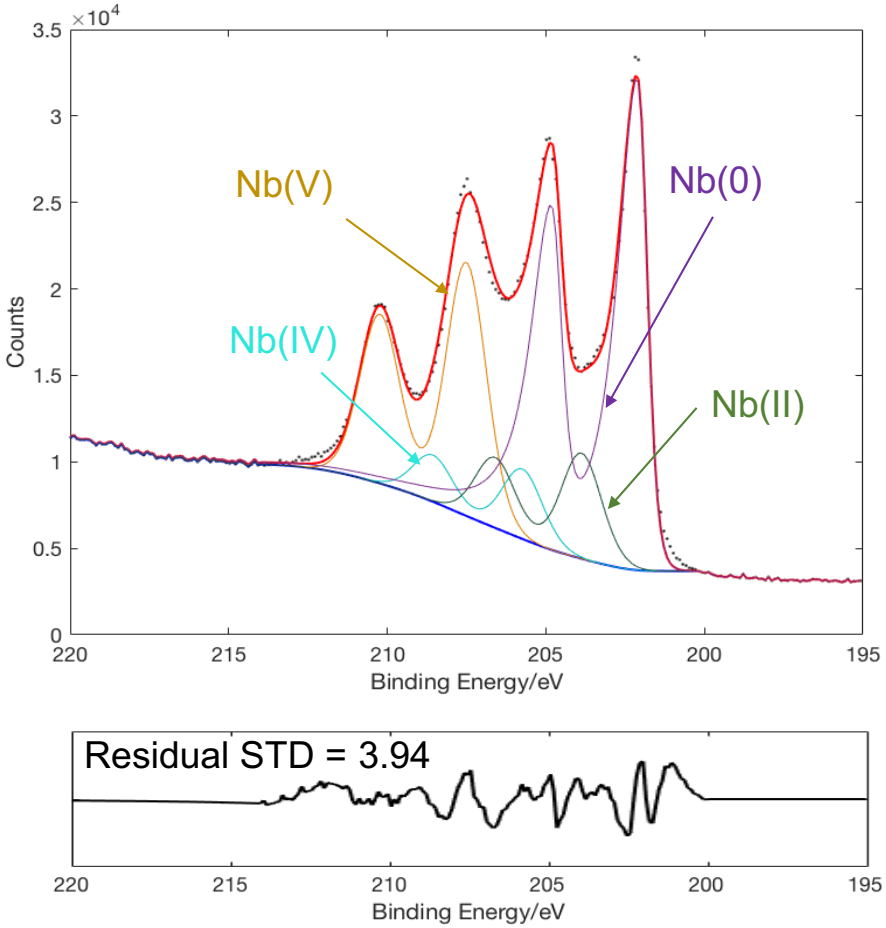


Figure 4.11: Top: Detailed scan of the niobium 3d region of a NbTi sample oxidised in laboratory air for one minute, taken on the ThermoScientific K-Alpha$^+$ spectrometer parallel to the surface normal. The contributions to the fit from each of the Nb(0), Nb(II), Nb(IV) and Nb(V) oxidation states are shown. Bottom: Residual plot from the fit

Species	Binding Energy/eV	Peak Splitting/eV	FWHM/eV	Peak Shape
Nb(0) $3d_{5/2}$	202.1	2.72	0.77	LA(1.2, 5, 12)
Nb(II) $3d_{5/2}$	+1.88	2.72	1.50	GL(30)
Nb(IV) $3d_{5/2}$	+3.77	2.72	1.50	GL(30)
Nb(V) $3d_{5/2}$	+5.41	2.72	1.50	GL(30)

Table 4.3: Summary of the fit used for the Niobium 3d region of a NbTi sample oxidised in laboratory air for one minute. The same fit was transferred to all other samples in this series, with only the total FWHM and position (but not the relative spacing) allowed to vary.

that the two had approximately the same FWHM, as would be expected. All other oxidations and angles in this series were fitted using this set of fit parameters, keeping the same relative spacings between peaks and same relative FWHM. The position of the entire fit was allowed to vary between samples to allow for any minor charging effects.

4.4 Air Oxidation Experiments

For the manufacture of persistent-joints, the most relevant regime of oxidation of NbTi is exposure to air for between a few seconds and a few hours, corresponding to the potential times wires may be exposed after an acid etch to remove the copper stabiliser. In industry it is well known that solder joints become ineffective after only a few minutes exposure. The literature is unclear as to the effect of any oxide layer on pressed joints, but unoxidised filaments require lower pressing pressures before good contact is made [63, 159]. Understanding the oxidation in this regime is therefore of utmost importance to industry.

4.4.1 Results

The ThermoScientific K-Alpha$^+$ had a fast-entry load lock that allowed the NbTi sheet samples prepared as described earlier to be exposed to air for short times and then measured. The HF acid etch required to remove the oxide layer was undesirable, and could not be performed without then exposing the sample surface to long periods of time in air, but a clean surface could instead be obtained in the spectrometer by ion-bombarding the surface to remove any oxide. These surfaces were then exposed to laboratory air for times between 10 seconds and 1 hour either in the load-lock for short exposures or by removing the sample platen and leaving it on the bench for the longer exposures to avoid contamination of the load-lock. The etch-pit on each sample was clearly visible, so when the platen was replaced it was easy to confirm that the sample had not moved. For each exposure, a survey scan was taken along with detailed scans of the Nb 3d, Ti 2p, O 1s and C 1s regions. For each region, angle-resolved data was

collected by tilting the sample from 0 to 70° in increments of 10°.

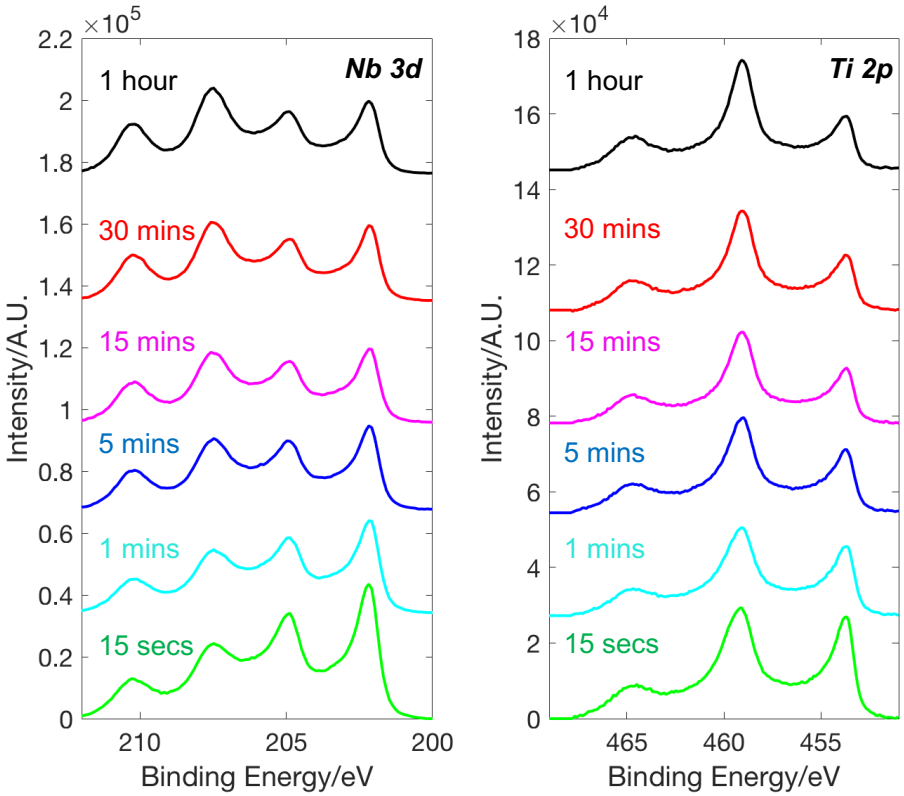


Figure 4.12: Detailed scans of the niobium 3d and titanium 2p regions of a NbTi sample oxidised in laboratory air for times between 15 seconds and 1 hour, taken on the ThermoScientific K-Alpha$^+$ spectrometer parallel to the surface normal

Figure 4.12 shows the detailed spectra for each oxidation time measured parallel to the surface normal, the most bulk-sensitive angle. Even at this angle and for the shortest times, there are two distinct doublets present for both niobium and titanium, corresponding to the formation of oxide on the surface of the NbTi sheet even after just 15 seconds. As oxidation time increases, the intensity of the higher binding energy oxide peaks increases at the expense of the lower binding energy metallic doublet. This is clearer by eye in the niobium spectra due to the overlap of the Ti(0) $2p_{1/2}$ and Ti(IV) $2p_{3/2}$ peaks, but is observable in both species. It is of immediate significance that both niobium and titanium spectra are present and demonstrate both metal and oxide peaks. In many metallic alloy systems such as stainless steels, the oxide that forms is dominated by one chemical species. The presence of oxide peaks in both the Nb and Ti spectra are indicative of a mixed oxide on the surface.

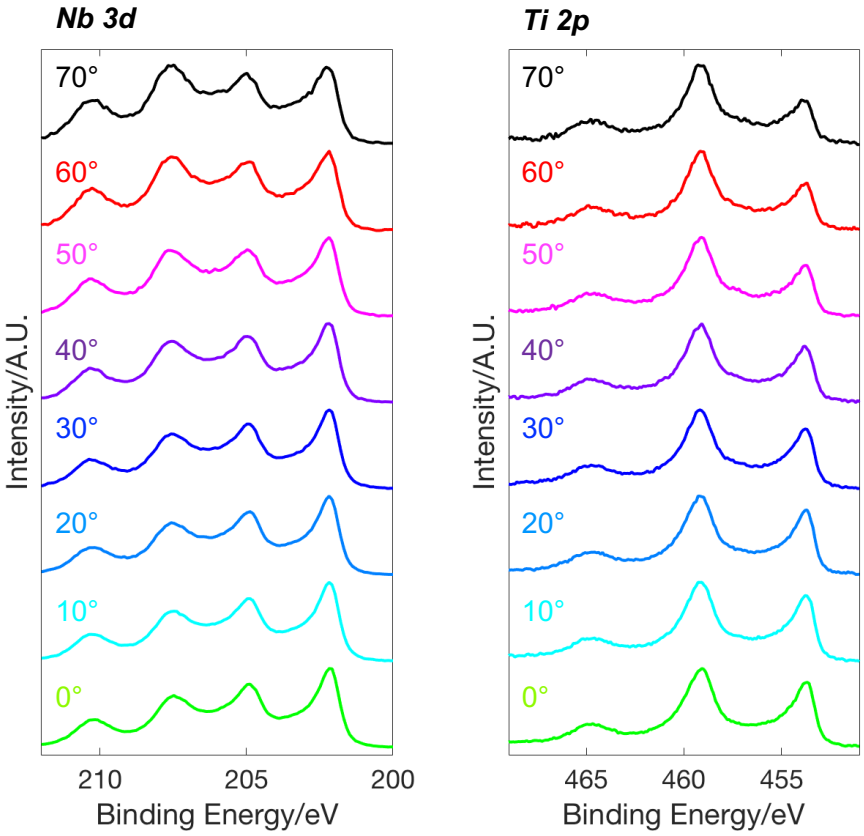


Figure 4.13: Detailed scans of the niobium 3d and titanium 2p regions of a NbTi sample oxidised in laboratory air for 1 minute, taken on the ThermoScientific K-Alpha$^+$ with detection angles between 0 and 70° from the surface normal

The angular data shown for the sample oxidised for 1 minute in Figure 4.13 also illustrates a key change in the oxide:metal intensity. The more bulk-sensitive low-angle measurements demonstrate a more intense metal peak compared to the oxide peak, whilst the opposite is true at high angles. This suggests surface localisation of the oxide. Again, similar trends appear in both the niobium and the titanium data.

4.4.2 Analysis

The following sections present the detailed interpretation of the data from the air oxidation experiments. The curves such as those shown in Figure 4.12 were fitted according to the model described in Section 4.3, and the areas or compositions calculated using the standard values for the sensitivity factors [132] used for further analysis. Due to limited access to the spectrometers at Cardiff and Diamond, it was not possible to

measure repeat measurements across multiple samples to build a statistical picture of the measurements. Instead, errors in the fits were estimated in CasaXPS using the in-built error analysis tool. This uses the Monte Carlo method to test the robustness of the fit to small changes in the data and fit parameters and is described in detail in the CasaXPS user manual [149]. This does not take into account errors in the sensitivity factor or in the escape depth, which are difficult to quantify and are expected to lead to a systematic error across the results, so the error bars can be considered a minimum error.

4.4.2.1 Oxide Composition and Structure

Understanding the chemical composition of the oxide that forms on NbTi is crucial to understanding how the presence of a thin layer may affect the superconducting properties of a persistent mode joint. Here, the sample oxidised for 1 minute is analysed in detail, but is representative of other samples with different layer thicknesses.

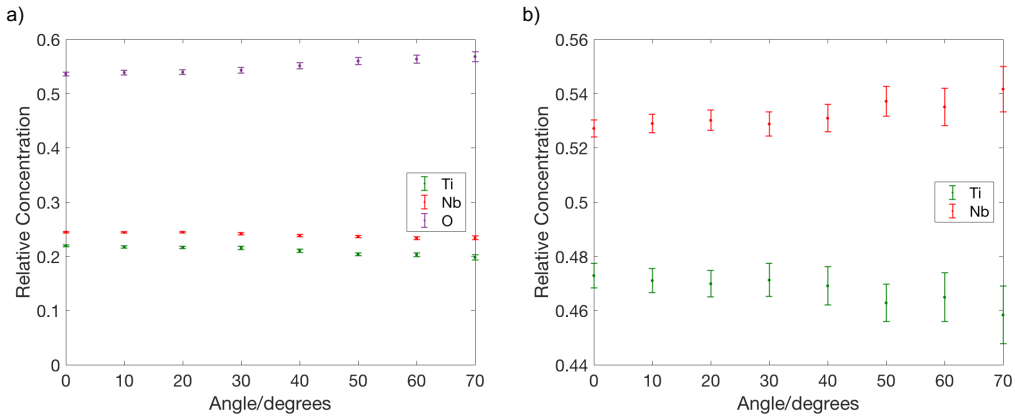


Figure 4.14: Relative concentrations calculated using the total intensity of a) O 1s, Nb 3d and Ti 2p peaks and b) just the Nb 3d and Ti 2p peaks for the NbTi sample oxidised in laboratory air for 1 minute, taken on the ThermoScientific K-Alpha$^+$ with detection angles between 0 and 70° from the surface normal

Figure 4.14a shows the relative composition of the three main expected components of the surface after exposure to air for 1 minute. There is also approximately 10% carbon present in each sample, mostly due to the presence of an organic contamination layer from the exposure to air, which has not been included in the analysis. The concentration of oxygen increases slightly with analysis angle at the expense of the metal species,

indicating a slight localisation of oxygen at the surface. However, relatively little can be drawn further than this as all changes are small due to the presence of all the species in the oxide. Focussing on the metallic components in Figure 4.14b shows no strong evidence for a change in the concentrations of Nb or Ti with angle, suggesting both are strongly present in both metallic surface and in the oxide. Further analysis using the overall compositions is difficult as it is strongly affected by the different inelastic mean free paths for the species. The concentration of titanium appears lower than expected, consistently around 45 at% in all samples measured in the XPS. This contrasts with 61 at% measured by EDX in agreement with most NbTi superconductors. XPS compositional analysis is based on the assumption that the material is homogeneous, and the sensitivity factors are derived from results on pure elements rather than alloys, so it is perhaps unsurprising that some difference occurs, especially as the inelastic mean free path, and so effective sampling depth, is slightly lower for titanium than niobium. There may also be some error attributable to how the background is fitted to the spectra. As the error is consistent in both clean and as-received material it is likely this error is systematic rather than a true difference in composition.

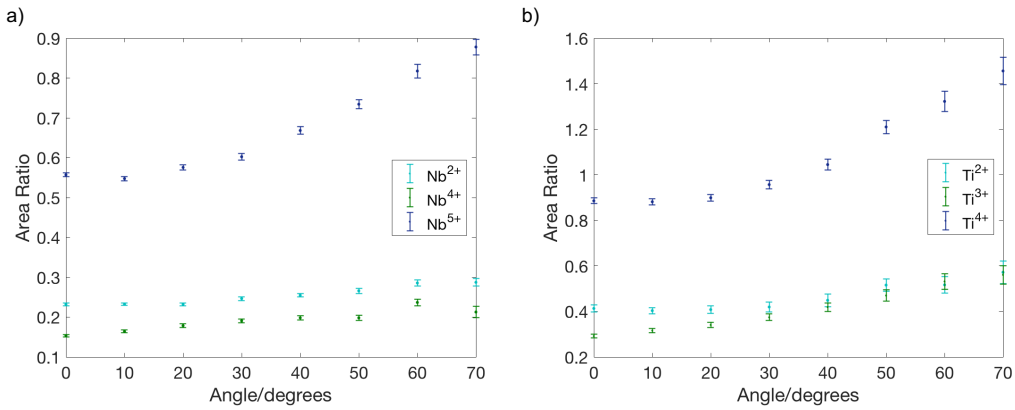


Figure 4.15: Relative area ratios (A_{Ox}/A_{Met}) for a) niobium and b) titanium oxide species for the NbTi sample oxidised in laboratory air for 1 minute, taken on the ThermoScientific K-Alpha$^+$ with detection angles between 0 and 70° from the surface normal

It is necessary to investigate the individual components of each species from the detailed fitting to gain a greater understanding of the oxide morphology. Figure 4.15 plots the ratios of the measured areas of each of the peaks attributable to metal in the oxidised state to the metallic peak area. There is a sharp increase with analysis angle in the

intensity of the highest oxidation species for noth niobium and titanium, indicating that these species are located preferentially at the surface of the material. The trend is less obvious for the intermediate oxidation states, but both show an increase in area ratio with increasing angle, though not as significant as for the highest oxidation state components. This suggests at least some surface localisation of these species, but it is likely they lie in a layer below the highest oxidation states. However, large errors in the fitting of the curves, particularly for the titanium species, make it difficult to interpret too much beyond this or to interpret the relative depth of the two species.

4.4.2.2 Thickness

The aim was to deduce an approximate thickness of the oxide at different times. For a simple oxide overlayer system this can be modelled using the Strohmeier equation (Equation 4.6) [134]. Whilst Figure 4.15 does suggest that the lower oxides exist at deeper depths than the highest oxidation states, their intensities are low, meaning they are relatively thin. A reasonable approximation is to treat the oxide as one layer with the properties of the outer oxidation states, but combining the intensities of all the oxide peaks to estimate the total thickness of all the oxide layers. The mixed two-phase nature of the oxide also has the potential to complicate the picture. In the Strohmeier equation, this can be accounted for by adjusting the values of the atomic density of the metal and oxide N_{met} and N_{ox} by the atomic fraction of Nb and Ti in each oxide such that the ratio becomes $f_{met}N_{met}/N_{ox}f_{ox}$. In Figure 4.14 it can be seen that f_{met} and f_{ox} are approximately equal, allowing these factors to cancel out. Assuming the oxide is mixed in this way, the thickness can be calculated independently from both the niobium and titanium data. If the assumptions made are good then the results from each calculation should be equal.

Element	λ_{ox}/nm	λ_{met}/nm	N_{ox}/mol cm^{-3}	N_{met}/mol cm^{-3}
Nb	3.25	2.78	0.035	0.092
Ti	2.73	2.33	0.053	0.094

Table 4.4: Summary of the parameters used in the Strohmeier equation for niobium and titanium in calculation of the oxide thickness

Values for the inelastic mean free path were calculated using the TPP-2M formula-

tion [139] for each species in both the metal and oxide. The atomic densities were approximated from the lattice parameter of the bulk materials. Whilst this may differ from the atomic densities in the thin oxides, it is a reasonable initial approximation. The parameters used for the calculation are shown in Table 4.4.

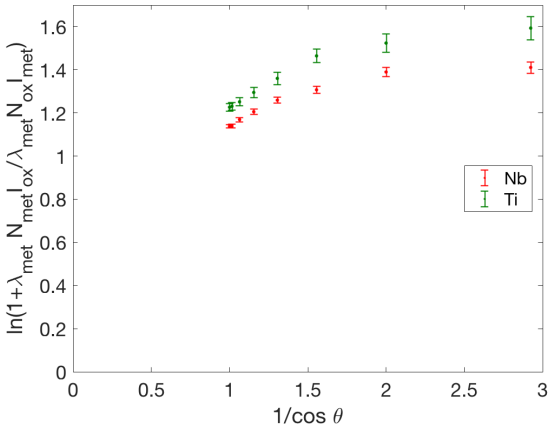


Figure 4.16: Strohmeier plot for the intensity ratios calculated as the sum of all oxide contributions for the niobium and titanium components. According to the Strohmeier equation this should give a straight line through the origin of gradient t_{ox}/λ_{ox}, which is not the case here. This will be discussed further in the main text.

In theory, for XPS measurements at different angles the Strohmeier equation predicts that plotting $1/\cos\theta$ against $\ln\left[1+\frac{\lambda_{met}N_{met}}{\lambda_{ox}N_{ox}}\frac{I_{ox}}{I_{met}}\right]$ should give a straight line of gradient t_{ox}/λ_{ox}. This is plotted for the sample oxidised for 1 minute using the combined oxide intensities for both niobium species and titanium species in Figure 4.16. Neither the titanium nor the niobium data give a straight line as would be expected, corresponding to decreased calculated thicknesses at high angles. This matches similar results reported by Darlinski [160] for pure niobium samples. Darlinski attributes this to serration of the oxide into the surface, however a better explanation is provided by Gunter [161, 162], who argues that surface roughness of the substrate will cause variation in measured thickness with angle. At low angles the thickness will be over estimated as much of the surface will be turned to angles away from the detector and so the effective sampling depth will be smaller than expected. At higher angles it will be underestimated as parts of the surface will be tilted parallel to the detector and so the assumed sampling depth will be too shallow. This is illustrated in Figure 4.17 a and b. However, through a combination of experiment and modelling, Gunter demonstrated

that for an angle between the surface normal and detector of approximately 40°, these effects were minimised and results were within 10% of the true surface thickness.

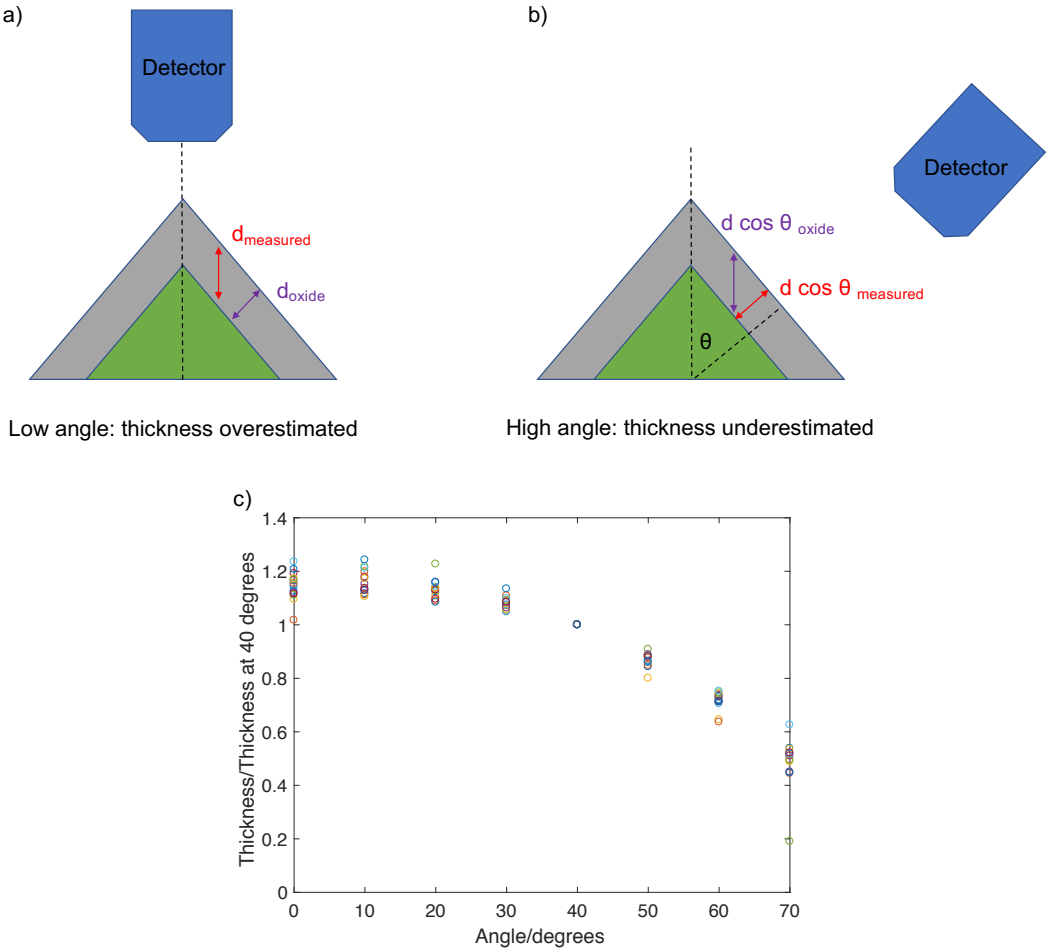


Figure 4.17: a) A roughened sample surface will give an overestimate of the overlayer thickness at low angles b) at higher angles the roughness will lead to an underestimate of the thickness. This is a simplified illustration and is more complicated for true rough surfaces with a more random morphology, but the same concept holds [162] c) Normalising all the calculated thicknesses for the air-oxidised NbTi sheet from each layer and each element (colours represent results for one particular layer and element) against the value calculated at Gunter's "magic angle" of 40° gives a common curve

Normalising all my calculated thicknesses for different layers and different oxidation times against the data at 40° for that layer and time gives Figure 4.17c, which can be seen to condense onto roughly one line. This suggests that the deviations are indeed down to a roughened substrate. It is worth noting that all oxidations were performed on the same sheet of metal, and so the roughness of the metallic substrate is unlikely to change from the as-polished state, though there could be some roughening due to

the sputter etching. From here on in, thicknesses will be calculated using Gunter's "magic angle" of 40°, which whilst a simplification of the true state of the sample should only give a small systematic error in the thickness, whilst not affecting the overall trend.

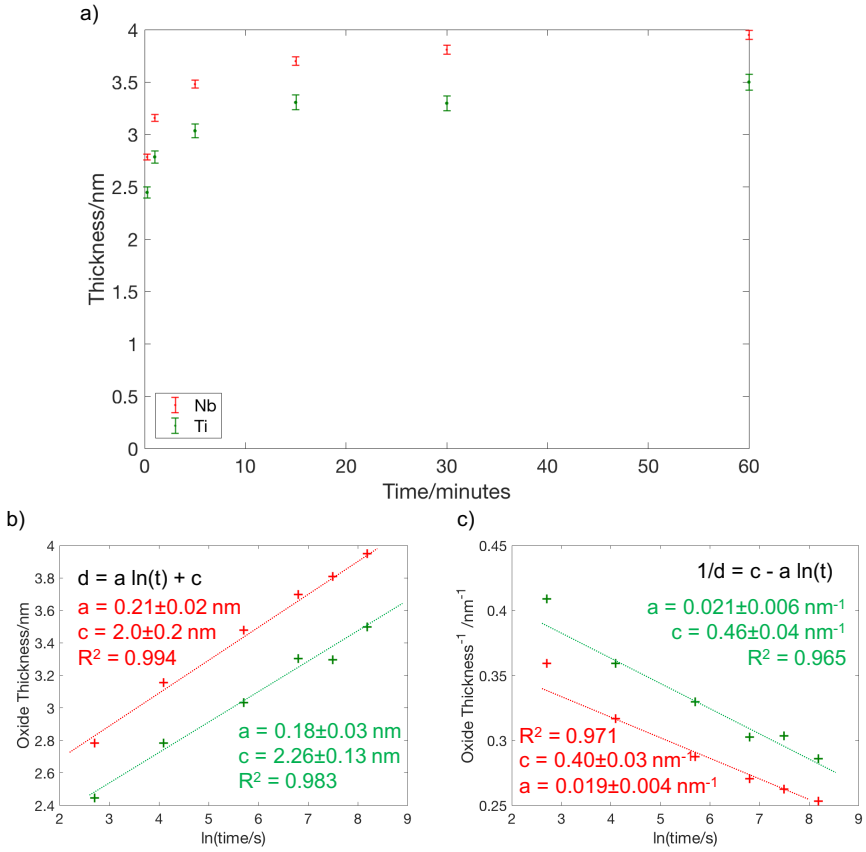


Figure 4.18: a) Oxide thickness calculated using the Strohmeier equation (Equation 4.6) for a NbTi sheet oxidised in air for different times. All measurements were calculated from data taken with the angle of 40° between the detector and sample surface normal. b) The same data set plotting logarithmic data $\ln(t)$ against thickness and fitted according to Boggio's model [163]. c) The same data set plotting $\ln(t)$ against 1/thickness and fitted according to the Cabrera-Mott model [164]

The thicknesses calculated separately from the niobium and titanium data at 40° from the surface normal are shown in Figure 4.18a. These reveal an oxide thickness growing with increasing time at a decreasing rate. The separate calculations from niobium and titanium give similar results, which suggests the initial assumptions about the oxide nature are reasonable. The first 15 seconds of oxidation forms an oxide of at least 2.5 nm, thickening to 3.5 nm after an hour. There is a consistent overestimate of approximately 10% from the niobium data compared to the titanium data. This may

be due to slight compositional variations in the oxide compared to the bulk (if the oxide is slightly niobium enriched). It is also worth noting that the error bars apply only to random errors due to the fitting of the curves and interpretation of the data. It is expected that there will be a systematic error in the estimation of the inelastic mean-free path, often quoted to be accurate to only about ± 10% for elements and nearly 20% for inorganic compounds such as oxides [139], that would affect all data for each element separately but not affect the trend. This is sufficient to account for the difference observed between the niobium and titanium data. XPS also only considers the oxide as homogeneous in the plane of the surface, so does not consider the possibility of, for example, island-type growth without considerably more interpretation [165–168]. For long-term oxidation where oxides are thick this is not much of a problem, but for the gas dosing experiments presented in Section 4.5 this requires more thought.

The oxide thickness, d, after time, t, appears to be given by $d = a \ln t + c$ as shown in Figure 4.18b. This is in good agreement with data presented by Grundner [89] for pure niobium samples, who also demonstrates similar growth kinetics for short times. Grundner correlates this to a growth mechanism limited by chemisorption or oxygen diffusion through the oxide. This mechanism is described in detail by Boggio for thin aluminium films [163]. Figure 4.18c presents a $1/d = c - a \ln t$ as presented for thin films by Cabrera and Mott [164]. This provides a less good fit for thicknesses calculated from both the niobium and titanium data, however it is worth noting that there is insufficient data to make a full conclusion in this regard.

My oxide thicknesses are generally thicker than those reported by Grundner, who reports Nb_2O_5 thicknesses of approximately 1-1.5 nm after 10 minutes depending on sample preparation. A full consideration of the lower oxides is not presented for all samples, so a detailed comparison is difficult, but those that are shown present an oxide always less than 1 nm, making a total that is still thinner than measured for my samples. This is in part due to my samples being oxidised in wet laboratory air rather than dry air, which Grundner shows leads to faster oxidation in niobium and Perez [113] shows the same in titanium, though Perez notes that this difference is reduced with the addition of niobium to the titanium. Grundner also shows that the initial surface

condition has some effect on the oxidation, with more damaged surfaces demonstrating thicker oxides at the starting times, which then grew at approximately the same rate. The sputter etching of my samples is likely to have led to a very high defect density in my surface, which would lead to fast initial oxidation before my measurements began.

4.5 Gas Dosing Experiments

To gain a greater understanding of the earliest stages of oxidation, it was necessary to explore the effects of the exposure of NbTi samples to much lower doses of oxygen. To do this samples were prepared as described in Section 4.2.3, and then any oxide was removed by sputter cleaning to expose the metal surface. Samples were measured in the Kratos Axis Ultra spectrometer at Cardiff and at the Diamond Light Source. To obtain a wide range of oxygen exposures, samples were exposed to a particular dose of oxygen in Langmuirs (1 L = 10^{-6} Torr.s^{-1}). This meant varying both the oxygen partial pressure and the time to ensure that doses between 5 and 50000 L could be achieved accurately and in reasonable times. The oxygen partial pressure was controlled by bleeding small amounts of gas into a separate preparation chamber through a needle valve, at pressures between 10^{-7} and 5×10^{-5} Torr for times from 50 to 5000 seconds as summarised in Table 4.5. The experiments at Cardiff were focussed on AR-XPS to explore the structure and initial growth of the oxide. The Diamond experiments provided higher energy resolution spectra and allowed a heat treated sample to be compared with the standard NbTi sheet.

4.5.1 Gas Dosing Results

After sputter cleaning, samples were measured to understand what a "clean" sample looked like. The oxygen signal in these samples did not drop to zero, so any fit to the curves had to also consider components relating to oxidised NbTi rather than representing the true metallic signal.

When fitted as in Figures 4.19a and b, detailed scans of the as-received sample con-

Sample	Spectrometer	Time/s	Pressure/Torr	Dose/L
AR NbTi	Kratos Axis Ultra (Cardiff)	50	1.7×10^{-7}	5
AR NbTi	Kratos Axis Ultra (Cardiff)	100	9.7×10^{-7}	100
AR NbTi	Kratos Axis Ultra (Cardiff)	100	1×10^{-5}	1000
AR NbTi	Kratos Axis Ultra (Cardiff)	1000	1×10^{-5}	10000
AR NbTi	Kratos Axis Ultra (Cardiff)	5000	1×10^{-5}	50000
AR NbTi	I-09 Diamond Light Source	120	0.75×10^{-5}	1000
AR NbTi	I-09 Diamond Light Source	1200	0.75×10^{-5}	9000
AR NbTi	I-09 Diamond Light Source	1080	3.75×10^{-5}	40000
HT NbTi	I-09 Diamond Light Source	120	0.75×10^{-5}	1000
HT NbTi	I-09 Diamond Light Source	1200	0.75×10^{-5}	9000
HT NbTi	I-09 Diamond Light Source	1080	3.75×10^{-5}	40000

Table 4.5: Summary of times and pressures used for gas dosing experiments. Samples were either as-received (AR), or heat treated for 60 hours at 420°C (HT). Note that the Diamond doses were performed sequentially without cleaning between runs to maximise experimental time, leading to total doses of 1000, 10000 and 50000 L respectively

firmed small amounts of oxidised niobium and titanium, particularly the Nb(II) and Ti(II) phase. This is confirmed by taking difference spectra in Figures 4.19c and d between measurements on the same sample normal to and at 60 degrees from the surface normal. The 60 degree measurement is much more surface sensitive, and so if a different species is present on the surface to the bulk its signal will be stronger in the high angle measurements. The difference spectra was chosen to cancel out the metallic peak, and it is clear in both cases that an extra contribution remains. The niobium plot is particularly clear, with a doublet at 203.6 eV that corresponds to my fit for Nb(II). Similarly, the titanium shows a peak in the difference spectra at 455.4 eV that corresponds to Ti(II). The rest of the titanium difference spectra is less clear, suggesting perhaps there is a more complicated set of oxides present. This agrees with the fitted curves where only Nb(II) produces a strong signal, whilst there are large contributions from Ti(II) and Ti(IV). A little care needs to be taken in trying to extract too much quantitative information from these fits, as small changes in the choice of background or peak shapes would cause a dramatic difference in the proportion of lower oxides. However, whilst there may be errors in the true values of each oxide intensity, the relative trends between oxidations are extremely informative as to the growth processes occurring. A small amount of oxide present on the surface is perhaps unsurprising as both niobium and titanium are highly reactive metals, and will getter any residual

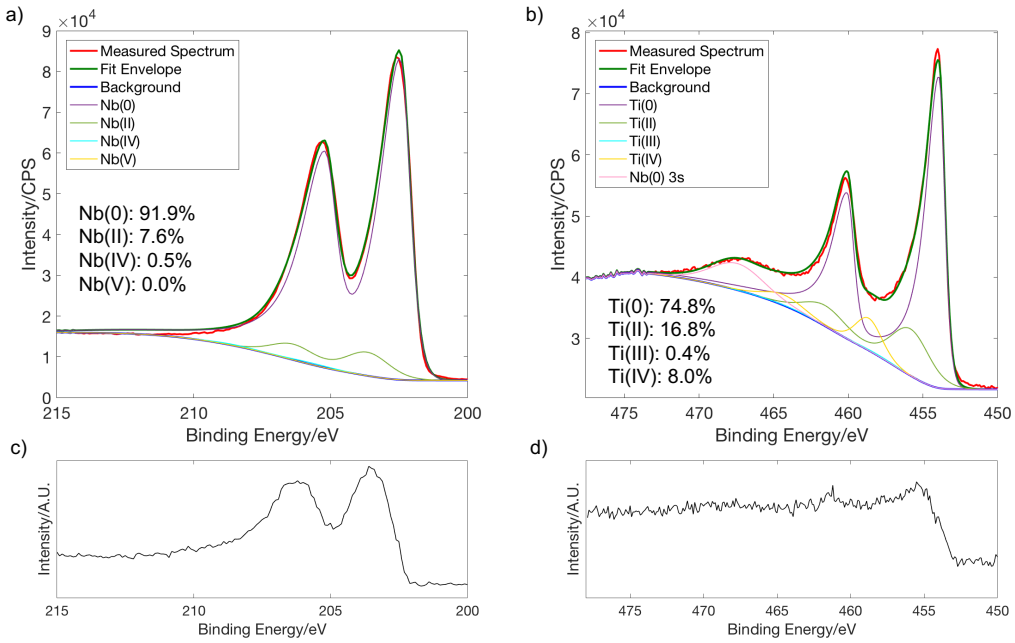


Figure 4.19: Detailed spectra of a) the Nb 3d and b) the Ti 2p region from a sputter cleaned NbTi sheet and measured parallel to the surface normal in the Kratos Axis Ultra spectrometer. The curve fits used for these are shown, demonstrating the presence of small amounts of oxidised species. The area fractions fitted of these are shown (note that the contribution from the Nb 3s peak is ignored for the titanium sample) Plots c) and d) are difference spectra taken by subtracting the spectra measured at 60 degrees from the surface normal from the spectra measured parallel to the surface normal for the niobium and titanium regions respectively

oxygen from the chamber even at very low oxygen partial pressures. It is also possible that oxygen dissolved deeper into the bulk material is drawn to the surface to form the layer, as noted by Delheusy for niobium [169] when the surface was exposed by heating under UHV.

The presence of this outer oxide is of little concern for the air-oxidation studies performed previously, which are interested in a significantly later stage of oxidation than occurs under the UHV conditions. More care must be taken when interpreting the gas-dosing experiments, where growth of the initial layers will be highly affected by the presence of some initial surface oxide. However, this is unlikely to affect the growth of the outer Nb(V) and Ti(IV) oxides allowing a good understanding of these to be gained.

The results from the Cardiff experiments of all the oxidations measured at the most surface-sensitive angle, 60° from the surface normal, are shown in Figure 4.20. For the

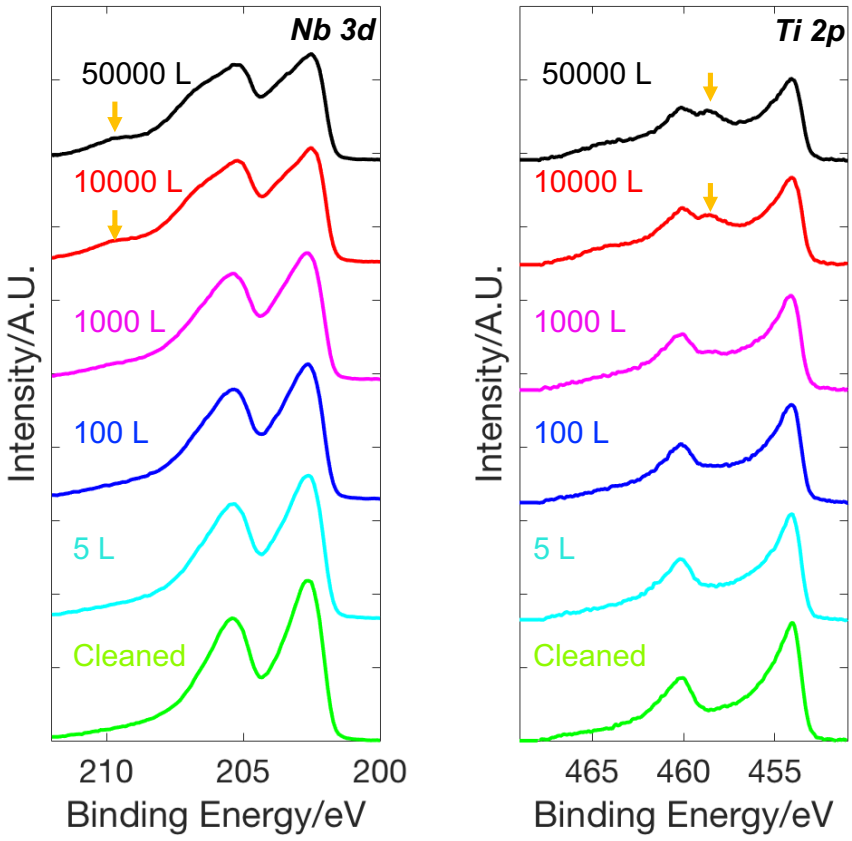


Figure 4.20: Detailed spectra of the Nb 3d and Ti 2p regions from a NbTi sheet and measured at 60° to the surface normal in the Kratos Axis Ultra spectrometer as cleaned and after exposure to between 5 and 50000 L. The emergence of distinct Ti(IV) and Nb(V) peaks, highlighted with gold arrows, becomes apparent after about 10000 L.

low gas doses, <1000 L, there is little change in which peaks are present, with only a slight broadening of the metallic peak. This indicates a growth of lower oxides, such as Nb(II) and Ti(II), which overlap with the metallic peaks. Only at 10000 L is there a clear emergence of new peaks, marked by gold arrows in Figure 4.20, corresponding to the presence of significant quantities of outer Ti(IV) and Nb(V) oxides. Whilst large for surface science experiments, 10000 L is still a very small dose of oxygen, corresponding to around 50 μs in air. This suggests it is near impossible to stop the formation of at least some oxide with exposure of the NbTi surface to air, and indeed suggests that storage of exposed filaments under anything other than a heavily reducing atmosphere is likely to lead to oxidation of the filaments. As such, measurements on NbTi surfaces must involve cleaning the surface immediately before measurement for

the best effect.

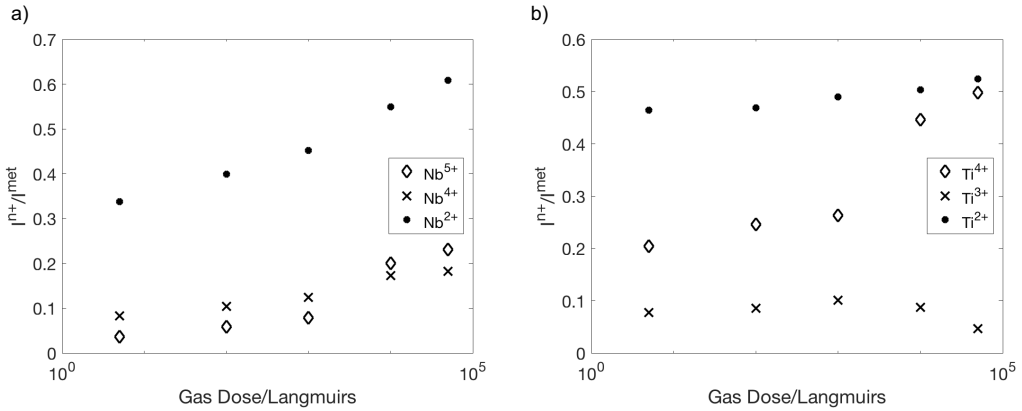


Figure 4.21: Intensity ratios of oxidised a) niobium and b) titanium species against intensity of the metal after different gas doses. Calculated from the Nb 3d and Ti 2p spectral regions from a NbTi sheet and measured at 60° to the surface normal in the Kratos Axis Ultra spectrometer after exposure to oxygen doses between 5 and 50000 L

Quantifying the peak areas from the detailed fits allows more conclusions about the oxide growth to be deduced. These are shown for the oxidised species normalised by the metallic intensity for measurements at 60° from the surface normal in Figure 4.21. The initial gas dose leads mostly to an increase in the Nb(II) and Ti(II) oxidation states corresponding to the growth of a NbO and TiO layer. There is a slight increase in the Nb(V) and Ti(IV) intensities up until 10000 L, where there is a sudden sharp increase corresponding to the presence of an outer layer, as expected from the emergence of the new peaks in Figure 4.20. This is in reasonable agreement with Carley's results for gas-dosed pure titanium [105], who found a fast initial growth of Ti(II) species that stabilised after a small dose, followed by a more gradual coarsening of the Ti(IV) species, with similar concentrations of outer and sub-oxide species observed after a dose of 12000 L.

Due to uncertainties in the exact positions and lineshapes of the different components used to fit the samples care must be taken when comparing across the two species. However, it appears that the intensity ratio of Nb(II) increases with dose much more than for Ti(II), suggesting that the initial oxide formed is more Ti-rich, with the Nb(II) components only forming at higher doses. A large increase in both Nb(V) and Ti(IV) appears to occur after 10000 L.

4.5.2 Initial Oxidation of Heat Treated NbTi

So far, I have just considered the oxidation of single-phase NbTi sheet. Real NbTi wires have a much more complicated microstructure containing fine α-Ti precipitates. Two NbTi sheets were measured at the Diamond Light Source, one as-received and one that had undergone a 60 hour heat treatment at 420°C to encourage precipitation of α-Ti, bringing it closer to the microstructure of commercial wires. Whilst it was impossible to resolve these precipitates in the SEM, their presence was confirmed by x-ray diffraction. The fact the precipitates were too small to resolve in the SEM is ideal for this experiment as it ensures there will be a large number of them illuminated by the x-ray spot, meaning the analysed region will be representative of the whole sample. Both samples were then polished and cleaned using the standard method, and then oxide was removed from the surface by sputter cleaning in a separate preparation chamber. Samples were measured as-received and after dosing with 1000, 10000 and 50000 L of pure oxygen.

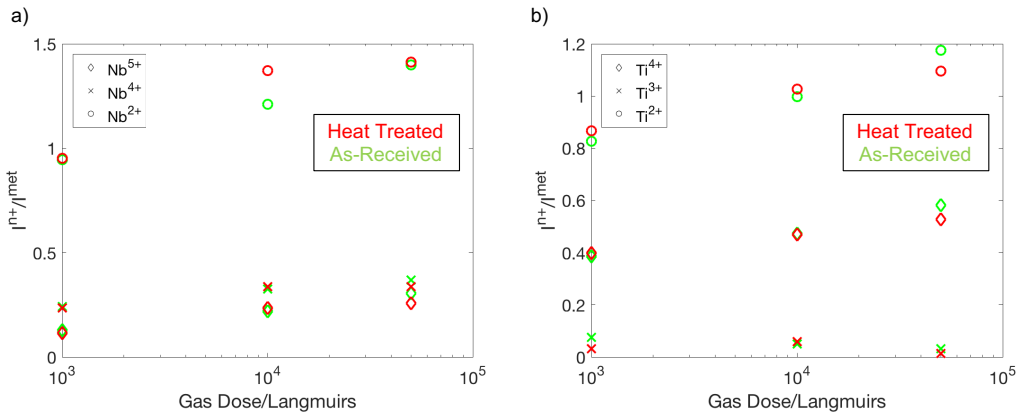


Figure 4.22: Intensity ratios of oxidised a) niobium and b) titanium species against intensity of the metal after different gas doses. Calculated from the Nb 3d and Ti 2p spectral regions from NbTi sheets as-received (green) and heat treated at 420°C for 60 hours (red). Measured at the Diamond Light Source after exposures of 1000, 10000 and 50000 L pure oxygen

As can be seen in Figure 4.22, there is very little difference between the behaviour of the as-received and heat treated sample. This suggests that the presence of α-Ti precipitates has no significant effect on the oxidation behaviour of the sample, meaning the as-received samples used throughout the project are a good substitute for real-

wire material. It is worth noting that the XPS spot sizes used throughout the project were always large, and XPS quantification typically assumes a sample is uniform in the plane of the surface. It is entirely possible that the precipitate-rich sample has local compositional variations that cannot be observed by XPS, but the important thing is that the overall oxide appears to undergo little change.

4.6 Chapter Conclusions

In this chapter, I have presented a detailed quantification of the oxidation of Nb–45wt%Ti using x-ray photoelectron spectroscopy. Samples exposed to laboratory air for times between 15 seconds and 1 hour demonstrate significant oxidation, forming layers approximately 2.5-2.8 nm thick after 15 seconds and coarsening with oxide thickness increasing with time as $d \propto \ln t$. This is of concern for industrial production of NbTi joints, where exposures of filaments to air for these timescales are common. The chemistry of the oxide was found to match that of the bulk, with a consistent ratio of Nb:Ti through the analysed depth of bulk and oxide. This information may help guide future modelling of the effect of any oxide layer on the superconducting properties of joints containing an oxide layer.

Experiments using small doses of gas demonstrated that formation of Nb(V) and Ti(IV) layers occurred after doses of 10000 L, equivalent to approximately 50 μs in air. This demonstrates that keeping a NbTi surface oxide free is in practice impossible. Some signs of oxide were found even on cleaned samples, demonstrating that storage of NbTi under anything other than a highly reducing atmosphere is likely to lead to the formation of surface oxide. In practice this suggests that current industrial practice of ensuring minimum time between exposing filaments and forming joints is likely not to be aided by, for example, performing the joint manufacture in low-oxygen environments.

Chapter 5

Performance of Solder Joints

For the development of future NbTi jointing techniques, it is first necessary to understand the key factors affecting the performance of current joints. Understanding the individual components of joint systems, and how they combine, is essential to future joint development. In this chapter, I consider the three main parts of a soldered joint: the superconducting wires, the interface between wire and solder, and the bulk solder. The importance of each part to the production of an effective superconducting joint is demonstrated. I use transport measurements to closely analyse the wires used throughout this project, which provide a fundamental limit to joint performance. There will be a particular focus on the potential damage caused to the wires during soldering and other moderate, long-term heat treatments that are essential to many current and future jointing techniques. Then I use a variety of measurement techniques to analyse joints made from commercial PbBi solder between wires with and without a niobium diffusion barrier surrounding each filament, demonstrating the strong influence of the barrier on joint performance. Finally, I show the first full characterisation of joints made using the best-performing lead-free solder known to date $Bi_{15}In_{50}Sn_{35}$.

5.1 Transport Properties of NbTi Wires

A key part of understanding the transport properties of joints is to first understand the properties of the wires needed to be joined. In transport, the critical current of the

wire will always provide the a limit to the current that can be put through the joint, so it is important to have a strong understanding of this wire behaviour before joint performance can be understood. Whilst there is abundant literature on the properties of particular NbTi wires, well summarised by Larbalestier and Lee [170], each wire is different and manufacturer-quoted performance is typically underestimated to provide a safe working level, so it was necessary to characterise each of the wires used in this project. The availability of new facilities in the Clarendon Laboratory enabled 4-point measurements at high currents and magnetic fields, allowing for detailed characterisation of the $I_c(B)$ properties of wires at 4.2 K. This section will also study how the jointing process affects wire performance, with a particular focus on the influence of temperature on wire performance.

5.1.1 Supercon, Inc. 54S43 Wire

The main NbTi conductor used throughout this project for joint making and testing was Supercon, Inc. 54S43 multifilamentary wire, with 54 NbTi filaments each of diameter ~45 μm embedded in a copper matrix as shown in Figure 5.1. The whole wire was 0.5 mm in diameter, with a 20 μm Formvar insulation layer and a copper to superconductor ratio of 1.3:1. This is a fairly typical NbTi conductor, perhaps narrower in diameter than many conductors used in the MRI industry, but this narrowness was essential for being able to make the small-scale magnetisation measurements of joints, where it could be easily wound onto a narrow former to fit into a commercial magnetometer. The narrow filaments and multifilamentary nature of the wire make flux jumping less common compared to the monofilamentary wire used by Brittles [33] in previous magnetic joint measurements by our group, allowing improved measurements at 4.2 K.

5.1.2 Transport Properties of As-Received Wire

4-point measurements were performed on approximately 1.3 m of wire wound onto an ungrooved barrel former, with a tap distance of 30 cm. In this geometry the applied

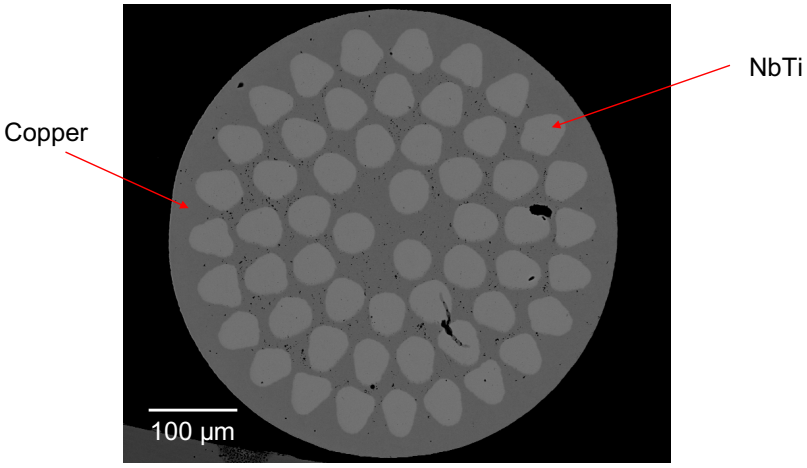


Figure 5.1: Backscattered SEM image of Supercon 54S43 wire. There are 54 filaments, each of ∼45 μm in diameter

field is approximately perpendicular to the current. The magnetic field was increased to 12 T, and then measurements were performed every 1 T from 12 T to 2 T. Critical current values were extracted using a 10 μV m^{-1} field criterion. The data are shown in 5.2, along with the manufacturer quoted values [171]. There is no field criterion stated with the manufacturer data, but it is highly unlikely to be lower than the 10 μV m^{-1} applied here. It is clear that the wire performed approximately 15 to 20% better than the manufacturer data, which is perhaps unsurprising due to conservative tolerance built into these values.

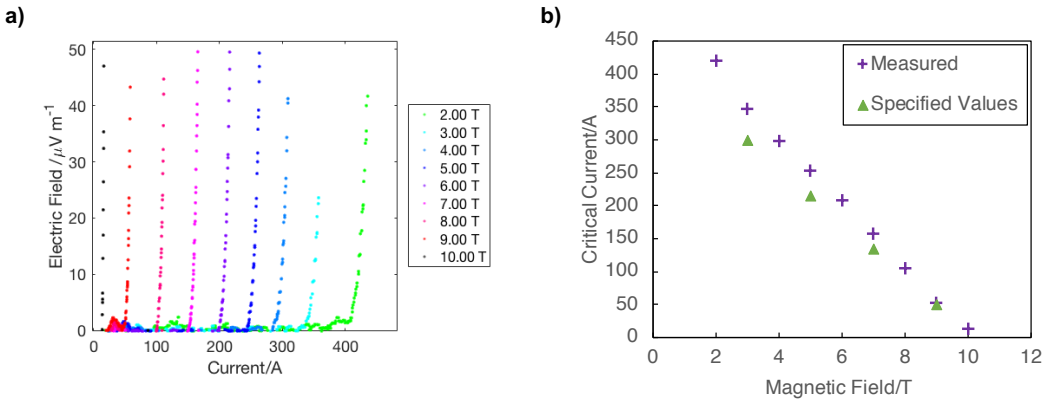


Figure 5.2: a) IV curves for as-received Supercon 54S43 NbTi conductor measured on a barrel holder in perpendicular field b) $I_c(B)$ data extracted from a) using a 10 μV m^{-1} electric field criteria and compared against manufacturer data

The IV data can be parameterised as $V = V_0(I/I_c)^n$ [172], with the value of n acting as a useful figure of merit for wire performance. The n-value is typically a compromise

between intrinsic factors (limited by chemical and microstructural features in the wire) and extrinsic factors (limited by differences in the shape of the filaments). In the intrinsic regime at high magnetic fields there is a strong linear dependence on the applied field, whilst at low fields the n-value is extrinsically limited, leading to a levelling out of the n-value [172]. The moderately fine multifilamentary nature of the Supercon 54S43 conductor leads to strong extrinsic behaviour, with the n-value levelling out at approximately 40 below 6 T as irregularities in filament cross section lead to variation in critical currents between filaments, broadening the superconducting transition.

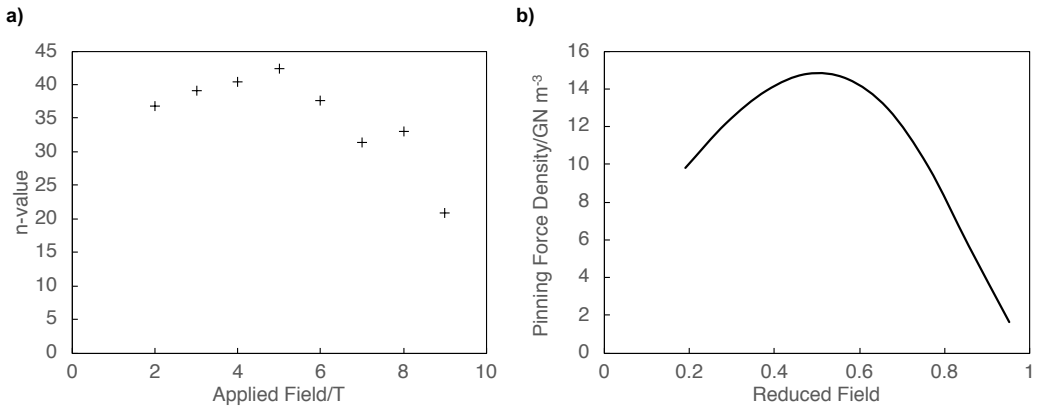


Figure 5.3: a) Measured n-value for Supercon 54S43 conductor b) Pinning force as a function of normalised field, $b = B_{app}/B_{c2}$ where $B_{c2} = 10.5$ T

Plotting the pinning force density as a function of normalised field $F_p(b) = J_c \times B$, where $b = B_{app}/B_{c2}$, allows for an understanding of the mechanisms of flux pinning at work in the conductor. The critical field of the wire was estimated by extrapolating the transport data to give $B_c2 = 10.5 \pm 0.3$ T, in good agreement with the values used in pinning force fits by Bottura [173]. As Meingast and Larbalestier note [174], most processed NbTi wire has peak pinning force density at reduced fields of $b \approx 0.5$. Fitting the pinning force curve to the form $F_p = Ab^p(1-b)^q$ gives coefficients of $p = 1.06 \pm 0.14$ and $q = 1.17 \pm 0.13$, suggesting from the Dew-Hughes model of flux pinning [18] that the dominant pinning mechanism is a volume $\Delta\kappa$ pinning, characteristically described by $F_p = Ab(1-b)$. A peak at a slightly higher value than $b = 0.5$ suggests some contribution from surface $\Delta\kappa$ pinning. At first glance, a $\Delta\kappa$ pinning mechanism is surprising in NbTi, where the pinning sites are expected to be non-superconducting α-Ti precipitates [175], but as noted by Meingast [174] the precipitates are typically

smaller than the coherence length in NbTi, meaning that superconductivity is not lost across the precipitates, making them act as $\Delta\kappa$ rather than normal pinning sites. Cooley et al. argue that the key pinning from such proximity coupled pins is instead a magnetic pinning [20], where the inability of shielding currents to flow in the precipitates leads to pinning. This is also suggested by Muzzi et al [176], who use a 2 component fit for their data. It is worth noting that both Muzzi and Cooley gain the majority of their data through magnetisation measurements, giving a much greater volume of data than transport measurements, and so allowing for better curve fits. With my transport data it is impossible to produce reliable fits with a large number of parameters, and an in-depth study of the pinning behaviour of NbTi is beyond the scope of this thesis. However, we can still learn much from the relative change in the shape of the pinning force curves between different samples.

5.1.3 Performance of Heat Treated NbTi

The fine α-Ti precipitate microstructure that provides the flux-pinning is well known to be very sensitive to the elevated temperatures required in many jointing processes. Any decrease in the wire performance during jointing leads to a decrease in the maximum possible current a joint can carry; no matter how good a joint is the performance will be limited by damaged wires. As such understanding how jointing processes affect wires is critical. Schneider and Turowski [30] demonstrate that degradation of wire performance occurs at temperatures > 550°C even after short times, whilst showing some degradation occurs at 400°C after two minutes. This agrees with Scheuerlein et al. [177] who used magnetisation measurements to demonstrate that after five minutes at 500°C there was a large decrease in critical current in fine filament NbTi conductor, with some evidence of change at 400°C. For Scheuerlein's data, the difference is much more pronounced at high magnetic fields, indicative of a change in pinning mechanism, though this is much less clear in Schneider's work. Scheuerlein et al. attribute their observed decrease in critical current to a change in α-Ti precipitate size and distribution, though they offer little evidence for this. In matrix replacement soldering, temperatures up to 400°C may be maintained for several hours, whilst many potential future

techniques would also include such heat treatments, so it is instructive to understand how heat treatments at medium temperatures and long times affect NbTi conductor performance.

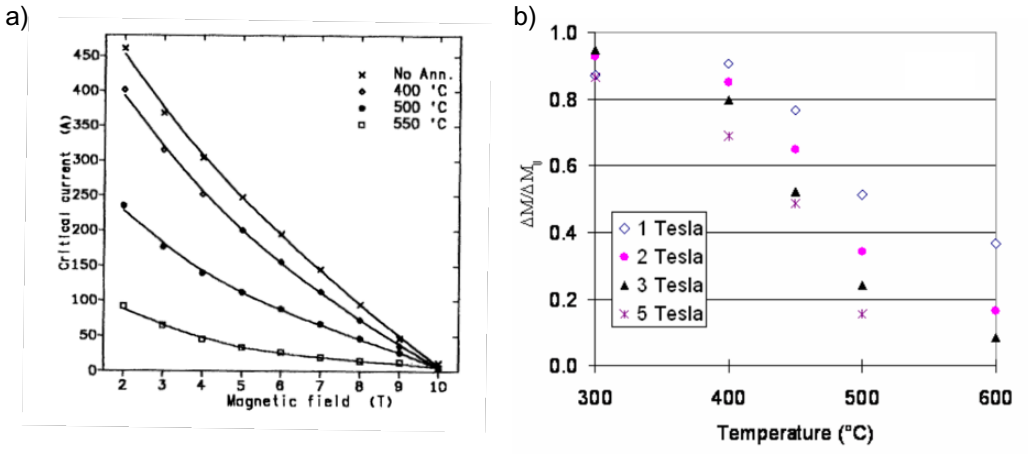


Figure 5.4: a) $I_c(B)$ plot for NbTi conductor heat treated for two minutes at varying temperatures from Schneider and Turowski [30] b) Reduction in magnetisation after heat treatment at various temperatures normalised against an untreated wire from Scheuerlein et al. [177]

Samples of Supercon, Inc. 54S43 were heat treated in air at temperatures of 350°C, 375°C and 400°C for times between 15 minutes and 3 hours. Insulation was left on all samples during heat treatment to limit oxidation of the copper matrix and allow for easy formation of electrical connections to the wire. This insulation was then was removed by lightly rubbing with grinding paper after the heat treatment. It was found the insulation charred almost immediately after the application of heat, and with prolonged heat treatment became easier to remove. However, there was little evidence of oxidation of the copper underneath, suggesting limited oxygen diffusion through the insulation.

Figures 5.5a, c and e show a clear difference between the $I_c(B)$ performance for the different heating temperatures. This is perhaps better illustrated in Figure 5.6 where the critical currents at specific fields are normalised by the critical current of the as-received wire. The 350°C treated wires generally show only small changes in critical current after even the longest times. This is more pronounced at higher fields, with decreases in critical current of more than 20% observed at 8 T after the three hour

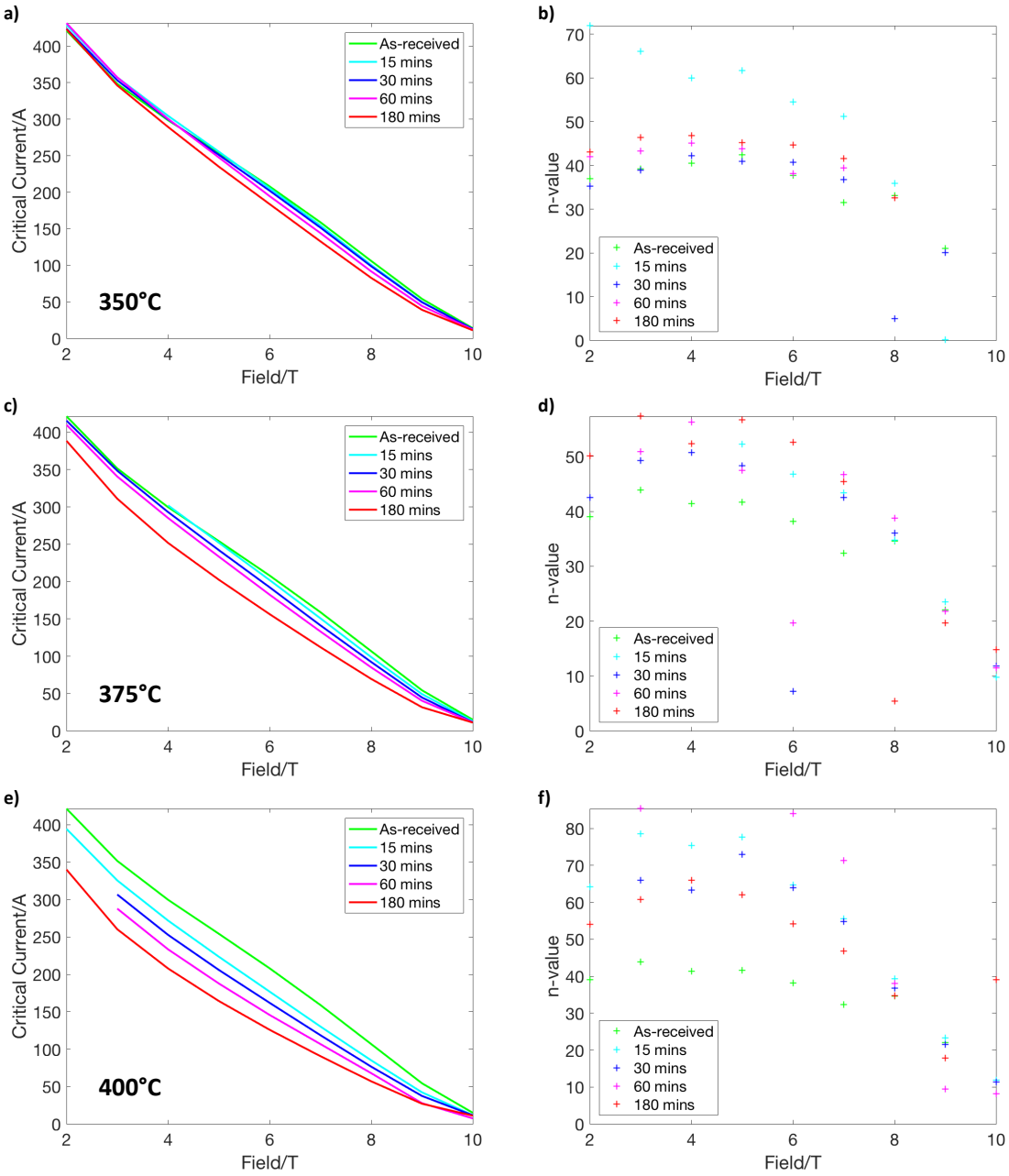


Figure 5.5: $I_c(B)$ and n-value plots plots for Supercon, Inc. NbTi 54S43 conductor heat treated at (a, b) 350°C, (c, d) 375°C and (e, f) 400°C

treatment. However at low fields there is no decrease observed; indeed some potentially demonstrate slightly improved critical currents at 3 T. This suggests 350°C is a very suitable temperature for current matrix replacement soldering, where the low B_{c2} of the solder will limit the operating field of the joint to roughly 1 T, at which point heat damage appears insignificant.

After heat treatment at 375°C, the damage to the wire becomes more significant, with

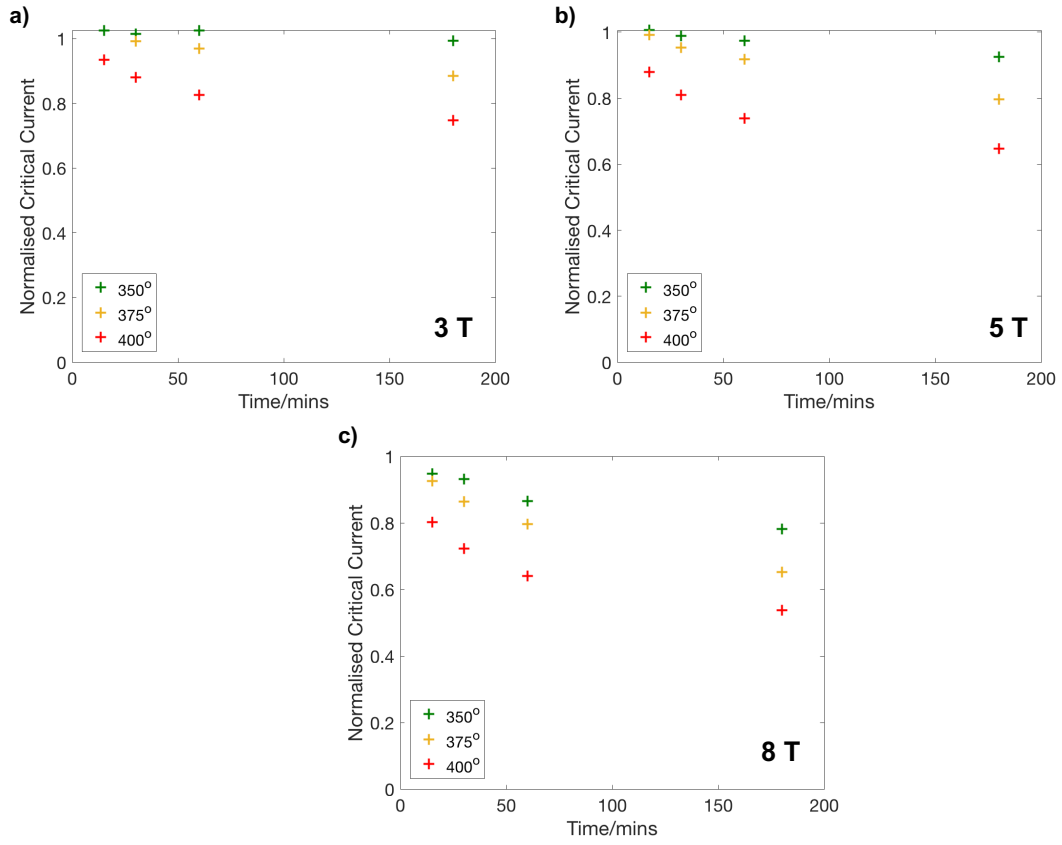


Figure 5.6: Normalised critical current $I_c/I_{c,\,as\ received}$ as a function of heat treatment time at 3, 5 and 8 T

decreases in performance at 8 T noticeable in Figure 5.6 for even the shortest times. After three hours there is degradation in wire performance even at 3 T, suggesting this might cause problems for joint performance. As such, whilst short periods at 375°C can be tolerated, holding wires at this temperature during jointing is likely to cause problems.

The 400°C samples show a greater decrease in performance, which continues to extend even down to low fields. At 3 T there is a reduction in critical current of roughly 25%, whilst even after just 15 minutes of heating the decrease is roughly 10%. At higher fields this decrease is much more pronounced, with critical current reduced by almost a half at 8 T after 3 hours. For low-field joints this is something to be aware of, but in a search for future persistent jointing techniques capable of performance up to the critical field of the NbTi wires this must be a key consideration - extended times at even medium temperatures can be fatal to wire performance. There is a sharp cut-off,

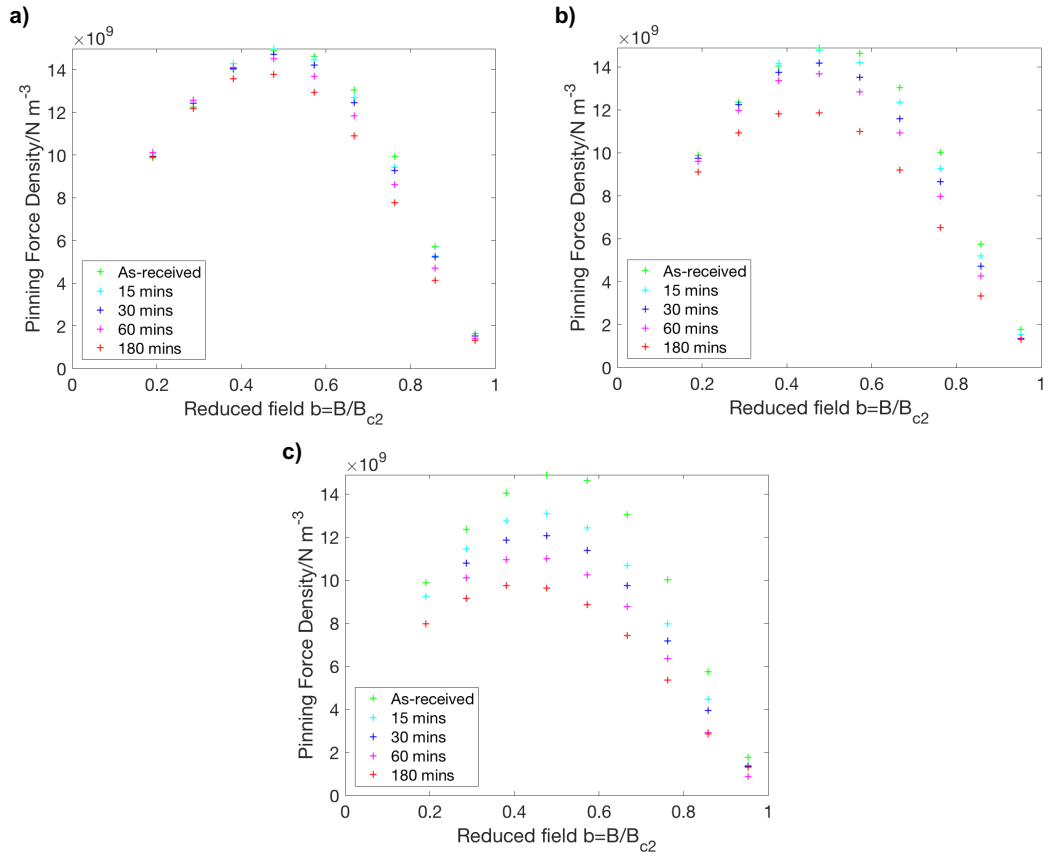


Figure 5.7: Pinning force density plots for 54S43NbTi 54S43 conductor heat treated at a) 350°C, b) 375°C and c) 400°C plotted against applied field.

where wires can be heat treated at 350°C for extended periods without damage, but even a small increase above this leads to wire degradation.

There is a much less clear trend in the n-values of the wires, shown in Figures 5.5b, d and f. Schneider and Turowski reported no obvious change in n-value for their samples heat treated for short times, but very different behaviour is observed here. At 350°C the n-value appears independent of heat treatment time except the possibly erroneous results at 15 minutes (which may be due to poor thermal connection between the sample and sample holder leading to an increase in the sharpness of the transition). For the 375°C and 400°C samples there is an increase in the n-value of the samples, with the biggest increases found in the 400°C samples, though there is a large scatter in this data, making the effect of time at each heat treatment unclear. The n-values reported by Schneider are higher than for the wires tested here, potentially due to a different wire geometry.

The extremely fine microstructure of NbTi wires is essential to their superconducting performance, and it is to be expected that these heat treatments cause at least some change to this structure. Scheuerlein attributes this in large part to a change in the size and distribution of the α-Ti precipitates. Whilst characterisation of this change on a microstructural level is beyond the scope of this thesis, plotting the pinning force curves for these wires in Figure 5.7 is instructive. From these it is clear that the peak in the pinning force moves to lower reduced fields with increasing heat treatment time. Many authors attribute the pinning behaviour in NbTi wires to two main mechanisms: a $\Delta\kappa$ pin due to α-Ti precipitates made superconducting by the proximity effect leading to a peak at a reduced field of around $b = 0.6$, and either a magnetic or normal pinning contribution leading to a peak at a reduced field of around $b = 0.2 - 0.33$. The combination of these two leads to the overall peak at around a reduced field of around $b = 0.5$. The clear decrease in the field at which the peak pinning force is attained as a result of the heat treatments is likely to be due to a reduction in the $\Delta\kappa$ pinning from the α-Ti precipitates as they coarsen [174]. There may also be a homogenisation of the compositional variations in the Nb(Ti) solid solution matrix phase, which Bormio-Nunes et al. identified as a key aspect to pinning in NbTi conductors [19] as it leads to local variations in the critical field and temperature, which would also lead to fluctuations in κ. In the case of the longer times at higher temperatures, the overall strength of the pinning is also reduced, suggesting that microstructural changes are making the pinning less effective, unsurprising due to the highly optimised starting condition of the NbTi wires.

5.1.3.1 Effect of Atmosphere

All of the above samples were heat treated in air. Whilst this is much more convenient for heat treating long lengths of wire, and is consistent with many industrial jointing techniques performed in open air, a concern is whether the heat damage observed is truly due to microstructural change or whether there is any reaction with the atmosphere. Even small changes in the chemistry of the wires are likely to lead to changes in the superconducting properties. To test this, a wire was coiled and placed in a tube

furnace under flowing argon gas. The furnace was heated at 400°C per hour up to 400°C and held there for three hours. It was then cooled to 340°C at approximately 200°C per hour and then removed and cooled in air. From the previous data, damage to the NbTi conductor below 350°C occurs extremely slowly so any damage in the heating and cooling steps is likely to be insignificant, and so this sample can be directly compared with the equivalent air-cooled sample.

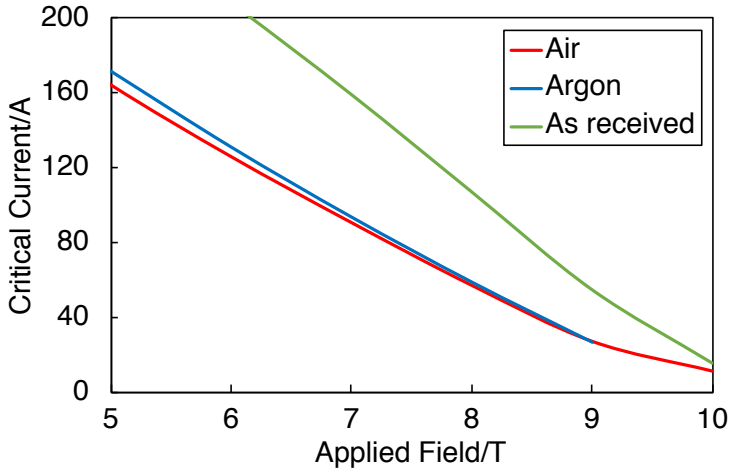


Figure 5.8: Critical current against field for wires heated for 3 hours at 400°C in air (red) and argon (blue) atmospheres. The two show very similar results and are both heavily suppressed compared to an as-received wire (green)

As can be seen in Figure 5.8, the inert sample performs slightly better than the air sample. However, this difference is small compared to difference to the as-received sample performance. It is clear any difference due to reaction with oxygen is insignificant, even for the samples with the longest times at highest temperature. Any effect would be expected to be smaller for the other samples. In Figure 5.9 it can be seen that there is little difference between the n-values for the wires heat treated in different atmospheres.

5.1.4 Conclusions on Wire Performance

These results are helpful for the development of replacement jointing processes. It is clear that the longer heat treatments at 350°C or below required for matrix replacement are not fatal to wire performance, especially at fields relevant to current jointing solders

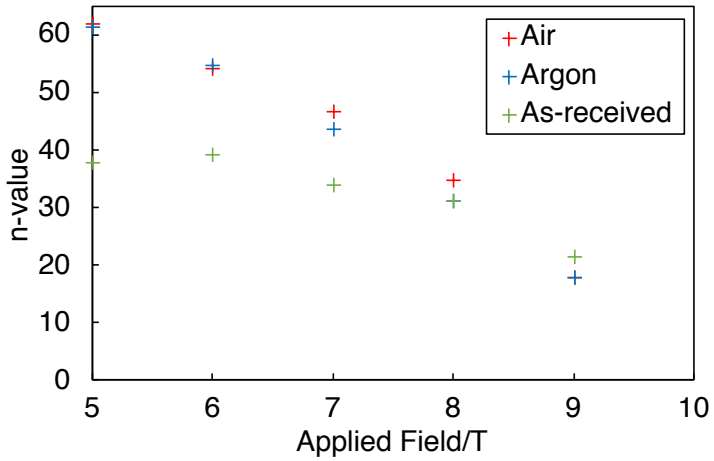


Figure 5.9: n-value of the superconducting transition against field for the wires heat treated in air and argon. The two again show very similar results and are both much higher at low fields compared to an as-received wire (green)

with low upper critical field. However, small changes in the soldering temperature can lead to large differences in the the wire damage. Even short times at 400°C can lead to large decreases in wire performance, leading to an unavoidable reduction in joint critical current. Care should be taken when employing any heat to the wires to ensure the maximum temperature does not exceed 350°C. It is worth noting this has significance for many mechanical bonding techniques, where low temperature heat treatments improve mechanical bonding. One example of this is the diffusion bonding technique utilised by both Mitzumaki [73] and Swenson [4], which requires extended heat treatments at 450°C. In both cases joint resistance is measured, rather than critical current, but it is likely the heat treatment used would lead to decreases in critical current through these joints at higher magnetic fields.

5.2 Lead-Based Joints

Whilst the focus of this project was the development of new, lead-free, jointing techniques, it was necessary to measure a small number of lead-based joints as a comparison. This served both to validate the measurement techniques on a well-known system and to better understand present industrial jointing.

5.2.1 The Effect of Interfaces on Joint Performance

Wire architecture may play a key role in joint behaviour. In particular, some wire manufacturers include a niobium diffusion barrier around the NbTi filaments. This prevents reactions of the NbTi with the copper during heat treatments, which can lead to the formation of hard $TiCu_4$ intermetallics that do not draw evenly with the wire [26] leading to non-uniform cross-sections and potential filament failure. In some jointing processes involving acid-etching, this barrier is removed. However, in matrix replacement soldering the diffusion barrier is untouched. The upper critical field of niobium, (0.8 T [33]) is considerably lower than that of NbTi (10.5 T) and PbBi (1.33 T). Understanding the effect this has on joint performance is therefore crucial, as the diffusion barrier is likely to be the poorest performing part of the superconducting circuit. Whilst industry understand there to be an issue with making matrix replacement joints from niobium barrier wires, there is no literature on the problem. To investigate this, it was decided to use commercial eutectic PbBi solder. This is better understood and of more immediate industrial relevance than lead-free solders. Also, no lead-free solder has a critical field higher than niobium, so any difference caused by the diffusion barrier is likely to be insignificant. These joints will also serve as a reference against which lead-free joints are compared later.

5.2.2 Niobium Diffusion Barrier Wire

The diffusion barrier wire chosen was manufactured by Luvata, with 54 filaments each of diameter 40 μm as shown in Figure 5.10a. The higher atomic weight of the niobium diffusion barrier is clear in these backscattered electron images as the rings of bright contrast around each filament in Figure 5.10b, suggesting it to be approximately 200 nm thick. Figure 5.10c gives the $I_c(B)$ performance of this wire, measured in transport on a barrel-type sample holder with critical current extracted using a 10 μV m^{-1} criterion. The wire shows similar behaviour to the Supercon 54S43 wire characterised in detail in the previous section, albeit with a slightly lower critical current due to the narrower filament diameter.

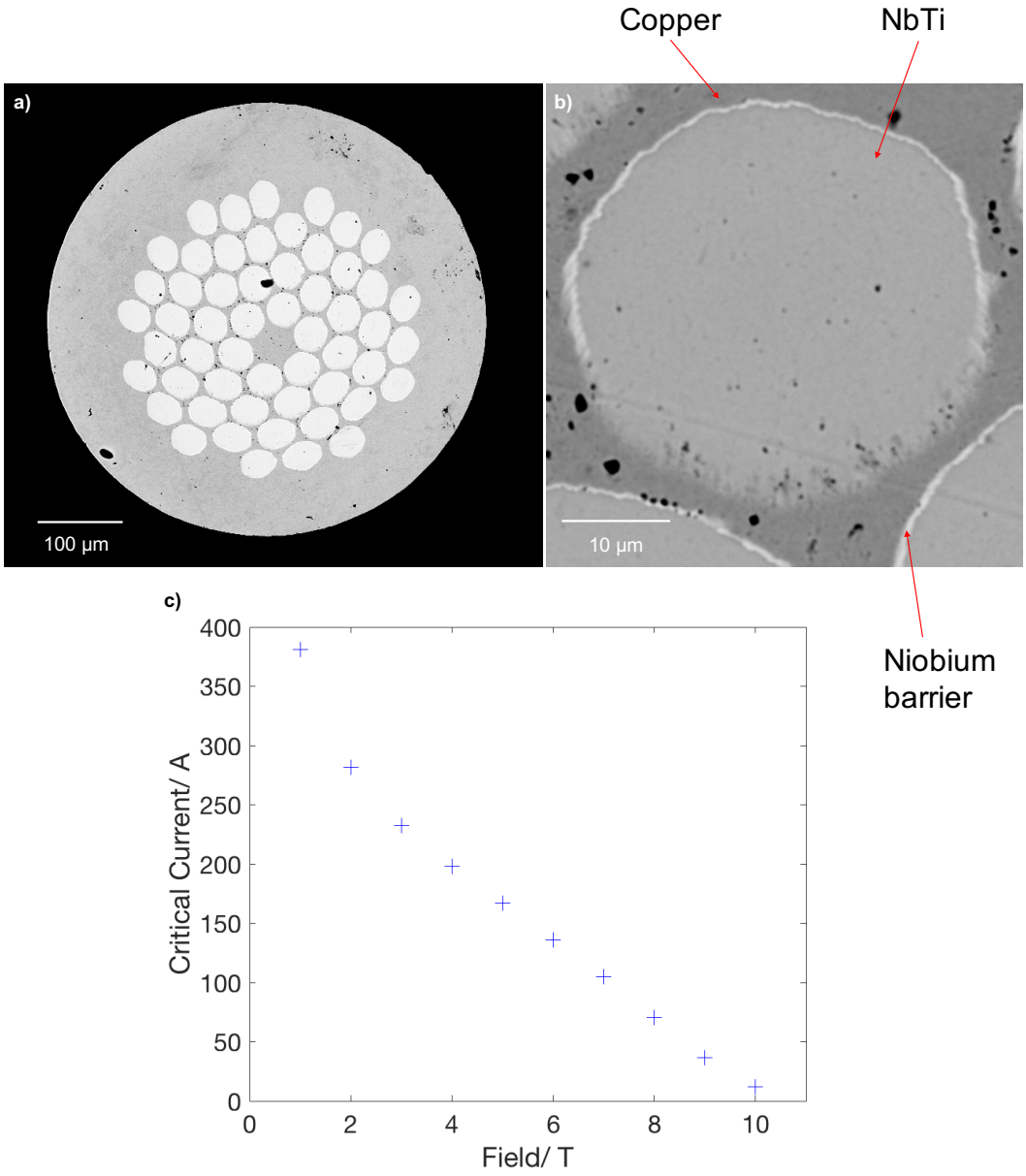


Figure 5.10: a) and b) Backscattered electron images of the Luvata wire with diffusion barrier. The light contrast around the edge of each filament is due to the higher atomic weight Nb diffusion barrier. c) shows the $I_c(B)$ performance of the wire, measured in transport on a barrel-type sample holder with a 10 μV m^{-1} criteria

5.2.3 Hysteresis Loop Analysis

Two joints were fabricated for testing in the PPMS, one with the Supercon 54S43 wire (with no diffusion barrier), and one with Luvata wire with a diffusion barrier. In each case, 15 mm of insulation was removed from each end of a 10 cm wire, and the copper stabiliser was dissolved in liquid tin for 30 minutes at 350°C. Eutectic $Pb_{55}Bi_{45}$

provided by Siemens Magnet Technology was melted at 325°C, and the tinned wire was immersed in this for 30 minutes. Solder was then cast into a 2.13 mm diameter mould and heated to 120°C. The wires were inserted into the molten solder and left to cool in the mould to form a cast solder cylinder with the wires embedded. The Supercon joint was 6 mm long and the Luvata joint 5 mm long, both being cylinders 2.13 mm in diameter. These joints were then wound onto a G10 former and characterised in the PPMS-VSM.

Moment-field loops were recorded for the Supercon 54S43 wire at different temperatures as seen in Figure 5.11a. The top right quadrant of these was used for a simplified conversion to critical current, shown in Figure 5.11b for joints between both wires measured at 4.2 K. This quadrant was chosen as there was flux-jumping evident in the top left and bottom right quadrants, obscuring large regions of the data from analysis. Whilst this is only a simplified approximation due to demagnetising currents in the wires, this is expected to affect both wires equally, and so comparisons between the joints is valid. The low-field plateau in the hysteresis loop and current plots for the Supercon wire is likely to be due to the induced current reaching the critical current of the jointing wire. The critical currents of the two joints are similar, though higher for the Supercon joint by about a factor of 2 at 0.5 T and a factor of three at 1.0 T. It is likely that the difference between these two fields is due to the Supercon wire starting to reach the wire-limited plateau. The Supercon joint was approximately 20% longer. This might be simplistically be expected to cause a 20% increase in current carrying capacity, not enough to account for the difference between samples. However, particularly with multifilamentary wires, filaments may bend and intertwine in the jointing region. This complicates the current paths, so care must be taken when analysing the data beyond a brief comparison of joint currents. Also, these joints were relatively short, and the PbBi solder was found to have a low viscosity, causing it to flow whilst liquid. This made the casting of controlled, uniform joints difficult. The critical current was not the focus of this investigation, if more accurate comparisons were required a more thorough casting process with greater control of wire geometry would be required.

The field performance of the two joints is very similar, with critical fields at 4.2 K of

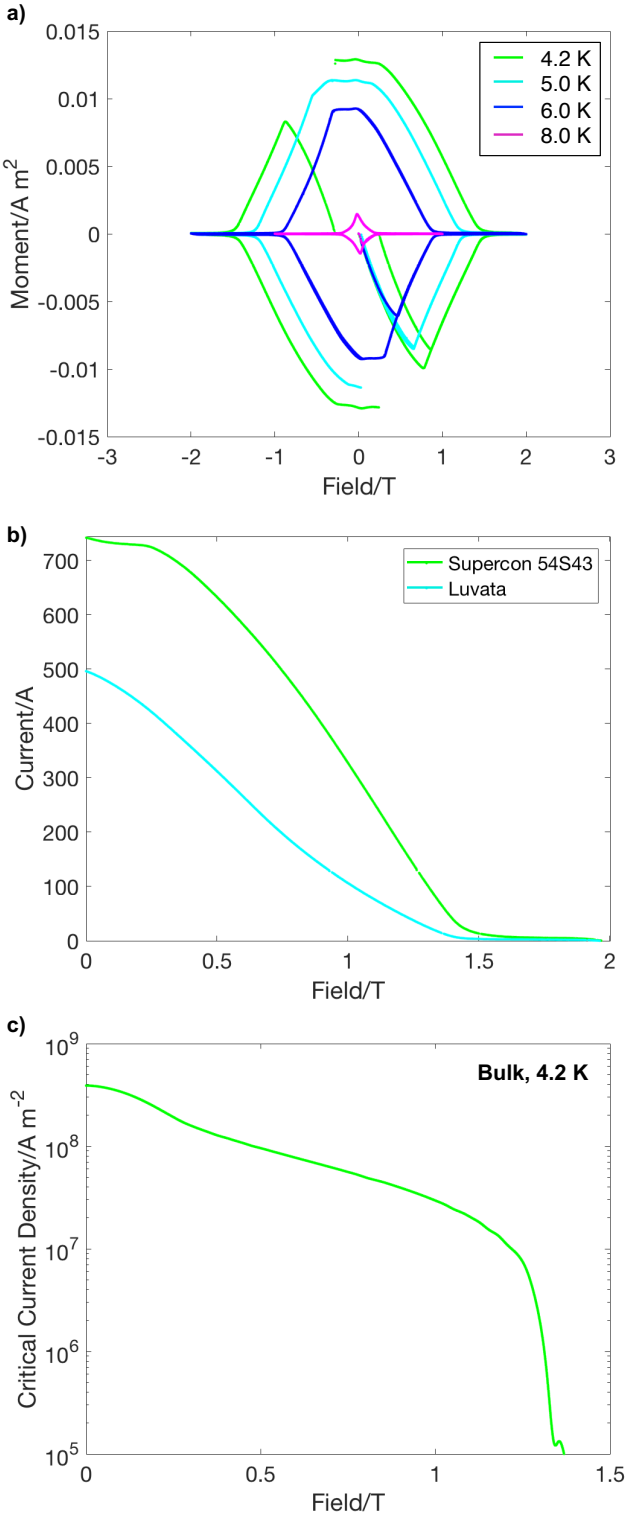


Figure 5.11: a) Hysteresis loop of eutectic PbBi joint with Supercon 54S43 at different temperatures. b) Conversion of the top right quadrant of a) into current at 4.2 K for PbBi joints made between Supercon 54S43 with no diffusion barrier and Luvata wire with a niobium diffusion barrier. c) $J_c(B)$ curve for a 2.13 mm cast bulk sample of eutectic PbBi

1.45 T recorded for both samples. This is slightly higher than the 1.33 T recorded for bulk solder in Figure 5.11c, but is in reasonable agreement with the critical field of 1.48 T noted using this measurement technique by Brittles [33] for joints in $Pb_{40}Bi_{60}$ solder. It is significant that the Nb barrier joint has a critical field defined by the bulk solder, rather than the considerably lower critical field of niobium. Indeed, there is no obvious transition in the Luvata joint that could reflect the diffusion barrier exceeding its critical field. It is possible that supercurrent can tunnel through these thin diffusion barriers. However, it is more likely that during field sweeping the changing field induces a current in the coil, and as the niobium barrier is thin its resistance is extremely low. As this is a dynamic measurement, any decay in magnetic moment caused by the thin resistive layer is negligible in the time spent at each field and so the effect of the barrier on the measurement is negligible. Whilst the sensitivity to such resistances using this technique is likely greater than for transport measurements (where the resistances detectable are typically limited by the sensitivity of voltmeters), care must be taken in analysing such results – as will be shown in the next section, even samples that give large hysteresis loops may still have resistances that cannot be detected but are higher than acceptable for persistent joint applications.

5.2.4 Decay Measurement Analysis

The only way to be certain a joint is suitable for persistent-mode use is to perform decay measurements. A great advantage of the magnetisation technique is that it allows both $I_c(B)$ and IRT (inductive resistive testing) measurements to be performed across the full range of fields and temperatures with no change in apparatus. To understand the effect of diffusion barriers, IRT measurements were performed on both PbBi joints directly after the m–B loops. This was performed at multiple fields, each time inducing the maximum possible current in the sample and measuring over a period of three or four hours to allow any settling effects to become negligible.

Whilst there was little difference in the field performance of the two samples evident from hysteresis loops, the decay measurements in Figure 5.12 provide a different picture. At low fields around 0.5 T there is little difference between the two joints, with both

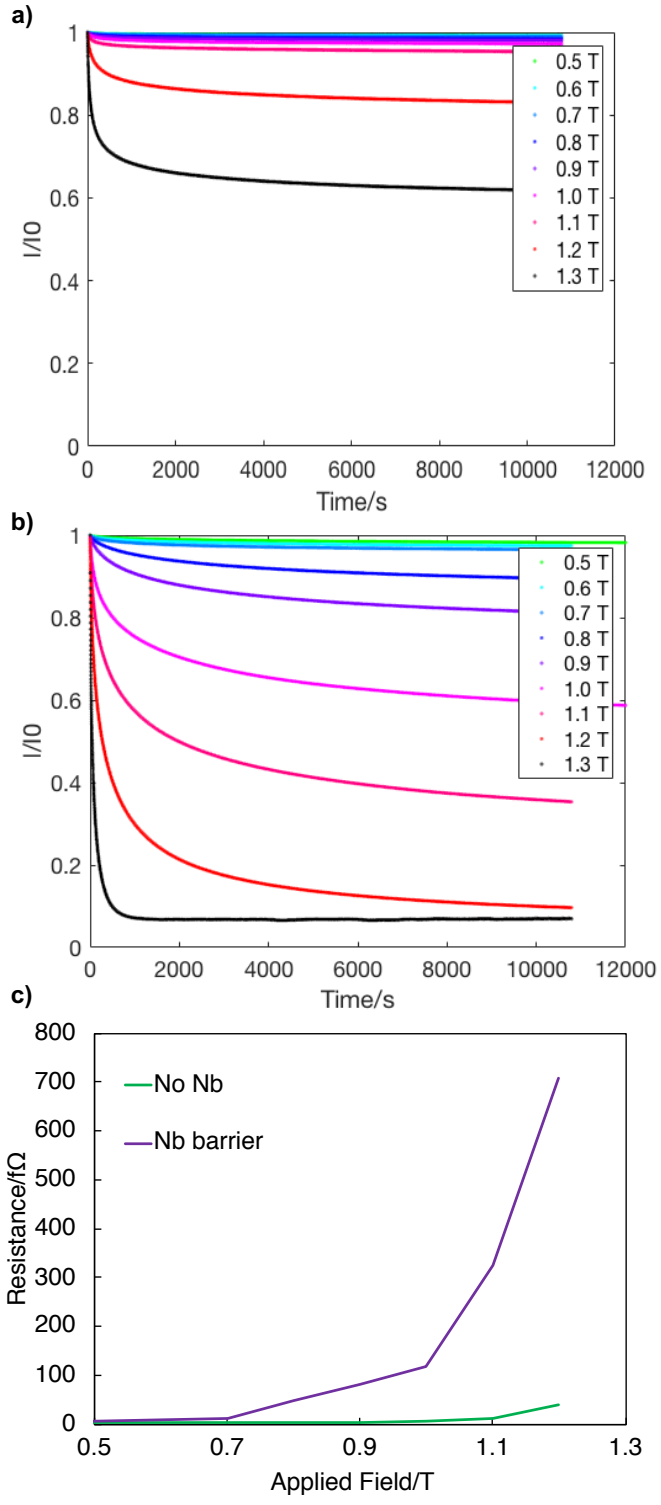


Figure 5.12: Normalised decay curves for a) Supercon 54S43 with no diffusion barrier and b) Luvata NbTi wire with a diffusion barrier. At each field the maximum current was induced in the sample. The final 1000 seconds of each data set were used for a straight line approximation to calculate a resistance, plotted for both samples in c)

demonstrating resistance values less than 5×10^{-15} Ω at currents of 600 A and 250 A for the Supercon and Luvata samples respectively, but at higher fields the sample with the diffusion barrier showed considerably more decay. This evidenced itself in two ways. First, the resistance of the Luvata joint shows a large upturn at around 0.7 T as shown in Figure 5.12c. This resistance is calculated from the final 4000 seconds of the measurement to reduce any contribution from settling effects. The field at which this upturn occurs is important as it corresponds to the critical field of bulk niobium at around 0.8 T [33]. This indicates that whilst the barrier has no noticeable effect on hysteresis loops, it does lead to a noticeably sharper decay profile. This is in keeping with the presence of a thin resistive layer above $B_{c2,\,\mathrm{Nb}}$. Whilst the sweeping of the background magnetic field is able to induce a current of $I_{c,\,\mathrm{joint}}$ as if no barrier were present, this current then decays away at a rate limited by the series resistance of the circuit, which is dominated by the resistance of the diffusion barrier. The Supercon wire with no diffusion barrier only starts to show this upturn in joint resistance as the magnetic field approaches the critical field of the solder. This suggests that it is the bulk solder, rather than any reaction layers between the NbTi and solder, that limits the decay properties. The decay measurements show that there is considerable decay at 1.3 T (close to the solder's critical field measured by magnetisation to be 1.33 T), suggesting the raised critical field observed in Figure 5.11b for the joints might be due to currents that are not truly persistent.

The PPMS decay technique is prone to measuring drifts associated with the magnet as well as from the sample, as the measurement, background field and current induction are all performed using the same magnet and measurement loop. However, these results clearly demonstrate a strong difference between the samples, with large effective resistances measured only, as expected, when the niobium stops superconducting. This data demonstrates the power of the PPMS decay technique for investigating the performance of joints.

There is a much greater difference in the early decay behaviour of the joints. For the Luvata sample, the measurements above the critical field of the niobium diffusion barrier demonstrate particularly large decreases in current over the first 1000 seconds,

before steadying to a slower decay rate. This suggests that there are settling effects occurring in the joint. One possible explanation for this is that the niobium barrier is not complete, and so a current path may form between some filaments. The initial current is induced as if the diffusion barrier is not present, and then a quick decay would occur until the critical current through the holes in the barrier is reached. However, this seems unlikely given the extra increase in resistance seen at the end of the measurements. Alternatively, it may be possible for tunnelling of current through the barrier to occur. This might be expected to be lower than the initial induced current, leading to a fast decay until the tunnelling current is reached, when more stable decay occurs.

5.2.5 Conclusions on PbBi Solder Joints

The results from this show clearly that the niobium diffusion barrier has a strong effect on joint performance, and it is likely these joints would not be suitable for use in MRI scanners where the typical operating field for joints is around 1 T. Moving the joints to lower field regions or adding increased magnetic shielding would have to be considered. This demonstrates that care must be taken when selecting jointing techniques for different architectures of wire, even if they have the same geometry. It also demonstrates that thin layers can greatly affect joint performance. Whilst the layers in this case are due to the niobium diffusion barrier, it is common to see at least some reaction layer between the solder and the wire [33, 34], and therefore unique to particular solder chemistry, heat treatment and even the wire chosen. This appears not to influence PbBi solders, with current decay in the Supercon sample limited by bulk solder, but is something that may need to be considered carefully for other systems with different reaction layers.

This section also shows the advantages and disadvantages of applying different measurements to superconducting joints. Even for these samples, consisting of a system with three well-understood components, mistakes could be made if using only measurements of critical current to assess joint behaviour. Decay measurements provide the sensitivity to extremely low resistances to confirm a joint is suitable for persistent-

mode operation, though hysteretic measurements still provide a useful gauge for joint behaviour across a range of different fields and temperatures.

5.3 Lead-Free Joints

To date there has been very little literature on the performance of lead-free superconducting joints, with almost all measurements on joints performed on PbBi solders [4, 7, 31, 34]. In this section, I study the performance of joints made from the best performing lead-free solder, $Bi_{15}In_{50}Sn_{35}$. Details of the microstructure/superconducting properties relationship between for $Bi_{15}In_{50}Sn_{35}$ solders have been investigated thoroughly by Mousavi [43] and Brittles [33] for bulk samples of this solder, but there has only been one study on joints of this material, which was potentially limited by poor manufacturing [33]. Mousavi showed lead-free solders are highly sensitive to exact processing conditions and thermal ageing [43], so it was essential to characterise the microstructure and superconducting properties of the solder under the particular conditions used for joint fabrication. Joints were then fabricated and characterised using traditional IV methods, magnetic measurements and decay measurements. Parts of this work have been included in an article accepted for publication in Materials and Design [56].

5.3.1 Joint Fabrication

Room temperature represents a high homologous temperature for many lead-free solders lead to fast diffusion, and so the microstructure of these solders is highly sensitive to processing history [33, 43, 51]. The joint manufacturing process was designed to be very slow, keeping the sample close to an equilibrium microstructure and so limiting any change in the samples with age. This was beneficial as it meant joints could be fairly and reproducibly tested. To form the joints, the individual metals were melted together in a crucible and held at 300°C for 15 minutes. 2 pieces of Supercon 54S43 wire had 15 mm insulation removed from one end, and had these ends placed in liquid tin at 350°C for 15 minutes to dissolve the copper matrix. These 'tinned' ends were

then placed in the liquid solder at 350°C for 15 minutes to coat the filaments. A 13 mm cylinder of this solder was cast into a cylindrical mould of diameter 2.13 mm, and then the mould was heated to 100°C to melt the solder. The soldered ends of the wire were immersed into this, then the mould was removed from the hot-plate to allow the solder to slowly cool back to room temperature, leaving a cast 13×2.13 mm cylinder of solder around the wires. The mould and an example joint are shown in Figure 5.13.

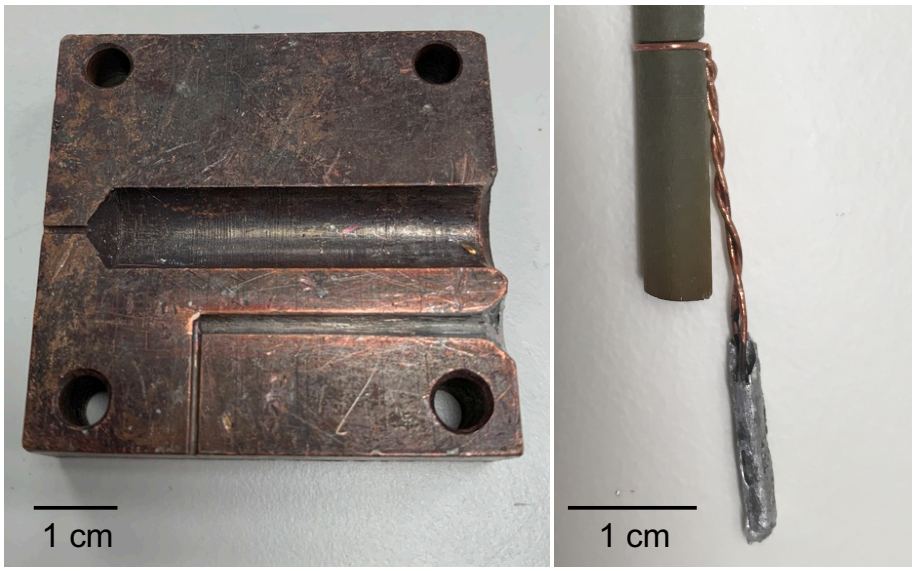
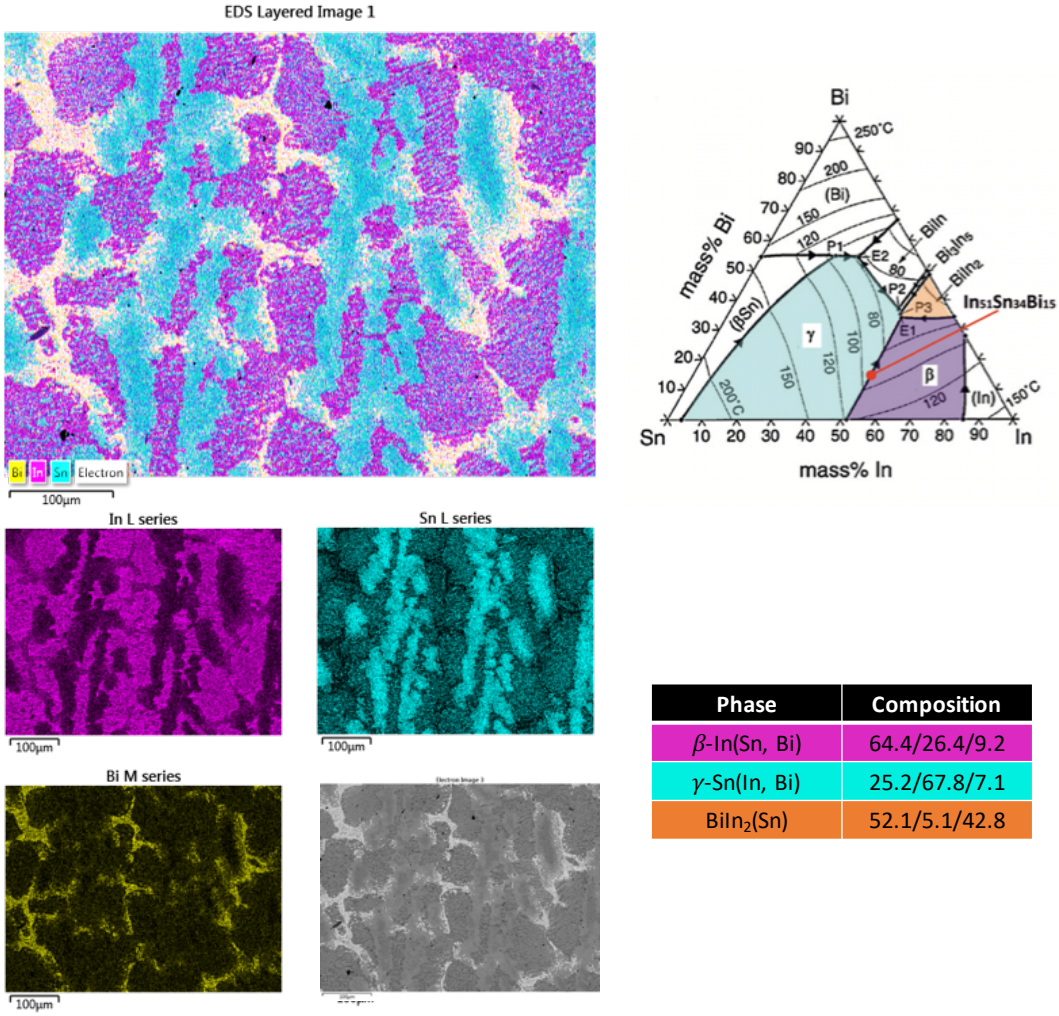


Figure 5.13: Left: The brass mould used to cast joints and bulk solders. There were two possible moulds, one 2.13 mm that was used for PPMS bulk and joint samples and the other 10 mm in diameter that was used for the large scale joints measured at SMT. Right: Cast $Bi_{15}In_{50}Sn_{35}$ solder joint mounted for PPMS measurement

5.3.2 Bulk Solder

Due to the strong process-history dependance of these solder materials, quick characterisation of the bulk solder under the particular process conditions used for jointing is essential. Solder from the same crucible used for jointing was melted at 300°C then cast into the 2.13 mm diameter copper mould at 100°C and allowed to cool with the mould back to room temperature without forming a joint but under the same conditions. Sections of this were cut for microscopy and for magnetic characterisation to ensure joint performance could be fairly related to the superconducting properties of bulk solder.



Phase	Composition
β-In(Sn, Bi)	64.4/26.4/9.2
γ-Sn(In, Bi)	25.2/67.8/7.1
$BiIn_2$(Sn)	52.1/5.1/42.8

Figure 5.14: Energy dispersive x-ray maps of the main components of the solder, plus the composite layered image. The sample is clearly divided into three phases an indium-rich β phase (in purple on the map), a tin-rich γ phase (in blue) and a $BiIn_2$(Sn) phase (in cream). The phase diagram for the ternary solder reproduced from [33] is also shown

The slow cooled solder in Figure 5.14 had a very coarse microstructure with three distinct phases: an indium-rich β phase ($In_{64}Sn_{26}Bi_9$ by weight percent), a tin-rich γ phase ($In_{25}Sn_{68}Bi_7$) and a $BiIn_2$(Sn) phase ($In_{52}Sn_5Bi_{43}$). The combination of the large length scale of the microstructure and relatively low indium content in the β phase mean relatively poor superconducting properties are expected for the solder [43]. The regions of poorly superconducting γ phase are also extensive, which may lead to obstruction of current in a joint. However, this microstructure is much more stable and so is better for repeatable measurements with no dependence on when the samples were made. To gain the most benefit from quenching, samples need to be cooled extremely

quickly, which would not be easily implementable on current production lines where the cast joints are large.

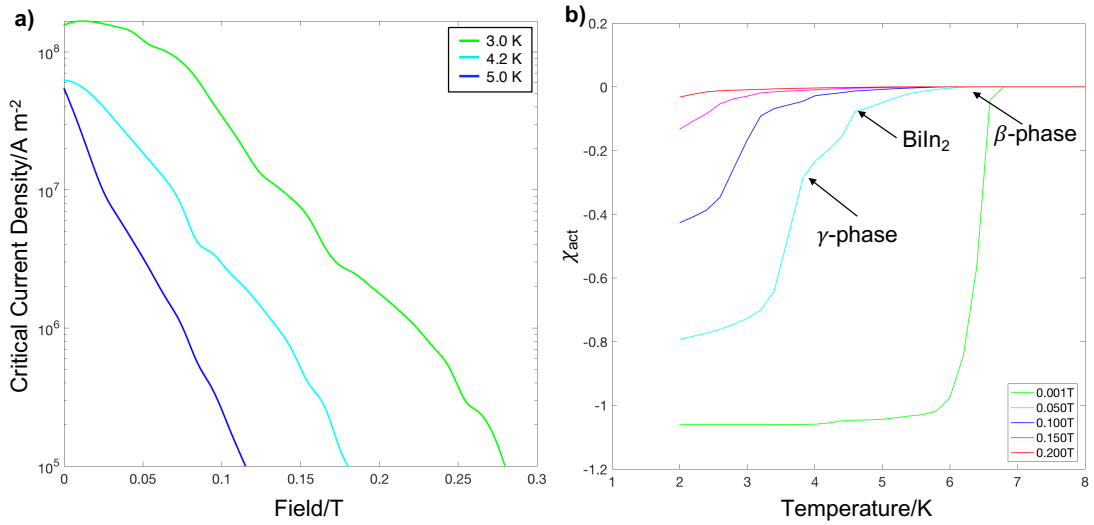


Figure 5.15: a) J_c(B) and b) $\chi(T)$ curves of $Bi_{15}In_{50}Sn_{35}$ solder cooled slowly in a brass mould

The measurements on the solder processed this way, shown in Figure 5.15 is consistent with measurements by Mousavi [43] and Brittles [33] under different cooling conditions. The B_{c2} of the solder at 4.2 K is 0.18 T and the critical temperature at 0 T is 6.7 K. As expected, the critical current density of this coarse microstructure sample is low, with J_c at 4.2 K and 0.01 T around 5×10^8 A m^{-2}. This is approximately half the value reported by Brittles and Mousavi for faster cooled samples.

The susceptibility measurements also provide an important insight into sample behaviour. The lowest field measurement suggests a susceptibility close to -1, meaning the entire sample volume is superconducting. However, as the field increases the transitions have distinct steps, corresponding to the onset of superconductivity in each of the three phases. The highest temperature region in particular (corresponding to superconductivity in the β phase), has a low moment, potentially indicating an inability for macroscale supercurrent to traverse the sample or a low volume fraction of superconducting phase, which could limit joint performance at higher applied fields.

5.3.3 Transport Measurements

Understanding the I–V properties of joints is essential to predicting their behaviour in real magnet systems. Joints were wound onto a customised steel barrel holder, and the ends soldered to the copper piece to ensure electrical contact. The rest of the wire was immobilised with vacuum grease to prevent movement under Lorentz forces that could cause a quench in the wire. The joint itself was pinned down by a piece of G10 to ease winding and allow only the ends of the wire to be soldered. The low melting point of $Bi_{15}In_{50}Sn_{35}$ meant extreme care had to be taken when soldering and preparing the sample holder to prevent damage to the joint.

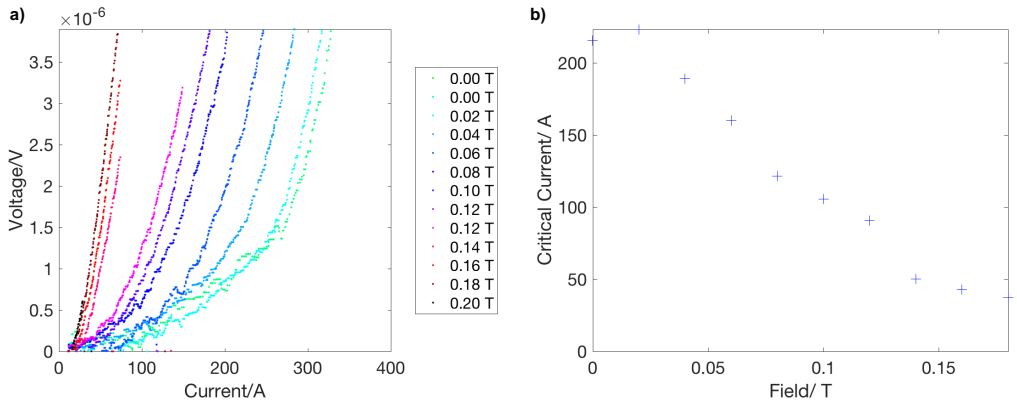


Figure 5.16: a) I–V characteristics of a cast $Bi_{15}In_{50}Sn_{35}$ joint at different magnetic fields. b) $I_c(B)$ extracted with a 1 μV criteria

Figure 5.16a shows the I–V characteristics of the joint. A 1 μV criteria was used to extract the critical current (a standard electric field criteria is not applicable to joints due to uncertainties in the length over which the voltage is generated). The extracted critical currents are shown in Figure 5.16b. As expected, the transport measurements closely reflect the behaviour of the solder, with the ability of the joint to carry current reducing significantly near the critical field of the solder at 0.18 T. At low fields, the joint demonstrates the ability to carry currents in excess of 200 A, suggesting good potential for use in future joints. However, the low critical field quickly limits this, meaning such joints would require considerable shielding and placement in extremely low magnetic field environments that are unlikely to be achievable in commercial MRI scanners. The joints may be of interest for smaller devices such as pre-clinical MRI

scanners, where the drop off in field with distance is much greater and so the necessary low-field regions are likely to exist much closer to the magnet coils.

5.3.4 Magnetic Measurements

Whilst transport measurements provide the most intrinsically real measure of wire performance, the limited sensitivity of 4-point measurements and the time involved with taking each data point limit the ability to fully understand the detailed performance of joints. The sensitivity is also a long way short of what is required to understand the persistent mode operation of such joints. As such, small scale single turn loops were also measured by VSM, allowing for variation of temperature and a considerably greater data collection rate. For this, joints were made as for the transport samples, with the only difference being that instead of two wires the joint was made between the two ends of a single piece of wire. As before, the joint was a 13×2.13 mm cast cylinder of solder around the wires. This is longer than the PbBi joints tested previously, partly to account for the expected lower critical current density of the solder, necessitating more solder to attain similar currents. The longer joint should also allow joints to be more consistent, with less random spreading of filaments along the length of the joint. The whole sample was then wound onto a former, leaving a single-turn loop to be measured.

The m–T curves for the joint in Figure 5.17a show three distinct transitions relating to each of the phases in the solder, and one extra one corresponding to the NbTi wire. These are marked in Figure 5.18 where the transitions for the different phases can be seen to occur at the same temperature in both the joint and the bulk solder. This demonstrates that the performance seen in the joint is indeed limited by the superconducting properties of the solder. Whilst the transitions occur in the same place, the shape of the two curves in field is noticeably different. This is likely to be because of the different requirements for current path across the two techniques. The joint measurement only requires current to flow from one wire to the other. There can be large amounts of the sample that do not superconduct as long as there is enough interconnected current path. When more regions of the sample become superconduct-

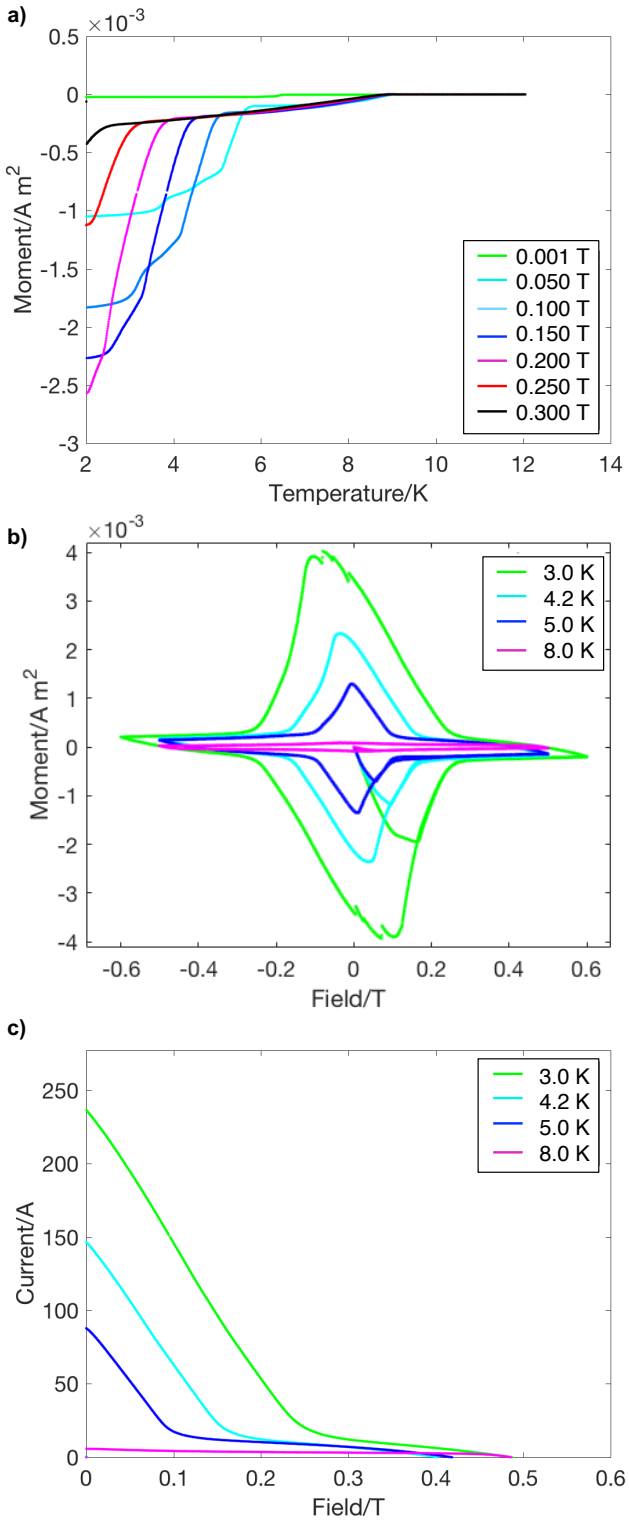


Figure 5.17: a) m–T and b) m–B loop of a cast $Bi_{15}In_{50}Sn_{35}$ joint with Supercon 54S43 NbTi wire. c) Conversion of the top right quadrant of b) into current

ing, this only affects the moment by increasing the maximum current that can flow through the joint, and hence the loop. The bulk measurement is reliant on currents circulating across the bulk for high moments, and any volume of sample not superconducting reduces the moment compared to the expected maximum moment. From the microstructure in Figure 5.14, it is clear that the bulk has long strips of the β-phase broken up by the other two phases. The joint measurement is likely to give a large signal as long as there is some continuous β-phase, but large macroscopic currents are unlikely to be able to circulate through the bulk sample until the other two phases are superconducting.

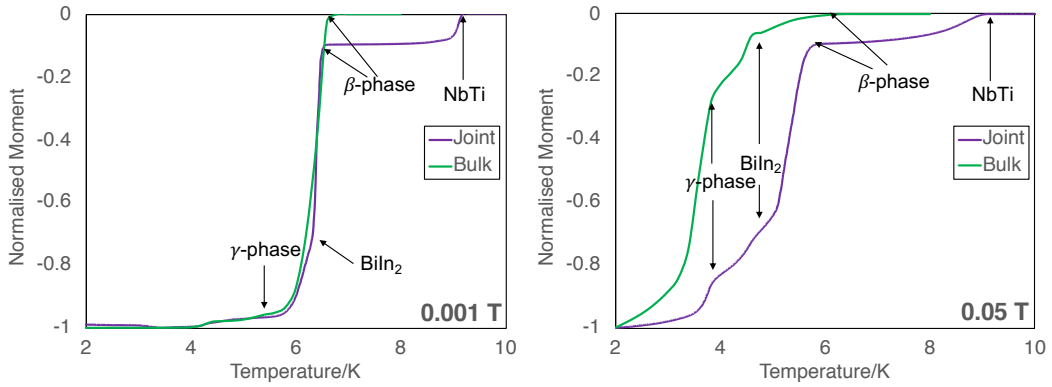


Figure 5.18: Normalised moment temperature curves for bulk solder and for the joint measured at a) 1 mT and b) 50 mT. There are three distinct features in the bulk solder, relating to each of the three phases present in the bulk, which correspond well to features in the joint. There is an extra small transition in the joint sample related to superconductivity in the NbTi wire

Figures 5.17b and c show the hysteresis loops, and the estimated current in a single turn loop to generate this signal. There is a noticeable asymmetry to the hysteresis loops, with the peak moment occurring at 0.04 T. This is likely to be due to the magnetic field generated by the current flowing through the sample (known as the self-field), particularly in the joint section. The critical field of the joint at 4.2 K is 0.16 T, slightly lower than the 0.18 T observed for the bulk solder. Extracting the critical field from the joint data is complicated by the signal given by the NbTi wire, and so it is possible that the 0.16 T is a slight underestimate. This is different to the PbBi solder joints, where the critical field of the joint was higher than expected from the bulk solder. I cannot suggest a convincing explanation for these differences. The joint

demonstrates the ability to carry a current of 150 A in zero current, enough for use in many small-scale systems. This is lower than for the PbBi joints described in the previous section, which reached 720 A before being limited by the critical current of the wire, despite those joints being 2-3 times shorter. However, from Figure 5.11c the critical current density of PbBi at 4.2 K and 0 T is approximately 3×10^8 A m^{-2}, about five times higher than the lead-free solder, so this will make up a large portion of that difference.

To see how dependent the joint performance is on the bulk properties of the solder, the bulk $J_c(B)$ from Figure 5.15a was plotted alongside the $I_c(B)$ performance of the joint in Figure 5.19a. In all the plots in Figure 5.19, the asymmetry of the hysteresis loop was removed by taking the average of the positive and negative legs, rather than just using the moment from top right quadrant. The two plots show distinctly different shapes, with the bulk solder demonstrating a sharp gradient change at 0.08 T, potentially due to one of the minor phases in the solder reaching its critical field. There is only a very slight change in the joint measurement at this point, suggesting that superconductive paths through the γ and $BiIn_2$ regions have not dramatically increased the current through the joint. A rough estimate of how much current the joint might be expected to carry can be made by assuming an area over which the current flows. As a first order estimate, this was chosen to be the cross section of the joint at its widest giving a 2×13 mm area. This comparison is shown in Figure 5.19b. At zero field, this suggests that the joint should be able to carry more than 1600 A. Even a more conservative estimate of the area for the current flow would give a much higher current than measured for the joint. One explanation for this would be that the area that can carry current is lower than expected. Yet at high fields, the agreement between the two measurements is quite close. This could be due to the calculation for the bulk sample assuming macroscopic current flow, which may not be attainable at high fields if the γ and $BiIn_2$ phases are not superconducting. This could lead to an underestimate in the superconducting performance of the bulk solder at these high fields. However, I think a more likely limitation to the joint performance is the self-field created. According to Ampere's law, any current generates a magnetic field around it. I know of no work that has

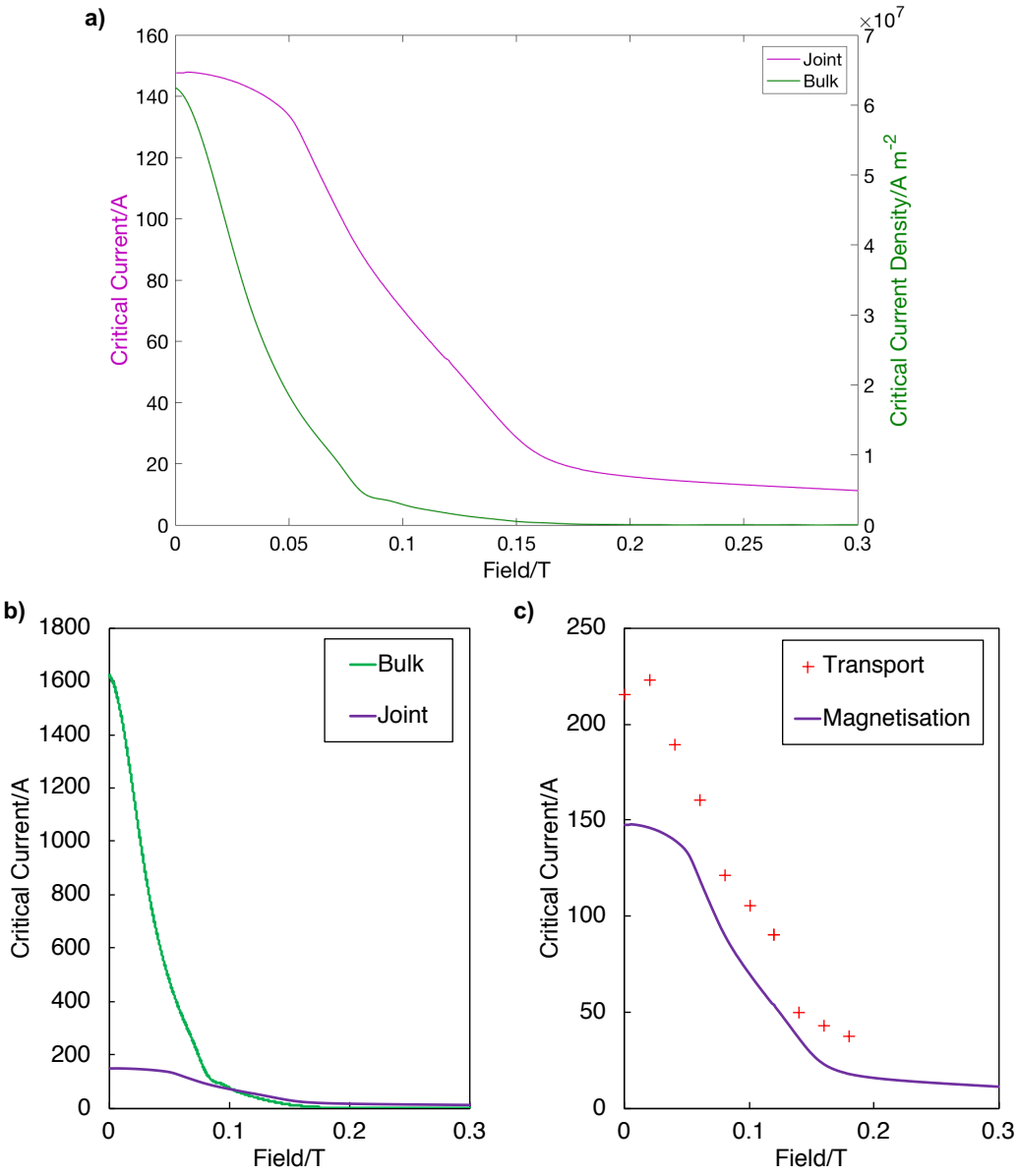


Figure 5.19: a) The joint current deduced from hysteresis loops in PPMS-VSM for a cast $Bi_{15}In_{50}Sn_{35}$ (left axis) and critical current density of bulk $Bi_{15}In_{50}Sn_{35}$ cooled under the same conditions (right axis) b) Joint current measured in PPMS-VSM and in transport for cast $Bi_{15}In_{50}Sn_{35}$ joints. c) Converting the bulk measurement into an equivalent critical current for solder of dimensions 13×2 mm and comparing with the joint performance

studied this effect in joints, however it is likely to cause problems in these low-critical field joints.

As an order of magnitude calculation, it is possible to estimate the self-field in the joints as the self-field around the wires carrying the current into the joint. Where the wire enters the joint, this can be considered simply by treating the wire as a single current carrying strand. The well-known equation for the magnetic field at the surface of an infinitely long wire is:

$$B = \frac{\mu_0 I}{2\pi r} \tag{5.1}$$

where r is the radius of the wire. Clearly, the wires in this case are not infinitely long, but it makes for a simple estimate. For a wire of diameter 0.5 mm and carrying the apparent critical current of these joints, 150 A, gives a field of 0.12 T around the wire. This is close enough to the critical field of the bulk solder to suggest it is likely to be affecting the performance of the joint, especially with extra contributions from the other wire in the joint which is likely to add to the self-field.

The calculated currents from the PPMS-VSM agree well with the results from the DC transport measurements as shown in Figure 5.19c, where measurements at 4.2 K on two cast $Bi_{15}In_{50}Sn_{35}$ joints are compared. Both joints were approximately the same size (13×2.13 mm cast cylinders), though there is likely to be slight differences in filament orientation in the joint due to spreading of filaments in the soldering process. The DC measurements give slightly higher critical currents, though this may well be due to the greater sensitivity of the PPMS measurements, equivalent to using a much lower voltage criterion for critical current in the transport measurement [127]. This difference in criteria is likely to lead to differences in extracted critical current, especially because the DC measurements show very broad transitions, meaning any change in voltage criterion has a greater effect. The favourable comparison with real-current measurements suggests that the assumptions made when extracting currents from hysteresis loops for our PPMS-VSM joint measurement technique are reasonable, and its ease, higher data collection rate and wider range of fields and temperatures make it preferable to DC

transport measurements for quick analysis of joint performance.

5.3.5 Decay Measurements

Whilst the current and magnetisation measurements on the lead-free joint show promise for joints in applications that need moderate currents at low fields, without decay measurements it is not truly possible to judge a joint's persistent-mode performance. Hence, decay measurements were performed at 4.2 K in three different background fields on the sample used for measuring hysteresis loops. The magnetic moment is converted to current, which decays as shown in Figure 5.20a. This is then normalised against the current 60 seconds after the desired background is reached to allow the magnet to stabilise to a constant field.

These decay measurements show encouraging results for the lead-free joint. Extracting a resistance with a linear fit over the final 4000 seconds of the decay gives a resistance in a 0.05 T background field of 1×10^{-15} Ω at a current of 108 A and 7×10^{-15} Ω at 49 A in a 0.1 T background field. As noted by Brittles [33] there is a contribution to the decay curves from decay of the background magnet using this technique due to the induction and background field for the measurement being provided by the same magnet. This means the measured values indicate a maximum resistance, as decay of the background field will inevitably lead to decay of the magnetic moment. Both of these values are well below the value of 10^{-12} Ω required for use in commercial MRI scanners [7,31]. This means that the joints would be suitable for use in smaller magnets where the required current is only moderate and the stray field decreases quickly [7], allowing joints to be positioned in low-field regions of the magnet. At 0.15 T, the resistance of the joint was higher at 4×10^{-14} Ω. Whilst this would still be low enough for persistent performance, the joint could only carry 4 A at this field, and it is doubtful how much of the calculated current is due to circulatory current through the joint and how much is due to demagnetising currents. Either way, this performance is not good enough for use in magnet applications, which is unsurprising considering how close it is to the critical field of the solder. This shows that whilst the $Bi_{15}In_{50}Sn_{35}$ solder can be used to make effective persistent joints for certain applications, it would require careful

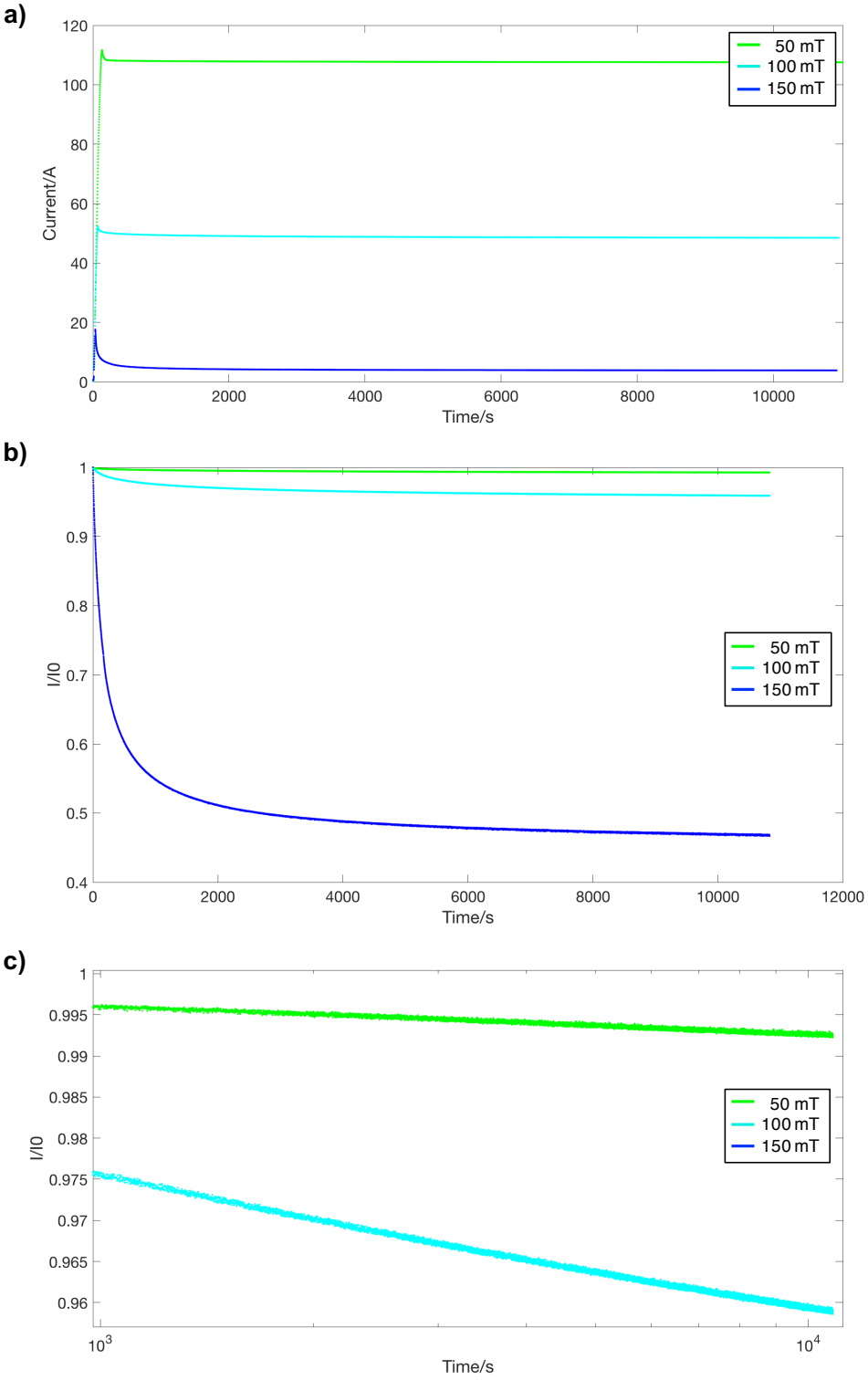


Figure 5.20: a) Current decay measurements performed in the PPMS-VSM for a cast $Bi_{15}In_{50}Sn_{35}$ joint b) These are normalised against the peak current during the decay (the current once the magnet has reached field and stabilised for 60 seconds). c) The same normalised data plotted with a logarithmic time axis. The curves are linear, suggesting a logarithmic decay

design to control the field the joints sit in. Whilst the joint is effective at 0.05 T, just increasing the field by 0.1 T would entirely restrict the ability of the joint to carry current, and even an increase of 0.05 T would halve the current that can be induced. Hence these joints are only really suitable if very effectively shielded from magnetic field or if operated considerably below their critical current.

The shape of the decay curves provides some insight into the physics of the processes involved. A sample decaying with a constant resistance would be expected to follow an exponential curve with time constant $\tau = L/R$. Figure 5.20c shows the decays curves with a logarithmic time axis. The results for $Bi_{15}In_{50}Sn_{35}$ solder joint are linear on this scale over a time period of 10,000 seconds, suggesting a logarithmic decay of the form:

$$\frac{I}{I_0} = \alpha - \beta \ln t \tag{5.2}$$

Logarithmic decays have occasionally been reported in decay measurements on superconducting joints by both Tominaka [61] and Liu [5], both for cold pressed joints. Tominaka reported a summation of two exponential decays for soldered joints, though this may be obscured by settling effects. Both Tominaka and Liu note that logarithmic decay is characteristic of losses due to flux-creep [5, 61], and so it would not be a surprise to see this in our joints as they are operating close to their critical current and temperature. However, as the measurements are close to the sensitivity limit, and the effect of background magnet decay are unclear, care must be taken before a definitive conclusion can be made as to the key mechanisms of this decay process.

5.3.6 Scaled-Up Samples

The decay rig at Siemens Magnet Technology allowed much larger samples to be measured, better representing industrial solder joints. Two solder joint samples were tested on this rig, one made from the industrial standard eutectic $Pb_{55}Bi_{45}$ and the other from our lead-free $Bi_{15}In_{50}Sn_{35}$ solder. Large wire loops for jointing were provided by Siemens Magnet Technology, with the wire produced by Bruker EAS. This wire had

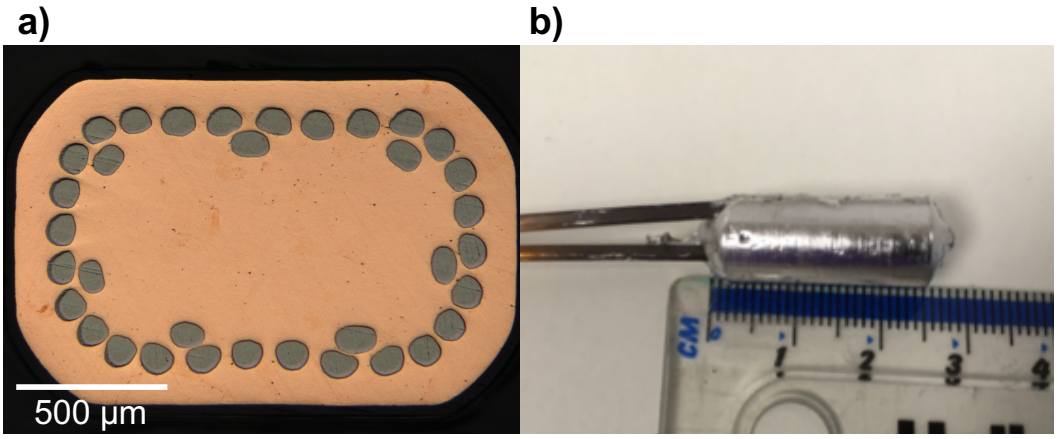


Figure 5.21: a) Micrograph of EAS wire used for decay measurements. b) Photograph of the cast PbBi joint

35 filaments, each of diameter 110 μm and arranged in a rectangular configuration as shown in Figure 5.21a. Joints were made using the matrix replacement method: 35 mm of insulation was removed then the copper stabiliser was dissolved in tin for 30 minutes at 350°C after which spreading of the wire filaments was clearly observed. The wires were soldered at 350°C for 20 minutes for the PbBi joint, and by swirling the wires in the solder for 10 minutes for the $Bi_{15}In_{50}Sn_{35}$ solder. The soldered wires were placed in a 10 mm mould and cast by pouring solder into the mould to more closely emulate industrial joint production, with the final cast shown in Figure 5.21b.

The PbBi joint was measured by inducing a current of approximately 1000 A, then leaving it for approximately three hours. The current in the loop was measured using a Hall-probe that was calibrated against the current induced initially, as described in the experimental methods chapter. During this process, the inductance of the joint coil was determined as 190 nH. The current decayed according to the curve in Figure 5.22. Fitting a straight line of form $I = I_0(1 - \frac{R}{L}t)$ to the data gave values of $I_0 = 1038$ A and $\frac{RI_0}{L} = -6.4 \times 10^{-5}$, giving a resistance of 1.1×10^{-14} Ω. This must be compared against the minimum resistance sensitivity for the decay measurement:

$$R_{min} = \frac{V_{min}}{I} = L\frac{|\delta I/I|}{\Delta t} \tag{5.3}$$

where $|\delta I/I|$ is the current sensitivity and Δt is the time period of the measurement.

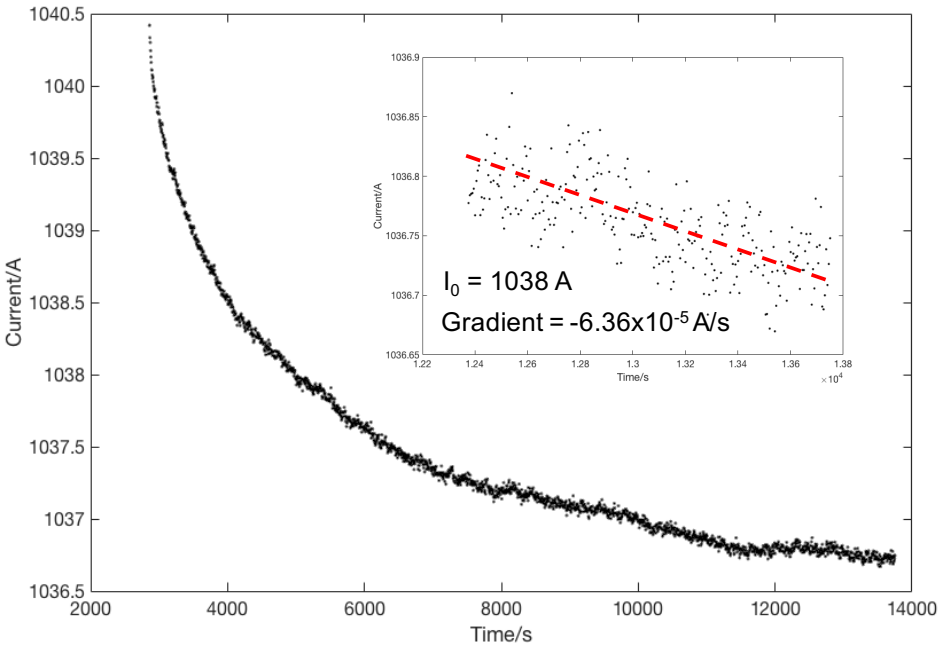


Figure 5.22: Decay measurement on large scale eutectic PbBi joint performed on the large decay rig at Siemens Magnet Technology. Inset shows a linear fit applied to the last 1200 seconds of the decay and used to extract a resistance as described in the text

From the results for the PbBi joint shown in Figure 5.22, the spread in current is approximately 0.05 A at a current of 1036 A, giving $|\delta I/I| = 5 \times 10^{-5}$. Resistance is calculated over the final 1200 seconds, giving an ultimate resistance sensitivity of 10^{-14} Ω. This sensitivity limit makes it difficult to compare with the more sensitive PPMS-VSM technique used on the small-scale joints reported in Section 5.2.4, but it is clear the joint had decayed to a resistance $\leq 10^{-14}$ Ω after an initial settling period whilst carrying a current of 1000 A. This resistance is considerably below what is required for persistent-mode operation, clearly demonstrating the success of current industrial PbBi joints.

There was a distinctly different behaviour observed in the $Bi_{15}In_{50}Sn_{35}$ joint, shown in 5.23, which again had an induced current of 1000 A and was measured over a period of 17 hours. The inductance of the sample was 120 nH. After the current of 1000 A was induced a rapid decay was observed, with the current quickly falling to around 120 A. Only after this did the decay rate considerably reduce. The resistance of the joint was calculated over the final 10000 seconds of the measurement, where the linear fit gave

$I_0 = 120$ A and $I_0 \frac{R}{L} = -3.8 \times 10^{-4}$, giving a resistance of 4×10^{-13} Ω for a current of around 100 A. The resistance sensitivity ceiling for the calculation was unchanged at approximately 10^{-14} Ω. The measured joint resistance is an order of magnitude higher than this, and therefore can be reasonably attributed to sample-related processes. This resistance is still suitably low for use in many persistent magnet systems, though the current carried is too low for use in commercial MRI magnets.

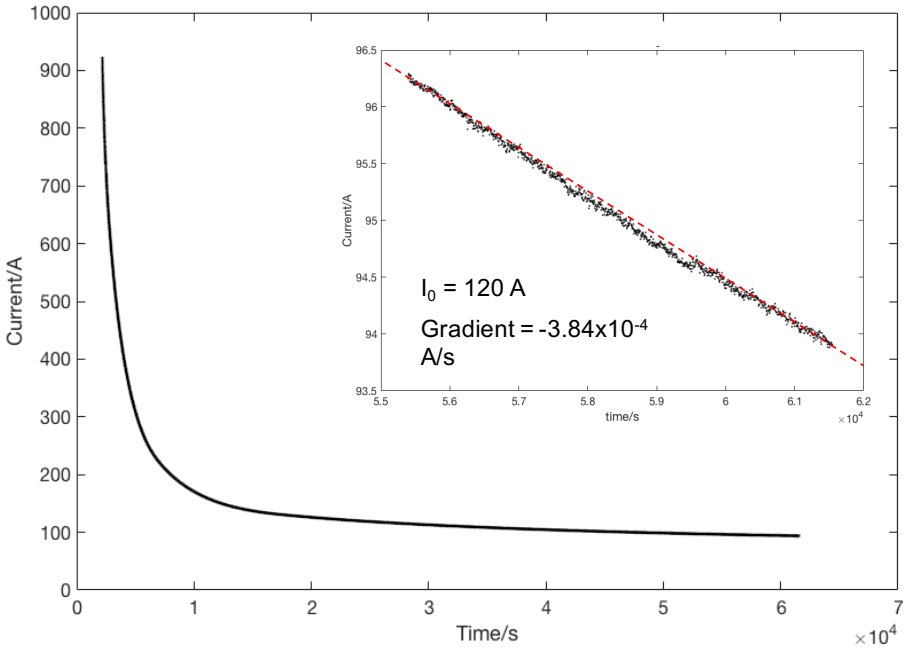


Figure 5.23: Decay measurement on large scale $Bi_{15}In_{50}Sn_{35}$ joint performed on the large decay rig at Siemens Magnet Technology. After initially inducing a current of 1000 A there was rapid decay until a stable current was formed at around 100 A. Inset shows a linear fit applied to the last 6000 seconds of the decay and used to extract a resistance as described in the text

The key problem with the performance of the joint was the inability to carry the initial 1000 A current, leading to rapid decay over the first three hours of the measurement. I have shown in the previous section that this type of joint has the ability to hold currents with persistent-level resistances, so the decay must be due to the critical current of the joint being exceeded. Only once below the critical current of the joint does the sample become truly superconducting, and so the resistance falls to the level expected from a persistent joint. This gives a rough way to interpret the critical current of the joint. This is important because the size and geometry of the joint meant it could not be

tested by transport measurements, and the large volume of low resistance solder meant that the voltages generated by the joint will be small even in the resistive state. The voltage generated in a decaying loop is simply deduced from Faraday's law as:

$$V = -L\frac{dI}{dt} \tag{5.4}$$

This is plotted in Figure 5.24, where the decay curve has been filtered to remove noise and then the gradient calculated. The scatter at currents below approximately 130 A is indicative of the voltage calculation being heavily noise affected. In this region, the sample needs to be treated as a persistent-mode sample and the voltage and resistance calculated over very long periods to avoid this noise. In the manner of transport experiments, a critical current can be extracted using a chosen criterion, in this case a 1 nV criterion on the joint gives a critical current of 157 A. This is very similar to the critical currents observed both in transport and in magnetic joint measurements for the small scale joints tested previously, where critical currents up to 150 A were observed. If the performance of the solder was limited by the bulk critical current then it would be expected that increasing the size of the joint would increase the critical current if the critical current density was constant. This is not the case, with similar critical currents observed despite a much greater joint area. It was hypothesised earlier that self-field effects could limit performance of the joint. Since this is likely to be mostly limited by the field at the surface of the superconducting wire then it will not be dramatically affected by the size of the joint, and so provides an explanation for why the current that could be trapped in the loop was so similarly low in the two different experiments.

The inset to Figure 5.24 plots the same curve as the main figure but on a linear axis. It is clear from this that the VI plot is linear with constant gradient between 130 A and 230 A, and then increases linearly with increased gradient. A possible explanation for this is that it reflects the availability of different current paths through the joint, allowing current to flow through different regions of the solder, perhaps because of the increased local self-field limiting particular current paths when the critical fields of the

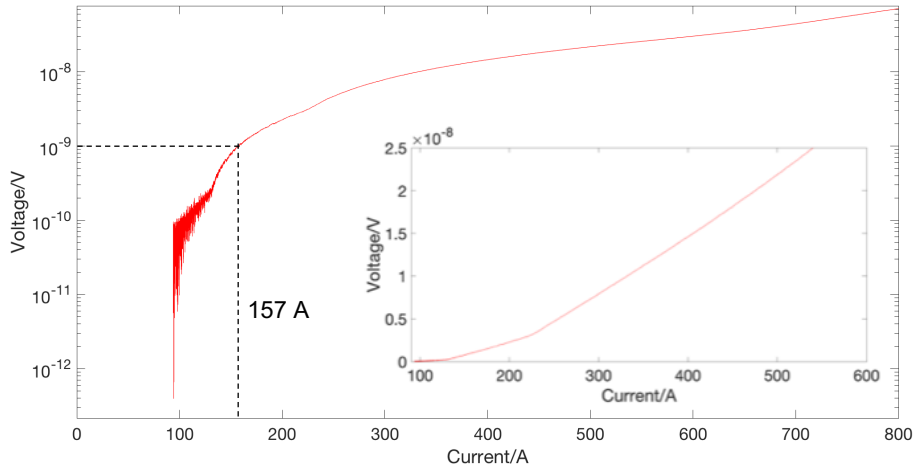


Figure 5.24: IV curve calculated from the gradient of the decay curve in 5.23 with a logarithmic voltage axis. For voltages below about 5×10^{-10} V, noise limits what voltage can be calculated. Calculating the gradient over a longer timescale as for the resistance measurements would help alleviate this, though that is not done here as it would induce errors in the fast-changing early section of the decay curve. A 1 nV criterion can be used to extract a critical current of 157 A. The inset shows the same plot with a linear voltage axis. There are two distinct transitions in this plot between different regimes at around 130 A and 230 A

different phases of the solder are exceeded.

5.3.7 Conclusions on Lead-Free Joint Measurements

This section presents a detailed characterisation of joints made using the best lead-free $Bi_{15}In_{50}Sn_{35}$ solder currently known in the literature, the first time such a characterisation has been performed for lead-free solder joints. Good agreement is found between transport critical currents and those extracted from magnetic measurements. At zero field, critical currents of around 150 A are found, both for the small-scale joint and for a scaled up version using a decay-based method. This is considerably less than expected from the solder J_c, and it is suggested that self-field from the joint could be the limiting factor.

Decay measurements demonstrate the ability to carry persistent currents in excess of 100 A in low fields, which would make it possible to implement these joints in some small magnet systems. However, there is a sharp decrease in performance with background field, meaning joints would have to be exceptionally well shielded and placed far from

the magnets. The inability even in large joints to attain persistent currents over around 150 A is significant for use in commercial MRI, where a typical joint must carry in excess of 500 A. This current will cause large self-fields, and so development of techniques with higher critical field is essential for the future. As there is no known lead-free solder with better field performance than $Bi_{15}In_{50}Sn_{35}$, a different approach to achieving higher fields is required.

5.4 Chapter Conclusions

In this chapter, essential performance issues of the three main components of joints have been analysed. The first section considers the wires, demonstrating that the heat treatments during matrix-replacement soldering are close to causing irrecoverable damage to the wire. When designing such a heat treatment, it is best that the temperature is kept below 350°C, though short times up to 375°C may be acceptable, especially for joints that only take low currents. This has a much starker warning for diffusion bonded joints where heat treatments at temperatures in excess of 400°C for extended time periods are commonplace [4, 73], which is shown to lead to degradation of wire critical current, especially at high magnetic fields.

The interface between joint and wire is also shown to have a significant effect on persistent mode performance. A thin niobium diffusion barrier is shown to dramatically increase wire resistance at magnetic fields above $B_{c2,\,Nb}$. This is only apparent through the use of decay measurements, and so care must be taken when using less sensitive techniques that there is not a small-scale resistive interface. Whilst not a problem in PbBi solders, the development of any future solder should carefully consider the nature of the interface between wire and solder, as this is also required to be superconducting for truly persistent performance.

The final section presents a detailed characterisation of a lead-free $Bi_{15}In_{50}Sn_{35}$ solder joint, comparing the properties of this joint with the bulk performance of the solder. It is found that the low critical-field of the bulk is problematic, leading to self-field limiting of the joint critical current. As such, in the hunt for a viable future lead-free joint, it is

essential to look for materials with high critical field to allow the true potential of the joint to be attained.

Chapter 6

A Novel Composite Solder

Even the best performing lead-free solder lacks the critical current and critical field for use in MRI magnets, and joints made from this are potentially fundamentally limited by the self-fields generated around the wires. As such the development of new solder-like materials with improved performance is key. In this chapter, the development of a novel composite superconductor is described. In this system, a lead-free superconductor with low melting point is used as a matrix, with long filaments of high-performance superconductor used as the main current-carrying elements of the jointing material.

This chapter starts by describing the development and processing of this novel system. The superconducting properties of the composite alone are then considered in detail, before finally the performance of some initial joints is presented.

6.1 Concept

As seen in both the literature [40, 51] and in Chapter 5, there are no lead-free solders suitable as a drop-in replacement for PbBi. All known alternatives have considerably lower critical current density and critical field than PbBi, making them unfeasible on a design level for MRI implementation. Furthermore, the low critical fields values are of similar size to the self-fields expected around a current carrying wire, potentially acting

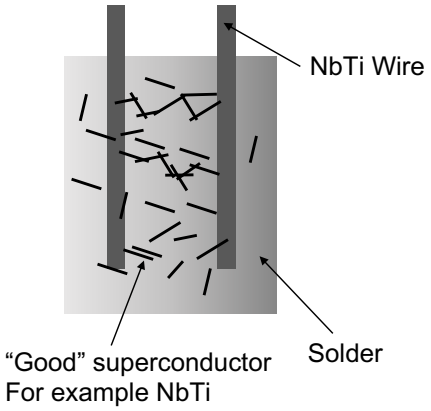


Figure 6.1: Schematic of composite solder. A low-melting point matrix allows ease of processing, whilst the strongly superconducting inclusions act to provide high J_c current paths between the wires

as a fundamental limitation on the amount of current, as opposed to current density, a lead-free solder joint could carry. Previous work in Oxford has revealed few new options for lead-free solders [43,46,55], with no material with low melting temperature obviously having a higher critical field than the current best lead-free solder $Bi_{15}In_{50}Sn_{35}$, let alone the currently used PbBi solders. The only metallic materials with higher critical fields are based around refractory metals such as niobium and tantalum, which have melting points considerably too high to make melt-processed joints.

My solution to this problem was to manufacture a composite solder, with particles of a "good" superconductor mixed into a low melting-point matrix. Much like a conducting polymer, where conducting material is loaded into a polymer matrix to give the electrical properties of the filler and the mechanical properties of the polymer, the composite solder aims to maintain the low melting temperature and ease of formation of standard solders, but have superconducting properties dominated by the filler network. This is shown schematically in Figure 6.1. The key to this is achieving percolation, where there is a high enough fraction of inclusions to form an effectively interconnected network. The loading fraction beyond which this network behaviour is observed is known as the "percolation threshold". Percolation theory suggests that high aspect ratio particles have lower percolation thresholds, with a volume fraction of inclusions below 1% required for ellipsoidal inclusions with aspect ratio of 100, as compared to 28% for spherical inclusions [178]. Thus it is clear that the optimal inclusion for the composite

system is long and thin. The inclusions ideally must also have high critical current to allow for good current transport throughout the composite even with low volume fractions of inclusion. The fine filaments of commercial NbTi conductor perfectly fulfil these requirements. The matrix must primarily have a low melting point so that joints can be formed without damage to the NbTi wires or inclusions. For the composite to work, there must also be minimal reaction between the inclusions and the matrix. Whilst not essential, a matrix that is itself a superconductor is beneficial as it will be able to carry supercurrent at low fields. As such, the current best-known lead-free solder $Bi_{15}In_{50}Sn_{35}$, with its low melting point of 78°C and reasonable superconducting properties makes the ideal initial choice as a matrix material.

6.2 Production

6.2.1 Preparation of Filaments

The conductor used to provide the inclusions for the majority of work in this chapter was a multifilamentary wire from the LHC project at CERN labelled LHC 46-B. This contained approximately 12,000 filaments of diameter approximately 3 μm and a copper:superconductor (Cu:SC) ratio of 3. Some composites were also made using LHC-Type 02 wire, which was a more conventional LHC conductor with approximately 6000 filaments of diameter 6 μm and a Cu:SC ratio of 2. Instead of a polymer coating for insulation, the wires instead were coated in a thin layer of Sn-Ag solder. The narrow filament diameter offered the high aspect ratios desired for the composite, whilst the high filament count and low Cu:SC ratio meant high loading levels of filament could be easily achieved.

The first step in the composite production was to coat the filaments for the filler in the matrix solder, much as when forming a conventional solder joint. The results from Chapter 4 have shown that NbTi is highly reactive metal, with any exposure of the filaments to air leading to oxidation of the NbTi and so poor wetting of solder to the filaments, potentially forming a barrier to superconductivity. As such it was necessary to prevent the filaments ever seeing air during the processing. The Thornton matrix

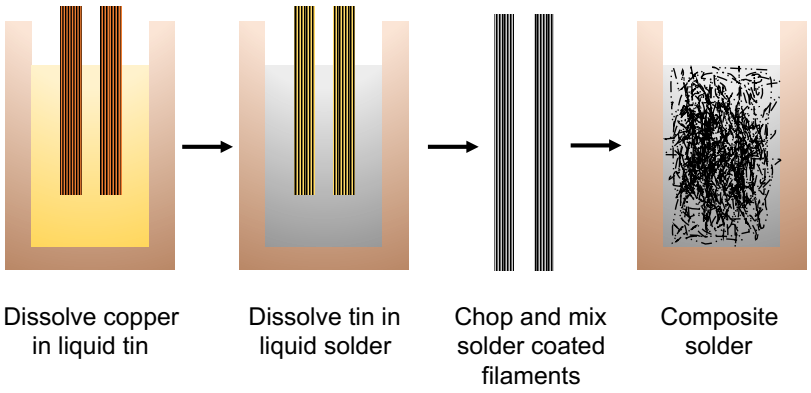


Figure 6.2: Schematic of composite solder production. The NbTi wire providing the filaments has its copper matrix dissolved in liquid tin at 350°C and then this is dissolved in solder at 350°C

replacement method [6] was ideal for this, allowing the copper to be displaced first by liquid tin, which also displaced the silver-tin solder outer coating, and then the low melting point solder desired for the matrix material. It was found that the very fine filaments and narrow copper regions meant that the tinning process was extremely slow, so much longer times were required for infiltration of tin and solder into the LHC wires than for the joints made with coarser filaments in Chapter 5. The final method for coating the filaments, illustrated in Figure 6.2 was:

1. Place filaments in liquid tin at 350°C for 45 minutes to dissolve copper matrix of the conductor and coat filaments with tin.

2. Place tin-coated filaments in liquid solder at 300°C for 30 minutes to dissolve tin and replace with solder.

This allowed for reliable removal of the copper, whilst limiting the time and temperature of heat treatment as much as possible to prevent damage to filaments or formation of reaction layers that might inhibit performance of the composite. It was found that stirring the tin and solder every 10 minutes was essential, otherwise the liquid tin and solder would not infiltrate to the centre of the conductor. This also helped break apart the bundle structure of the conductor as can be seen in Figure 6.3, which allowed for greater randomisation of filaments in the composite and so increased the chance of forming a percolative network [178].

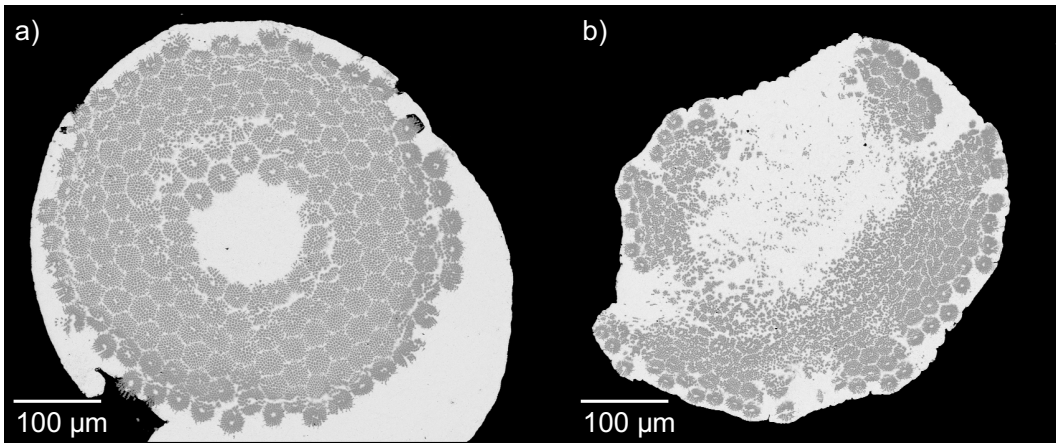


Figure 6.3: Backscattered SEM images of LHC 46-B wire immersed in liquid tin at 350°C for a) 15 minutes with little agitation still clearly shows the original bundle structure of the wire b) 60 minutes in tin with lots of agitation allows filaments to break out from the bundle structure. The white regions are tin and the grey regions are the NbTi filaments.

6.2.2 Composite Consolidation

Once the filaments were coated in solder, they were placed back into the solder bath and agitated to encourage filaments to spread out from their original bundled structure. This was found to greatly increase the randomness of orientation in the final composite. After removal from the solder-bath, the solder coated wires chopped by hand into small pieces < 1 mm in length. These were then melted together into a small crucible and stirred to form the composite network. Samples were cast into a 2.13 mm diameter cylinder in the brass mould shown in Figure 5.13 to allow a consistent sample geometry suitable for magnetisation measurements. For this, the mould was heated to 100°C on a hotplate and the composite pushed in from the top. The composite was more viscous than typical solder, and so had to be lightly pressed down into the mould to ensure the best casting. The hot mould was then removed from the hotplate and allowed to cool slowly back to room temperature. This procedure was used for all composites, with slight adaptions to the casting temperature when matrix materials with different melting temperatures were used.

The consolidated composite behaved more like a paste than a true liquid whilst molten – it could be easily shaped and moulded when above the melting temperature of the

matrix, but the tangled filaments meant it kept its shape much more than would be expected for a liquid. Some care had to be taken; matrix material was lost if heated above its melting temperature for extended periods as the liquid phase slowly flowed out of the composite.

6.2.3 Microstructure

To understand the microstructure of the composite, 2.13 mm cylindrical samples cast as described in Section 6.2.2 were mounted in cold-set epoxy, ground with SiC grinding paper then polished down to a final stage using 1 μm diamond suspension to prepare them for scanning electron microscopy.

The backscattered SEM image in Figure 6.4a demonstrates the type of microstructure desired from the composite. The NbTi filaments show little sign of the original bundle structure, and show at least some randomisation in direction, with many filaments of lengths of a few hundred microns running in the plane of the image as well many running out of the plane. It is possible to make a first-order estimate of the angle of the filament to the image from the shape of the filaments as shown schematically in Figure 6.4b, with the angle the filament cuts the image plane given by $\cos\theta = r/l$ where r/l is the aspect ratio of the filaments in the plane of the image [179]. This was calculated for Figure 6.4a by manually thresholding in ImageJ then using the particle analysis tool to calculate the aspect ratio of each filament, and is shown in Figure 6.4c. This analysis assumes the filaments are perfectly circular, which in reality is likely not to be true, explaining the drop-off at low angles. The fact that the filaments aren't rigid means that the angle will vary along the length of the filament, meaning relatively few will lie fully in the image plane for long lengths, meaning the number observed at high angles is also reduced. A full analysis of this type is beyond the scope of this work, but as a first order estimate it suggests there is a wide distribution of filament directions in the composite, which is desirable for percolation. This region of the composite has a high proportion of NbTi filaments (an area fraction of $\approx$25% estimated by thresholding in ImageJ), above the level of loading expected for percolation, and low porosity.

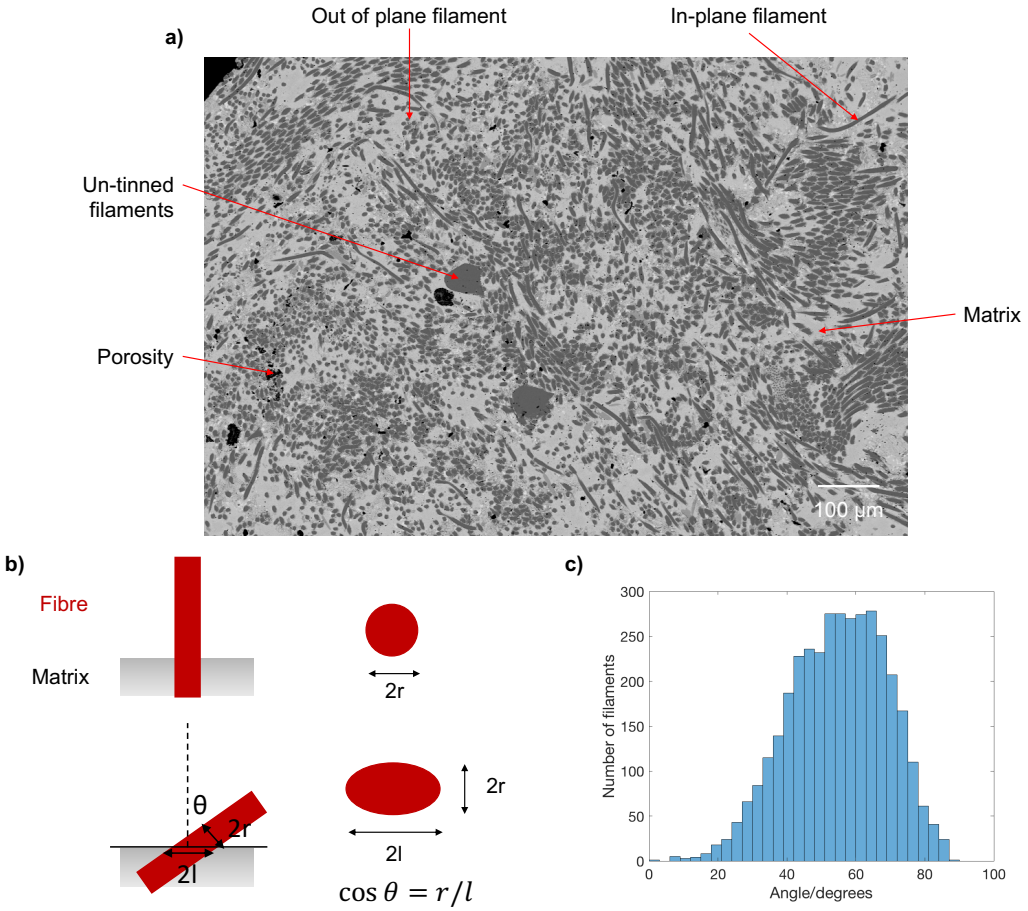


Figure 6.4: a) Backscattered SEM image of a composite with LHC Type-02 NbTi filaments and a $Bi_{15}In_{50}Sn_{35}$ matrix, typifying the desired microstructure for solder matrix composites. b) Schematic of filaments crossing a plane of the matrix and the projection of this in plan view. Based on this the approximate angle of the filament to the plane of an image can be calculated, shown for this image in (c)

Unfortunately, the small-scale production of the composite led to large variations in the microstructure, with many regions exhibiting little NbTi or bundling of the filaments. Pores could form where the solder had not consolidated well and many samples had regions including filaments with incomplete removal of the copper matrix. This variability made correlating properties such as filament proportion with superconducting properties impossible. Most of these problems were symptomatic of the small-scale of the production process, and could be minimised by employing scaling-up techniques used for many thixotropic solids, particularly involving applying high shear stresses to the melt [180], but this process optimisation was beyond the scope of this project.

Chemical analysis of the composite in Figure 6.5 reveals the same three matrix phases

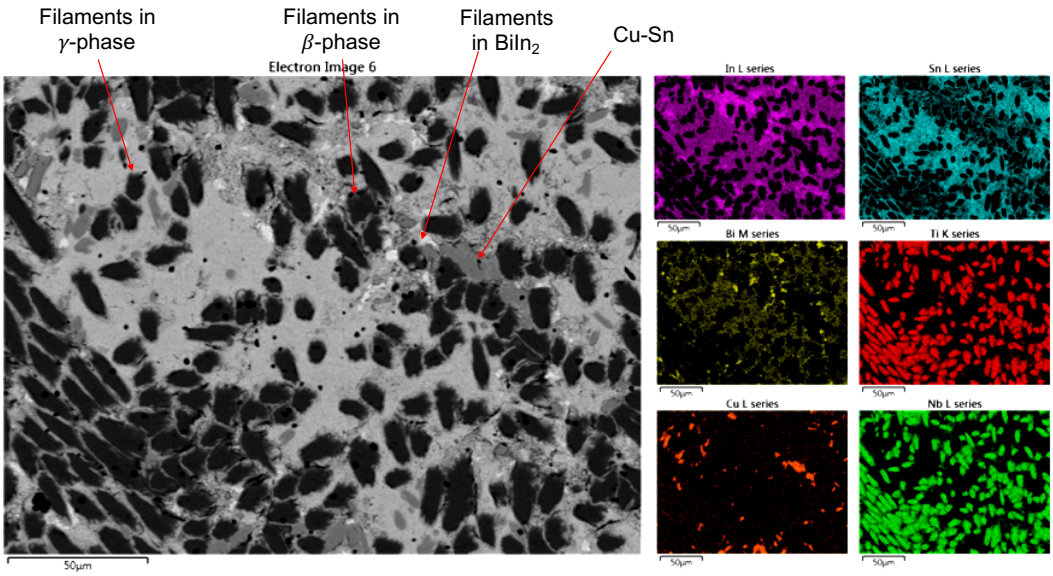


Figure 6.5: Backscattered SEM image of a composite with LHC Type-02 NbTi filaments and a $Bi_{15}In_{50}Sn_{35}$ matrix and energy dispersive x-ray maps of each of the main elements found in the composite over the same region

as detailed in the previous chapter for the bulk solder (the indium-rich β phase, the tin-rich γ phase and a $BiIn_2$-based phase) and there is no reason to expect the presence of the NbTi to change this. From the chemical maps it is clear all three of the main phases can be found in contact with filaments rather than one phase nucleating preferentially at the NbTi surface. This particular composite has small copper-tin precipitates, formed during the first tin-scavenging stage of composite formation. With coarser filaments, these are normally left in the tin-bath, but the extremely fine, tightly bundled nature of the fine-filament conductor makes it more likely that some of these copper-rich precipitates will be trapped. Ultimately, there is nothing in the microstructure that would be expected to cause significant problems for the transfer of current between the filaments and the matrix.

6.3 Bulk Superconducting Properties

As with any new solder for joint-making, the first key step is to understand the bulk performance of the material. This is particularly important with this composite solder consisting of two separate superconducting components, where the performance may be

dominated by either of the main components. To assess this, I used a variety of different techniques, including low current transport measurements and multiple magnetisation techniques, allowing the properties of the composite to be understood.

6.3.1 Resistivity Measurements

Perhaps the simplest way to probe a material's superconducting properties is by 4-point transport measurements, where a small current is applied across the sample and the voltage this produces is recorded as a function of magnetic field or temperature. In the superconducting state the resistivity of the sample is zero, so only once outside the superconducting state can a voltage be measured, allowing $B_{c2}(T)$ data to be determined. A composite solder sample with a $Bi_{15}In_{50}Sn_{35}$ matrix and LHC Type-02 NbTi filaments was prepared in the standard wire then cut to an approximately 2×2.13 mm cylinder. The ends were ground with coarse SiC grinding paper to ensure they were flat. A sample of just the $Bi_{15}In_{50}Sn_{35}$ matrix was cast in the same way. Both samples were simultaneously mounted onto the rotator sample holder of the Quantum Design PPMS and measured using the electro-transport option with an AC measurement current of 10 mA.

Temperature sweeps were performed by cooling the sample to 2 K, applying the required field, then sweeping the temperature up to 16 K and back down to 2 K all at 0.5 K min^{-1}. Figure 6.6 plots the warming curves, though no differences to these results were found for the cooling curves. The composite and the matrix-only sample demonstrate very different behaviour. The matrix, as expected, shows a critical temperature in good agreement with the magnetisation data presented on a similar sample in Figure 5.15b, whilst the critical temperature of the composite varies only slightly with applied fields and closely relates to the critical temperature of NbTi at 9.2 K [173]. The normal-state resistivity of the composite is approximately twice that of the solder alone. Both resistivity values are similar to those presented by Tsui [181] for $In_{48}Sn_{52}$ solder (9×10^{-8} Ω m at 10 K) and for $Bi_{57}In_{26}Sn_{17}$ (4.1×10^{-7} Ω m at 77 K).

A similar result was observed when the field was swept at a constant temperature to

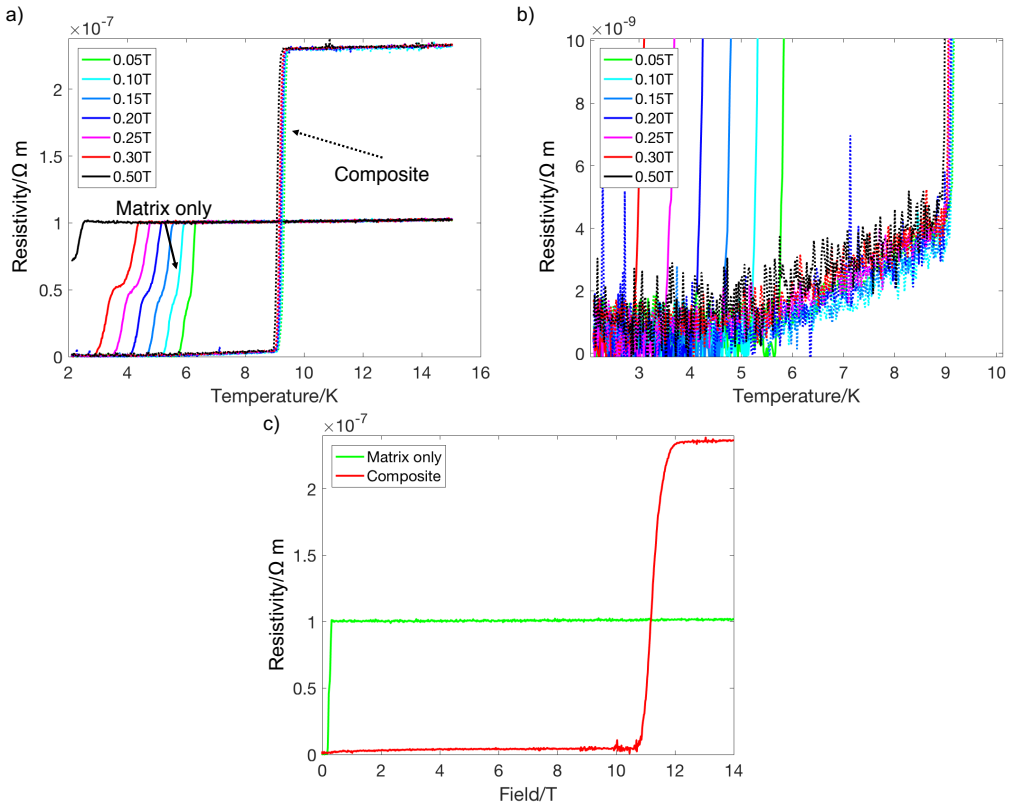


Figure 6.6: a) Resistivity against temperature plots at different fields of composite NbTi/$Bi_{15}In_{50}Sn_{35}$ (dotted) and $Bi_{15}In_{50}Sn_{35}$ only samples prepared as described in the text. The matrix-only sample demonstrates significant reduction in critical temperature with applied field, whilst the composite behaviour is dominated by the higher critical temperature and field of NbTi. b) the low-resistivity region for the composite solder in more detail, where the composite seems to slightly increase in resistivity with temperature. c) Resistivity against applied field for the same samples at 4.2 K. Again, the composite behaviour is dominated by NbTi whilst the matrix-only sample is limited by the low critical field of $Bi_{15}In_{50}Sn_{35}$

16 T and back to zero at 5 mT s^{-1}. Figure 6.6c shows the data for the matrix-only and composite sample measured as the field was removed at 4.2 K. Again, the transition in the matrix-only sample at approximately 0.18 T corresponds to the critical field of the $Bi_{15}In_{50}Sn_{35}$ solder, whilst the transition in the composite at around 11 T corresponds to the critical field of the NbTi.

In both the temperature and field sweeps, the composite solder resistance does not entirely drop to zero. This is well illustrated in Figure 6.6b which shows the low-resistivity region of the ρ–T plots in more detail, where a linear increase in resistivity is apparent above 5 K. One possible reason for this is that there are small resistive

sections that current must flow through, for example between filaments. However, it is clear in Figure 6.6b that this region follows a relatively field-independent increase in resistivity. Were the increase due to current-flow through the resistive matrix, the linear increase resistivity would be expected to closely match the performance of the matrix, with the resistivity increase starting as the solder transitions. This is not what is observed, and so the increase is most likely an experimental effect, potentially due to a slightly poor current or voltage contact.

These results are strongly indicative that there is a viable superconducting current path in the composite through the superconducting filament network, with the composite performing as would be expected if the majority of current is carried in the NbTi matrix rather than having any influence from the matrix. This is extremely promising for the composite solder, suggesting that it is possible to achieve the desired superconducting current paths through the matrix. However, it is worth noting that these low-current measurements are highly "filamentary" – the applied currents are low enough that if there is even one current path through the sample then the resistance will be measured as zero (the critical current of each filament, for example 100 mA at 4.2 K and 6 T from data supplied by the manufacturer, is much greater than the measurement current of 10 mA). At lower applied fields the critical current of each filament will be higher. In the case of the composite it is also possible that any junction resistances are too small to be detected.

6.3.2 Magnetisation Measurements

The low-current transport measurements indicate that there is superconductivity across the sample in along at least one path. However, these measurements are not necessarily reflective of bulk effects and so it is necessary to investigate the composite samples by other means. Magnetic measurements are sensitive to both superconducting effects in localised regions and across the entire sample, so are ideal for this. 2.13 mm cylindrical samples prepared in the standard way were cut to approximately 2 mm in length and the ends ground flat with SiC grinding paper. Magnetisation measurements were performed in the PPMS-VSM by mounting the cylinder in a brass sample holder fixed

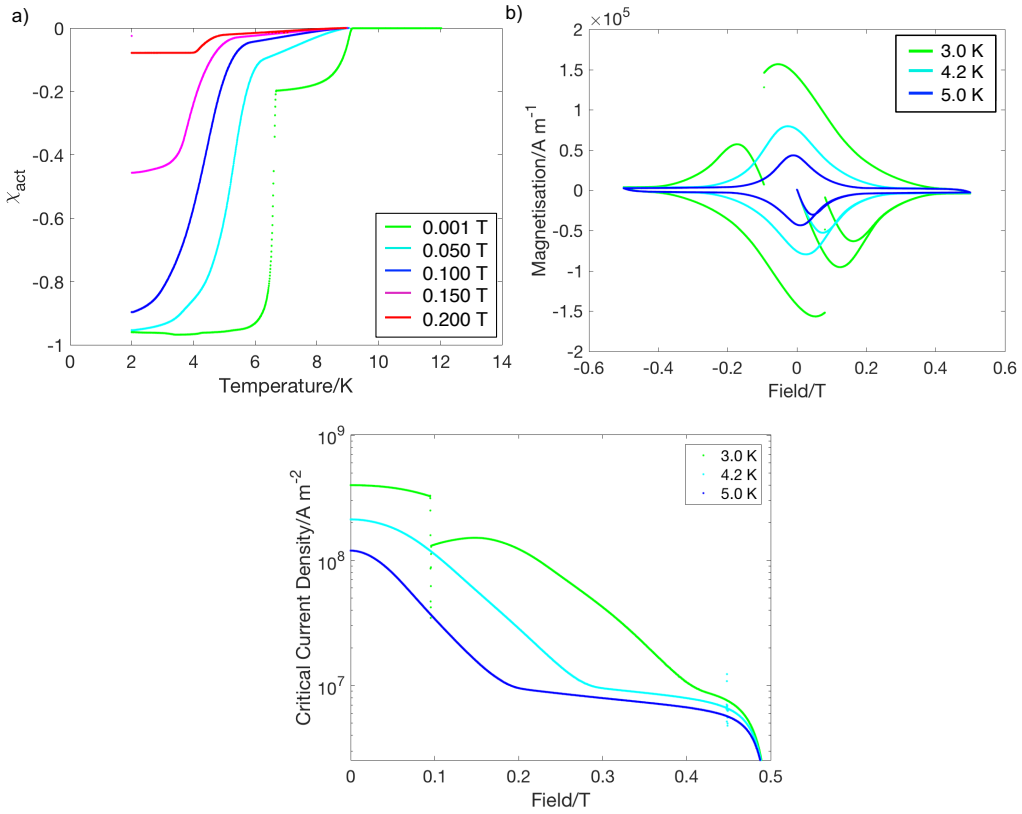


Figure 6.7: a) $\chi(T)$ curves for composite $Bi_{15}In_{50}Sn_{35}$ solder with 6 micron LHC Type-02 NbTi filaments at different applied fields b) Magnetic hysteresis loops for the same sample at different temperatures c) Calculated critical current densities assuming bulk current flow

between two pieces of quartz.

The $\chi(T)$ curves are shown in Figure 6.7a. In the 1 mT measurement there are two distinct transitions: one at 9.1 K corresponding to the critical temperature of NbTi and a second at 6.7 K corresponding to the critical temperature of $Bi_{15}In_{50}Sn_{35}$. This additive effect of the two components is to be expected in the low-field regime, where both components are in the Meissner state, with perfect expulsion of magnetic flux. Below 6.7 K the susceptibility is close to -1, suggesting that the whole sample is superconducting at low temperatures. Between 6.7 and 9.1 K the susceptibility is around -0.2, suggesting a rough superconducting volume fraction of 20%. This is a loose approximation of the fraction of NbTi present, as the NbTi filaments are the only superconducting components at that temperature. However, large-scale connectivity of the NbTi network would lead to increased shielding of the central region, leading to increased susceptibility, so this can be considered a minimum volume fraction. At higher applied fields there

is a linear increase in susceptibility between 9.1 K and a lower temperature, where the susceptibility starts to suddenly increase dramatically. In these fields the superconductor is in the mixed state where flux penetrates the sample as temperature is increased, leading to non-constant susceptibility. The transition to a large susceptibility corresponds to the onset of superconductivity across a bulk region of the sample, indicating that the matrix of the composite has become active.

Similar features are seen in the hysteresis loops shown in Figure 6.7b. At low fields for all three temperatures measured the sample demonstrates a very large magnetisation. This drops to a much lower value as field is increased and then levels out, but the loops do not quite close at higher fields right up to the maximum applied field. This is perhaps clearer when plotting the Bean-model calculated critical current density on logarithmic axes in Figure 6.7c. The critical current density decreases approximately linearly on the semi-logarithmic plot, and then flattens out to a much shallower gradient. Magnetic measurements are sensitive to all the components in a sample, so this behaviour is again indicative of a transition from superconductivity just in the filaments to superconductivity in the bulk of the composite. In this higher field regime, the magnetic measurement will detect only the moment created by currents flowing in the individual filaments as the matrix is no longer superconducting. It is important to note the low critical current density of this regime; the filaments alone are capable of critical current densities well in excess of 10^{10} A m^{-2}. However, the critical current calculation assumes that currents can flow around the entire bulk. Whilst this might be the case if the composite behaved as originally predicted, it seems as though current loops are restricted to existing just in individual filaments at these high fields. The sharp increase in critical current density at lower fields indicates a transition to a regime where currents circulate in the entire bulk.

Predicting the moment expected from the filament network alone is difficult due to the randomised directions and length, however it is possible to do a quick calculation of the moment expected from a single filament radius, r_f, and height, h_f, oriented parallel to the applied field by using the Bean model approximation for the critical current density of a superconducting cylinder [123]. Multiplying this by the number of filaments, N,

allows the expected moment from the filaments alone to be estimated as:

$$\Delta m = N\frac{2\pi r_f^3 h_f J_{c,NbTi}}{3} \tag{6.1}$$

Taking approximate values of N = 60000, $J_{c,NbTi} = 10^{10}$ A m^{-2}, $r_f = 3$ μm and $h_f = 500$ μm gives a moment of 2×10^{-5} A m^2. The moment measured for these samples in the high field can be seen in Figure 6.9 to be 5×10^{-5} A m^2, of the order of magnitude calculated. Filaments lying at high angles to the applied field will contribute a larger moment due to the increase in surface area in the plane perpendicular to the applied field, and so it is unsurprising that the measured value is high compared to the calculated value. However, the fact that the two are similar suggests that currents are indeed restricted to flowing only in individual filaments.

Characterising the fields and temperatures at which these transitions to bulk behaviour occur is not necessarily as clear, though the important thing is to define a consistent regime. A simple method for calculating the temperature of the transition involves taking a linear fit for the $\chi(T)$ data at a sufficiently high field that just the NbTi is superconducting. I will define the critical temperature for bulk superconductivity in these samples as the temperature at which the susceptibility deviates from this straight line as shown in Figure 6.8a. A similar process is possible for extracting critical fields from $J_c(B)$ plots, where a straight line is fitted on a logarithmic current scale. Deviation from this marks the onset of superconductivity in the bulk of the sample as shown for 4.2 K in Figure 6.8b. In theory the $B_{c2}(T)$ and $T_c(B)$ data should be interchangeable, which is seen in Figure 6.8c where plotting both extracted values together reveals consistent results, suggesting that the criteria used for extraction of the critical values are consistent.

It might be expected that the transition to bulk-like behaviour occurs at the critical field or temperature of the $Bi_{15}In_{50}Sn_{35}$ matrix; when the matrix starts superconducting a sudden increase in the length scale of the current paths is to be expected as current can flow through the entire sample. However, it is immediately apparent from Figure 6.9b that the transition to bulk-like behaviour occurs at a higher field than the critical

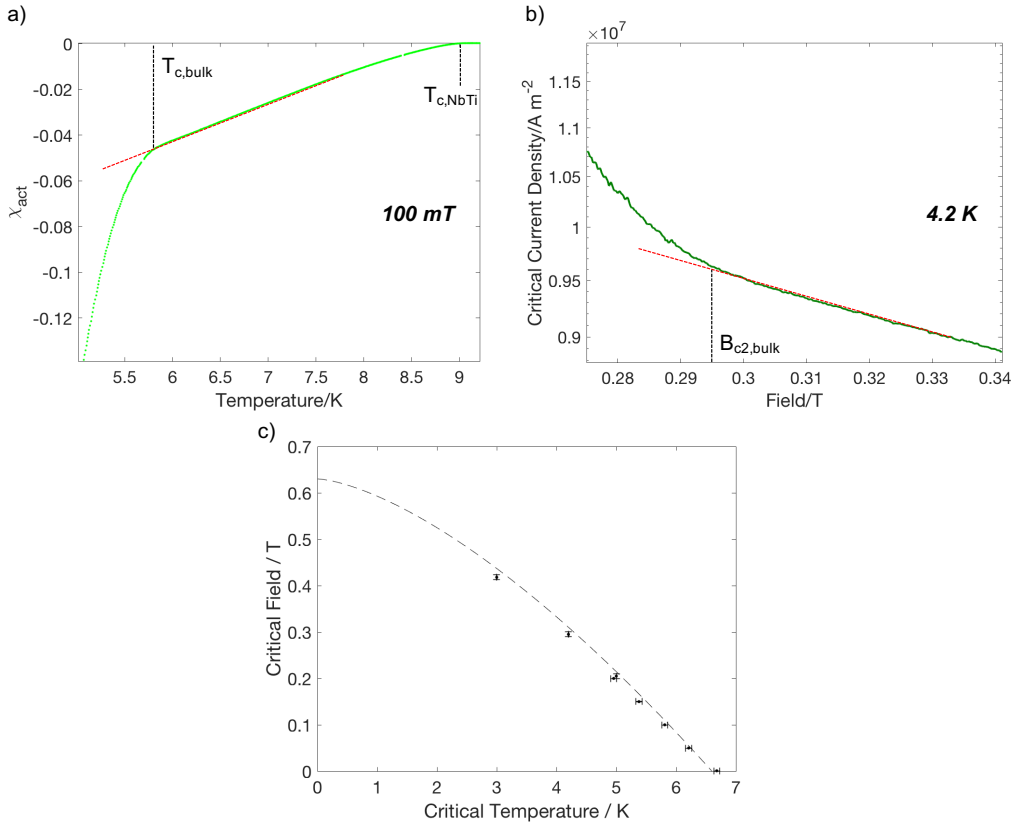


Figure 6.8: a) Critical temperature extraction for bulk superconductivity from a $\chi(T)$ measurement at 100 mT in composite $Bi_{15}In_{50}Sn_{35}$ with 6 μm diameter NbTi filaments b) Critical field for bulk superconductivity extracted for the same sample from the $J_c(B)$ curve at 4.2 K plotted on semi-logarithmic axes c) Plot of the critical fields and temperatures for bulk-like behaviour for the composite solder. The data from field sweeps (vertical error bars) and temperature sweeps (horizontal error bars) appear consistent. The dashed line shows the fit determined for the B_{c3} of $Bi_{15}In_{50}Sn_{35}$ solder by Brittles [33]

field of the matrix. For example, at 4.2 K the critical field for bulk behaviour is 0.29 T compared to the critical field of 0.18 T for $Bi_{15}In_{50}Sn_{35}$ alone. A similar story is seen in the temperature sweeps in Figure 6.9a, where there is a change in susceptibility at temperatures where the susceptibility of the matrix alone should be zero. This suggests that large currents are able to flow through the whole of the filament network in the composite at temperatures and fields beyond what could be contributed by just the matrix phase "turning on".

Interestingly, the onset temperature at which the composite transitions to bulk behaviour appears very close to the temperature at which that the magnetic moment of the solder-only sample first becomes zero. The $\chi(T)$ performance of this solder-only

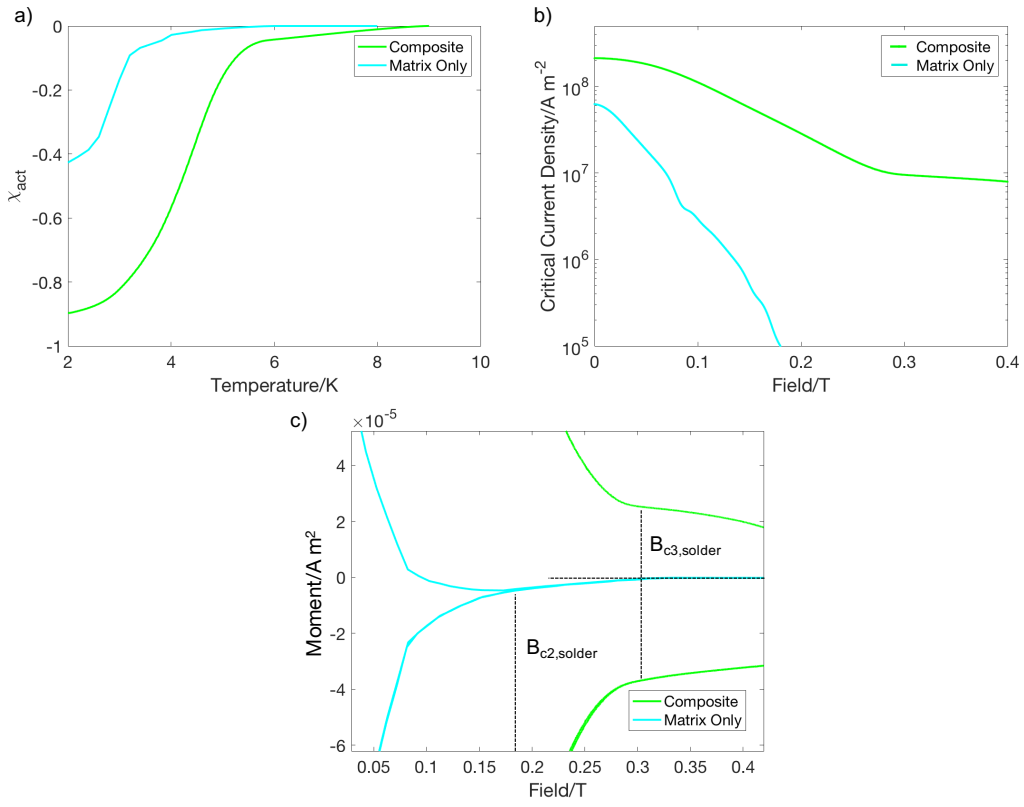


Figure 6.9: Comparison between the composite $Bi_{15}In_{50}Sn_{35}$ with 6 μm diameter NbTi filaments and the slow-cooled $Bi_{15}In_{50}Sn_{35}$ solder alone for a) $\chi(T)$ curves at 100 mT and b) $J_c(B)$ curves at 4.2 K c) Magnetisation against field curves for the same two samples, with a focus on the critical field region. The critical field for surface superconductivity (as described by Brittles for this material [33]), B_{c3}, and the conventional critical field B_{c2} for the matrix are clearly marked.

sample is shown in Figure 6.9a and shows a very slight deviation from zero at a temperature of 5.9 K, though the susceptibility does not change considerably until much lower temperatures. This effect was also noted by Brittles [33] in his study of this material. In particular, he noted that when plotting magnetisation as a function of applied field, the field at which the hysteresis loops closed did not match the field at which the magnetisation returned to zero, also observed in my samples in Figure 6.9c. He notes that whilst this behaviour is common in HTS materials where irreversibility fields can be much lower than the upper critical field, this is not expected in LTS systems. Instead, he postulates that the behaviour is due to surface superconductivity, where Cooper-pairs are able to exist at superconductor-insulator boundaries up to a higher field, sometimes known as B_{c3}. This was shown by Saint-James and de Gennes to be $B_{c3} = 1.695 B_{c2}$ [182], which was experimentally verified for the $Bi_{15}In_{50}Sn_{35}$ system

by Brittles [33]. The closeness of the critical conditions for bulk behaviour and this surface superconductivity condition is shown in Figure 6.8c. The experimental data extracted for the composite are shown alongside the fit derived by Brittles for $B_{c3}(T)$ for $Bi_{15}In_{50}Sn_{35}$. Whilst they do not agree exactly, possible differences in criteria used to extract the data mean they are still close enough for further consideration. In the case of the composite solder, it is unlikely that surface superconductivity plays a role in the increase of the critical conditions for bulk superconductivity as this effect is only expected at superconductor-insulator or vacuum interfaces, and certainly not at the interface between two superconductors. However, it may still be a sign that the behaviour at the interfaces between neighbouring NbTi filaments is critical to the overall behaviour of the composite.

Whatever the case, the fact that the hysteresis loops open at this field in the composite is indicative that the samples have the ability to carry currents at higher fields than the bulk solder, which is not typically the case for surface superconductivity. Whilst not the effect expected, this is promising for improved lead-free solder joints, with the composite solders demonstrating a roughly 60% increase in the critical field for bulk behaviour. It is worth stating that the value of 0.29 T observed is to the best of my knowledge higher than the B_{c2} of any other lead-free solder material. There is also an increase in the critical current density of the composite, with the value of Jc (0.01 T, 4.2 K) recorded as 2.3×10^8 A m^{-2}, approximately four times higher than the value of 5.7×10^7 A m^{-2} found in $Bi_{15}In_{50}Sn_{35}$ solder cooled under the same conditions, and also higher than the highest value of 1.3×10^8 A m^{-2} observed by Mousavi et al for $Bi_{15}In_{50}Sn_{35}$ [43], even though cooling conditions were not optimised for matrix performance. This again suggests the composite should lead to improved lead-free solder joints.

6.3.2.1 Effect of Filament Diameter

In an attempt to better understand the behaviour of composite solders, a second sample was made using LHC 46-B NbTi wire supplied by CERN. This wire had approximately 13,000 filaments of diameter 3 μm. The Cu:SC ratio was 2.95. The higher Cu:SC ratio

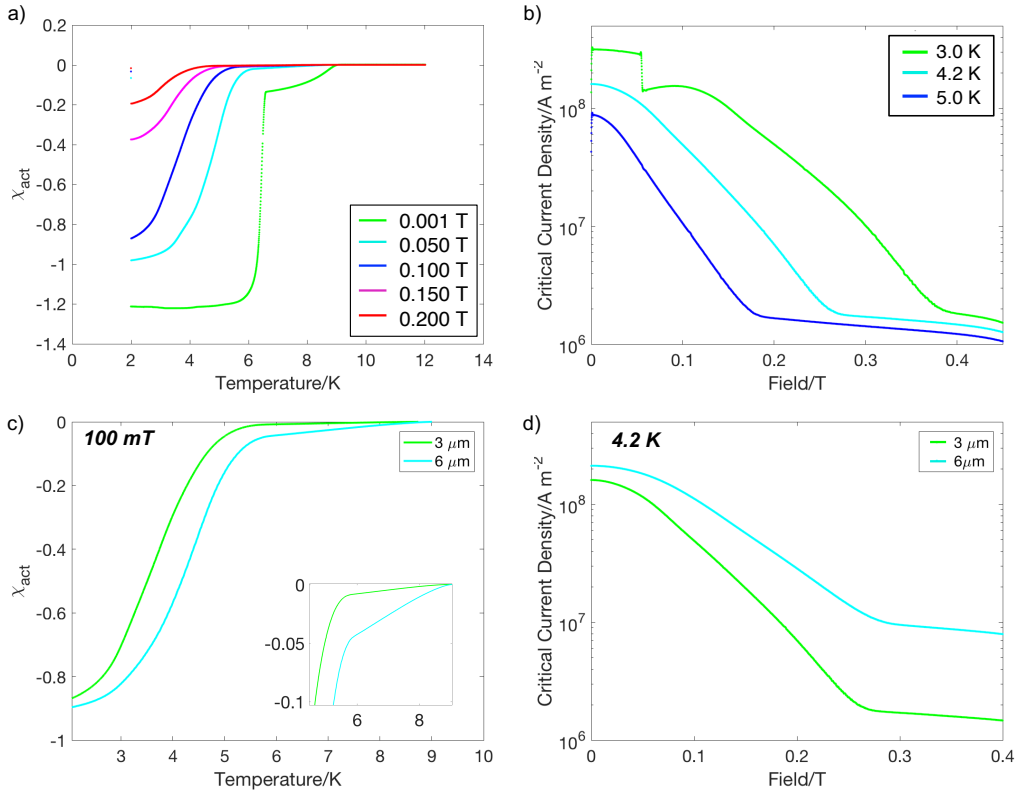


Figure 6.10: a) $\chi(T)$ curves and b) calculated $J_c(B)$ curves for a composite of $Bi_{15}In_{50}Sn_{35}$ with 3 μm LHC 46-B NbTi filaments. Comparison of c) $\chi(T)$ curves at 100 mT (inset zooms in on transition region) and d)$J_c(B)$ curves at 4.2 K for the 3μm composite compared to the composite with 6μm LHC Type-02 NbTi filaments described previously

is likely to mean a slightly lower loading of filaments in the final composite, but still high enough for percolation. The critical current density of this wire was approximately 30% lower than for the more highly optimised Type-02 conductor. Samples of composite with these filaments were prepared for PPMS-VSM measurement following the same procedure as for the Type-02 composite.

The features of the $\chi(T)$ curves for the 3 μm composite in Figure 6.10a are much the same as for the 6 μm composite described previously. In the 1 mT measurement there are two distinct transitions: one corresponding to the critical field in NbTi and one corresponding to the critical temperature of $Bi_{15}In_{50}Sn_{35}$. At low temperatures the susceptibility appears to be -1.21, probably due to remanent field in the magnet leading in practice to a slightly higher applied field than used in the susceptibility calculation. The removal of remanent fields in the PPMS was improved as the project

went on to minimise this effect in later samples. The susceptibility just above $T_{c,\,\mathrm{matrix}}$ is -0.14, which suggests that the volume fraction of the NbTi is approximately 11%, slightly lower than seen for the Type-02 composite, though again this is very much a lower bound estimate. The comparison of the $\chi(T)$ curves at higher fields in Figure 6.10c reveals that the temperatures at which the transition to bulk-like behaviour of the two composites are very similar. This suggests similar mechanisms are at play in both samples.

Figure 6.10b shows the critical current density of the composite as calculated from the Bean model. Again, there is a transition between a flat area of low apparent critical-current density at high fields before a transition to a region of increasing critical current at lower fields. This is compared at 4.2 K to the 6 μm composite in Figure 6.10d. The critical field for the bulk-like behaviour is similar for each sample, though the transition is at slightly a lower field for the 3 μm composite (0.27 T compared to 0.29 T). The critical current in the 6 μm composite is higher at all fields than for the 3 μm composite. Whilst the difference is small at low fields, it is considerably greater in the region above the bulk-superconductivity transition. One possible explanation for this is that there is poorer connectivity between filaments, but care has to be taken in interpreting this, because currents are likely to be limited to circulating just in individual filaments. This is likely to explain the majority of the difference, as the narrower filaments give smaller current loops and so a smaller magnetic moment, which the Bean model calculation for the sample critical current density (which is based on the assumption currents flow around the entire sample) interprets as a lower critical current density. The Bean model approximation for aligned filaments in Equation 6.1 shows a cubic dependence of moment from isolated currents on the filament radius, so the narrower filaments will produce a lower moment, and so a lower sample critical current density will be calculated. From the susceptibility measurements, the loading of filaments also appears slightly lower in the 3 μm composite, and the critical current density of the filaments is lower, all leading to the high-field region having a lower critical current density.

Composites were also fabricated with much coarser filaments, such as the 54S43 NbTi strand with 40 μm filaments by Supercon, Inc used for jointing throughout the project.

These composites demonstrated no improvement over the standard solder, potentially due to a lack of crossover points between filaments. Constraints on the number of filaments in these wires (54 compared to >6000 in the LHC Type-02 wire) limited the ability to get large numbers of larger filaments into a composite and required much longer lengths of wires to be used for composite manufacture, so this was not investigated further.

6.3.2.2 Length Scale Measurements

The theory that the composite demonstrates a transition from localised magnetisation only in the NbTi filaments to macroscale supercurrents across the whole sample presents a problem for the traditional Bean critical state approach to magnetic measurements, where samples are typically assumed homogeneous [123]. Typically magnetic measurements probe only these bulk properties, as the measured magnetic moment is an average over all the magnetic moments generated by current loops in the sample. However, Angadi et al. devised a way to understand the length scales over which currents in their samples were acting [183]. Strictly this analysis is only valid for very thin samples, but the analysis still provides at least a reasonable estimate for my thicker samples. The filamentary nature of the composite solder is inherently three-dimensional and so reducing composite samples to the thin disc geometry used by Angadi would have been representative of the bulk sample.

The critical state model assumes that only currents of $\pm J_c$ or 0 flow in a superconductor. Angadi's method considers the behaviour of minor hysteresis loops, where the field is reversed below the critical field as illustrated in Figure 6.11. Considering one half of the sample (the other half will be the same with the sign of the current reversed), elements of current density $-J_c$ flow throughout, as illustrated in plot (a) in Figure 6.11. When the field is reversed, currents penetrate from the outside to switch the field, causing an outer region of the sample to carry $+J_c$ (b). Angadi considers an incremental field change δH from this, which causes a change in the current in corresponding region of width δr. Note that the net change in current is $2J_c t\delta r$. The rest of the flux distribution is unchanged and so can be ignored. Thus the change in flux is linked to the change in

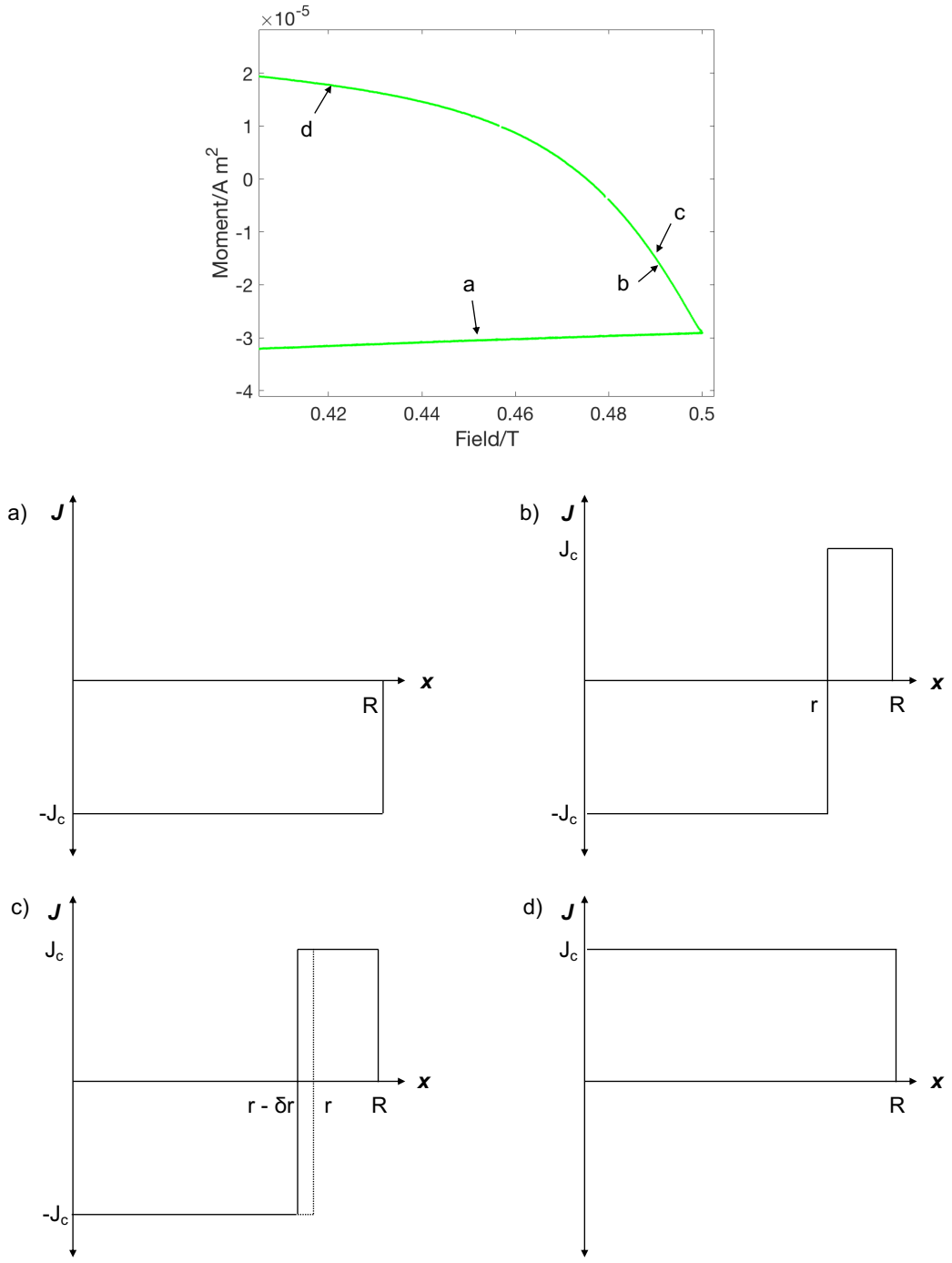


Figure 6.11: Zoomed view of the edge of the hysteresis loop for the $Bi_{15}In_{50}Sn_{35}$ composite with 6 μm LHC Type-02 filaments. Graphs a) to d) correspond to the spatial distribution of critical current densities perpendicular to the applied field predicted by the critical state model in one half of a cylindrical sample, radius R. Details of these are described in the main text

current by:

$$\mu_0 \pi r^2 \delta H + L(r) 2 J_c t \delta r = 0 \tag{6.2}$$

Where $L(r)$ is the inductance of a ring of radius, r, height t and thickness δr. This is given by the standard formula [183]:

$$L(r) = \mu_0 r \left[\ln\left(\frac{8r}{t}\right) - \frac{1}{2} \right] \tag{6.3}$$

Combining these equations gives:

$$\frac{\mathrm{d}r}{\mathrm{d}H} = -\frac{\pi r}{2 J_c t} \frac{1}{\left[\ln\left(\frac{8r}{t}\right) - \frac{1}{2}\right]} \tag{6.4}$$

The changing of current in the ring δr leads to a change in moment δm:

$$\delta m = \pi r^2 2 J_c t \delta r \tag{6.5}$$

and so:

$$\frac{\mathrm{d}m}{\mathrm{d}r} = \pi r^2 2 J_c t \delta r \tag{6.6}$$

$$\frac{\mathrm{d}m}{\mathrm{d}H} = \frac{\mathrm{d}m}{\mathrm{d}r} . \frac{\mathrm{d}r}{\mathrm{d}H} = -\frac{\pi^2 r^3}{\left[\ln\left(\frac{8r}{t}\right) - \frac{1}{2}\right]} \tag{6.7}$$

At the start of the return leg, $r \approx R$, where R is the radius of currents flowing in the fully penetrated sample. For samples of moderate aspect ratios, $\frac{R}{t}$, the logarithm term changes only slowly compared to the power term. As such, Angadi approximates the logarithmic term as a constant, $\Theta = \ln\left(\frac{8R}{t}\right) - \frac{1}{2}$. Once an initial estimate of R has been determined then it can be refined by changing the value of the logarithmic term. This leaves a simple equation linking the initial gradient of the hysteresis loop on reversal of the field to the initial radius of current loops flowing in the sample, R:

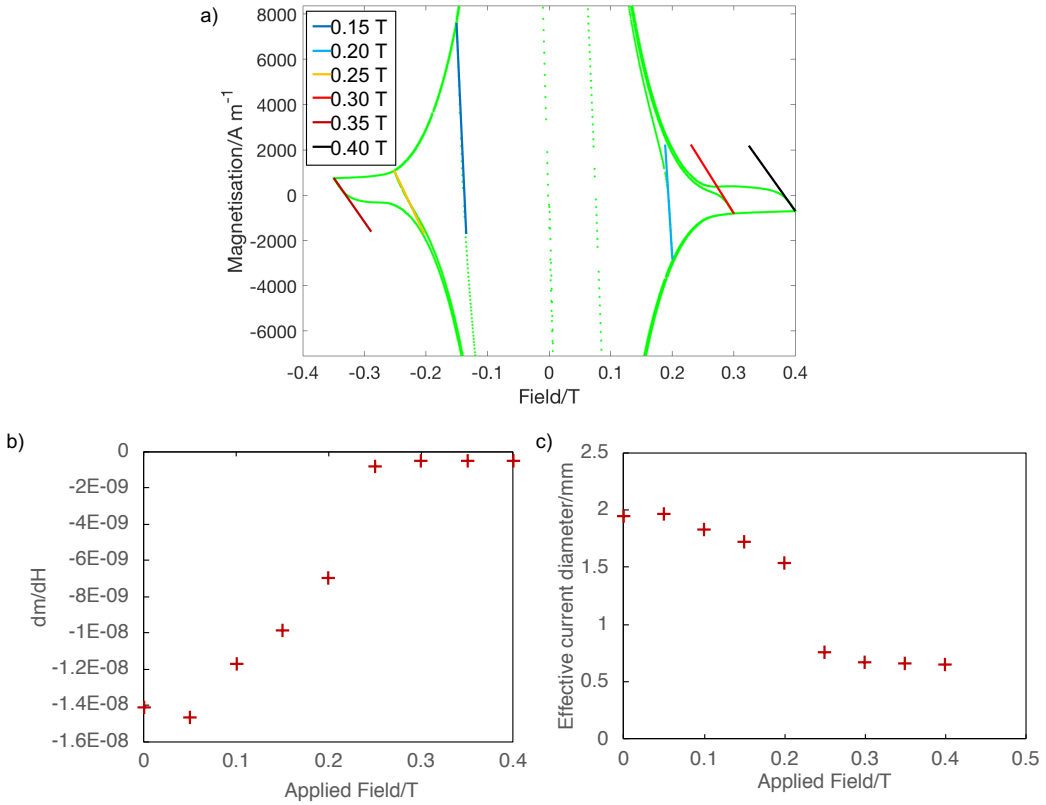


Figure 6.12: a) A succession of minor hysteresis loops for the LHC 46-B composite with 3 μm filaments at 4.2 K. Lines have been added at each field reversal to guide the eye b) The initial gradient $\frac{\mathrm{d}m}{\mathrm{d}H}$ at each field change plotted as a function of the field at which the reversal occurred. c) From this the effective current size is calculated using Equation 6.8

$$\frac{\mathrm{d}m}{\mathrm{d}H} = -\frac{\pi^2 R^3}{\Theta} \tag{6.8}$$

The PPMS-VSM provides a good platform for performing these measurements, allowing for the small field steps and high data collection rates required to investigate the earliest stages of field reversal. Measurements were performed by cycling the field out to the desired value, then reducing the field, always allowing the moment to recover to the original hysteresis loop before the field reversal. The value of $\frac{\mathrm{d}m}{\mathrm{d}H}$ upon field reversal could then be calculated at each different field.

For this measurement, the composite with 3 μm LHC 46-B NbTi filaments and $Bi_{15}In_{50}Sn_{35}$ matrix described in the previous section was used. Figure 6.12a shows the magnetisation hysteresis loop for this sample for multiple minor hysteresis loops with decreasing

maxima in applied field. From this, there is a clear difference in the initial gradients when the field is reversed at a large value compared to a smaller one. This is plotted in Figure 6.12b, where the value of $\frac{\mathrm{d}m}{\mathrm{d}H}$ stays approximately constant for values well above the bulk transition field in the solder of 0.27 T. Note that both the positive and negative sides of the hysteresis loop have been used to populate this plot due to the symmetry of the hysteresis curve. At fields below 0.25 T, $\left|\frac{\mathrm{d}m}{\mathrm{d}H}\right|$ starts to increase, and continues to increase as the reversal field is further reduced. Figure 6.12c uses Equation 6.8 to approximate the corresponding current loop size required to give such a gradient, assuming a constant value of Θ. At low fields, the value of around 2 mm is in good agreement with the diameter of the sample (2.18 mm), suggesting that the calculations made (which are strictly more valid for the much lower t/R samples investigated by Angadi) are reasonable for at least a first-order estimate.

As the field is increased the effective current length stays close to the sample diameter until 0.2 T, even though the critical field of the matrix alone is only 0.18 T. This suggests that at this stage in the composite, super-current is still able to flow on a large scale. As the field is increased further the effective current length falls, until it levels out above 0.3 T. This is in good agreement with the interpretation of the $J_c(B)$ curves, where below 0.27 T the sample appears to demonstrate an increase in critical current density. These measurements suggest that it is the increase in physical size of the current loops that leads to the increase in moment observed, rather than just an increase in the current flowing. This helps support the theory that as the field is reduced below 0.27 T in this sample, currents go from circulating only in the filaments to circulating on a macroscale across the whole sample, suggesting that the apparent improvement in critical field should allow samples that carry real-current through the filament network at fields higher than typically allowed by the matrix material alone. This gives hope that this technique might be used in jointing to boost the critical fields of materials that would otherwise be too low for use in magnet applications.

6.3.3 A Model for the Magnetic Behaviour of Composites

The magnetic response of the composite can be understood through a simple model. When magnetically measuring any superconductor, the irreversible component of magnetic moment is given as the sum of the contribution of all the current loops of size $\vec{J}$ and radius $\vec{r}$ in the sample:

$$\vec{m_{irr}} = \frac{1}{2} \int \int \int_V (\vec{J} \times \vec{r}) dV \tag{6.9}$$

A key consideration for the composite is that the radius of the the current loops has a significant effect on the moment contributed, even at constant J. The magnetic performance of the composite is strongly influenced by currents flowing over larger distances, which provide a major contribution to the magnetic moment. These regimes are illustrated in Figure 6.13, where possible current paths are shown that cause the measured moment. The simplest regime is below $B_{c2,\,\mathrm{matrix}}$ (a). In this regime, the sample generally behaves as a uniform bulk, with currents able to flow anywhere in the superconductor, limited by the critical current density of the matrix.

At high fields, greater than a field I shall refer to as $B_{c2,\,\mathrm{network}}$, the sample enters regime (c). At this point, current loops are only able to flow with any considerable current in individual NbTi filaments. Even though the current density of these loops is high, the size of each of the current loops is much smaller than the bulk, leading to only a small contribution to magnetic moment. As the critical field of NbTi is high at 4.2 K, the moment only changes very slowly with increasing field in this regime, and it is expected that this would continue out to the critical field of NbTi at 10.5 T.

The unexpected behaviour was in region (b), where $B_{c2,\,\mathrm{matrix}} < B < B_{c2,\,\mathrm{network}}$. In this regime there is a considerably larger magnetic moment than at fields exceeding $B_{c2,\,\mathrm{network}}$. As the response of the NbTi filaments alone should be relatively flat in this region, and supercurrents are not expected to start in the matrix alone, this suggests that the physical size of the current loops must be increasing. Suggestions for the reason behind this will be presented later, but for this model all it requires is to state that

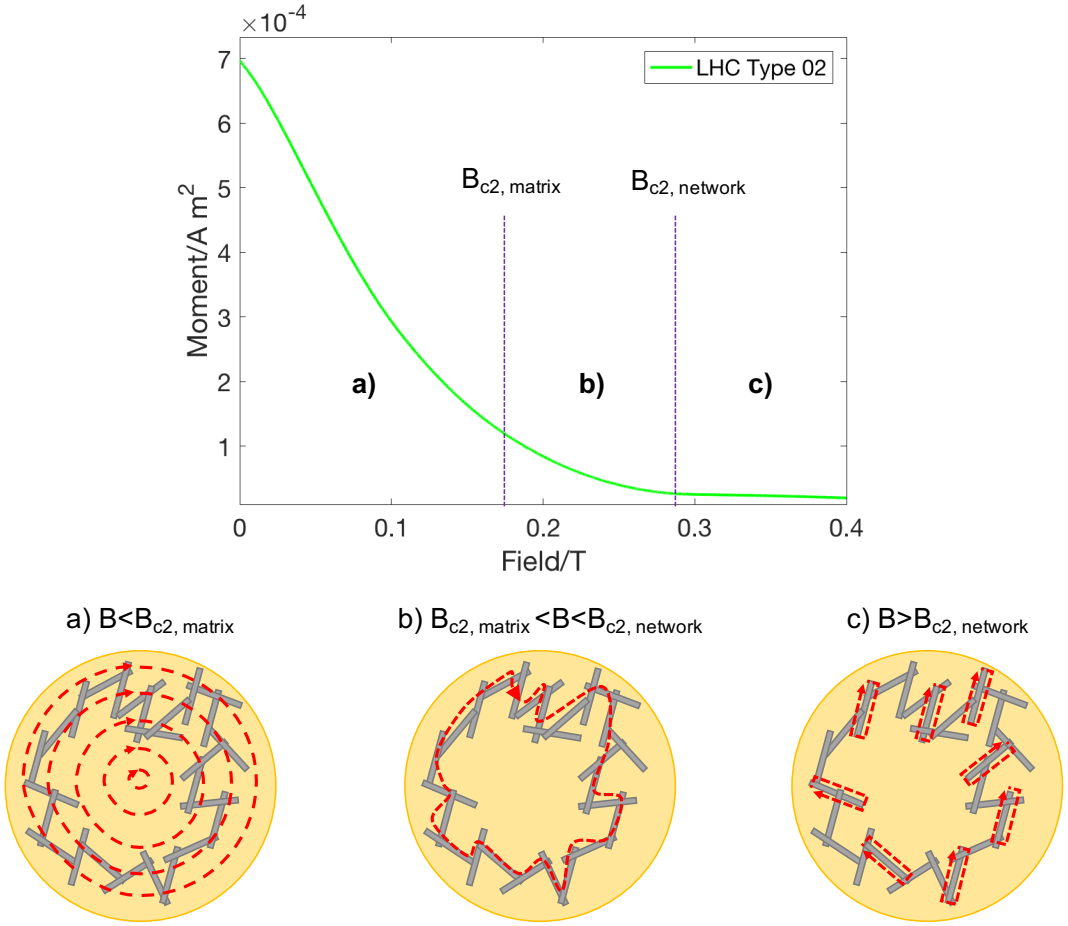


Figure 6.13: The top-right quadrant of the moment-applied field for the $Bi_{15}In_{50}Sn_{35}$ matrix composite with 6 μm LHC Type-02 NbTi filaments. Below are illustrations of the current loops causing the magnetic moment in the three possible distinct regions a) $B < B_{c2,\,\mathrm{matrix}}$, b) $B_{c2,\,\mathrm{matrix}} < B < B_{c2,\,\mathrm{network}}$ and c) $B > B_{c2,\,\mathrm{network}}$. This is discussed further in the main text

supercurrents start to be able to flow across the junctions between filaments, connecting it up as an entire network. It is worth noting that this is not an instant, sharp transition, but instead a gradual transition, suggesting that whilst the network behaviour starts to occur below $B_{c2,\,\mathrm{network}}$ the exact field each junction becomes superconducting varies, leading to a slow increase in effective current loop size and so magnetic moment. This seems to agree with the current loop size measurements, where there is a clear decrease in effective current loop size between $B_{c2,\,\mathrm{matrix}}$ and $B_{c2,\,\mathrm{network}}$, though these calculations simplify the matter by considering only the effective size of sample that would give such an mH gradient.

In all the composites measured there is no clear transition associated between regimes

(a) and (b). This suggests that the real paths of the currents are more complicated than in the simplified regimes presented here. It is worth noting that the critical current density of the NbTi filaments is orders of magnitude higher than the solder matrix, so currents flowing around the bulk via the filaments are likely to have a greater influence on the measured moment of the sample than those through the matrix alone, leaving little distinction between regions (a) and (b).

6.3.4 Performance of Composites with Different Matrices

Whilst I was limited by the wires that composites could be fabricated from, there are a huge variety of possible materials for the matrix material. It was instructive to explore multiple matrix materials to understand the nature of the composite performance and to determine whether the apparent increase in critical field was unique to the $Bi_{15}In_{50}Sn_{35}$ system.

6.3.4.1 Tin Matrix Composites

To separate matrix and filament based effects, a matrix with limited superconducting performance at the measurement temperatures was used. A simple solution for this was to use a tin matrix, which could be easily fabricated by tinning the NbTi wires as for previous samples and then proceeding straight to consolidating these tin coated filaments as a composite. Tin has a critical temperature of 3.7 K [184], making it a non-superconducting matrix material at 4.2 K, whilst still providing a clear superconducting signal at 2 K to allow easy centring of the sample in the magnetometer for magnetic measurements. A sample was made by dissolving the copper matrix of 10 cm LHC 46-B NbTi wire in molten tin for 90 minutes at 350°C as for the previous composites. Filaments were then spread, chopped into <1 mm pieces and then melted together to form the composite. This composite was then cast in the hot mould at 215°C and allowed to cool with the mould back to room temperature. A 2 mm section was cut from this and the ends flattened with SiC grinding paper to prepare it for magnetic measurements in the MPMS.

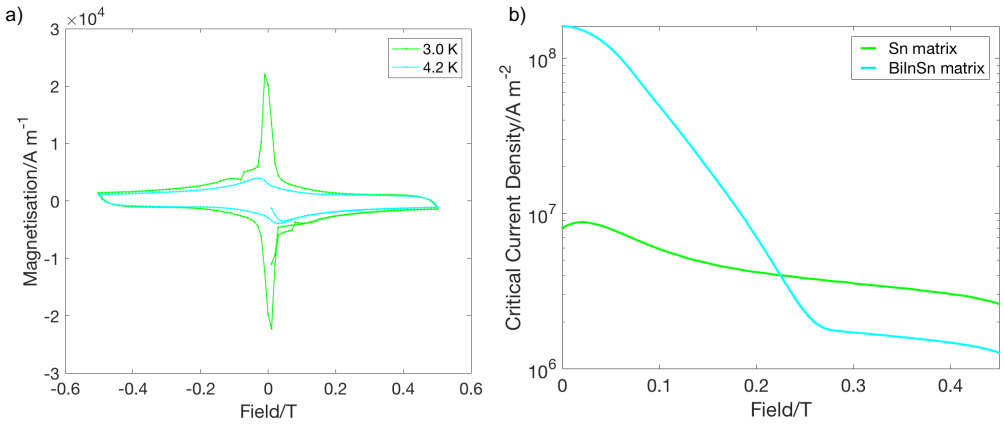


Figure 6.14: a) Magnetisation against applied field a composite of tin matrix with 3 μm LHC 46-B NbTi filaments. b) Comparison of $J_c(B)$ curves at 4.2 K for the tin matrix composite compared to the $Bi_{15}In_{50}Sn_{35}$ matrix with 3 μm LHC 46-B NbTi filaments composite described previously

There is a noticeable difference in the hysteresis loops of the tin composite above and below the critical temperature of tin in Figure 6.14a. At 4.2 K, comfortably above the critical temperature of the tin matrix, the behaviour is relatively field independent, with only a slight upturn at very low fields. This differs from the 3 K results, where there is a sharp increase in magnetisation below 0.04 T. It is likely that at no stage does the sample exhibit macroscale supercurrents at 4.2 K, with supercurrent confined only to individual NbTi filaments, whilst at 3 K there is a region at very low applied magnetic fields during which the matrix can also carry supercurrent, leading to bulk-scale current flow.

The 4.2 K data is useful as a reference comparison with other measured samples. Figure 6.14b compares the calculated critical current densities at 4.2 K of the tin sample with the $Bi_{15}In_{50}Sn_{35}$ matrix and 3 μm filament composite sample described earlier on a semi-logarithmic scale. Both follow a similar pattern at high fields, with only a very slow change in critical current. At this point both samples have currents flowing solely in the NbTi filaments, and probably isolated from all other filaments, so the calculated critical current densities calculated have limited meaning. However, there is a factor of approximately two different between the samples, likely due to slightly higher loading and possibly longer filaments which would lead to longer current paths and so a higher magnetic moment in the tin-matrix composite. At lower fields, the transition to

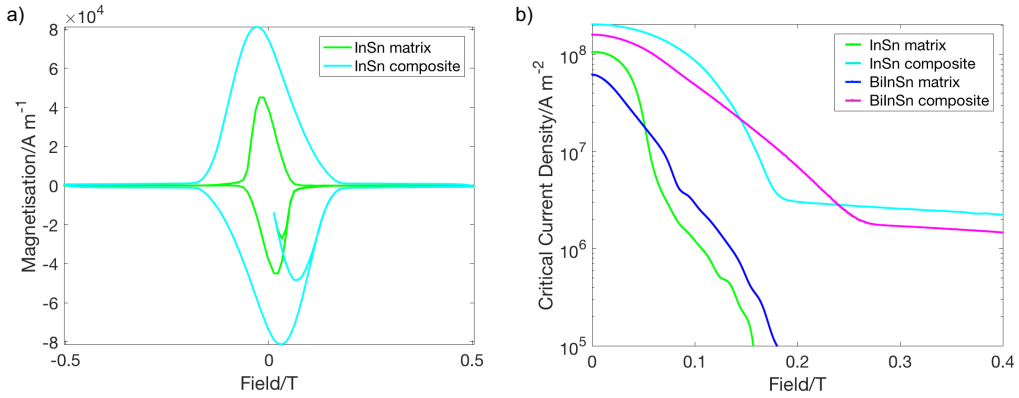


Figure 6.15: a) Magnetisation-applied field curves for approximately eutectic $In_{53}Sn_{47}$ solder with and without 3 μm LHC 46-B NbTi filaments at 4.2 K. b) The $J_c(B)$ curves at 4.2 K calculated for the same two samples on a semi-logarithmic scale. The calculated values for the $Bi_{15}In_{50}Sn_{35}$ solder samples with and without 3 μm LHC 46-B NbTi filaments previously described are included for reference

network-like behaviour is only observed in the $Bi_{15}In_{50}Sn_{35}$ matrix sample, indicating that deviations from the high-field trend are indeed linked to effects in the matrix, rather than being a feature of the filaments alone.

6.3.4.2 Indium-Tin Matrix Composites

To understand whether the boost in field-performance was unique to the $Bi_{15}In_{50}Sn_{35}$ matrix it was instructive to cast and measure composites made with other similar lead-free solders. Two compositions from the InSn system investigated by Mousavi et al. [43] were chosen for this: approximately the eutectic composition $In_{53}Sn_{47}$ and the single β phase $In_{80}Sn_{20}$. These were made by weighing the solder metals in the desired ratios into a crucible and melting at 300°C for 15 minutes to allow the solder to homogenise. For each composition, a sample from was cast into a hot mould at 170°C and cooled to room temperature to allow the properties of the matrix alone to be characterised. The composites were formed in the same way as for previous composites, though the casting temperature was higher at 170°C to account for the higher melting temperatures of the solder matrices.

The hysteresis loops of the eutectic $In_{53}Sn_{47}$ sample, shown in Figure 6.15a, again demonstrate an increase in performance for the composite sample compared to the

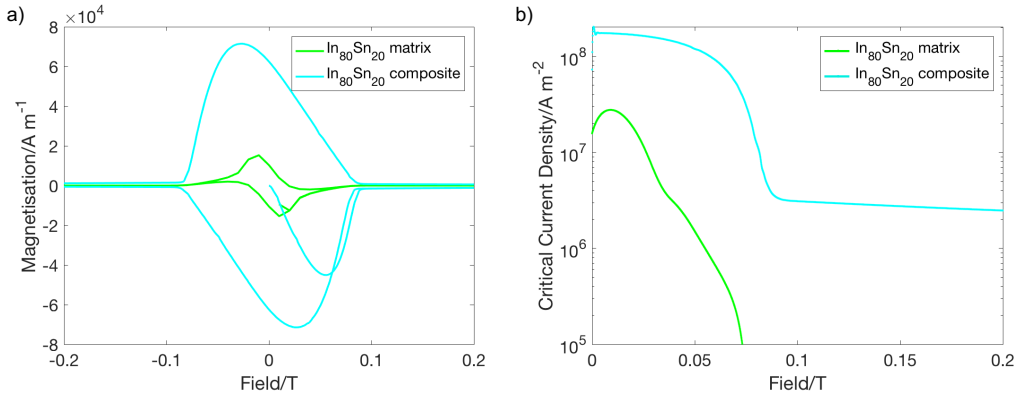


Figure 6.16: a) Magnetisation-applied field curves for β phase $In_{80}Sn_{20}$ solder with and without 3 μm LHC 46-B NbTi filaments at 4.2 K. b) The $J_c(B)$ curves at 4.2 K calculated for the same two samples on a logarithmic scale

matrix samples alone. The critical field of the composite network is to 0.190 T compared to the bulk critical field of the matrix alone of 0.157 T and, as can be seen in the $J_c(B)$ curves in Figure 6.15b, the critical current at zero field is increased by approximately a factor of two. However, the combination of slightly increased critical field and the critical current density staying high to larger fields for the composite lead to two orders of magnitude difference in the apparent critical current at 0.1 T. Whilst the eutectic sample does not show as much increase in network critical field as the $Bi_{15}In_{50}Sn_{35}$ sample, there is still a small increase, but it is the increase in critical current density at higher fields that makes this interesting for joint development. This might be expected in a composite solder, where allowing supercurrent to flow through the filament network greatly increases the magnetisation of the sample.

The $In_{80}Sn_{20}$ in Figure 6.16 shows a similar increase in critical field, 0.073 T for the bulk solder alone compared to 0.090 T for the composite, an increase of approximately 23%. Interestingly this is very close to the 21% increase observed for the the eutectic solder, suggesting that similar factors may be involved in both. Again this corresponds to the field at which the magnetisation returns to zero, suggesting perhaps that the behaviour of the composite is related to similar effects as surface superconductivity. However, both InSn samples show a smaller increase in critical field than the 70% difference observed in the $Bi_{15}In_{50}Sn_{35}$ solder. The exact reason for this is unclear, though it is worth noting that Santra's work on interfaces in this type of solder suggests that $Bi_{15}In_{50}Sn_{35}$ is

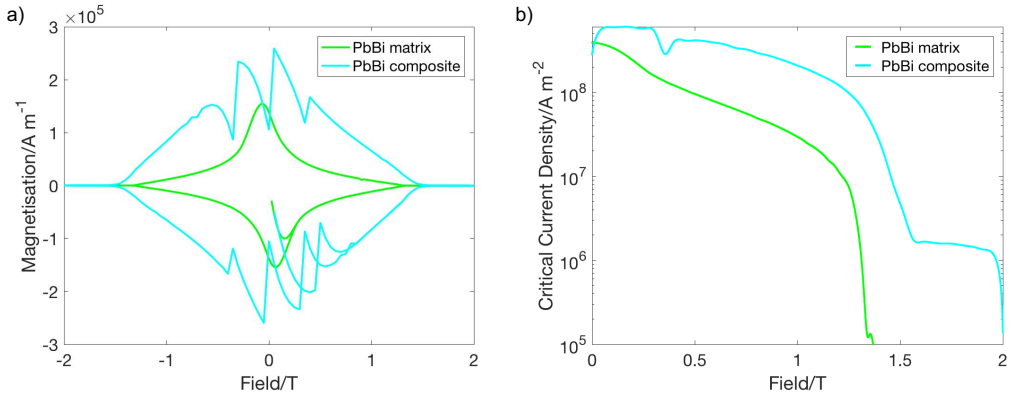


Figure 6.17: a) Magnetisation-applied field curves for commercial PbBi solder with and without 3 μm LHC 46-B NbTi filaments at 4.2 K. b) The $J_c(B)$ curves at 4.2 K calculated for the same two samples on a logarithmic scale

considerably less likely to form a reaction layer with NbTi than InSn solders [56]. Whilst on the considerably shorter timescales involved in the preparation of the composites any reaction layers are expected to be very thin, they could still increase the minimum separation between filaments or provide different electronic properties.

6.3.4.3 PbBi Composites

The InSn system is still closely related to the BiInSn system, so it was desirable to create composite solders with a different superconducting matrix material. As such, a composite was made from the most industrially relevant material, eutectic $Pb_{55}Bi_{45}$ provided by Siemens Magnet Technology. A composite was made from this using the 3 μm LHC 46-B NbTi filaments, consolidating the composite by casting in a mould at 135°C. A sample of the solder alone was cast under the same conditions to act as a reference.

For the PbBi composite in Figure 6.17, the network critical field of the composite, 1.57 T, is larger than the critical field of the bulk material, 1.34 T, an increase of 17%. This is comparable to the increases seen in the InSn solders, but much lower than those seen in the BiInSn solder. However, it is interesting that there appears to be no region of non-zero magnetisation attributed to surface superconductivity in the bulk PbBi sample above the field at which the hysteresis loop closes (when $\Delta M = 0$, $M^+ = M^- = 0$), suggesting this is not fundamental to the increase in critical field of

the composite solder.

6.4 Discussion

The composites measured have all demonstrated a $B_{c2,\ \text{network}}$ considerably higher than the B_{c2} of the original matrix phase cooled under the same conditions as summarised in Table 6.1

Matrix material	Filament type	$B_{c2,\ \text{matrix}}$	$B_{c2,\ \text{network}}$	% increase
$Bi_{15}In_{50}Sn_{35}$	6 μm LHC Type-02	0.18	0.29	61
$Bi_{15}In_{50}Sn_{35}$	3 μm LHC 46-B	0.18	0.27	50
$In_{53}Sn_{47}$	LHC 46-B	0.157	0.190	21
$In_{80}Sn_{20}$	LHC 46-B	0.073	0.090	23
$Pb_{55}Bi_{45}$	LHC 46-B	1.34	1.57	17

Table 6.1: A summary of the properties of bulk composite solders measured in this chapter

The model proposed for the composite's behaviour relies on a transition between current flowing in individual filaments and current flowing around the whole network. On a simple level, there is a superconducting junction at each point where the filaments meet. However, this system is far more complicated than systems described in the literature, with the potential for several different materials between the NbTi filaments depending on what phase is present, irregular interface geometry and possibility of interface layers. A simplified model for the behaviour between NbTi filaments considers it as a classic SNS (superconductor-normal-superconductor) junction, with the NbTi filaments acting as the superconductor and the matrix material as the normal material that has been pushed out of the superconducting state. There is little literature on high-field performance of these junctions, but some limited conclusions can be drawn based on the better studied temperature response. De Gennes first showed that supercurrent could be carried through such a junction via the superconducting proximity effect, where Cooper pairs are able to exist for a short distance into the normal material [185]. When the middle layer is a superconductor of critical temperature $T_{cN} < T_c$ the current through a junction of width d when $T_{cN} < T < T_c$ is given by [186]:

$$J_c(d,T) = \left[\frac{\pi}{2e\rho_N\xi_N}\frac{|\Delta_i(T)|^2}{k_B T_c}\right]\exp[-d/\xi_N(T)] \tag{6.10}$$

where ρ_N is the resistivity of the normal layer, Δ_i is the superconducting band gap and ξ_N is a parameter called the normal coherence length, indicative of the distance superconductivity persists in the normal layer. This in turn is given by:

$$\xi_N(T) = \left(\frac{\hbar D_N}{2\pi k_B T}\right)^{1/2}\left[1+\frac{2}{\ln(T/T_{cN})}\right]^{1/2} \tag{6.11}$$

$$\cong \left[\frac{\hbar D_N}{2\pi k_B(T-T_{cN})}\right]^{1/2} \text{ if } (T-T_{cN})/T_{cN} \ll 1 \tag{6.12}$$

where D_N is the diffusion constant of the normal layer. The crucial parameters here are the balance between the junction width, d, and ξ_N. It is worth noting that a typical value for ξ_N in many metals is between 100 and 600 nm [187], of comparable size to the filament spacing. The smaller the gap between filaments, and so the smaller the junction width, and the larger the critical current density. ξ_N decreases as the temperature is increased above T_{cN}. Adding a large applied field is likely to complicate the picture, but we see instantly that it suppresses T_{cN} and so reduces ξ_N. This in turn reduces the critical current through the junction. As such, it is likely that the junction will only be effective at temperatures just above T_{cN}, which is in agreement with the network behaviour only apparent for a small region just outside the usual critical surface of the solder. To insert this into the simple model described previously, at high temperatures, only a very low current can be carried though the junctions, and so current is induced only in individual filaments. When close to the critical surface, the junctions become able to carry large currents, and so currents can circulate through the full filament network. Once the matrix becomes superconducting, there is no limitation to junction regions, and so current can flow anywhere. However, this is still a very simplified model, particularly because each junction will have a different orientation, geometry and even chemistry, making quantitative predictions extremely difficult.

Whilst there is little difference between the two filament diameters, both the percent-

age and true differences in B_{c2} between the matrix and network vary considerably with changing matrix material. This might suggest that the solder-filament interface plays a significant part in the behaviour of the composites. Interestingly, Brittles demonstrated reaction layer formation between NbTi and PbBi solders [33], whilst Santra demonstrated the same for InSn solders [56]. However, Santra found that adding bismuth greatly reduced the reactivity, leading to no observable interface layer formation. Any interface layer formed between the NbTi filaments and the matrix is likely to affect the behaviour of the composite, with the superconducting properties of this interface dependent on the composition and electronic properties of the layer. Even if the layer does not have different superconducting properties to the matrix material, any layer means greater minimum separation between filaments and so a greater minimum junction width. As can be seen in Equation 6.10, the current carrying ability of superconducting SNS junctions decreases with distance [186], and so increasing the separation of the NbTi filaments via a reaction layer would decrease the field at which observable current can flow across the junction. This satisfactorily explains why the BiInSn solders demonstrate larger increases – with no reaction layer the minimum separation between filaments can be smaller and so the junction current higher for a particular value of $(T - T_{cN})/T_{cN}$.

6.5 Composite Joints

With the composite solder appearing to have improved performance over conventional solder, some preliminary joints were made using the composite solder to see if this performance enhancement in bulk material could be transferred into bulk performance.

6.5.1 Joint Production

Composite solders with 3 μm LHC 46-B NbTi filaments and $Bi_{15}In_{50}Sn_{35}$ matrix were made and consolidated using the same method as for the bulk samples described in the previous section. The joints were made between NbTi wire by Supercon Inc. with 54

NbTi filaments of diameter 45 μm. Before forming the joint with composite solder, the matrix-replacement method was used to remove the copper matrix from the joint wire and replace it with $Bi_{15}In_{50}Sn_{35}$ solder as used for the joints in Section 5.3.

At this point, the first difficulty in joint making with composite solder is apparent. In an ideal world, the tin matrix would have been dissolved in a large bath of the composite solder with a volume of at least a few cm^3. This was much more than could be manufactured in one go using my small-scale process, and was also restricted by limited quantities of the fine-filament wire. As such, the wires to be joined had to be soldered in just the matrix solder and added in to a pre-consolidated composite. The high filament loading meant that getting the coarser filaments of the joint wire well incorporated into the composite network was difficult - it is clear from the composite microstructure in Figure 6.4 that there are few gaps in the ideal microstructure large enough to fit a filament from the joint wire. Also, the considerably more viscous nature of the composite meant the filaments of the jointing wire tended to spread out rather than tunnel their way into the composite. All this meant that incorporating filaments on the small scale of my samples was tricky. Again, this would be much more simply solved if larger amounts of composite could be fabricated, where incorporating the joint wires could be performed easily during the consolidation of the composite.

Instead, the wires had to be incorporated after composite consolidation. This involved heating the composite above its melting temperature on top of a hotplate at around 100°C. The solder coated ends of the wire were also heated until the solder ran. They were then pressed into the viscous molten composite, and the wires and composite were stirred and agitated together. When well mixed, the combination of wire and composite was pressed into the 2.13 mm diameter mould to allow a cylindrical joint to be formed, allowing better comparison with the conventional solder joints. Whilst this technique would eventually lead to a well formed joint, it was inconsistent and quite often it was hard to get both of the joint wires incorporated into the composite matrix.

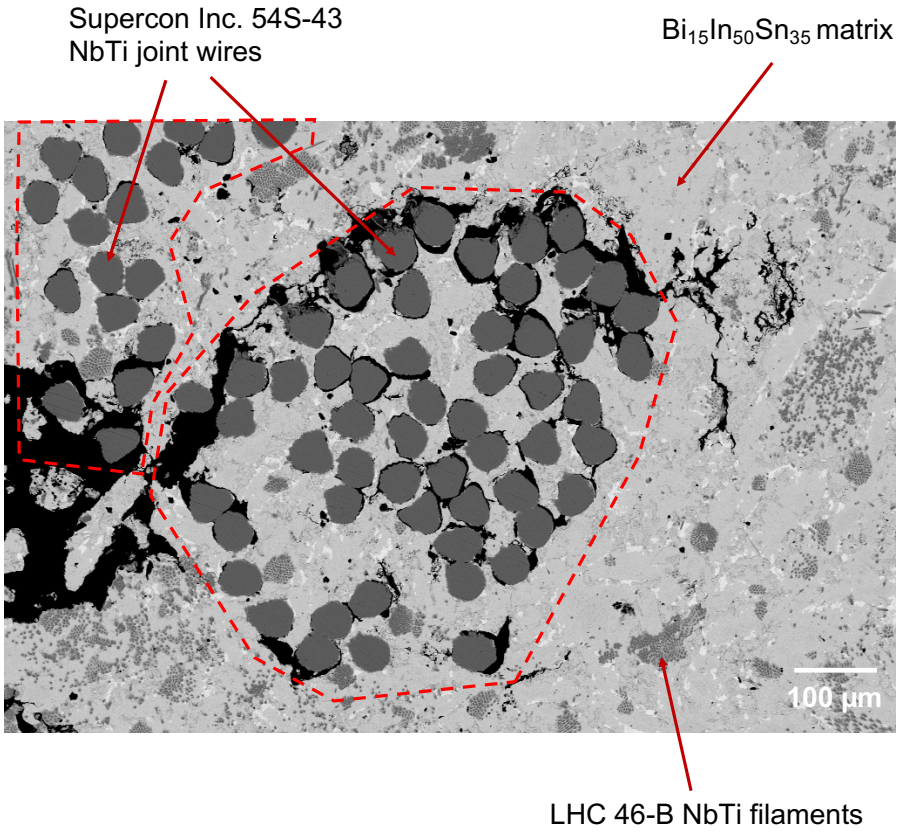


Figure 6.18: Backscattered electron image of a composite joint with $Bi_{15}In_{50}Sn_{35}$ matrix and 3 μm LHC 46-B filaments. The joint is made between two Supercon Inc, 54S43 multifilamentary NbTi wires, marked on the image

6.5.2 Microstructure

To understand how the joint was incorporating into the filament network, a test joint between two pieces of Supercon Inc. 54S43 NbTi wire was cast. The joint was then cut perpendicular to the joint wires and set in cold-set epoxy for analysis in the SEM. Particular care was taken during grinding and polishing to only apply light pressure to prevent any frictional heat which could cause melting of the sample surface or embed polishing media in the surface.

The backscattered SEM image in Figure 6.18 reveals a couple of potential issues. The first is that several of the filaments of the joint wire appear to be poorly wet, perhaps down to the relatively rough procedure required to embed them in the composite network. The poorly wet joint filaments are unable to interact with either the solder or the composite network, and so would not be able to carry current. Secondly, there are

only a very small number of filaments from the composite network in close proximity to the joint wires. This is likely to be because the joint wires were soldered separately to the composite consolidation, and so tended to be pressed into the composite network in one mass with bulk solder, not composite material, between the joint filaments. Few contacts with the composite network are likely to limit the ability of the joint to carry current through the composite network. Similar features were observed in a range of different samples, even when steps were taken to ensure a better connection between joint wires and composite network, such as by pressing the composite after manufacture.

6.5.3 Superconducting Properties

To assess the superconducting properties of one of these preliminary joints, a joint was prepared between the two ends of a 10 cm piece of Supercon, Inc. 54S43 wire. Each end had 15 mm of insulation removed, and was then the joint was formed between the two ends as described above so that it could subsequently be wound onto a former for characterisation in the PPMS-VSM. Forming joints between the two ends proved tricky as the two ends naturally wanted to spring apart, making them hard to merge with the composite. This is isolated to my small-scale test joints, and is not expected to prove problematic on a large scale. The joint was cast in a brass mould at 100°C and allowed to cool slowly in the same way as the solder-only joints in Section 5.3, leaving a roughly 15 mm cast cylinder of composite solder surrounding the thicker joint wires.

The m–T curves for the joint in Figure 6.19a demonstrate a simple two-step transition, with one transition attributable to the critical temperature of the jointing wire and the other to the joint becoming active. As can be seen in Figure 6.19c, this contrasts with the $Bi_{15}In_{50}Sn_{35}$ joint described in Section 5.3.4 where distinct steps in the transition were attributable to different phases of the solder becoming active. One possible reason for this is that the filaments in the composite bridge across the phases, allowing macroscale currents to flow even when only one of the phases is superconducting. There is also a slight increase in the critical temperature at which the composite joint deviates from the signal attributable only to NbTi.

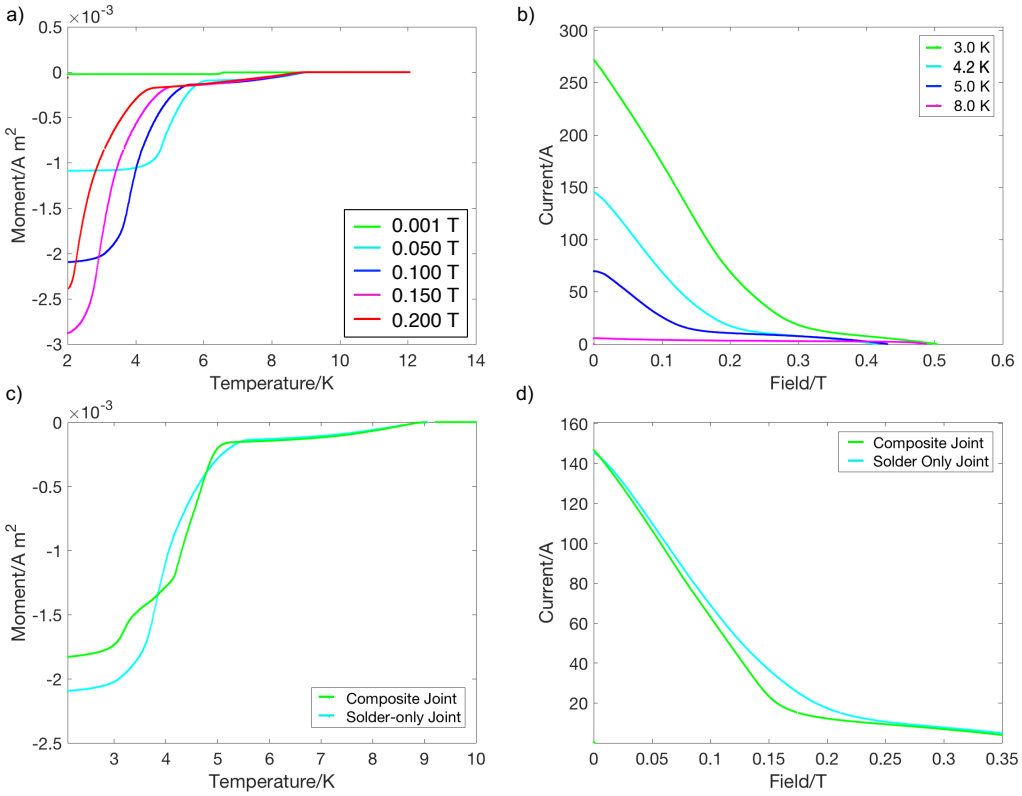


Figure 6.19: a) Moment-Temperature curves for a loop of Supercon, Inc 54S43 NbTi wire jointed with a composite solder with a $Bi_{15}In_{50}Sn_{35}$ matrix and 3 μm LHC 46-B NbTi filaments b) Joint current as a function of field calculated from the top right corner of the hysteresis loops of the same sample at different temperatures. Comparison of c) the moment-temperature curves at 0.1 T and d) the calculated current of the composite joint at 4.2 K with that of a similarly sized joint made from $Bi_{15}In_{50}Sn_{35}$ alone (described in detail in the previous chapter)

The estimated current in the joint is presented in Figure 6.19b. Much as for previous joints, as the field is reduced from the maximum field there is a region where there is an apparent low current, during which currents circulate in the NbTi loop alone without passing through the joint. This is well illustrated in the 8 K sweep, where the joint is never superconducting and so all the signal is due to the NbTi wire. Below the critical field of the joint material the estimated current increases as circulatory currents can flow round the entire circuit, limited by $I_{c,\,\mathrm{joint}}$. When compared to the non-composite solder joint at 4.2 K in Figure 6.19d, it is interesting to note that the high field regions are extremely similar. This suggests that the NbTi filaments in the solder are failing to provide a true bridging effect between the two joint wires as originally intended, which agrees with the measurements on composite bulks in Section 6.3.2. Similar to the bulk

composite, there is an apparent increase in the critical field of the joint, with the joint having $B_{c2,\,\mathrm{joint}}(4.2\ \mathrm{K}) = 0.25$ T, in reasonable agreement with the 0.27 T measured for the bulk composite samples. However, the critical current increase observed for bulk samples is not apparent, with the composite critical current tending towards the non-composite sample at lower fields. This agrees with what was observed in the mock samples analysed in the SEM, where only a few joint filaments appeared to make contact with the filament network. If only a few composite filaments are in contact with the joint wires then their small cross section will only allow a low current to flow. Only once the matrix material truly starts carrying current can the joint be effective. It was noted in Section 5.3.4 that lead-free solder joints are particularly prone to self-field limitation, which makes the area around the joint wires, where self-fields are likely to be highest, the most important region to have good current and field-behaviour. Hence the network-free gap around the joint wires is likely to prove a major obstacle to current flow.

Considering the relatively poor microstructure of most of the joints observed, these early measurements of joint performance are promising. As mentioned previously, scaling up the joint and composite manufacture may allow for improved integration of joint wires into the composite network, allowing for the effect of the composite network to be better transferred to joint behaviour.

6.6 Chapter Conclusions

In this chapter, a novel composite-based approach for improving lead-free solders has been explored. Long, thin filaments of high-performance superconductor with a high melting point, taken from high-performance NbTi wire, were mixed into a low-melting point matrix using the matrix-replacement method to ensure good wetting of the filaments and matrix material.

The superconducting properties of these composites were studied with resistive transport and magnetisation measurements using the best performing lead-free solder known to us, $Bi_{15}In_{50}Sn_{35}$, as the matrix. The transport measurements showed a critical tem-

perature for the composite in line with that of NbTi alone, suggesting at least some chance of connectivity between the filaments. In magnetic measurements, improvements at high field were low. But at fields higher than $B_{c2,\ \mathrm{matrix}}$ macroscale currents could flow in the composite. In the $Bi_{15}In_{50}Sn_{35}$ composite this $B_{c2,\ \mathrm{network}}$ was 60% higher than $B_{c2,\ \mathrm{matrix}}$, which is better than any lead-free solder in the literature to date. Similar effects were noted when the matrix material and the filament diameter were changed, though the effect was noticeably less strong in other matrix systems.

Early attempts have been made at making joints out of the composite solder. However, it was found that the small-scale nature of the composite manufacture limited the ability to truly mix the wires to be jointed into the composite network, leading to only a very limited difference in performance.

I believe that scaling up the composite manufacture would allow for improvement of the process. By melting together larger volumes of the composite and mixing with a high shear rate it would be possible to make much more uniform composite bulks, and would enable much greater control of parameters such as filament loading. A larger melt would also enable longer lengths of joint wires to be incorporated more easily into the bulk, which would increase the ability of the joint to carry current at fields up to $B_{c2,\ \mathrm{network}}$. However, even with this scaling-up it is unlikely that either bulks or joints would demonstrate considerably increasee $B_{c2,\ \mathrm{network}}$.

Even with the increase in performance, the best value of $B_{c2,\ \mathrm{network}}$ for a lead-free composite of 0.29 T is still substantially lower than $B_{c2,\ \mathrm{PbBi}}$, and so a different approach may be required to form high-field lead-free joints. However, even a small increase in the performance of lead-free solders would be extremely helpful in the design of more compact pre-clinical MRI or laboratory magnets, where the stray field can be considerably lower. A suggestion for improving the performance of joints for higher fields will be presented in Chapter 7.

Chapter 7

Concluding Remarks

The search for a drop-in replacement for PbBi solders has so-far proved unsuccessful, with no substitute solder able to operate in the 1 T magnetic fields required by the MRI industry. This has necessitated new jointing techniques and required a better understanding of the science surrounding joint making. In Chapter 4, I investigated one of the key issues for both solder and mechanical jointing of NbTi – oxidation of exposed NbTi surfaces. Using angular-resolved XPS measurements, the oxides formed in air for times between 15 seconds and one hour were characterised, with a layer approximately 2.5 nm thick forming in the first 15 seconds and then thickening to around 4 nm after an hour. The ratio of niobium to titanium in the oxide was found to be similar to that in the bulk.

In Chapter 5, I investigated three key factors that could limit the potential of solder joints. Firstly, the effect of long heat treatments of NbTi wires in a regime relevant to matrix replacement soldering was investigated. Heat treating at 350°C was found to be safe for long times with minimal degradation of the wires at low field. Above this, wires started demonstrating reduced critical current, with wires heat treated at 400°C demonstrating significantly reduced critical current even after short times. Secondly, the effect on PbBi joints of using wires with and without niobium diffusion barriers was investigated. Whilst there was little difference in m–B measurements of the joints, decay measurements showed a notable upturn in resistance of the samples with diffusion

barriers above the critical field of niobium. Finally, the performance of the best lead-free solder joint was found to be limited by the low upper critical field of the lead-free solder. As well as limiting the background field that the joints can operate in, this also acted to provide a practical limit to the current that these lead-free joints can carry due to the self-field around the current carrying wires.

In Chapter 6 I detailed the development of a novel composite solder, mixing NbTi filaments into a low-melting temperature matrix. With a $Bi_{15}In_{50}Sn_{35}$ matrix, this was found to demonstrate bulk-like superconductivity at fields around 60% higher than the upper critical field of the matrix material. I proposed a mechanism involving SS′S junctions between filaments to describe this behaviour. Preliminary joints were fabricated and tested, with some indication of the same increase in field performance. However, these were generally limited by difficulties incorporating the jointing wires into the composite network. Scaling up the process should alleviate this problem. Whilst the composite technique has some potential for increasing the operating fields of lead-free joints, the lead-free composite solders still have considerably lower upper critical field than PbBi joints, and so potentially a new technique is required.

7.1 Suggestions for Future Work

There is no clear candidate for further exploration of lead-free solders, so further improvements in lead-free jointing are likely to require an entirely new technique. The ultimate persistent joint for MRI would involve the direct jointing of NbTi wires to themselves, but this has often been limited by heat-damage in techniques like spot-welding [57] that involve short times at very high temperatures or, based on the work on heat treatments in this thesis, in proposed techniques like diffusion bonding [4] where the wires must be subjected to moderate temperature for long periods of time. Cold pressing of wires has been used to some success [5], but is often restricted by low surface contact area between wires [1, 33].

A potential solution to the low contact area of cold pressing would be to densify a bulk of superconductor around the ends of exposed NbTi filaments as shown in Figure 7.1.

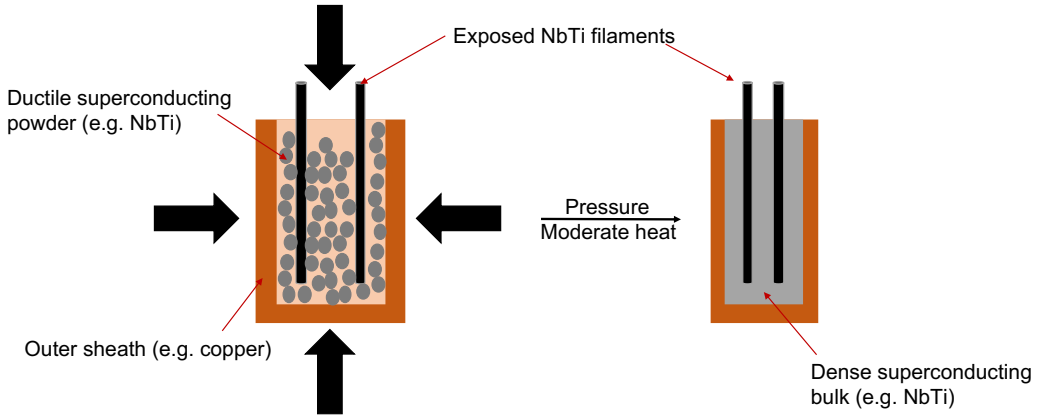


Figure 7.1: Concept for a joint between NbTi wires by densifying ductile superconducting powder (ideally NbTi) around the wires using mechanical pressure and potentially moderate heat. The outer sheath material serves both to contain the powder during pressing and also to provide stabilisation of the joint in operation.

The easiest solution for which would be to use NbTi powder, enabling a joint where current can flow entirely through NbTi, in effect surrounding the filaments with a NbTi solder. This has been attempted with reasonable success with both MgB_2 [78] and BSCCO [82] wires using high temperatures and pressures to sinter powder particles together. For ductile NbTi the powder the densification should prove much simpler, with the ability to form cold-pressed joints demonstrating that it is possible to form good superconducting bonds without the addition of high temperatures that would damage the NbTi wires. Some preliminary joints of this type are now being made and tested by other members of my group in Oxford, with the ultimate goal to demonstrate a joint that can match the critical current of the NbTi wires all the way up to the upper critical field of the wire.

Bibliography

[1] G. D. Brittles, T. Mousavi, C. R. M. Grovenor, C. Aksoy and S. C. Speller. *Persistent current joints between technological superconductors.* Supercond. Sci. Technol., 28(9), 2015.

[2] A. M. Campbell and D. A. Cardwell. *Bulk high temperature superconductors for magnet applications.* Cryogenics, 37(10): pp. 567–575, 1997.

[3] *https://conectus.org/market/.*

[4] C. Swenson and W. Markiewicz. *Persistent joint development for high field NMR.* IEEE Trans. Appiled Supercond., 9(2): pp. 185–188, 1999.

[5] J. Liu, J. Cheng, F. Zhou, Q. Wang, K. Chang and X. Li. *Electrical properties of cold-pressing welded NbTi persistent joints.* Cryogenics (Guildf)., 58: pp. 62–67, 2013.

[6] R. F. Thornton. *Superconducting joint for superconducting wires and coils and method of of forming.* patent, US4907338, 1990.

[7] J. Cheng, J. Liu, Z. Ni, C. Cui, S. Chen, S. Song, L. Li, Y. Dai and Q. Wang. *Fabrication of NbTi superconducting joints for 400-MHz NMR application.* IEEE Trans. Appl. Supercond., 22(2), 2012.

[8] *L174/88.* Off. J. Eur. Union, 2011.

[9] *L4/61.* Off. J. Eur. Union, 2014.

[10] W. Buckel and R. Kleiner. *Superconductivity: Fundamentals and Applications.* Wiley-VCH, 2 edn., 2004.

[11] H. K. Onnes. *Further experiments with liquid helium. D. On the change of electrical resistance of pure metals at very low temperatures, etc.* Proc. KNAW, 14(1): pp. 113–115, 1911.

[12] H. K. Onnes. *Further experiments with liquid helium. J. The imitation of an Ampere molecular current or a permanent magnet by means of a supra-conductor.* Proc. KNAW, 17: p. 278, 1914.

[13] H. K. Onnes. *Further experiments with liquid helium. D. On the change of electrical resistance of pure metals at very low temperatures, etc.* Commun. Phys. Lab. Univ. Leiden Suppl., 29, 1911.

[14] J. Bardeen, L. N. Cooper and J. R. Schrieffer. *Theory of superconductivity.* Phys. Rev., 108(5): pp. 1175–1204, 1957.

[15] W. Meissner and R. Oshsenfeld. *Ein neuer Effekt bei Eintritt der Supraleitfähigkeit.* Naturwissenschaften, 21: p. 787, 1933.

[16] V. L. Ginzburg and L. D. Landau. *On the theory of superconductivity.* Zh. Eksp. Teor. Fiz., 20: p. 1064, 1950.

[17] A. A. Abrikosov. *Nobel Lecture: Type-II superconductors and the vortex lattice.* Rev. Mod. Phys., 76(3): pp. 975–979, 2004.

[18] D. Dew-Hughes. *Flux pinning mechanisms in type II superconductors.* Philos. Mag., 30(2): pp. 293–305, 1974.

[19] C. Bormio-Nunes, M. J. R. Sandim and L. Ghivelder. *Composition gradient as a source of pinning in Nb-Ti and NbTa-Ti superconductors.* J. Phys. Condens. Matter, 19(44), 2007.

[20] L. D. Cooley. *Flux-pinning mechanism of proximity-coupled planar defects in conventional superconductors : Evidence that magnetic pinning is the dominant pinning mechanism in niobium-titanium alloy.* Phys. Rev. B, 53(10): pp. 6638–6652, 1996.

[21] E. Giannini, R. Gladyshevskii, N. Clayton, N. Musolino, V. Garnier, A. Piriou and R. Fluekiger. *Growth, structure and physical properties of single crystals of pure and Pb-doped Bi-based high Tc superconductors.* Current Applied Physics, 8: pp. 1115–1119, 2008.

[22] D. Larbalestier, A. Gurevich, D. M. Feldmann and A. Polyanskii. *High Tc superconducting materials for electric power applications.* Nature, 414: pp. 368–377, 2001.

[23] M. Tomsic, M. Rindfleisch, J. Yue, K. McFadden, D. Doll, J. Phillips, M. D. Sumption, M. Bhatia, S. Bohnenstiehl and E. Collings. *Development of magnesium diboride (MgB2) wires and magnets using in situ strand fabrication method.* Phys. C Supercond., 456(1-2): pp. 203–208, 2007.

[24] B. Bordini, A. Ballarino, M. Macchini, D. Richter, B. Sailer, M. Thoener and K. Schlenga. *The bundle-barrier pit wire developed for the HiLumi LHC project.* IEEE Trans. Appl. Supercond., 27(4): pp. 1–6, 2017.

[25] Y. Huang, H. Miao, S. Hong and J. A. Parrell. *Bi-2212 round wire development for high field applications.* IEEE Trans. Appl. Supercond., 24(3): pp. 1–5, 2014.

[26] P. J. Lee. *Abridged Metallurgy of Ductile Alloy Superconductors*, 1999.

[27] D. Uglietti. *A review of commercial high temperature superconducting materials for large magnets: from wires and tapes to cables and conductors.* Supercond. Sci. Technol., 32(5): p. 053001, 2019.

[28] J. F. Kwak, E. L. Venturini and D. S. Ginley. *The consequences of intergrain Josephson coupling in ceramic high-temperature superconductors.* Phys. B, 148: pp. 426–428, 1987.

[29] C. Senatore, M. Alessandrini, A. Lucarelli, R. Tediosi, D. Uglietti and Y. Iwasa. *Progresses and challenges in the development of high-field solenoidal magnets based on RE123 coated conductors.* Supercond. Sci. Technol., 27(10), 2014.

[30] T. Schneider and P. Turowski. *Critical current degradation of a NbTi-multifilament conductor due to heat treatment.* IEEE Trans. Magn., 30(4): pp. 2391–2394, 1994.

[31] S. Liu, X. Jiang, G. Chai and J. Chen. *Superconducting joint and persistent current switch for a 7-T animal MRI magnet.* IEEE Trans. Appl. Supercond., 23(3): pp. 1–4, 2013.

[32] T. Fukuzaki, H. Maeda, S. Matsumoto, S. Nimori, S. Yokoyama and T. Kiyoshi. *Development of a superconducting joint for high field NMR.* IEEE Trans. Appl. Supercond., 16(2): pp. 1547–1549, 2006.

[33] G. Brittles. *Persistent current joints between NbTi superconducting wires.* Ph.D. thesis, University of Oxford, 2016.

[34] M. Kodama, K. Okamoto, Y. Koga, T. Yamamoto and H. Watanabe. *Analysis for formation of current path in the superconducting joint between Nb-Ti wires with the solder matrix replacement method.* Supercond. Sci. Technol., 28(4): p. 045019, 2015.

[35] K. Seo, S. Nishijima, K. Katagiri and T. Okada. *Evaluation of solders for superconducting magnetic shield.* IEEE Trans. Magn., 27(2): pp. 1877–1880, 1991.

[36] M. Hansen and K. Anderko. *Constitution of Binary Alloys.* McGraw-Hill, New York, 1958.

[37] C. Malseed and W. A. Rachinger. *Superconductivity in the lead-bismuth system.* Scr. Metall., 3(2): pp. 139–142, 1969.

[38] S. W. Yoon and H. M. Lee. *A thermodynamic study of phase equilibria in the Sn-Bi-Pb solder system.* Calphad, 22(2): pp. 167–178, 1998.

[39] H. W. King, C. M. Russell and J. A. Hulbert. *Superconducting transition temperatures in ϵ-phase Pb-Bi alloys.* Phys. Lett., 20(6): pp. 600–601, 1966.

[40] J. E. Evetts and J. M. A. Wade. *Superconducting properties and the phase diagrams of the Pb-Bi and Pb-In alloy systems.* J. Phys. Chem. Solids, 31(5): pp. 973–982, 1970.

[41] A. M. Campbell, J. E. Evetts and D. Dew-Hughes. *Pinning of flux vortices in type II superconductors.* Philos. Mag., 18(152): pp. 313–343, 1968.

[42] J. D. Livingston. *Superconducting properties of eutectics.* J. Appl. Phys., 38: pp. 2408–2410, 1967.

[43] T. Mousavi, C. Aksoy, C. R. M. Grovenor and S. C. Speller. *Microstructure and superconducting properties of Sn–In and Sn–In–Bi alloys as Pb-free superconducting solders.* Supercond. Sci. Technol., 29(1): p. 015012, 2016.

[44] S. A. Levy, Y. B. Kim and R. W. Kraft. *Effect of structure on the superconducting properties of eutectic alloys.* J. Appl. Phys., 37(10): pp. 3659–3665, 1966.

[45] W. H. Warren. *Superconductivity measurements in solders commonly used for low temperature research.* Rev. Sci. Instrum., 40(1): pp. 180–182, 1969.

[46] C. Aksoy, T. Mousavi, G. Brittles, C. R. M. Grovenor and S. C. Speller. *Lead-free solders for superconducting applications.* IEEE Trans. Appl. Supercond., 26(3): pp. 3–5, 2016.

[47] T. Heumann and O. Alpaut. *Das Zustandsdiagram Indium-Zinn.* J. Less Common Met., 6: pp. 108–117, 1964.

[48] H. Meissner. *Measurements on superconducting contacts.* Phys. Rev., 109(3): pp. 686–694, 1958.

[49] J. H. Wernick and B. T. Matthias. *Superconductivity in the In-Sn system.* J. Chem. Phys., 34(6): p. 2194, 1961.

[50] M. F. Merriam and M. Von Herzen. *Superconductivity in the indium-tin system.* Phys. Rev., 131(2): pp. 637–643, 1963.

[51] T. Mousavi, C. Aksoy, C. Grovenor and S. Speller. *Phase evolution of superconducting Sn–In–Bi solder alloys.* IEEE Trans. Appl. Supercond., 26(3): pp. 0–3, 2016.

[52] S. F. Bartram, W. G. Moffatt and B. W. Roberts. *The In-Sn Phase diagram and superconductivity in In_3Sn.* J. Less-Common Met., 62(C): pp. 9–12, 1978.

[53] I. Ohnuma, Y. Cui, X. J. Liu, Y. Inohana and S. Ishihara. *Phase equilibria of Sn-In based micro-soldering alloys.* J. Electron. Mater., 29(10): pp. 1113–1121, 2000.

[54] R. Kubiak, M. Wolcyrz and W. Zacharko. *Crystallization, decomposition and superconductivity of In_3Sn.* J. Less-Common Met., 65: pp. 263–269, 1979.

[55] T. Mousavi, W. Darby, C. Aksoy, T. Davies, G. Brittles, S. Speller, C. Grovenor and S. Speller. *Novel superconducting joints for persistent mode magnet applications.* MRS Adv., pp. 1–6, 2016.

[56] S. Santra, T. Davies, G. Matthews, J. Liu, C. Grovenor and S. Speller. *The effect of the size of NbTi filaments on interfacial reactions and the properties of lead-free superconducting solder joints.* Materials and Design, https://doi.org/10.1016/j.matdes.2019.107836, 2019. Accepted.

[57] G. D. Brittles, C. Aksoy, C. R. M. Grovenor, T. Bradshaw, S. Milward and S. C. Speller. *Microstructural properties and magnetic testing of spot-welded joints between Nb–Ti filaments.* IEEE Trans. Appl. Supercond., 26(3): pp. 11–14, 2016.

[58] J. Nuding. *Method of making a superconductive joint.* patent, US3422529: pp. 1963–1965, 1969.

[59] M. J. Leupold and Y. Iwasa. *Superconducting joint between multifilamentary wires 1. Joint-making and results.* Cryogenics (Guildf)., 16(4): pp. 215–216, 1976.

[60] D. G. Blair, H. Paik and R. C. Taber. *How to make high critical current joints in Ni–Ti wire.* Rev. Sci. Instrum., 46(8): p. 1130, 1975.

[61] T. Tominaka, S. Kakugawa, N. Hara and N. Maki. *Electrical properties of superconduciting joint between composite conductors.* IEEE Trans. Magn., 27(2): pp. 1846–1849, 1991.

[62] S. Phillip, J. V. Porto and J. M. Parpia. *Two methods of fabricating reliable superconducting joints with multifilamentary Nb-Ti superconducting wire.* J. Low Temp. Phys., 101: pp. 581–585, 1995.

[63] J. Cheng, L. Li, F. Zhou, J. Liu, C. Cui, X. Hu, Y. Dai, L. Yan, S. Cheng and Y. Li. *Contact resistance properties of cold-pressing superconducting joints.* IEEE Trans. Appl. Supercond., 25(3), 2015.

[64] N. Bay. *Mechanisms producing metallic bonds in cold welding.* Weld. J., 62(5): p. 137, 1983.

[65] F. Zhou, J. Cheng, Y. Dai, Q. Wang and L. Yan. *Numerical simulation of mold shape's influence on NbTi cold-pressing superconducting joint.* Phys. C Supercond., 498(6): pp. 9–13, 2014.

[66] F. Zhou, J. Cheng, J. Liu, Y. Dai, Q. Wang, N. Xiao and L. Yan. *Numerical simulation of NbTi superconducting joint with cold-pressing welding technology.* IEEE Trans. Appl. Supercond., 23(6), 2013.

[67] E. S. Rosenblum, S. H. Autler and K. H. Gooen. *The dependence of the upper critical field of niobium on temperature and resistivity.* Rev. Mod. Phys., 36: pp. 77–80, 1964.

[68] M. Kodama and T. Wakuda. *Superconducting joint and method for manufacturing same.* patent, US8385994, 2013.

[69] E. Thomson. *Spot welding thin sheets.* patent, US1085769, 1914.

[70] E. Karvonen and J.-M. Rayroux. *Electrical connection between superconductors.* patent, US3527876, 1970.

[71] G. Luderer, P. Dullenkopf and G. Laukien. *Superconducting joint between multifilamenary wires.* Cryogenics (Guildf)., 14(9): pp. 518–519, 1974.

[72] H. Wen, L. Lin and S. Han. *Joint resistance measurement using current-comparator for superconducting wires in high magnetic field.* IEEE Trans. Magn., 28(1): pp. 834–836, 1992.

[73] S. Mizumaki and A. Yamamoto. *Experimental study of current sharing and transfer in superconductor joint.* IEEE Trans. Appl. Supercond., 7(2): pp. 805–807, 1997.

[74] J. Hafstrom, D. Killpatrick, R. Niemann, J. Purcell and H. Thresh. *Joining NbTi superconductors by ultrasonic welding.* IEEE Trans. Magn., 13: pp. 94–96, 1977.

[75] M. D. Bird, S. Member, H. Bai, I. R. Dixon and A. V. Gavrilin. *Test Results of the 36 T , 1 ppm Series-Connected Hybrid Magnet System at the NHMFL.* IEEE Trans. Appl. Supercond., 29(2): pp. 1–5, 2019.

[76] H. W. Weijers, W. D. Markiewicz, A. V. Gavrilin, A. J. Voran, Y. L. Viouchkov, S. R. Gundlach, P. D. Noyes, D. V. Abraimov, H. Bai, S. T. Hannahs and T. P. Murphy. *Progress in the Development and Construction of a 32-T Superconducting Magnet.* IEEE Trans. Appl. Supercond., 26(4): pp. 1–7, 2016.

[77] H. Maeda, J.-I. Shimoyama, Y. Yanagisawa, Y. Ishii and M. Tomita. *The MIRAI Program and the New Super-High Field NMR Initiative and its Relevance to the*

Development of Superconducting Joints in Japan. IEEE Trans. Appl. Supercond., 29(2): p. 4602409, 2019.

[78] W. Yao, J. Bascunan, S. Hahn and I. Yukikazu. *A superconducting joint technique for MgB_2 round wires.* IEEE Trans. Appl. Supercond., 19(3): pp. 2261–2264, 2009.

[79] J. Ling, J. Voccio, Y. Kim, S. Hahn, J. Bascunan, D. K. Park and Y. Iwasa. *Monofilament MgB2 wire for a whole-body MRI magnet: Superconducting joints and test coils.* IEEE Trans. Appl. Supercond., 23(3): pp. 10–13, 2013.

[80] D. Patel, M. S. Al Hossain, K. Wai See, X. Xu, S. Barua, Z. Ma, S. Choi, M. Tomsic and J. Ho Kim. *MgB ₂ superconducting joints for persistent current operation.* Supercond. Sci. Technol., 28(6): p. 065017, 2015.

[81] D. Nardelli, S. Angius, A. Capelluto, D. Damiani, R. Marabotto, M. Modica, M. Perrella, M. Tassisto and A. Cables. *Persistent Mode MgB 2 Short Windings.* IEEE Trans. Appiled Supercond., 20(3): pp. 1998–2001, 2010.

[82] P. Chen, U. P. Trociewitz, D. S. Davis, E. S. Bosque, D. K. Hilton, Y. Kim, D. V. Abraimov, W. L. Starch, J. Jiang, E. E. Hellstrom and D. C. Larbalestier. *Development of a persistent superconducting joint between Bi-2212/Ag-alloy multifilamentary round wires.* Supercond. Sci. Technol., 30(2), 2017.

[83] Y. Park, M. Lee, H. Ann, Y. H. Choi and H. Lee. *A superconducting joint for $GdBa_2Cu_3O_7$ coated conductors.* NPG Asia Mater., 6(5): p. e98, 2014.

[84] X. Jin, Y. Yanagisawa, H. Maeda and Y. Takano. *Development of a superconducting joint between a $GdBa_2Cu_3O_7$ coated conductor and $YBa_2Cu_3O_7$ bulk: towards a superconducting joint between RE (rare earth) $BaCu_2O_7$ coated conductors.* Supercond. Sci. Technol., 28(7): p. 075010, 2015.

[85] X. Jin. *Measurement of Persistent Current in a Gd123 Coil With a Superconducting Joint Fabricated by the CJMB Method.* IEEE Trans. Appl. Supercond., 28(3): pp. 1–4, 2018.

[86] K. Ohki, T. Nagaishi, T. Kato, D. Yokoe, T. Hirayama, Y. Ikuhara, T. Ueno, K. Yamagishi, T. Takao, R. Piao, H. Maeda and Y. Yanagisawa. *Fabrication , microstructure and persistent current measurement of an intermediate grown superconducting (iGS) joint between REBCO-coated conductors.* Supercond. Sci. Technol., 30: p. 115017, 2017.

[87] R. Matsumoto, H. Iwata, A. Yamashita, H. Hara, G. Nishijima, M. Tanaka, H. Tayeka and Y. Takano. *Superconducting joints using Bi-added PbSn solders.* Appl. Phys. Express, 10: p. 093102, 2017.

[88] T. Mousavi, T. Davies, Z. Melhem, C. R. M. Grovenor and S. C. Speller. *Development of Superconducting Soldered Joints Between Bi-2212 / Ag Wires.* 28(4): pp. 5–7, 2018.

[89] M. Grundner and J. Halbritter. *On the natural Nb_2O_5 growth on Nb at room temperature.* Surf. Sci., 136: pp. 144–154, 1984.

[90] D. Eastman. *Photoemission energy level measurements of sorbed gases on titanium.* Solid State Commun., 10(10): pp. 933–935, 1972.

[91] K. R. Lawless. *The oxidation of metals.* Reports Prog. Phys., 37(1): pp. 231–316, 1974.

[92] T. Hurlen. *Oxidation of niobium.* J. Inst. Met., 89(1): pp. 273–280, 1960.

[93] J. S. Sheasby. *The oxidation of niobium in the temperature range 450°–720°C.* J. Electrochem. Soc., 115(7): pp. 695–700, 1968.

[94] I. Lindau and W. E. Spicer. *Oxidation of Nb as studied by the uv-photoemission technique.* J. Appl. Phys., 45(9): pp. 3720–3725, 1974.

[95] J. Halbritter. *Low temperature oxidation of Nb and of Nb-compounds in relation to superconducting application.* J. Less-Common Met., 139(1): pp. 133–148, 1988.

[96] A. Daccà, G. Gemme, L. Mattera and R. Parodi. *XPS analysis of the surface composition of niobium for superconducting RF cavities.* Appl. Surf. Sci., 126(3-4): pp. 219–230, 1998.

[97] M. Delheusy, A. Stierle, N. Kasper, R. P. Kurta, A. Vlad, H. Dosch, C. Antoine, A. Resta, E. Lundgren and J. Andersen. *X-ray investigation of subsurface interstitial oxygen at Nb/oxide interfaces.* Appl. Phys. Lett., 92(10): pp. 9–12, 2008.

[98] T. Hryniewicz, K. Rokosz and H. R. Z. Sandim. *SEM / EDX and XPS studies of niobium after electropolishing.* Appl. Surf. Sci., 263: pp. 357–361, 2012.

[99] T. Hurlen, H. Bentzen and S. Hornkjol. *Passive behaviour of niobium.* Electrochim. Acta, 32(11): pp. 1613–1617, 1987.

[100] B. R. King, H. C. Patel, D. A. Gulino and B. J. Tatarchuk. *Kinetic measurements of oxygen dissolution into niobium substrates: in situ X-ray photoelectron spectroscopy studies.* Thin Solid Films, 192: pp. 351–369, 1990.

[101] Q. Ma and R. A. Rosenberg. *Angle-resolved X-ray photoelectron spectroscopy study of the oxides on Nb surfaces for superconducting r.f. cavity applications.* Appl. Surf. Sci., 206(1–4): pp. 209–217, 2003.

[102] K. J. S. Sokhey, S. K. Rai and G. S. Lodha. *Oxidation studies of niobium thin films at room temperature by X-ray reflectivity.* Appl. Surf. Sci., 257(1): pp. 222–226, 2010.

[103] M. David Henry, S. Wolfley, T. Monson, B. G. Clark, E. Shaner and R. Jarecki. *Stress dependent oxidation of sputtered niobium and effects on superconductivity.* J. Appl. Phys., 115(8): p. 083903, 2014.

[104] C. O. A. Olsson and D. Landolt. *Atmospheric oxidation of a Nb-Zr alloy studied with XPS.* Corros. Sci., 46(1): pp. 213–224, 2004.

[105] A. F. Carley, P. R. Chalker, J. C. Riviere and M. W. Roberts. *The identification and characterisation of mixed oxidation states at oxidised titanium surfaces by analysis of X-ray photoelectron spectra.* J. Chem. Soc. Faraday Trans. 1, 83(2): p. 351, 1987.

[106] J. Pouilleau, D. Devilliers, F. Garrido, S. Durand-Vidal and E. Mahé. *Structure and composition of passive titanium oxide films.* Mater. Sci. Eng. B, 47(i): pp. 235–243, 1997.

[107] E. McCafferty and J. Wightman. *An X-ray photoelectron spectroscopy sputter profile study of the native air-formed oxide film on titanium.* Appl. Surf. Sci., 143(1-4): pp. 92–100, 1999.

[108] G. Lu, S. L. Bernasek and J. Schwartz. *Oxidation of a polycrystalline titanium surface by oxygen and water.* Surf. Sci., 458(1): pp. 80–90, 2000.

[109] A. Platau, L. I. Johansson, A. L. Hagström, S. E. Karlsson and S. B. M. Hagström. *Oxidation of cerium and titanium studied by photoelectron spectroscopy.* Surf. Sci., 63: pp. 153–161, 1977.

[110] N. R. Armstrong and R. K. Quinn. *Auger and X-ray photoelectron spectroscopic and electrochemical characterization of titanium thin film electrodes.* Surf. Sci., 67(2): pp. 451–468, 1977.

[111] B. Siemensmeyer and J. Schultze. *XPS and UPS studies of gas-phase oxidation, electrochemistry and corrosion behaviour of Ti and Ti-5Ta.* Surf. Interface Anal., 16: pp. 1–6, 1990.

[112] M. F. Sunding, I. T. Jensen, P. M. Stenstad and S. Diplas. *ARXPS and high energy XPS characterisation of titanium surfaces for medical implants.* Surf. Interface Anal., 40(3-4): pp. 751–753, 2008.

[113] P. Pérez, V. A. C. Haanappel and M. F. Stroosnijder. *The effect of niobium on the oxidation behaviour of titanium in N_2/20% O_2 atmospheres.* Mater. Sci. Eng. A, 284(1-2): pp. 126–137, 2000.

[114] Y. Wouters, A. Galerie and J.-P. Petit. *Thermal oxidation of titanium by water vapour.* Solid State Ionics, 104(1-2): pp. 89–96, 1997.

[115] A. Azoulay, N. Shamir, V. Volterra and M. Mintz. *Water vapor interactions with polycrystalline titanium surfaces.* Surf. Sci., 422: pp. 141–153, 1999.

[116] G. Zorn, A. Lesman and I. Gotman. *Oxide formation on low modulus Ti-45Nb alloy by anodic versus thermal oxidation.* Surf. Coatings Technol., 201(3-4): pp. 612–618, 2006.

[117] N. Ohtsu, N. Masahashi and Y. Mizukoshi. *Angle resolved XPS studies on an anodic oxide formed on Ti-Nb-Sn alloy and the photo-induced change in carbon contaminants adsorbed on its surface.* Appl. Surf. Sci., 258(16): pp. 6052–6055, 2012.

[118] M. F. Lopez, L. Soriano, F. J. Palomares, M. Sanchez-Agudo, G. G. Fuentes, A. Gutierrez and J. A. Jimenez. *Soft x-ray absorption spectroscopy study of oxide layers on titanium alloys.* Surf. Interface Anal., 33: pp. 570–576, 2002.

[119] M. Göttlicher, M. Rohnke, A. Helth, T. Leichtweiß, T. Gemming, A. Gebert, J. Eckert and J. Janek. *Controlled surface modification of Ti–40Nb implant alloy by electrochemically assisted inductively coupled RF plasma oxidation.* Acta Biomater., 9(11): pp. 9201–9210, 2013.

[120] Y. Tanaka, M. Nakai, T. Akahori, M. Niinomi, Y. Tsutsumi, H. Doi and T. Hanawa. *Characterization of air-formed surface oxide film on Ti-29Nb-13Ta-4.6Zr alloy surface using XPS and AES.* Corros. Sci., 50(8): pp. 2111–2116, 2008.

[121] R. Prozorov and V. G. Kogan. *Effective demagnetization factors of diamagnetic samples of various shapes.* pp. 1–13, 2017.

[122] A. M. Campbell, F. J. Blunt, J. D. Johnson and P. A. Freeman. *Quantitative determination of percentage superconductor in a new compound.* Cryogenics, 31: pp. 732–737, 1991.

[123] C. P. Bean. *Magnetization of hard superconductors.* Phys. Rev. Lett., 8(6): pp. 250–253, 1962.

[124] D. N. Zheng, P. L. Lang, J. Y. Xiang and Z. X. Zhao. *Determination of irreversibility fields in low temperature superconductors.* Phys. C Supercond., 386: pp. 14–17, 2003.

[125] G. D. Brittles, P. Noonan, S. A. Keys, C. R. M. Grovenor and S. Speller. *Rapid characterisation of persistent current joints by SQUID magnetometry.* Supercond. Sci. Technol., 27(12), 2014.

[126] D. Ryan, H. Jones, W. Timms and N. Killoran. *Critical current measurements at electric fields in the $pV\ m^{-1}$ regime.* IEEE Trans. Appl. Supercond., 7(2): pp. 1455–1458, 1997.

[127] A. V. Pan, I. A. Golovchanskiy and S. A. Fedoseev. *Critical current density: Measurements vs. reality.* EPL, 103(1), 2013.

[128] D. Ryan. *Critical currents of commercial superconductors in the picovolt per metre electric field regime.* Ph.D. thesis, University of Oxford, 1997.

[129] L. Goodrich and F. Fickett. *Critical current measurements: A compendium of experimental results.* Cryogenics (Guildf)., 22(5): pp. 225–241, 1982.

[130] A. Einstein. *Über einen die erzeugung und verwandlung des lichtes betreffenden heuristischen gesichtspunkt.* Annalen der Physik, 17(6): pp. 132–148, 1905.

[131] P. J. Cumpson. *Angle-resolved XPS and AES: Depth-resolution limits and a general comparison of properties of depth-profile reconstruction methods.* J. Electron Spectros. Relat. Phenomena, 73(1): pp. 25–52, 1995.

[132] J. H. Scofield. *Hartree-Slater subshell photoionization cross-sections at 1254 and 1487 eV.* J. Electron Spectros. Relat. Phenomena, 8(2): pp. 129–137, 1976.

[133] D. F. Mitchell, K. B. Clark, J. A. Bardwell, W. N. Lennard, G. R. Massoumi and I. V. Mitchell. *Film Thickness Measurements of SiO_2 by XPS.* Surf. Interface Anal., 21(August 1993): pp. 44–50, 1994.

[134] B. R. Strohmeier. *an Esca Method for Determining the Oxide Thickness on Aluminum-Alloys.* Surf. Interface Anal., 15(1): pp. 51–56, 1990.

[135] C. Chen, S. J. Splinter, T. Do and N. S. McIntyre. *Measurement of oxide film growth on Mg and Al surfaces over extended periods using XPS.* Surf. Sci., 382(1–3): pp. L652–L657, 1997.

[136] P. van der Heide. *X-ray Photoelectron Spectroscopy: An Introduction to Principles and Practices.* Wiley, 2012.

[137] R. W. Paynter. *An ARXPS primer.* J. Electron Spectros. Relat. Phenomena, 169(1): pp. 1–9, 2009.

[138] M. Seah and W. Dench. *Quantitative electron spectroscopy of surfaces: A standard data base for electron inelastic mean free paths in solids.* Surf. Interface Anal., 1(1): pp. 2–11, 1979.

[139] S. Tanuma, C. J. Powell and D. R. Penn. *Calculations of electron inelastic mean free paths. V. Data for 14 organic compounds over the 50–2000 eV range.* Surf. Interface Anal., 21(3): pp. 165–176, 1994.

[140] A. Regoutz, M. Maschek, T. Wiell, C. Liljenberg, S. K. Eriksson, B. A. D. Williamson, D. O. Scanlon, K. Tetzner and P. Palmgren. *A novel laboratory-based hard X-ray photoelectron spectroscopy system.* Rev. Sci. Instrum., 89(7): p. 073105, 2018.

[141] S. Oswald and W. Brückner. *XPS depth profile analysis of non-stoichiometric NiO films.* Surf. Interface Anal., 36(1): pp. 17–22, 2004.

[142] J. B. Gilbert, M. F. Rubner and R. E. Cohen. *Depth-profiling X-ray photoelectron spectroscopy (XPS) analysis of interlayer diffusion in polyelectrolyte multilayers.* Proc. Natl. Acad. Sci., 110(17): pp. 6651–6656, 2013.

[143] I. N. Demchenko, Y. Melikhov, Y. Syryanyy, I. Zaytseva, P. Konstantynov and M. Chernyshova. *Effect of argon sputtering on XPS depth-profiling results of Si/Nb/Si.* J. Electron Spectros. Relat. Phenomena, 224: pp. 17–22, 2018.

[144] P. C. Karulkar. *Effects of sputtering on the surface composition of niobium oxides.* J. Vac. Sci. Technol., 18(2): pp. 169–174, 1981.

[145] T. Choudhury, S. O. Saied, J. L. Sullivan and A. M. Abbot. *Reduction of oxides of iron, cobalt, titanium and niobium by low-energy ion bombardment.* J. Phys. D. Appl. Phys., 22(8): pp. 1185–1195, 1989.

[146] T. A. Carlson. *Basic assumptions and recent developments in quantitative XPS.* Surf. Interface Anal., 4(4): pp. 125–134, 1982.

[147] D. A. Shirley. *High-resolution x-ray photoemission spectrum of the valence bands of gold.* Phys. Rev. B, 5(12): pp. 4709–4714, 1972.

[148] S. Tougaard. *Quantitative analysis of the inelastic background in surface electron spectroscopy.* Surf. Interface Anal., 11(9): pp. 453–472, 1988.

[149] N. Fairley. *CasaXPS Manual 2.3.15.* Casa Software Limited.

[150] P. Kofstad. *High-temperature oxidation of titanium.* J. Less Common Met., 12(6): pp. 449–464, 1967.

[151] M. Wolff, J. W. Schultze and H. Strehblow. *Low-energy implantation and sputtering of TiO_2 by nitrogen and argon and the electrochemical reoxidation.* Surf. Interface Anal., 17: pp. 726–736, 1991.

[152] M. C. Biesinger, B. P. Payne, A. P. Grosvenor, L. W. M. Lau, A. R. Gerson and R. S. C. Smart. *Resolving surface chemical states in XPS analysis of first row transition metals, oxides and hydroxides: Cr, Mn, Fe, Co and Ni.* Appl. Surf. Sci., 257(7): pp. 2717–2730, 2011.

[153] R. Nyholm, N. Martensson, A. Lebuglet and U. Axelsson. *Auger and Coster-Kronig broadening effects in the 2p and 3p photoelectron spectra from the metals 22Ti-30Zn.* J. Phys. F Met. Phys., 11(8): pp. 1727–1733, 1981.

[154] T. A. Sasaki and Y. Baba. *Chemical-state studies of Zr and Nb surfaces exposed to hydrogen ions.* Phys. Rev. B, 31(2): pp. 791–797, 1985.

[155] M. K. Bahl. *ESCA studies of some niobium compunds.* J. Phys. Chem. Solids, 36: pp. 485–491, 1975.

[156] R. Fontaine, R. Caillat, L. Feve and M. J. Guittet. *Deplacement chimique ESCA dans la serie des oxydes du niobium.* J. Electron Spectros. Relat. Phenomena, 10(4): pp. 349–357, 1977.

[157] Q. Ma, P. Ryan, J. W. Freeland and R. A. Rosenberg. *Thermal effect on the oxides on Nb(100) studied by synchrotron-radiation x-ray photoelectron spectroscopy.* J. Appl. Phys., 96(12): pp. 7675–7680, 2004.

[158] M. C. Biesinger. *ww.xpsfitting.com/2009/04/niobium.html.*

[159] J. Liu, J. Cheng and Q. Wang. *Evaluation of NbTi superconducting joints for 400 MHz NMR magnet.* IEEE Trans. Appl. Supercond., 23(6): pp. 2–7, 2013.

[160] A. Darlinski and J. Halbritter. *Angle-resolved XPS studies of oxides at NbN , NbC , and Nb surfaces.* Surf. Interface Anal., 10: pp. 223–237, 1987.

[161] P. L. J. Gunter and J. W. Niemantsverdriet. *Thickness determination of uniform overlayers on rough substrates by angle-dependent XPS.* Appl. Surf. Sci., 89(1): pp. 69–76, 1995.

[162] P. Gunter, O. Gijzeman and J. Niemantsverdriet. *Surface roughness effects in quantitative XPS: magic angle for determining overlayer thickness.* Appl. Surf. Sci., 115(4): pp. 342–346, 1997.

[163] J. E. Boggio and R. C. Plumb. *Theory of formation of very thin oxide films on metals.* The Journal of Chemical Physics, 44(3): pp. 1081–1086, 1966.

[164] N. Cabrera and N. F. Mott. *Theory of the oxidation of metals.* Reports Prog. Phys., 12(1): pp. 163–184, 1944.

[165] S. Tougaard and H. S. Hansen. *Non-destructive depth profiling through quantitative analysis of surface electron spectra.* Surf. Interface Anal., 14(11): pp. 730–738, 1989.

[166] M. Schleberger, D. Fujita, C. Scharfschwerdt and S. Tougaard. *Growth and in-depth distribution of thin metal films on silicon (111) studied by XPS: inelastic peak shape analysis.* Surf. Sci., 331-333(PART B): pp. 942–947, 1995.

[167] E. D. Richmond. *X-ray photoelectron spectroscopy analysis of the growth kinetics of Ge on Si(001).* Thin Solid Films, 252(2): pp. 98–104, 1994.

[168] A. I. Martín-Concepción, F. Yubero, J. P. Espinós and S. Tougaard. *Surface roughness and island formation effects in ARXPS quantification.* Surf. Interface Anal., 36(8): pp. 788–792, 2004.

[169] M. Delheusy, A. Stierle, N. Kasper, R. P. Kurta, A. Vlad, H. Dosch, C. Antoine, A. Resta, E. Lundgren and J. Andersen. *X-ray investigation of subsurface interstitial oxygen at Nb/oxide interfaces.* Appl. Phys. Lett., 92(10), 2008.

[170] D. C. Larbalestier and P. J. Lee. *New developments in niobium titanium superconductors.* Proc. Part. Accel. Conf., 2: pp. 1276–1281, 1995.

[171] *http://www.supercon-wire.com/content/nbti-superconducting-wires.*

[172] W. H. Warnes. *A model for the resistive critical current transition in composite superconductors.* J. Appl. Phys., 63(5): p. 1651, 1988.

[173] L. Bottura. *A practical fit for the critical surface of NbTi.* Tech. rep., 2000.

[174] C. Meingast and D. C. Larbalestier. *Quantitative description of a very high critical current density Nb-Ti superconductor during its final optimization strain. II. Flux pinning mechanisms.* J. Appl. Phys., 66(12): pp. 5971–5983, 1989.

[175] C. Meingast, P. J. Lee and D. C. Larbalestier. *Quantitative description of a high Jc Nb-Ti superconductor during its final optimization strain. I. Microstructure, Tc, Hc2, and resistivity.* J. Appl. Phys., 66(12): pp. 5962–5970, 1989.

[176] L. Muzzi, G. De Marzi, C. Fiamozzi Zignani, L. Affinito, M. Napolitano, R. Viola, C. O. Dominguez, L. Bottura, S. Le Naour, D. Richter and A. Della Corte. *Pinning properties of commercial Nb-Ti wires described by a 2-components model.* IEEE Trans. Appl. Supercond., 20(3): pp. 1496–1499, 2010.

[177] C. Scheuerlein, I. Pong, C. Senatore, M. D. Michiel, L. Thilly, A. Gerardin, B. Rehmer, L. Oberli, G. Willering and L. Bottura. *Temperature induced degradation of Nb-Ti/Cu composite superconductors.* J. Phys. Conf. Ser., 234(2): p. 022031, 2010.

[178] E. J. Garboczi, K. A. Snyder, J. F. Douglas and M. F. Thorpe. *Geometrical percolation threshold of overlapping ellipsoids.* Phys. Rev. E, 52(1): pp. 819–828, 1995.

[179] B. Y. Lee, S. T. Kang, H. B. Yun and Y. Y. Kim. *Improved sectional image analysis technique for evaluating fiber orientations in fiber-reinforced cement-based materials.* Materials, 9(42), 2016.

[180] Z. Fan. *Semisolid metal processing.* Int. Mater. Rev., 47(2): pp. 1–37, 2002.

[181] Y. Tsui, E. Surrey and D. Hampshire. *Soldered joints—an essential component of demountable high temperature superconducting fusion magnets.* Supercond. Sci. Technol., 29(7): p. 075005, 2016.

[182] D. Saint-James and P. Gennes. *Onset of superconductivity in decreasing fields.* Phys. Lett., 7(5): pp. 306–308, 1963.

[183] M. A. Angadi, A. D. Caplin, J. R. Laverty and Z. X. Shen. *Non-destructive determination of the current-carrying length scale in superconducting crystals and thin films.* Phys. C Supercond., 177(4-6): pp. 479–486, 1991.

[184] B. W. Roberts. *Superconductive materials and some of their properties.*

[185] P. G. De Gennes. *Impurity and boundary effects in superconductors.* Rev. Mod. Phys., pp. 225–237, 1964.

[186] Y. Chong, N. Hadacek, P. D. Dresselhaus, C. J. Burroughs, B. Baek and S. P. Benz. *Josephson junctions with nearly superconducting metal silicide barriers.* Appl. Phys. Lett., 87(22): pp. 1–3, 2005.

[187] K. A. Delin and A. W. Kleinsasser. *Stationary properties of high-critical-temperature proximity effect Josephson junctions.* Supercond. Sci. Technol, 9: pp. 227–269, 1996.